The Dissertation Committee for Justin Lawrence Wagner Certifies that this is the approved version of the following dissertation:

Experimental Studies of Unstart Dynamics in Inlet / Isolator Configurations in a Mach 5 Flow

Committee:

Clemens, Noel T., Supervisor

Bogard, David G.

Dolling, David S.

Raman, Venkat

Varghese, Phillip L.

Experimental Studies of Unstart Dynamics in Inlet / Isolator Configurations in a Mach 5 Flow

by

Justin Lawrence Wagner, B.S.

Dissertation

Presented to the Faculty of the Graduate School of

The University of Texas at Austin

in Partial Fulfillment

of the Requirements

for the Degree of

Doctor of Philosophy

The University of Texas at Austin

May 2009

Dedication

I would like to dedicate this to my parents who have always encouraged me that anything worth doing requires hard work and to Crystal for her loving support, which seemed to make everything a whole lot less stressful.

Acknowledgements

First and foremost I would like to thank my advisor Dr. Noel T. Clemens for giving me the chance to work on this project. I greatly appreciate the opportunity and all that he has taught me. I also would like to acknowledge the others who have worked directly on this project. Without them, this work would pale in comparison. Thank you to Jeff Searcy who always remained cool, calm and collected no matter what. I also thank Dr. Bharath Ganapathisubramani or Bugs, for all of his help, advice and encouragement. I feel that I learned a lot from observing his attitude on research and on life in general. Thank you to Agustin Valdivia who always worked very hard and helped make the experiments run smoothly. Thanks are owed to Dr. Bulent Yuceil who was invaluable to this project and spent very many long days and nights helping to get PIV data. In addition, I thank Eddie Zihlman for his help answering general questions that no else knew the answer to and for his extra effort in trying problems such as a broken compressor. I also thank each of the members on my committee for their advice and support. Thanks are also owed to Donna Soward for making life easier by seamlessly dealing with paper work, orders and travel arrangements. An acknowledgement is also given to machinist David Gray for making many challenging parts and taking great pride in their perfection. I also greatly appreciate the help and friendship of my fellow graduate students. Thanks are given to Pablo Bueno, Mirko Gamba, Krishna Lakshminarasimhan, Kevin Marr, Zach Murphree, Venkat Narayanaswamy and Mike Ryan for all of their help over the years.

Finally, this work was supported by the U.S. Air Force Office of Scientific Research under the MURI grant FA9550-04-1-0387. This source of support is gratefully acknowledged.

Experimental Studies of Unstart Dynamics in Inlet / Isolator Configurations in a Mach 5 Flow

Publication No._____________

Justin Lawrence Wagner, Ph.D.
The University of Texas at Austin, 2009

Supervisor: Noel T. Clemens

The dynamics of the unstart process in inlet / isolator models mounted to the floor of a Mach 5 wind tunnel are investigated experimentally. The most extensively studied model has an inlet section that contains a 6-degree compression ramp and the isolator is a rectangular straight duct that is 25.4 mm high by 50.8 mm wide by 242.3 mm long. Unstart is initiated by raising a motor-driven flap that is located at the downstream end of the isolator section. Unstart proceeds with the formation of a shock system that propagates upstream at an average velocity of about 37 m/s (in the lab frame of reference), which is five percent of the freestream velocity. Unstart is seen to be associated with strong shock-induced separation that leads to reverse flow velocities up to about 300 m/s as measured by PIV. Both the schlieren imaging and PIV data suggest the dynamics and flow structure of the unstart process are dependent on inlet geometry. Furthermore, the PIV data indicate the unstart process to be highly three-dimensional. Finally, tripping the ceiling and sidewall boundary layers was seen to result in slower unstart processes.

In addition, results are presented for 0-degree (no inlet) and 8-degree inlet / isolator models. In the 0-degree model, the experimental data show that the flow structure and propagation velocities of the unstart shock system are much more constant than those measured in unstart events with an inlet. In addition, an increased inlet compression angle appears to result in an increased unstart propagation velocity in the isolator. This is possibly related to the fact that with an increased compression ramp angle, the unstart shock system propagates against a lower momentum opposing flow. Furthermore, the inlet geometry is also seen to affect the flow that follows the unstart process.

Experiments were also conducted with each of the three inlets attached to a shortened isolator. The short-isolator experiments showed it was possible to form a stable high-compression shock system in the isolator by raising the flap. This was not the case in longer isolator tests.

Table of Contents

List of Figures

List of Tables

Nomenclature

A_i = inlet entrance area

A_t = inlet throat area

a = speed of sound

b = isolator aspect ratio (width: height)

C_p = specific heat at constant pressure

C_v = specific heat at constant volume

D_θ = asymmetry parameter (Wang. et al. 2006)

d_e = particle image diameter

d_I = interrogation window diameter (width)

d_p = agglomerated TiO_2 particle diameter

d_r = CCD pixel width

d_s = diffraction limited spot size of particle

d_τ = recorded particle image diameter

f = frequency

f^* = normalized frequency $= f\,L\,/a_0$

$f^\#$ = lens f-number (aperture setting)

H_0 = inlet entrance height

h = isolator height

Kn = Knudsen number

k_B = Boltzmann’s constant

L = model length

M = Mach number

M_0 = image magnification

n = number of samples

P = pressure

Pr = Prandtl number

Re = Reynolds Number

RMS = root-mean-square

S_t = Stokes number

SPL = sound pressure level (reference pressure = 20 μPa)

t = time

T = temperature

U = streamwise velocity

u_1 = velocity upstream of a velocity step change (i.e., shock)

u_2 = velocity downstream of a velocity step change (i.e., shock)

u_p = particle velocity

V = wall-normal velocity

W = spanwise velocity

x = streamwise coordinate

X_p = particle distance traveled

y = wall-normal coordinate

w = spanwise coordinate

α = correlation fit parameter (Wang et al. 2006)

γ = ratio of specific heats (C_p / C_v)

δ = boundary layer thickness

δ^* = displacement thickness

δ_{Cal} = PIV calibration (image registration) uncertainty

δ_{Prec} = PIV precision uncertainty

δ_{Proc} = PIV processing and camera noise uncertainty

$\delta_{\Delta t}$ = laser pulse separation time uncertainty

δ = boundary layer thickness

θ = momentum thickness

θ_i = flow turning angle for incipient separation

θ_f = flap angle

λ = wavelength

Λ = mean free path

μ = dynamic viscosity

ρ_p = particle diameter (Wang et al. 2006)

σ = standard deviation

σ_{coll} = molecular collision diameter

τ = formation of high-compression shock system time

τ_p = particle response time

ϕ = high-amplitude unstarted flow cycle time

Subscripts

0 = plenum

1 = at the entrance of a high-compression shock system

∞ = freestream condition

ci = combustor entrance

cl = centerline

d = downstream

m = mean

p = particle

u = upstream

CHAPTER 1

1. Introduction

1.1 THE DUAL-MODE ENGINE CONCEPT

High-speed air breathing propulsion is an active area of research and development. For flight Mach numbers less than about 3.5 to 4, thermodynamic analysis shows that it is beneficial to use an engine with a turbine-driven compressor (i.e, a turbojet). However, for flight Mach numbers greater than 3.5 to 4, thermodynamic analysis shows that a compressor is no longer required and the ramjet engine becomes more efficient than the turbojet engine (Hill and Peterson, 1992). In the ramjet engine, the incoming airflow is slowed to subsonic speeds prior to combustion through a system of shock waves. A typical ramjet engine has two physical throats. The first throat is used to bring the flow to subsonic speeds necessary for combustion and the second is used to expand the post-combustion flow to supersonic exit velocities.

Scramjet and ramjet engines are developing technologies that will enable a future generation of hypersonic atmospheric and space vehicles. Ramjet engines are typically used for high-supersonic to low-hypersonic flight Mach numbers of about 3 to 6 (Heiser and Pratt, 1994). If the flight Mach number is greater than about 6, problems associated with compressing the flow to subsonic speeds render the ramjet ineffective. These problems include high normal shock losses, pressures too great for burner structural integrity, large wall heat transfer rates and chemical energy losses resulting from dissociation (Hill and Peterson, 1992 and Heiser and Pratt, 1994). A way to avoid these problems is to have lower compression by allowing the flow to remain fully supersonic throughout the engine. If the flow remains supersonic throughout, the engine is known as a supersonic combustion ramjet or scramjet. In the scramjet no throat is needed since the flow remains supersonic throughout and can therefore be expanded by a simple diverging nozzle.

The dual-mode engine concept proposed by Curran and Stull (1964) combines the ideas behind the ramjet and scramjet engine. The dual-mode concept allows the engine to act in ramjet mode at lower supersonic to hypersonic flight Mach numbers and then transition to scramjet mode at higher hypersonic flight Mach numbers. Since the dual-mode proposal in 1963, much work has gone into understanding the complex flow fields involved, improving the performance of such engines, and developing methods of practical implementation.

An example dual-mode engine schematic from Andreadis (2004) is given in Fig. 1.1. The flow in the figure is from right to left. Note the figure is meant to illustrate an engine mounted on the underside of a vehicle, such as the case of the X-43 (e.g., Cokrell et al., 2002). The compression of the freestream air begins with the vehicle forebody shock seen on the far right of the figure. Proceeding downstream, the flow then enters the inlet, which is seen in semi-transparent shade with aft-swept sidewalls. The flow is compressed further in the internal inlet with a series of three oblique shock waves. The next component seen in Fig. 1.1 is the isolator. This component provides for further compression and flow stabilization (Heiser and Pratt, 1994 and Curran et al., 1996). The type of flow within the isolator depends on the mode of operation of the engine (i.e., ramjet or scramjet mode). Moving downstream, the next component seen is the combustor. As will be discussed, the conditions in the combustor dictate the pre-combustion flow that will be present in the isolator. After combustion, the flow is expanded with both the internal nozzle and the geometry of the vehicle afterbody. Note that like the conventional scramjet engine, the dual-mode engine does not require a physical throat. Therefore, in principal variable geometry is not required for transition from the ramjet to scramjet mode of operation or vice-versa.

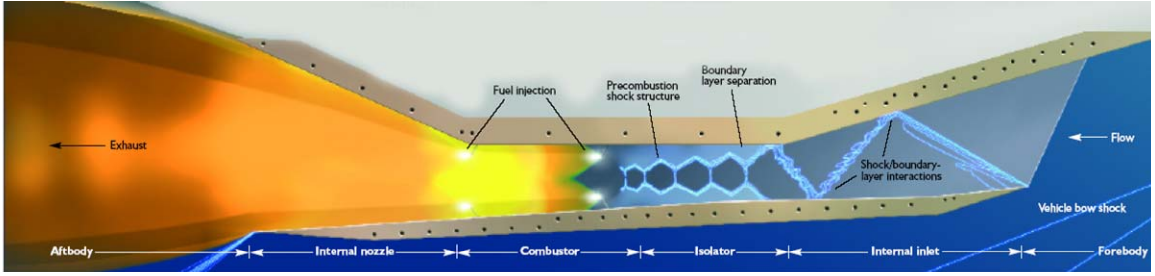

Figure 1.1 Schematic of a dual-mode engine (Andreadis, 2004).

1.2 DUAL-MODE ENGINE COMPONENTS AND MODES OF OPERATION

1.2.1 Combustor

Since the inlet and isolator components are designed to meet the conditions required for combustion, combustor design considerations, specifically maximum entrance temperature are first discussed. A significant reduction in thermodynamic efficiency is associated with combustor temperatures that are high enough to cause significant gas dissociation (Heiser and Pratt, 1994). The energy lost in dissociating the gas decreases the nozzle exit velocity and therefore lowers the propulsive, thermal and overall efficiencies of the engine. In order to avoid dissociation, the gas temperature must be kept below a threshold value. This can be achieved by keeping the temperature at the combustor entrance below about 1560 K (Heiser and Pratt, 1994). Taking the pre-combustion compression process to be adiabatic, a relationship can be derived that gives the combustor entrance Mach number (M_{ci}) in terms of the combustor entrance temperature (T_{ci}), freestream temperature (T_∞) and freestream Mach number (M_∞):

$$M_{ci} = \sqrt{\frac{2}{\gamma-1}\left\{\frac{T_\infty}{T_{ci}}\left(1+\frac{\gamma-1}{2}M_\infty^2\right)-1\right\}} \qquad (1.1)$$

where γ is the specific heat ratio (i.e., C_p / C_v). For example, substituting unity for the combustor entrance Mach number gives the limiting flight Mach number for subsonic combustion. Taking the freestream temperature to be 220 K, which is appropriate for flight in the lower stratosphere, and taking T_{ci} to be 1560 K results in a freestream Mach number of about 6.1 for sonic combustion. Therefore, for flight Mach numbers greater than about 6, supersonic combustion is required. Further simplification is made in the hypersonic limit where Equation 1.1 reduces to

$$M_{ci} = M_{\infty}\sqrt{\frac{T_{\infty}}{T_{ci}}} \tag{1.2}$$

Again, if the freestream temperature is taken to be 220 K and T_{ci} = 1560 K, equation 1.2 becomes the common rule of thumb (Heiser and Pratt, 1994)

$$M_{ci} = 0.38M_{\infty} \tag{1.3}$$

The above discussion shows that the pre-combustion compression system must be designed to give the appropriate flow conditions for combustion.

1.2.2 Compression Components: The Inlet

Following initial compression from the vehicle forebody oblique shock, additional compression is achieved in the inlet portion of the engine. This section addresses some inlet basics, but more in depth details on supersonic and hypersonic inlet design can be found in Mahoney (1990), Seddon and Goldsmith (1999) or Van Wie (2001). Note that while Fig. 1.1 shows an internal inlet, it is possible to have external compression components. For example upstream of the internal inlet could be one or more compression ramps or an isentropic compression surface (e.g., Heiser and Pratt, 1994). Figure 1.2 shows an example of an inlet containing an external compression ramp. The model in this schematic is similar to the dual-mode engine model used in the experiments of Emami et al. (1995). Note the compression ramp can be considered analogous to a vehicle forebody that would also generate an oblique shock. Following the initial compression ramp shock are three oblique shocks with the first originating at the cowl leading edge. For inlets that utilize one or more oblique shocks, the inlet adiabatic compression efficiency is nearly constant with respect to M_∞, but varies with the number of oblique shocks utilized. For example, with an amount of compression appropriate for supersonic combustion, an inlet that uses one oblique shock will have a compression efficiency, η_c of about 0.7. In comparison, an inlet that has four oblique shocks will have $\eta_c > 0.9$ (Heiser and Pratt, 1994). Moreover, as will be discussed in the isolator section below, it is generally considered desirable to have the flow entering the isolator as uniform as possible (Emami et al., 1995 and Bachchan and Hillier, 2004). As demonstrated in Fig. 1.2, a more uniform isolator entrance flow can be achieved if the "shock-on-shoulder" condition is achieved. When this occurs, all flow entering the isolator is parallel to the walls and therefore no expansion waves or oblique shock reflections are present.

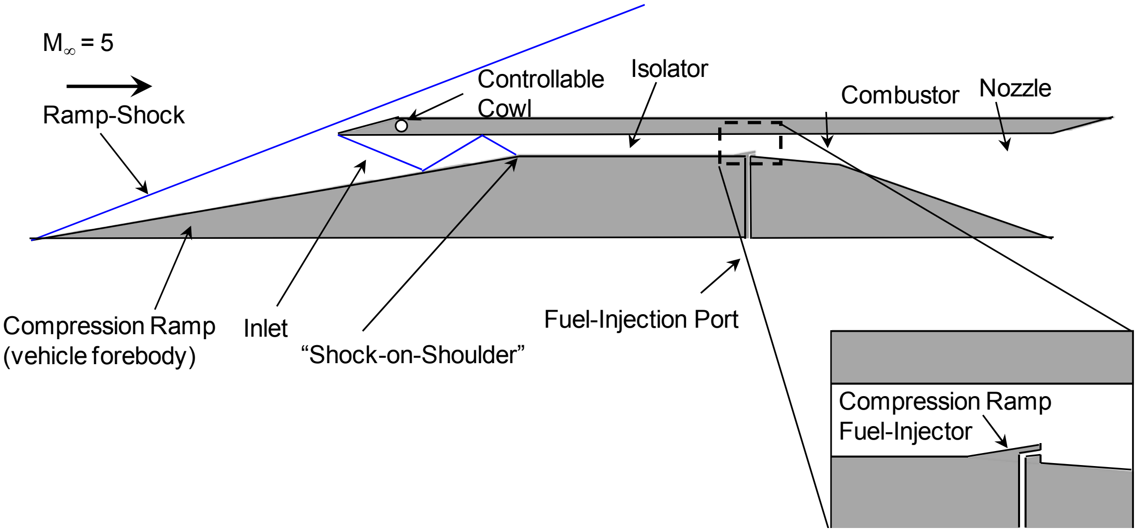

Figure 1.2 Schematic of a dual-mode engine model similar to that used in the experiments of Emami et al. (1995).

Of course viscous interactions such as shock wave boundary layer interactions (SWBLI) can be important in the operation of inlets. Three different types of SWBLIs are pertinent in inlet flows. The three interactions include originating interactions, impinging interactions and glancing interactions. As the name implies originating interactions occur at the origination of the shock, such as a compression ramp interaction. The impinging interaction occurs when an oblique shock impinges on a solid surface and subsequently reflects. Naturally, this interaction can be especially troublesome as it creates a stronger adverse pressure gradient than a single oblique shock of equivalent strength. According to Love (1955), the following inequalities can be used to estimate when shock induced boundary layer separation will occur:

$$\left(\frac{M_d}{M_u}\right)_{\text{laminar}} < 0.898 \tag{1.4}$$

$$\left(\frac{M_d}{M_u}\right)_{\text{turbulent}} < 0.762 \tag{1.5}$$

where M_d and M_u denote the Mach number outside of the boundary layer downstream and upstream of the interaction respectively. Thus, the propensity for boundary layer separation is primarily a function of shock strength and the state of the boundary layer (i.e., laminar vs. turbulent). However, it should be noted that the above relations were only experimentally verified for M_u between one and four. The third type of interaction, the glancing interaction, occurs when an oblique shock generated on the floor or ceiling of an inlet interacts with the inlet sidewall. According to Korkegi (1975), for Mach numbers greater than two, these interactions tend to cause boundary layer separation more readily than compression ramp interactions. Korkegi suggested the semi-empirical correlation

$$M_\infty \theta_i = 0.3 \qquad (1.6)$$

where θ_i is flow compression angle in radians, which gives the condition for incipient separation for these interactions. The correlation was generated using data with Reynolds numbers based on boundary layer thickness that ranged between 10^5 and 10^7 and freestream Mach numbers that ranged between about 2 and 6.

1.2.2.1 Inlet Starting

Besides the ability to provide compression with minimal losses, another important consideration in the operation of the inlet is its starting capability. The current discussion on inlet starting and the corresponding Fig. 1.3 follow directly from Shapiro (1953); however, the nomenclature corresponding to the types of flow seen in Fig. 1.3 is after Heiser and Pratt (1994). In Fig. 1.3, a converging-diverging nozzle with variable geometry is used to demonstrate the starting process of an inlet designed to start at M_∞. For the sake of discussion, the flow is assumed to be isentropic, except across shock waves. The dashed lines seen in Figs. 1.3a to 1.3d represent the nozzle geometry at which the inlet is designed to start, and the solid lines represent the actual geometry for the given case. In case 1 of Fig. 1.3a, the nozzle throat area is less than that required to start the inlet, and so it is too small to accommodate the mass flow that would be found behind a normal shock exactly at the inlet entrance. As a result, a detached bow shock sits upstream of the inlet entrance and some mass flow spills around the inlet entrance. This is defined to be the sub-critical mode of operation. Case 2 of Fig. 1.3b, demonstrates the critical mode. In this case, the throat area equals that required to pass the mass flow behind a normal shock that sits exactly at the inlet entrance. In other words, the throat area is such that the flow after the normal shock is isentropically brought to unity in the converging section. This critical case was discussed by Kantrowitz and Donaldson in 1945. As a result, the ratio corresponding to the inlet entrance area to throat area (A_i / A_t) for this case is referred to as the Kantrowitz limit in the literature. Assuming a calorically perfect gas, the Kantrowitz limit is

$$\frac{A_i}{A_t} = \frac{1}{M_\infty}\left[\frac{(\gamma+1)M_\infty^2}{(\gamma-1)M_\infty^2+2}\right]^{\frac{\gamma}{\gamma-1}}\left[\frac{\gamma+1}{2\gamma M_\infty^2-(\gamma-1)}\right]^{\frac{1}{\gamma-1}}\left[\frac{1+\frac{\gamma-1}{2}M_\infty^2}{\frac{\gamma+1}{2}}\right]^{\frac{\gamma+1}{2(\gamma-1)}} \tag{1.7}$$

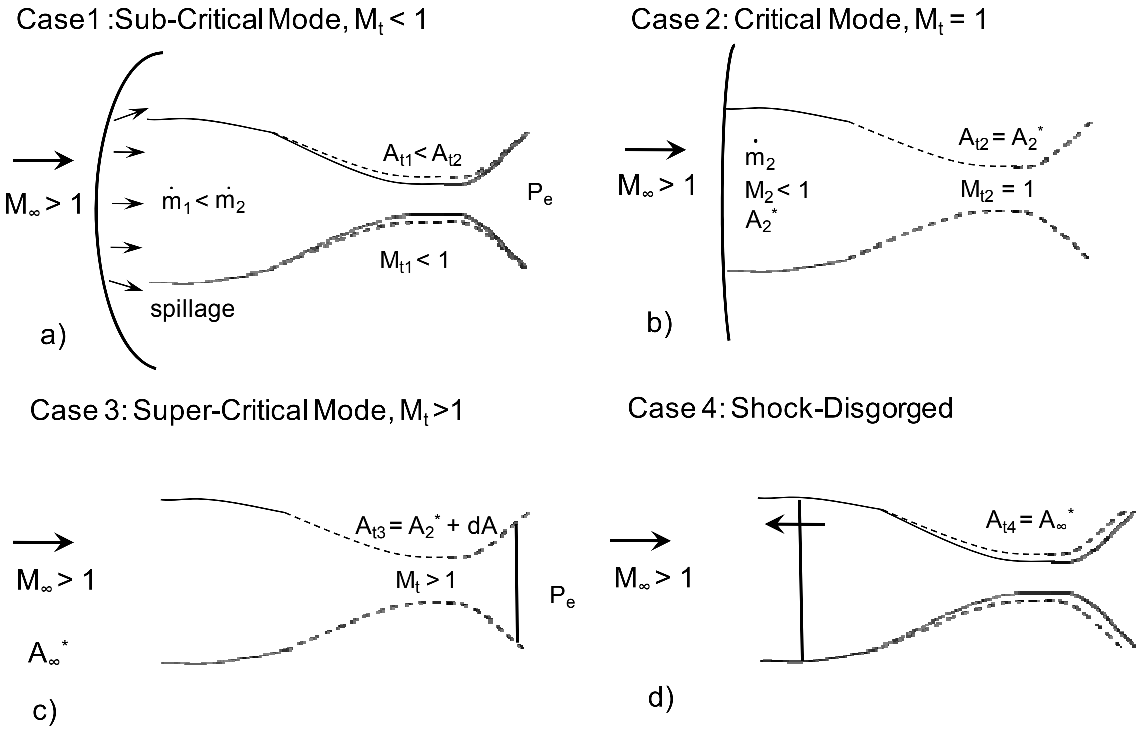

Figure 1.3 Demonstration of the inlet starting process with a similar approach to that used by Shapiro (1953).

If the throat area is increased by the slightest amount, the normal shock will move downstream and pass through the converging section of the inlet. The resulting case 3 seen in Fig. 1.3c is known as the super-critical mode. In this case the inlet is said to be started. The position of the normal shock in the diverging section depends on the pressure at the inlet exit P_e. After the inlet starts, it is possible (in this ideal analysis) to obtain a shock free flow by decreasing the throat area to the value required to isentropically bring the flow to the sonic condition (i.e, A^*_∞). This would therefore render the diverging section a subsonic diffuser. However, like the critical mode, this would be an extremely unstable flow. For example a further slight decrease in throat area or a decrease in flight Mach number would force a shock to propagate upstream and be disgorged out of the inlet. In other words the inlet would unstart. This case is demonstrated in Fig. 1.3d. After the unstart, the flow would once again be in the subcritical mode of Fig. 1.3a (Heiser and Pratt, 1994). Note that the above discussion indicates a hysteresis in the area contraction ratio required to start and unstart the converging-diverging inlet of Fig. 1.3. At high Mach numbers this hysteresis can be significant. For example at $M_\infty = 5$, the Kantrowitz limit dictates that $A_i / A_t < 1.54$ for starting. However, after starting the inlet and according to the inviscid limit, the maximum contraction ratio possible without unstart is $A_i / A_\infty = 25$. This example shows how variable geometry could improve the compression of a given inlet by increasing the contraction ratio after inlet starting. Of course in reality, after starting, the converging-diverging nozzle is not an isentropic flow due to a high adverse pressure gradient as well as the inevitable formation of shocks. Owing to the complexity of actual inlet flows, there is not a clear analytical method for predicting the maximum contraction ratio that can be achieved after inlet starting. However, Mahoney (1990) suggests that the maximum contraction ratio can be estimated as the area contraction that would be required to isentropically choke the flow at $M_\infty / 2$.

Similarly, the Kantrowitz limit gives only an approximate limit as to the contraction ratio required for inlet starting. Van Wie et al. (1996) compared data from various experiments of inlet starting and noted the Kantrowitz limit to become conservative at high Mach numbers. This was stated to be a result of the fact that the Kantrowitz limit assumes a normal shock which might not be the case in reality. Furthermore, a way to the increase contraction ratio for starting is to have bypass ducts or bleed holes in the inlet contraction section. For example using the data of Mahoney (1990), Van Wie et al. (1996) showed inlets could start at contraction ratios greater than two times the limit of equation 1.7. However, it was noted that the increased complexity in bypass duct design as well as the additional drag due to the bypass flow have limited the use of such techniques. Finally, viscous effects have also been seen to affect the starting characteristics of inlets. For example, Goldberg and Hefner (1971) found that for inlets with thick boundary layers, the Kantrowitz limit became invalid (too high for starting) if $\delta / A_i > 0.5$.

1.2.3 Compression Components: The Isolator

In the dual-mode engine, the pre-combustion compression component following the inlet is the isolator (Curran et al., 1996). The isolator is a duct connecting the inlet to the combustor. As explained by Emami et al. (1995), an important performance measure for an inlet / isolator is its capability to provide an increase in static pressure prior to the combustor. The reason for this can be thought of as follows. In either the ramjet or scramjet mode of operation, the flow entering the isolator is supersonic. Considering Rayleigh flow arguments, combustion heat addition will increase the pressure in a supersonic flow. Therefore, the ability for the inlet / isolator to contain a pressure increase necessary for combustion is a very relevant performance consideration. In fact, the amount of pressure increase that the inlet / isolator can tolerate without unstarting is a direct measure of the amount of fuel that can be burned in combustion and therefore a direct measure of the thrust that an engine can create (Rodi et al., 1996). The extent of necessary compression provided by the isolator depends on the mode of operation for the dual-mode engine. This section will focus on the role of the isolator in both the ramjet and scramjet modes of operation. At first for the sake of simplicity, isolator flows will be discussed without the presence of an inlet.

1.2.3.1 Ramjet Mode

As discussed above, at flight Mach numbers below about Mach 6, the combustor entrance flow must be subsonic. In this case, the engine is acting in the ramjet mode and a strong pre-combustion shock system must exist within the isolator. The combustion in this mode of operation creates a significant pressure increase, which causes significant boundary layer separation. The combustion pressure increase propagates upstream through separation and results in the formation of a pre-combustion shock structure in the isolator. This strong pre-combustion shock structure serves to match the combustor pressure (Heiser and Pratt, 1994 and Curran et al., 1996). Since the flow entering the combustor is subsonic in the ramjet mode, the Mach number must be brought to unity prior to expansion in the nozzle. However, Fig. 1.1 and Fig. 1.2 show there is not a physical throat downstream of the combustor. In the ramjet mode of operation this apparent problem is solved by means of a "thermal throat." In other words, the combustion process adds heat to the subsonic combustor entrance flow which eventually "thermally chokes" ($M = 1$) the combustor flow. The exhaust flow can then be expanded to supersonic velocities. (Heiser and Pratt, 1994 and Curran et al., 1996).

In the ramjet mode, the pressure rises in the pre-combustion shock system typically through a series of shocks known as a "shock-train". Depending on the isolator entrance conditions this can be either a "normal shock-train" containing a series of bifurcated normal shocks or an "oblique shock-train" which contains a series of crossing oblique shocks (Heiser and Pratt, 1994 and Matsuo et al. 1999). Normal shock-trains occur for lower entrance Mach numbers of about 2 to 3, whereas oblique shock-trains occur for higher entrance Mach numbers (Heiser and Pratt 1994). If the duct or isolator is sufficiently long, a mixing region containing further compression will follow a shock-train. This shock-train, in combination with the subsequent mixing region, has been referred to as a "pseudo-shock" in the literature (Matsuo et al. 1999). The name pseudo-shock was first given by Crocco (1958) since the complicated series of shock boundary layer interactions in a duct replace what would be a normal shock in an inviscid duct.

Matsuo et al. (1999) point out that perhaps a more appropriate name would have been a “pseudo-normal-shock.” The maximum pressure rise in a pseudo-shock is less than, but can be near, the value given by a single normal shock at the entrance Mach number. Extensive work has been directed at investigating the characteristics of internal flows containing shock-trains. An excellent review of shock-trains and pseudo-shocks is given by Matsuo et al. (1999). Figure 1.4 shows a schematic of a pseudo-shock from that review. Figure 1.4 shows a flow structure sketch inferred from schlieren and pressure measurement experiments. In addition, Fig. 1.4 shows both the duct pressure distribution at the wall and along the centerline. At the entrance of the duct is a strong bifurcated normal shock wave which is followed by boundary layer separation. Note that after the initial separation, the boundary layer does not reattach. Proceeding downstream, the separated flow thins. Note that this thinning serves to turn the outer flow downward resulting in the creation of expansion waves. After the thinning of the separated flow, the flow once again thickens in the presence of another normal bifurcated shock. This pattern continues throughout the shock-train region labeled in Fig. 1.4a. Note this shock-train is a normal shock-train as it consists of a series of bifurcated normal shocks. The static pressure distributions of Fig. 1.4b show the centerline pressure within the shock-train oscillates as the flow passes through the series of shocks and expansions. However, at the wall the oscillations are not observed and the pressure steadily increases. At the end of the shock-train region, the flow pressure at the centerline equals that of the walls. Finally, a further gradual increase in pressure is seen to occur in the subsequent mixing region. Again the combination of the shock-train and mixing region is known as a pseudo-shock.

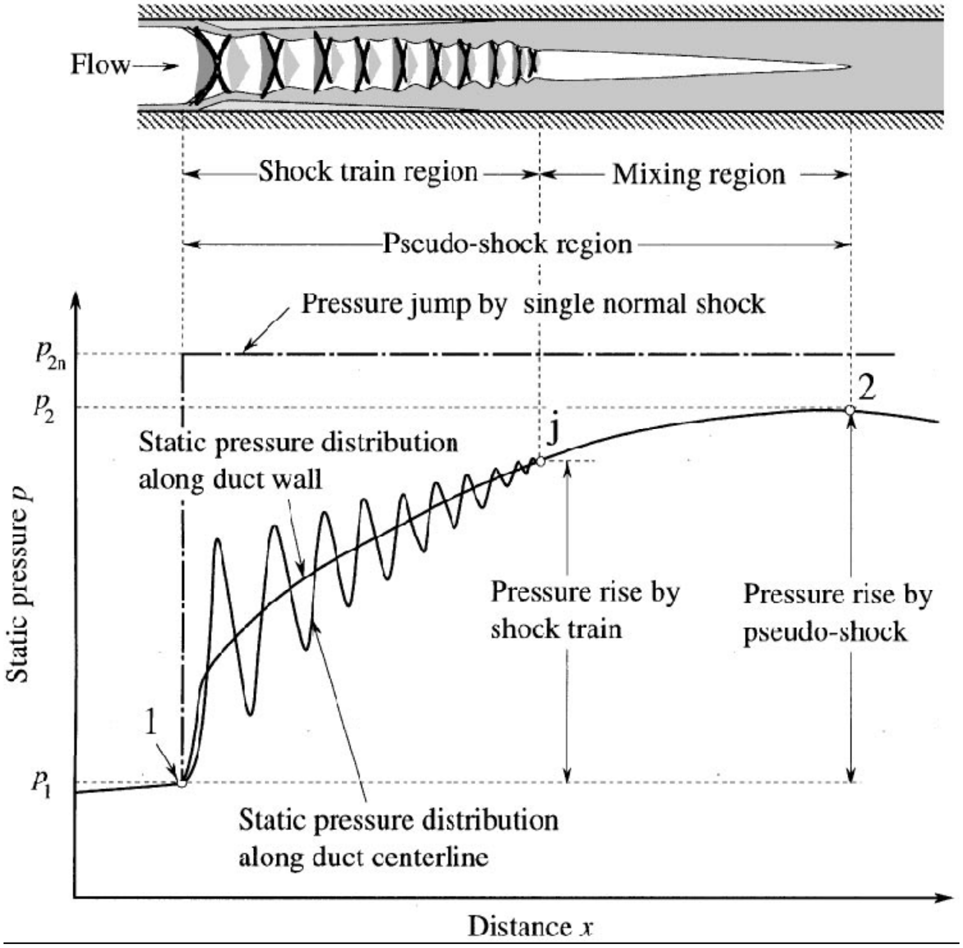

Figure 1.4 Schematic of a pseudo-shock containing a shock-train and subsequent mixing region (Matsuo et al., 1999).

1.2.3.2 Correlations for Pseudo-Shocks and Shock-Trains

Since the pressure increase in an isolator is an important isolator performance parameter, it is useful to understand how the pressure distribution in an isolator is influenced by the incoming flow properties and the geometry of the isolator itself. To provide this insight, Waltrup and Billig (1973) conducted experiments in circular ducts and came up with a semi-empirical correlation for the pressure rise in a circular duct as a function of the duct entrance Mach number (M_1), duct diameter, duct length (L), entrance boundary layer momentum thickness (θ) and Reynolds number based on momentum thickness Re_θ. A similar correlation was also given by Billig (1993), but for a rectangular duct with height h

$$\frac{(M_1^{\,2}-1)(L/h)\,\mathrm{Re}_\theta^{\;0.2}}{\sqrt{\theta/h}}=50\left(\frac{P}{P_1}-1\right)+170\left(\frac{P}{P_1}-1\right)^2 \tag{1.8}$$

Equation 1.8 has been seen to accurately match the wall pressure distribution in several studies. For example, in the experiments of Sullins and McLafferty (1992), a rectangular isolator with an aspect ratio (width:height) of 2.5 was mounted to the floor of Mach 2 and Mach 2.85 wind tunnels. The floor boundary layer thickness entering the isolator was about 25% the isolator height. The rest of the isolator boundary layers were much thinner as they developed naturally beginning at the isolator entrance. Following the isolator was a diffuser section in which a gate valve was used to induce back pressure and set up a shock-train within the isolator. It was found that equation 1.8 gave reasonable agreement with the measured wall pressure distribution of the shock-train. It is worth noting that the boundary layer properties used in the correlation of Equation 1.8 corresponded to those of the thick floor boundary layer. Reinartz et al. (2003) studied the performance of a dual-mode inlet / isolator model experimentally and computationally at freestream Mach numbers of 2.4 and 3.0. In this study, a CFD code was used to solve the three-dimensional, unsteady Reynolds-averaged Navier-Stokes (RANS) equations to compute the isolator exit pressures corresponding to inlet / isolator flows containing shock-trains. The pressures computed at the isolator exit were seen to be in good agreement with those predicted by Equation 1.8. These examples therefore highlight the potential of this correlation to be used as an isolator design tool. Furthermore, Sullins and McLafferty (1992) suggest using the stream-thrust-averaged Mach number, M_{sta} in the place of M_1 above. From McLafferty and Krasnoff (1955), M_{sta} can be calculated using the geometric and flow properties at the beginning of the shock-train (point 1) and the following three equations

$$F = PA\left[1 + \gamma M_{cl}^{2}\left(1 - \frac{\delta_1^*}{A} - \frac{\theta_1}{A}\right)\right] \tag{1.9}$$

$$U = \frac{\gamma}{\gamma - 1}\frac{F}{\dot{m}} + \left[\left(\frac{\gamma}{\gamma + 1}\frac{F}{\dot{m}}\right)^2 - \frac{2\gamma}{\gamma + 1}RT_0\right]^{1/2} \tag{1.10}$$

$$M_{sta} = U / \left[\gamma R\left(T_t - \frac{U^2}{2C_p}\right)\right]^{1/2} \tag{1.11}$$

where F equals the stream thrust, P is the pressure, A is the area of the isolator, M_{cl} is the centerline Mach number, δ^* is the boundary layer displacement thickness, U is the stream-thrust-averaged streamwise velocity, R is the gas constant and C_p is the specific heat at constant pressure. In another pseudo-shock (shock-train) study, Wang et al. (2006) set out to understand how the presence of a thick boundary layer can affect the isolator wall pressure distribution. This scenario is consistent with a dual-mode inlet ingesting a thick vehicle forebody boundary layer. To do this a rectangular isolator duct with an aspect ratio of 1.5 (width: height) was directly connected to the exit of Mach 1.5, 1.8 and 2 nozzles. To create the non-uniform case of one thick and three thin boundary layers, a splitter plate was inserted into the flow as seen in Fig. 1.5. Next an asymmetry parameter was defined to quantify the resulting difference in momentum thickness of the thick and thin boundary layers. This parameter was

$$D_\theta = \left(\frac{\theta_{\max} - \theta_{\min}}{\theta_{\max}}\right) \tag{1.12}$$

where max and min are with respect to the thick and thin boundary layers respectively. In the study a modified version of equation 1.8 was proposed to account for the boundary layer asymmetry

$$\frac{(M_1^{\,2}-1)(L/h)\,\mathrm{Re}_\theta^{\,0.2}}{\left(1+D_\theta\right)^\alpha \sqrt{\theta/h}} = 50\left(\frac{P}{P_1}-1\right)+170\left(\frac{P}{P_1}-1\right)^2 \qquad (1.13)$$

where α was a parameter used to fit the correlation to the data they acquired in a variety of cases that included changing the isolator entrance Mach number, degree of asymmetry, and thickness of the incoming boundary layers. It was found that $\alpha = 0.3$ resulted in the best fit to the measured pressures. The correlation of Equation 1.13 was seen to give better agreement with the measured pressures than the classic Waltrup and Billing correlation of equation 1.8. However, it was noted that the centerline Mach number range tested was rather limited as it varied only over the range from 1.33 to 1.85.

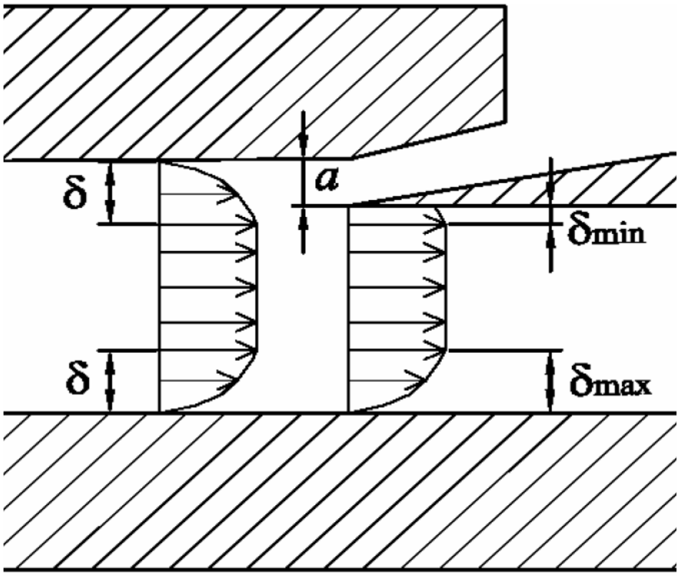

Figure 1.5 Schematic illustrating the technique used to create a thick floor boundary layer at the isolator entrance in the experiment of Wang et al. (2006).

1.2.3.3 The “Separation-Shock” Flow in Isolators

For high isolator entrance Mach numbers and/or high aspect ratio (width: height) isolators, another type of shock system other than the pseudo-shock has been observed in ducts. This type of shock-system has been termed the “separation-shock” by Penzin (1998). According to Penzin, the borderline conditions for which the separation-shock flow will exist are given by the following relation

$$b = \left(\frac{M_1 - 2.5}{150} \right)^{-0.25} \tag{1.14}$$

where M_1 and b are the duct entrance Mach number and aspect ratio respectively. Note that equation 1.14 holds for b less than about 3. For example, according to Penzin, if the duct aspect ratio b is greater than the right hand side of Equation 1.14, the shock system will be the separation-shock and not the pseudo-shock. This type of flow is characterized by regions of separated corner flow (Penzin, 1998 and Sabel’nikov and Penzin, 2000). Compared to the pseudo-shock flow, the separation-shock flow is seen to have greater cross-sectional asymmetries. For example, in the pseudo-shock flow, the wall pressure at a given streamwise location has been seen to be nearly constant over the entire cross section (Sullins and McLafferty, 1992). However, in the separation-shock flow, the pressure can vary significantly at different locations within a cross-sectional area. In addition, regions of separated flow are larger and pressure fluctuations tend to be higher in this duct flow compared to the pseudo-shock. Finally, the separation-shock flow requires a longer isolator for an equivalent pressure rise. These disadvantages of the separation-shock flow therefore make it undesirable compared to the pseudo-shock flow.

There are not many studies in the literature on the separation-shock flow other than the work of Penzin. In experimental tests, Rice (2003) found three-dimensional pressure distributions similar to Penzin (1998). In other work, a computational RANS investigation was undertaken by Nedungadi and Van Wie (2004) to understand better the separation-shock flow. In these computations, rectangular isolators with aspect ratios of 2.5 and 10 were investigated with inflow Mach numbers of 2 and 4. The isolator entrance flow was simulated to contain one thick boundary layer with a thickness of 25 % the duct height to simulate that found on the forebody of an actual vehicle. In all cases, the regions of separated corner flow that characterize the separation-shock flow were observed. The separated corner regions were seen to occur near the surface for which the thick boundary layer was prescribed. In addition, the extent of these regions was seen to vary with the isolator entrance Mach number. For the Mach 2 computations, the separated corner flow was seen to reattach in both isolator cases. This was not the case in the both Mach 4 simulations where the corner flow did not reattach after separation. In order to compare the amount of pressure gain that occurred in each case, the pressure at the isolator exit was compared to the theoretical pressure increase that would be given by a normal shock. Using this metric, it was found that the higher Mach number cases could not support as great of a pressure rise without unstart occuring. It was therefore suggested that the large regions of separated flow had a destabilizing effect in the separation-shock flow. Finally, although this was not pointed out directly, it is interesting to note that the separation-shock flow was observed in cases where equation 1.14 predicts the pseudo-shock flow should have occurred. Although, equation 1.14 is valid for b less than about 3, Penzin (1998) conducted tests with higher aspect ratios and noted that for $M_1 < 2.5$, the pseudo-shock always occurred, not the separation-shock mode, regardless of b. Therefore according to Penzin, three of the four case simulated by Nedungadi and Van Wie should have yielded a pseudo-shock, not the separation-shock they reported.

1.2.3.4 Scramjet Modes

The isolator also plays an important role in the scramjet mode of operation of the dual-mode engine. As demonstrated in Fig. 1.2, the combustor section is typically diverging (Heiser and Pratt, 1994 and Curran et al., 1996). Through expansion of a supersonic flow, the diverging section serves to alleviate some of the pressure increase caused by combustion processes. However, if the rate of area expansion is not enough to overcome the combustor pressure increase, a strong adverse pressure gradient can exist in the combustor section. As is often the case, the adverse pressure gradient can lead to separation of the boundary layers. The combustor pressure disturbance then propagates upstream and results in the formation of an oblique shock-train (with a supersonic core flow) in the isolator (Heiser and Pratt, 1994 and Curran et al. 1996).

In other cases there is no need for an isolator at all. For example, if the rate of area increase in the combustor section is great enough to prevent significant boundary layer separation, than the combustion disturbance is not felt upstream in the isolator. At flight Mach numbers greater than about 8, the combustion process no longer creates significant boundary layer separation (Anderson et al. 2001). In this case the engine is acting in the pure scramjet or shock free scramjet mode and the isolator is not needed (Heiser and Pratt, 1994). In fact, in the pure scramjet mode, the isolator only serves to add weight and drag to the vehicle. Therefore, it is important to understand all of the operation modes that a given engine may cycle through. The isolator should not be any longer than is necessary to contain the shock-systems necessary for combustion.

1.2.3.5 Effects of the Inlet on Isolator Shock Systems

Another factor influencing the maximum possible pressure gain in a given isolator is the degree of uniformity of the isolator entrance flow profile. The above sections on shock-trains showed that the properties of the incoming boundary layer can directly affect the isolator pressure distribution (e.g., equations 1.8 to 1.13). However, other non-uniformities can exist that are a function of the inlet geometry and the freestream conditions. Again, consider the inviscid flow that would exist in the case of the schematic of Fig. 1.2. The shock-on-shoulder condition causes all of the flow entering the isolator to be parallel to the isolator walls and to have uniform flow properties. Now consider if the cowl were adjusted such that the third oblique shock impinged on the isolator upstream of the shoulder. Or consider how the flow would change if M_∞ decreased. These changes would mean the engine was operating at off-design conditions. In either off-design case, an expansion fan would be required at the shoulder to turn the flow parallel to the lower wall. In addition, the third oblique shock would no longer be "cancelled" at the shoulder, but rather it would reflect and propagate into the isolator entrance. The result would be a non-uniform isolator entrance flow. In the literature, non-uniformities due to the inlet are often referred to as inlet "distortion." While there are quite a few published studies on shock-trains in ducts, there is often no inlet. However, there have been some experiments that have looked into the effects of inlet / isolator coupling. For example, in an extensive parametric investigation, Emami et al. (1995) varied parameters such as cowl length, cowl contraction angle (inlet contraction ratio) and isolator length to generate a large database of wall pressure information for different inlet / isolator configurations. In this study, the pressure increases due to combustion were simulated by raising a flap in the diffuser section that followed the isolator. A particular focus was to understand what factors contributed to the maximum possible pressure gain (and therefore the maximum amount of fuel burned in the combustion process) that could be obtained in the isolator without unstart. Data were found that suggested that increasing the level of inflow distortion to the isolator degraded the isolator's ability to generate a pressure increase. Furthermore, a computational investigation by Bachchan and Hillier (2004) also tested the effects of non-uniformities on isolator flows with an imposed back pressure. In these computations, the flow in an axisymmetric ramjet engine with a design flight Mach number of 5.5 was simulated. Of particular interest was to understand better how the engine would perform at off-design conditions. They found that non-uniformities could significantly degrade the ability for the isolator to generate a stable pressure increase. For example at a simulated Mach number of 6, the inlet / isolator could not support the level of compression that would be expected to correspond to combustion.

In addition to providing compression, the isolator also serves to reduce the sensitivity of the inlet to combustor pressure perturbations (Heiser and Pratt, 1994, Emami et al., 1995 and Curran et al., 1996). In other words the isolator helps to prevent unstart from occurring.

1.3 UNSTART

Disturbances, such as those due to combustion can lead to a transient process known as unstart (Curran et al., 1996). When unstart occurs the original inlet / isolator compression (shock) system is displaced upstream out of the inlet and it can eventually take the form of a detached bow shock (Heiser and Pratt, 1994). The unstart process can be severe with high transient pressure loads and it can lead to a loss of engine thrust.

Heiser and Pratt discussed three causes of unstart. The first cause is when the vehicle flight Mach number drops below the starting value. This is similar to decreasing the throat area in Fig.1.3d to a value below that which would choke the throat at a given M_∞. A second cause of unstart is the unexpected distortion of the incoming inlet flow. Causes of this distortion include boundary layer separation such as due to an unexpected change in angle of attack or the ingestion of exhaust gases. A third cause of unstart is an increase in pressure downstream of the inlet / isolator that cannot be supported by the inlet / isolator shock system. As discussed in the ramjet mode of operation, a strong pre-combustion shock system exists within the isolator to slow the flow to subsonic speeds. If the combustion pressure rises to a value that cannot be matched by this shock system the engine will unstart (Curran et al., 1996). Combustion perturbations can also lead to unstart in the scramjet mode of operation. As was also discussed, combustion in the scramjet mode can often lead to boundary layer separation. In this circumstance, an oblique shock-train forms in the isolator to match the combustor pressure. However, if the isolator is not long enough to contain this shock-train, it will propagate into the inlet and result in unstart (Curran et al., 1996). In addition, severe separation in the combustor during the scramjet mode has been seen to cause unstart in CFD simulations (e.g., McDaniel and Edwards, 2001). This study will be discussed further in section 1.3.2.

1.3.1 Unstart Experiments

Unstart has been the subject of a number of experimental studies. For example, Wieting (1973) used a three-dimensional model scramjet in a Mach 5.3 flow and initiated unstart by inserting a cylindrical pin to create blockage. Peak pressures during unstart were seen to be up to 20 times the started values. It was found that the peak pressures could be conservatively estimated by the pressure that would be found behind a stationary normal shock with an upstream pressure equal to that of the freestream. Propagation velocities of the unstart shock system as calculated by pressure measurements, ranged from 10-27 m/s (in the lab frame of reference). Wieting noted that the propagation velocities were not dependent on the insertion velocity of the pin used to induce unstart.

In another experimental study by Rodi et al. (1996), unstart was investigated in a two-dimensional dual-mode model. The model could be pressurized to a maximum and eventually unstarted by raising a flap in the model's nozzle section. In addition, the inlet cowl could be adjusted to vary the inlet contraction ratio (i.e., the ratio of the cross-sectional area of the captured stream tube to the inlet throat area). Higher inlet contraction ratios were seen to result in what were defined as "hard unstarts", whereas lower inlet contraction ratios resulted in "soft unstarts." A hard unstart was defined to be that which resulted in an unstarted flow with much "flatter" (lower) mean pressures in the isolator and combustor sections compared to the maximum pressures before unstart occurred. Also, some hard unstarts were seen to result in oscillatory (periodic) unstarted flows with frequencies of about 300 Hz. Soft unstarts were defined as those which occurred "gradually" while maintaining a pressure distribution more similar to that prior to unstart. Unstart propagation velocities were reported to range from 55 to 70 m/s. Rodi et al. also unstarted their dual-mode inlet / isolator by increasing the inlet contraction ratio. In these experiments, the flap at the back of the model was left in the fully-down position and the adjustable cowl was closed until the unstart position was reached. The cowl angle could be adjusted to create flow turning angles greater than those predicted to cause incipient separation for both impinging and glancing shock wave boundary layer interactions according to the semi-empirical correlations of Korkegi (1975). Interestingly, the inlet / isolator did not unstart when either angle predicted to correspond to the incipient separation of an impinging or glancing shock wave / boundary layer interaction was reached. Rather, the inlet was seen to unstart a at a greater flow turning angle.

Emami et al. (1995) also investigated how the inlet geometry affects the conditions that induce inlet unstart. Three different cowls, of different lengths were used for these tests and the inlet incoming flow was kept constant. The different length cowls allowed for different contraction ratios to be achieved for the same cowl deflection (convergence) angle. However, it was found that regardless of the amount of contraction, the angle at which unstart was induced was nearly the same for all three cowls. It was therefore concluded that shock-induced separation due to glancing interactions was the cause of unstart for these cases. However, the cowl angles at which unstart was induced were seen to be about 2 to 3.5 degrees greater than the angle predicted by Korkegi's correlation given in Equation 1.7. Thus, both Emami et al. and Rodi et al. found the cowl could be deflected to angles greater than those predicted to cause incipient separation according to the correlations of Korkegi. Reasons for the disagreement with the correlation were not given in either study.

Van Wie et al. (1996) also investigated the effects of inlet geometry on unstart. In these experiments, only an inlet consisting of an adjustable cowl was used. The length of the cowl and height of the cowl with respect to the floor were varied. Note that varying the cowl height with respect to the floor served to vary the proportion of ingested entrance flow that was floor boundary layer. In all tests, the cowl was rotated about its leading edge until unstart occurred. Similar to Rodi et al. (1996), what were defined to be "hard unstarts" and "soft unstarts" were observed. Soft unstarts here were defined to occur gradually as the flap deflection angle was increased. The process was seen to be associated with an increase in separation that occurred at a rate similar to rate of increase of the cowl angle. Hard unstarts were said to occur, "when the flow at the aft end of the inlet (cowl) chokes, creating a disturbance that propagates forward at nearly the local speed of sound." Note that this reference does not describe how the propagation velocity was calculated, nor does it explain how they concluded that the flow was choked. In addition, it is not clear whether the "local" speed of sound they refer to is that at the wall.

These are important points considering that Wieting (1973), Rodi et al. (1996) and O'Bryne et al. (2000) all measured unstart propagation velocities to be significantly lower than the local (wall) speed of sound. In general, Van Wie et al. (1996) showed that hard unstarts occurred at configurations with greater cowl heights and shorter cowls lengths.

In another set of experiments, Shimura et al. (1998) induced unstart in a three-dimensional combusting scramjet model by increasing the mass flow rate of hydrogen fuel. For fuel flow rates near that which caused unstart, distinct pressure spikes were observed upstream of the isolator entrance. It was therefore suggested that unstart could be avoided and controlled by monitoring this pressure and reducing the fuel rate accordingly.

The studies of Hawkins and Marquart (1995) used a two-dimensional supersonic / hypersonic inlet and initiated unstart by raising flaps at the rear of the model. Shadowgraph imaging showed the inlet flow to be highly separated after unstart. Similar to Rodi et al. (1996), oscillatory unstarted flows were observed with frequencies of 150-180 Hz.

A more fundamental experimental study by O'Byrne et al. (2000), focused on the thermal choking process in a model scramjet. Tests were conducted at duct entrance Mach numbers of 2.5 and 3.8. The model consisted of only a constant area duct that was used as the combustor and a fuel injector. Measurements made included fast-response wall pressures and shadowgraph imaging. The Mach number distribution in the duct was calculated using a one-dimensional finite difference method based on the measured wall pressures and the known conditions at the combustor entrance. Heat addition due to supersonic combustion was seen to lead to the formation of a normal shock that subsequently propagated upstream. The flow behind this normal shock was seen to have a Mach number near unity and it was suggested that heat addition forced the shock upstream. Furthermore, the wall pressure data was used to calculate the effective Mach number of the upstream traveling normal shock (using the measured pressure values upstream and downstream of the shock). Using this Mach number, the known upstream conditions against it was propagating and unsteady one-dimensional supersonic flow theory allowed for a theoretical shock propagation velocity to be calculated. In the case of the Mach 3.8 entrance flow, the theoretical propagation velocity was close to the measured propagation velocity. However, in the case of the Mach 2.5 entrance flow, the theoretical velocity calculated was much slower than that measured. In fact the calculated velocity (from the reference point of moving with the shock) was seen to be lower than the flow velocity the shock was propagating against. It was suggested that heat release effects not accounted for in the theoretical propagation velocity calculation might be an important factor in the Mach 2.5 case, but not the Mach 3.8 case. However, the reasons behind this discrepancy were stated to be not well understood.

1.3.2 Unstart CFD Simulations

CFD simulations have also been used to study unstart. Sato and Kaji (1992) used an explicit MacCormack differential scheme (MacCormack and Baldwin, 1975) to simulate unstart in a two-dimensional scramjet engine. They proposed that the process of unstart occurs as the “boundary layer flow spreads and pushes out the main flow” of the engine inlet. Neaves et al. (2001) simulated unstart of the model dual-mode engine studied by Emami et al. (1995) and made some interesting observations. Their simulation used a three-dimensional RANS technique that utilized an adaptive grid. In the experiment and the simulation, unstart was induced with the raising of a flap in the nozzle section. Prior to unstart, the model was pressurized resulting in the formation of a shock system near the isolator exit. During unstart, the unstart system seemed to stop its upstream propagation momentarily in the isolator while the reflected oblique shocks due to the inlet cowl became stronger and induced separation. Propagation of the unstart system then continued with increasing separation. Three-dimensional computations by McDaniel and Edwards (2001) were made to investigate unstart in the model scramjet used in the experiments of Masuya et al. (1995). In the computations, the Favre-averaged Navier-Stokes equations were solved along with separate conservation equations for each important chemical species. The simulations gave much physical insight into the possible cause of unstart in the experiments. Supersonic combustion was seen to result in an increase in the strength of the fuel injector recompression shocks, which caused boundary layer separation. Hydrogen was then entrained into the hot portions of the separated flow resulting in ignition and "massive" shock-induced separation. This blockage was seen to lead to unstart before the thermally choked condition was reached. At the end of the unstart process, the isolator flow was seen to be highly three-dimensional; for example, flow in the spanwise center plane was seen to be supersonic, whereas flow near the sidewalls was highly reversed with a peak velocity of 420 m/s.

1.4 MOTIVATION AND SCOPE OF THE CURRENT WORK

The discussion above shows that although substantial work has been aimed at understanding unstart, much remains unknown about unstart dynamics. Lack of understanding of the unstart process is particularly critical if new strategies for controlling it are to be developed. The current work describes the results of experimental studies of unstart and unstarted flows in inlet / isolator models that were mounted on the floor of a Mach 5 wind tunnel. The models, which were designed with simple compression surfaces and straight rectangular isolators, represent simplified forms of dual-mode scramjet inlet / isolators. Unstart was initiated by deflecting a flap located at the exit of the isolators. The unstart process and resulting unstarted flow were studied by using high-speed schlieren imaging, wall-pressure measurements and particle image velocimetry (PIV). The data were used to characterize the flow structure during unstart and to determine the relevant time-scales and velocities involved in unstart and unstarted flows.

Results are first presented for what is termed the 6-degree inlet / long-isolator model. Since this model was the most extensively studied, it is considered to be the baseline case. As will be discussed, the unstart process in the baseline case was shown to be dependent on the geometry of the inlet. Therefore, additional experiments were conducted with two different inlet geometries. The results of these experiments follow the baseline discussion.

In addition, to the unstart dynamics and unstarted flows, high-compression shock systems analogous to those which may be found in the ramjet mode of operation were also studied. As will be discussed, it was not possible to form high-compression shock systems by raising the flap in any of the models that used the baseline isolator without first inducing unstart. However, with a shorter isolator it was found that high-compression shock systems could be formed in what are termed the inlet / short-isolator models. The effects of inlet geometry on these high-compression shock systems are discussed.

CHAPTER 2

2. Experimental Program

2.1 FACILITY, WIND-TUNNEL DETAILS AND TEST SECTION CONDITIONS

The experimental data were taken in the Mach 5 blow-down wind tunnel at the J.J. Pickle Research Campus of The University of Texas at Austin. The wind tunnel air was supplied by storage tanks with a volume of 4 m^3 (140 ft^3) at a pressure of 17.6 MPa (2550 psia) that were charged using a four stage compressor (Worthington HB4). Typically, in this facility the air is heated prior to the stagnation chamber through two 420 kW nichrome wire resistive heater banks. However, for much of the current work, one heater bank was being repaired and was not available. The nominal freestream conditions are given below for both one and two heater banks. The air flow through the heaters was regulated with a 1.5 *in* valve (Dahl) and a controller (Moore 352) to maintain the stagnation pressure. An analog controller (Love 1543) was used to control the heater banks and set the stagnation temperature. The plenum conditions were monitored with a pressure transducer (Setra model 204) and a J-type thermocouple whose outputs were used by the controllers to set the plenum conditions. The constant area test section was 15.2 cm (6 *in*) wide by 17.8 cm (7 *in*) tall and had a length of 76.2 cm (30 *in*). Fused silica windows 38.1 cm (15 *in*) long and 5.1 cm (2 *in*) tall were placed in the test section side walls for optical access.

2.1.1 Freestream and Plenum Conditions for Tests with Two Heater Banks

The experiments with two heater banks were conducted at plenum temperatures, T_0 between about 339 and 355 K (150-180° F). The plenum pressure, P_0 ranged from 2.48 and 2.52 MPa (360-365 psia). The freestream Reynolds number, velocity and Mach number were about 49.5×10^6 m^{-1} (15.1×10^6 ft^{-1}), 750 m/s and 5.1 respectively. The freestream turbulence intensity was measured with PIV to be no more than 0.3%. A detailed discussion regarding these freestream values is given in Appendix D.

2.1.2 Freestream and Plenum Conditions for Tests with One Heater Bank

The experiments with one heater bank were conducted at plenum temperatures, T_0 between about 317 and 339 K (110 and 150° F). The plenum pressure, P_0 was in the range between 2.41 and 2.52 MPa (350-365 psia). The freestream Mach number, velocity and unit Reynolds number were about 4.9, 740 m/s (2428 ft/s) and 49.5×10^6 m^{-1} (15.1×10^6 ft^{-1}), respectively. Similar to the two heater bank conditions, the freestream turbulence intensity was measured to be no more than 0.3%. A detailed discussion of the one heater bank freestream conditions is given in Appendix D. The run conditions for both the one and two heater bank experiments are summarized in Table 2.1. In addition to the nominal conditions, the models tested with the one and two heater bank conditions are given.

Table 2.1 Wind tunnel flow conditions and corresponding inlet / isolator models tested.

Heater Banks, #	M_∞	P_0, MPa	T_0, K	Models Tested
1	4.9	2.41-2.52	317-339	Both 6-degree inlet models
2	5.1	2.48-2.52	339-355	All four 0- and 8-degree inlet models

2.2 INLET / ISOLATOR MODELS, WIND TUNNEL WALL INSERTS AND FLAP DRIVE SYSTEM DESIGN

2.2.1 Design and Assembly Details

Figure 2.1 is an overall schematic showing a 6-degree inlet / isolator model mounted to the floor of the Mach 5 test section with one test section sidewall removed. This figure is meant to provide an overview of the components involved in simulating dual-mode engines flows. As labeled in the figure, the tunnel sidewalls contained long fused-silica windows that allowed for the entire lengths of the inlet / isolator models to be imaged. In addition, the tunnel ceiling could be instrumented with a plug that contained a fused silica window insert (10 × 25 cm) to provide optical access for PIV measurements. Unless otherwise noted, all wall plug inserts were sealed using conventional O-ring designs. The models were mounted to a floor plug insert that fit into the test section floor. The servo-motor driven flap actuation system that was used to raise the flap at the exit of the isolator models is also seen in Fig. 2.1.

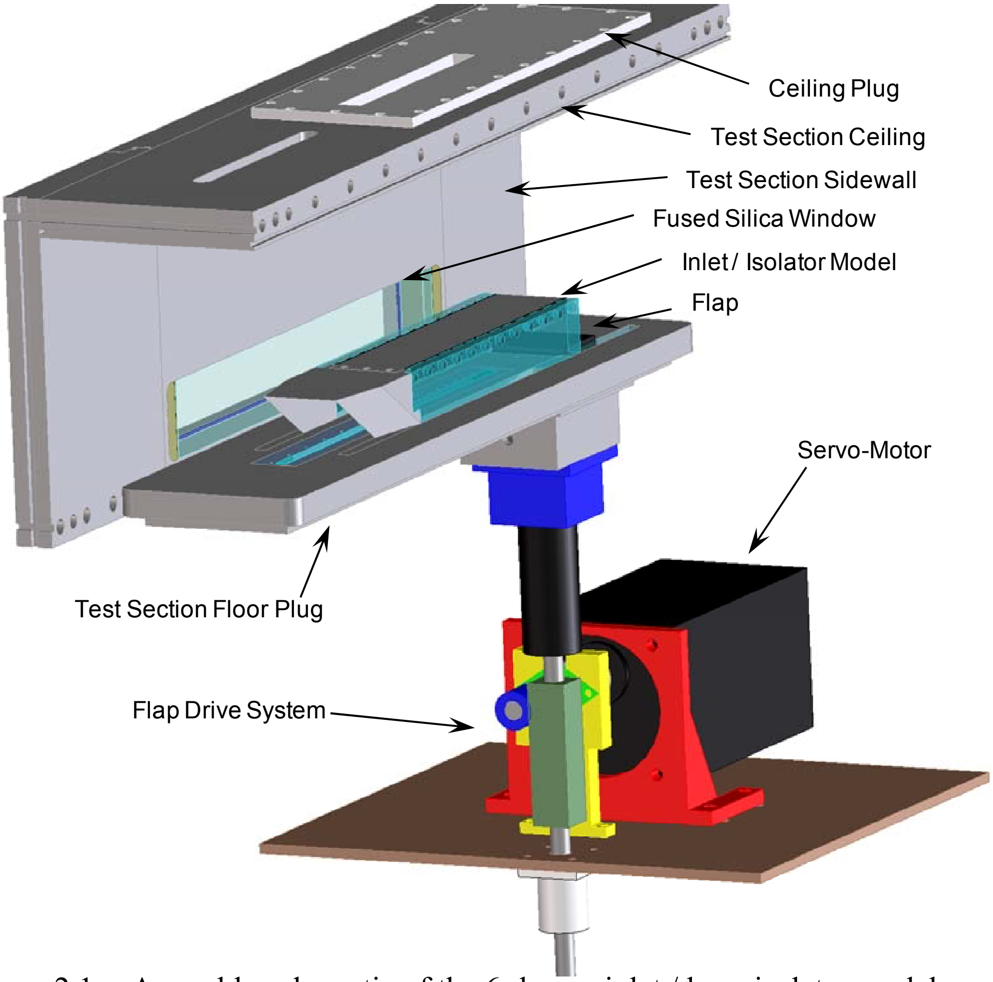

Figure 2.1 Assembly schematic of the 6-degree inlet / long-isolator model mounted in the test section along with the flap drive system.

Fig. 2.2 shows an exploded view of the 6-degree inlet / isolator model used for side-view measurements. The model consisted of four pieces that were bolted together using #8-32 machine screws. The inlet section contained an internal compression ramp. The inlet section had swept sidewalls that were machined in such a way that the inlet entrance flow along the sidewalls would not contain shock waves. The isolator section was a combination of three pieces. The two sidewalls were acrylic (Acrylite ®) as to provide optical access. The ceiling was either aluminum or acrylic depending on the optical diagnostic technique used in a given experiment. Neoprene gaskets were placed in between the sidewall and ceiling to seal the internal model flow. The bases of the inlet and isolator sidewalls contained feet that were machined to slip into slots in the floor plug. Below these feet, neoprene gaskets were also inserted. Finally, the model was mounted to the test section floor plug using #10-24 bolts that entered the bottom of the floor plug. Figure 2.3 shows a schematic of the 6-degree inlet / long-isolator model that was used to acquire plan-view PIV data. The model is similar to that in Fig. 2.2 except the isolator was designed to have bolt holes normal to the ceiling in order to not visually obscure the isolator flow.

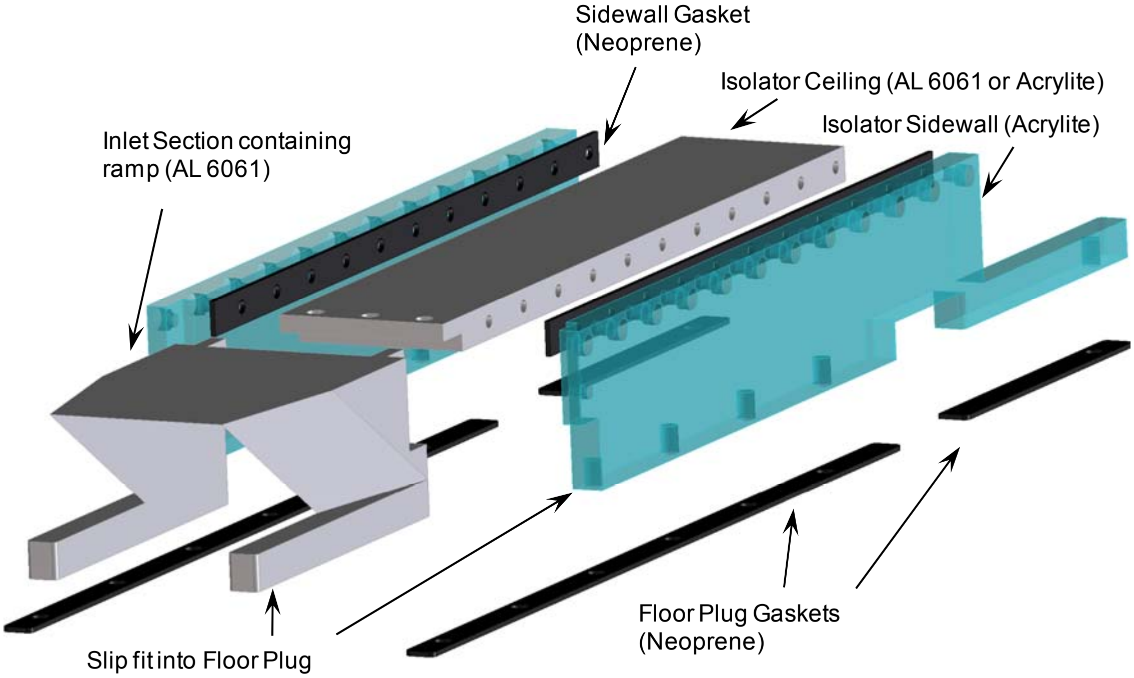

Figure 2.2 Exploded view of the 6-degree inlet / long-isolator model. This configuration was used for side-view PIV and schlieren imaging.

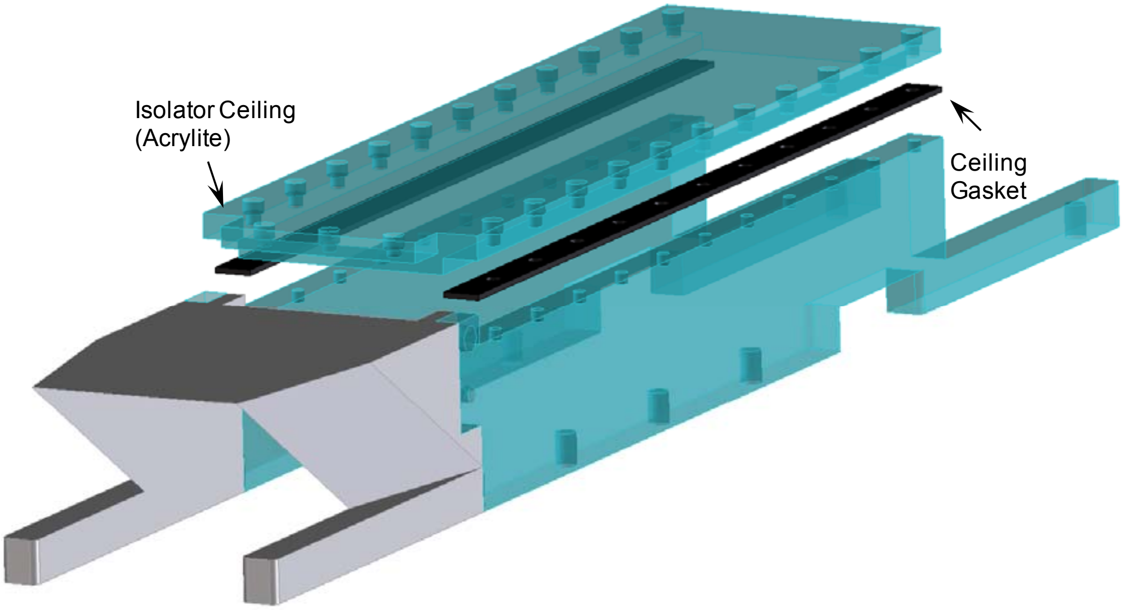

Figure 2.3 Exploded view of the 6-degree inlet / long-isolator model used for plan-view PIV measurements.

Figure 2.4 provides an exploded view of the floor plug, a transducer plug and a cavity enclosure part. As labeled, slots in the floor plug allowed for the securing of the inlet / isolator models. In the center of the floor plug is an additional plug that was used to house the fast-response pressure transducers. In addition, the transducer plug was fitted with a laser exit window used in side-view PIV measurements. The presence of the flap drive system components prevented the transducer plug from spanning the entire streamwise length of the isolator. Therefore, an additional transducer hole was milled directly into the floor plug that could be used to fit a transducer near the exit of the isolator models. At the downstream end of the floor plug, a cavity was cut where the flap and its associated drive system components resided. Finally, as labeled, a cavity enclosure piece was used to seal the flap cavity. The flap drive components will be discussed below. In addition, the flap cavity required a hole (sealed with wax) to accommodate transducer cables for the transducer near the isolator exit that was mentioned above.

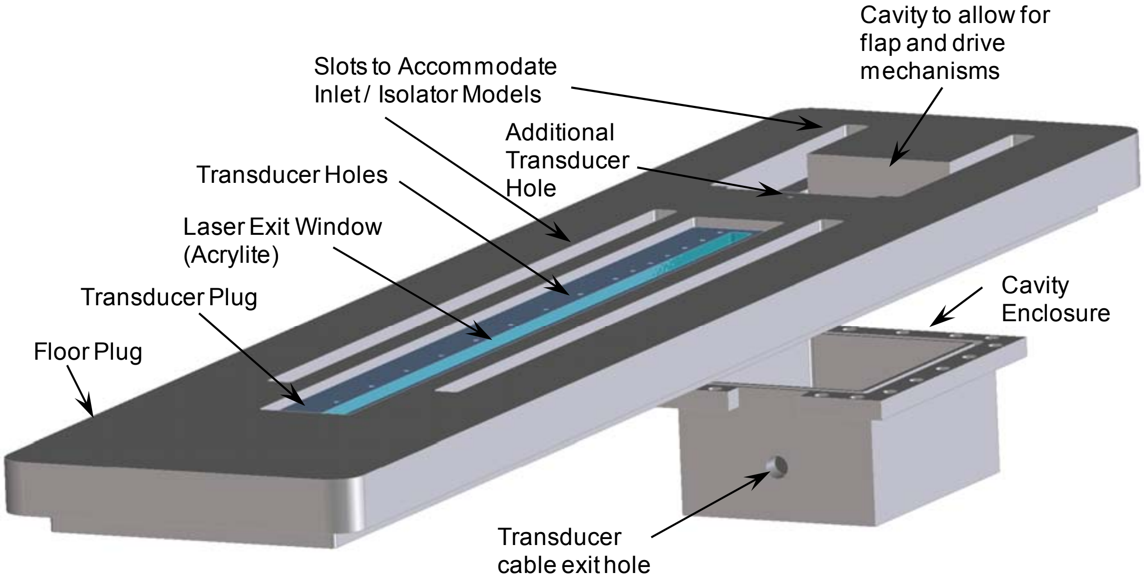

Figure 2.4 Schematic showing the floor plug, transducer plug and the cavity enclosure.

Figure 2.5 shows the system components used to drive the flap shaft. As labeled, a servo-motor (Oriental Motor BX Series) was used to drive a rack and pinion. The motor was mounted to a table top that was welded to an in house built motor stand. The motor stand was then secured to the floor using machine clamps. A horizontal drive shaft was built that was connected to the servo motor with a coupling. A bearing and bearing stand were used to prevent an excessive bending moment load on the motor. At the end of the horizontal drive shaft, a one inch pinion gear was press fit to engage the rack. To enable assembly, an upper and a lower drive shaft were threaded into the one inch rack section. As seen in Fig. 2.5, the shaft motion was kept co-linear with linear bearings, one for the lower shaft and one for the upper. In order to seal the upper drive shaft, a rubber bellows (moving seal) was utilized. This seal was attached to the upper drive shaft with a standard hose clamp and mounted to the cavity enclosure with epoxy. Finally, the flap in the fully down position can be seen above the floor plug in Fig. 2.5.

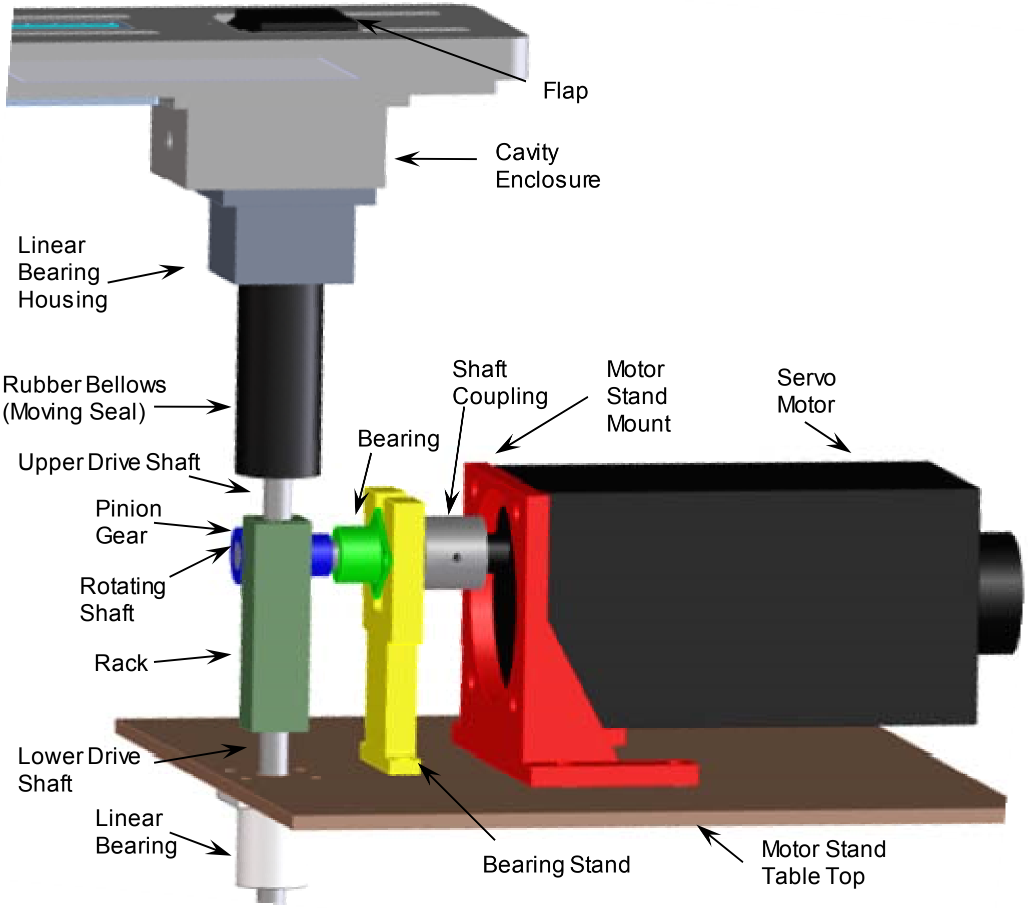

Figure 2.5 Schematic showing the flap drive shaft components.

Figure 2.6 provides additional details on the flap and its associated components internal to the cavity enclosure. The flap was connected to the upper shaft with a linkage bar and two pins (Fig. 2.6a). Upon upward motion of the upper shaft, the linkage bar rotated as the flap angle increased. The flap was assembly is shown in Fig. 2.6(b). The upper flap piece contained press fitted dowel pins which tightly fit into the lower flap piece. In between these pins, a hinge was inserted that had holes to pass the pins and fix the hinge in place. The upper flap, lower flap, and flap linkage pieces each had collinear holes allowing for the three pieces to be bolted together and the hinge to be held in between the upper and lower flap pieces. As seen in Fig. 2.7, a “flap bolt-on” piece was used to mount the flap assembly to the bottom of the floor plug. The flap bolt-on contained holes to accommodate dowel pins which were press fit into the bottom of the floor plug. To mount the flap, the hinge (containing holes for the dowel pins) was placed in between the floor plug and flap bolt-on piece. It is also noted that the flap bolt-on part was designed to allow for the most downstream transducer to be flush mounted above it.

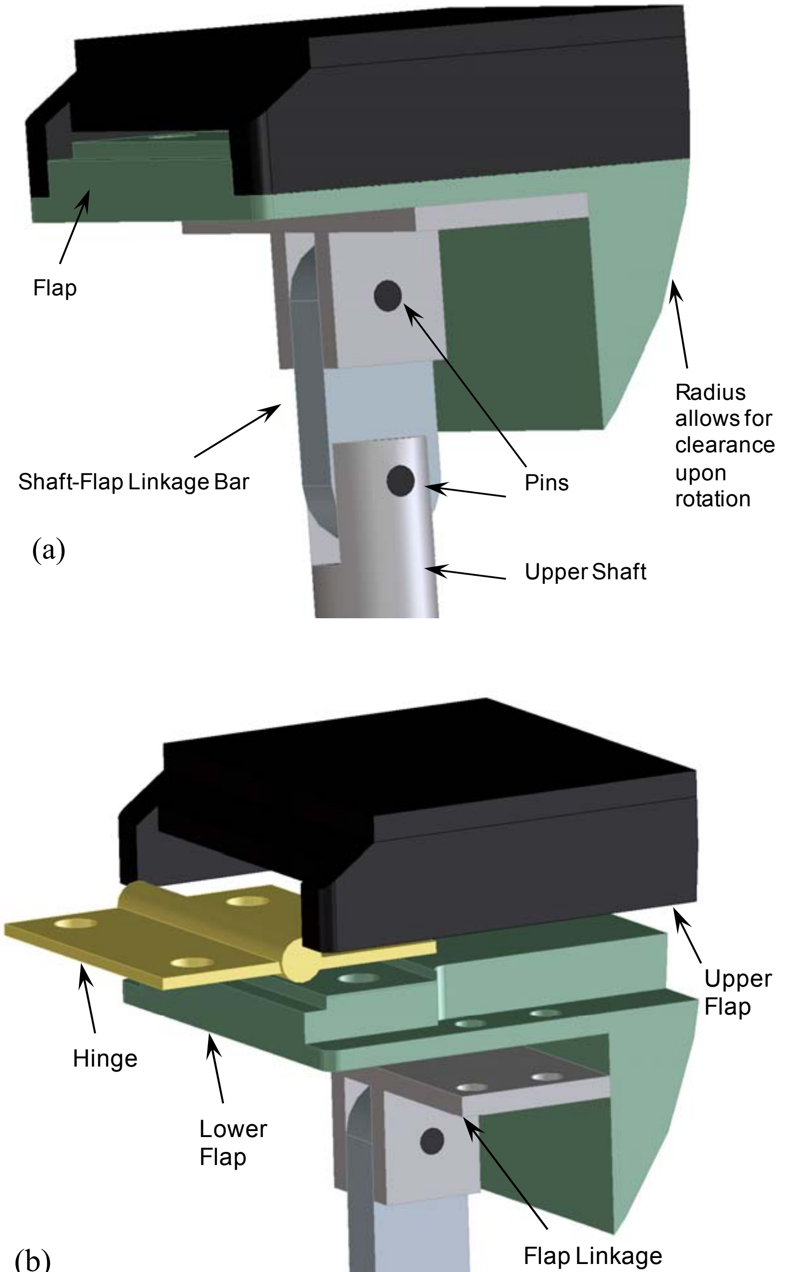

Figure 2.6 Schematic showing the design of the flap mechanism: a) flap / shaft linkage components, and b) flap assembly.

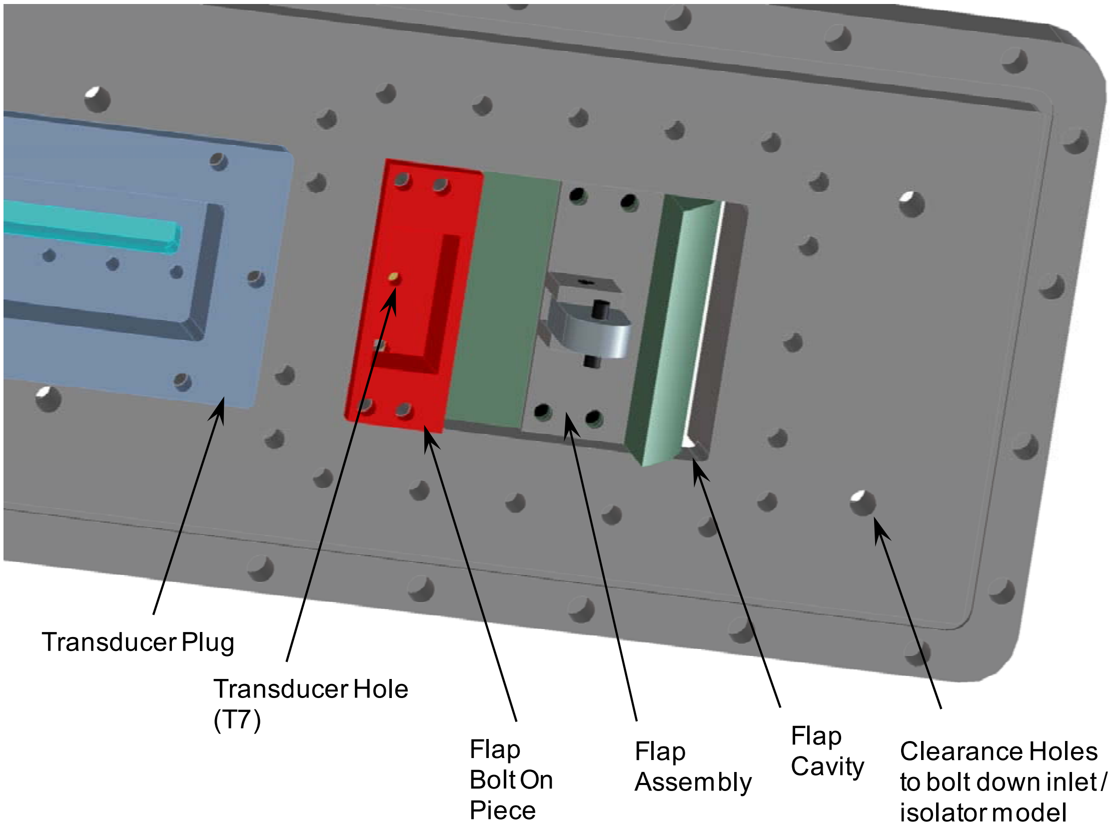

Figure 2.7 Schematic showing the mounting of the flap to the bottom of the floor plug.

2.2.2 Model Geometry Details

In total, six models were tested that represented various combinations of three inlet- and two isolator-models. Figure 2.8 shows what is termed the 6-degree inlet / long-isolator model. This model was the baseline case and it was studied in greater detail than the other 5 configurations. The inlet / isolator model was mounted on the floor of the test section. Figures 2.8a and 2.8b show schematics of the model with one sidewall removed with the flap fully down and the flap raised to an angle 28 degrees which was seen to be great enough to induce unstart. Figure 2.8c shows a photograph of the model. The coordinate system is in non-dimensional units normalized by the isolator height *h*. The inlet portion of the model consisted of a six degree compression ramp with aft-swept sidewalls. The sidewall sweep angle was 53.5 degrees with respect to the wall normal *y* axis. The inlet entrance height H_0 was 34.9 mm (1.375 *in*) and the throat height at the entrance of the isolator section was 25.4 mm (1.00 *in*). The constant area isolator and inlet were 242.3 mm (9.54 *in*) and 90.7 mm (3.57 *in*) long, respectively. The inner width of the model was 50.8 mm (2.00 *in*) giving an inlet entrance aspect ratio of 1.45 and an isolator aspect ratio of 2. As discussed above, the model was a bolted assembly of four pieces. The upstream piece, made out of aluminum, contained the ramp and the isolator throat. A small portion of the isolator, 11.2 mm (0.44 *in*) long, was also contained within the aluminum upstream piece. The rest of the isolator was formed from an aluminum or acrylic ceiling and two acrylic sidewalls to allow optical access. This resulted in a streamwise length of 231.1 mm (9.06 *in*) where the flow within the isolator could be visualized. The thickness of the all three isolator pieces was 9.5 mm (0.375 *in*).

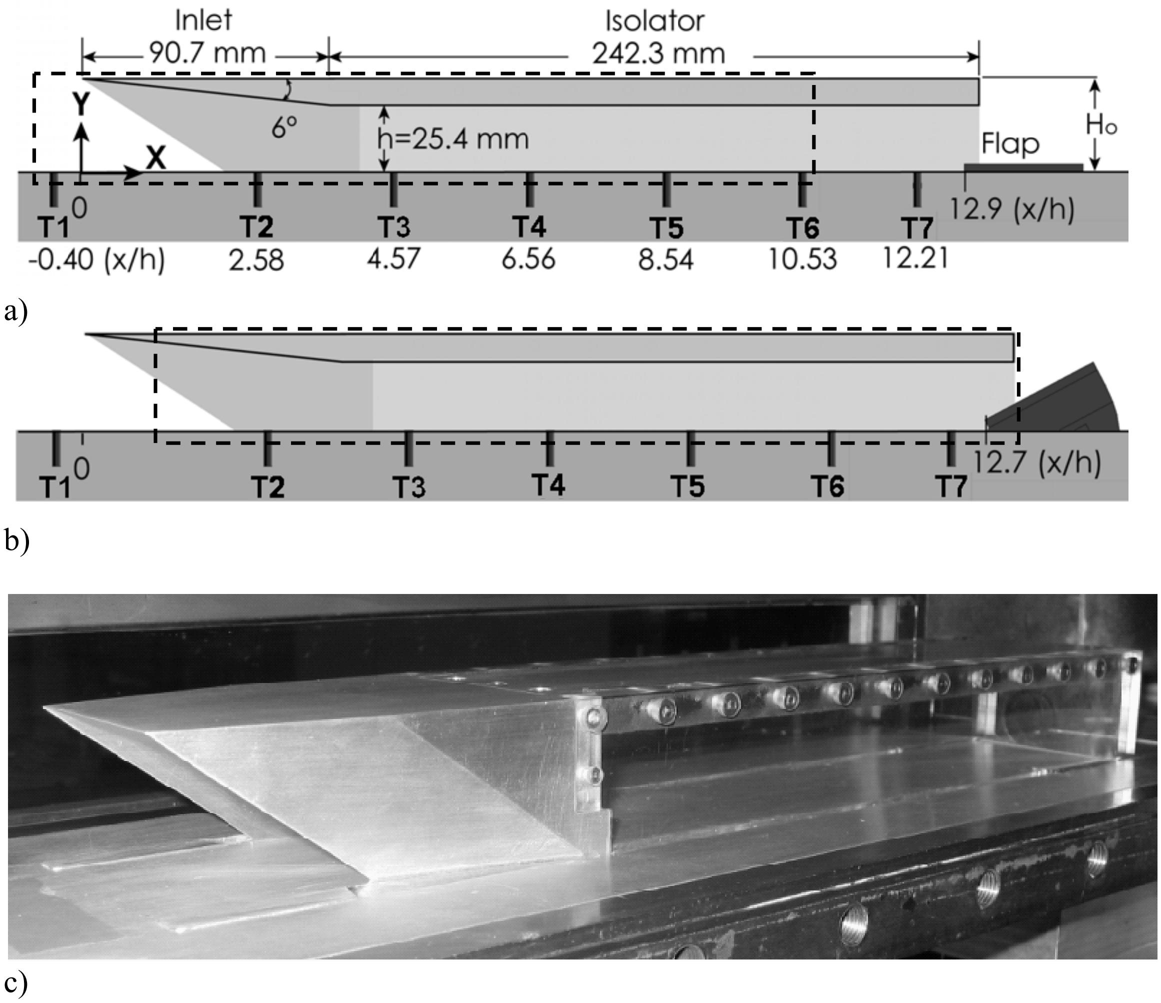

Figure 2.8 The 6-degree inlet / long-isolator model instrumented for simultaneous optical and pressure measurements: a) schematic of the model with flap fully down, b) with flap up at an angle of 28 degrees (model was seen to unstart at 26.6 ± 0.6 degrees), and c) photograph of the inlet / isolator model mounted on the wind tunnel floor.

As discussed, a mechanical flap was raised to simulate the combustor pressure rise. As shown in Fig. 2.8a, in the fully down position, the top of the flap was 3.2 mm (0.125 *in*) above the isolator floor. In the fully down position the leading edge of the flap was at the streamwise coordinate of $x/h = 12.9$. This model was seen to unstart when the flap was raised to an angle, θ_F of 26.6 degrees. The uncertainty in determining all flap angles reported herein is estimated to be ± 0.6 degrees. Further details on the flap position uncertainty are given in Appendix B.2. The flap was hinged to the wind tunnel floor at a location below $y = 0$. As shown in Fig. 2.8b, this resulted in the leading edge of the flap moving upstream to $x/h = 12.7$ at the unstart angle. Further details on the flap geometry and the hinge (pivot point) location can be found in Appendix B.1. Finally, note that the drive system was able to move the flap from its fully down position to the unstart angle in about 140 ms.

The modular design of the inlet / isolator models allowed for the inlets and isolators used to be interchangeable. Two other inlets were used in combination with the long-isolator. Figure 2.9a shows a schematic of an 8-degree inlet connected to the long-isolator. In this 8-degree inlet / long-isolator model, all geometry except the compression ramp angle, length of the inlet and length of the isolator remained constant with respect to the 6-degree inlet / long-isolator geometry. Figure 2.9b shows a schematic of what is called the "0-degree inlet" attached to the long isolator. The 0-degree inlet is just a flat plate inlet with an external compression ramp. In this case the entire model is nothing more than a constant area isolator and the inlet contraction ratio is unity (compared to 1.375 for the 6- and 8-degree inlets).

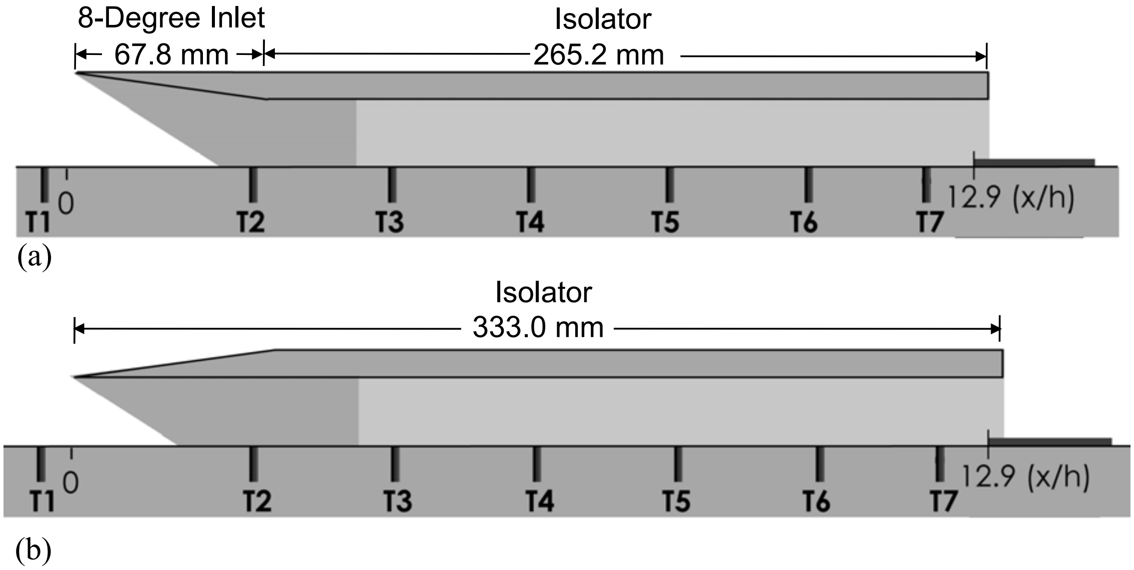

Figure 2.9 Schematics of the two additional inlet / long-isolator models tested: a) 8-degree inlet / long-isolator model, and b) 0-degree inlet / long-isolator model.

Additional experiments were also conducted using what is termed a "short-isolator." Note the short-isolator was only 15.2 mm shorter than the long-isolator. However, as is discussed in chapter 5, this resulted in substantial changes to the flow that could be created upon raising the flap. Figure 2.10 shows the 6-degree inlet / short-isolator mounted to the test section floor. This model has the exact same geometry as the 6-degree inlet / long-isolator except the isolator is shorter. Note the 15.2 mm of length difference is with respect to the exit of the long-isolator. Also note that small sidewall steps as labeled in Fig. 2.10 were present at the isolator exit. These steps were necessary to keep each isolator sidewall and its two feet as one continuous piece. This was necessary for securing the model to the floor plug (e.g., See Figs. 2.2 to 2.4). The step heights and lengths were 6.4 mm (0.25 *in*) and 9.5 mm (0.375 *in*) respectively. In addition to tests of the 6-degree inlet / short-isolator model, experiments were also conducted using the short isolator in conjunction with the 0- and 8-degree inlets. Schematics for these models are not given as they are redundant. The only difference between the 0-degree inlet / long-isolator and 0-degree inlet / short-isolator models was that the latter contained an isolator with a length of 317.8 mm (compared to 333.0 mm for the long case). Similarly, the only difference in the 8-degree models was the short model had an isolator length of 250.0 mm (compared to 265.2 mm for the long model).

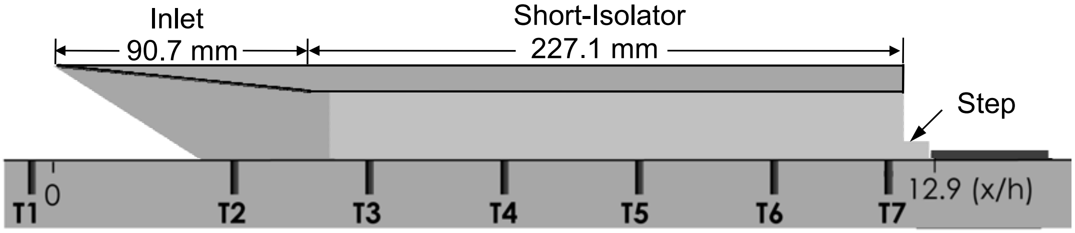

Figure 2.10 Schematic of the 6-degree inlet / short-isolator model.

Owing to the floor-mounted configuration, the inlets in each case ingested the test section floor boundary layer, which was turbulent and quite thick as compared to the inlet heights. The floor boundary layer had the following properties: 99% thickness δ = 19.3mm (0.76 *in*), displacement thickness δ^* = 9.1 mm (0.35 *in*), momentum thickness θ = 0.75 mm (0.03 *in*), and Reynolds number based on momentum thickness, $Re_\theta = 39{,}000$ (Barter, 1996). Unless otherwise noted, the boundary layers on the other walls of the inlet developed naturally.

2.3 HIGH-SPEED SCHLIEREN, FAST RESPONSE PRESSURE MEASUREMENTS AND MOTOR CONTROL SYSTEMS

A schematic of the high-speed schlieren imaging, fast response pressure measurements and motor control systems is shown in Fig. 2.11. Again, a rack and pinion system driven by a servo-motor (Oriental Motor BX Series) was used to control the flap. The servo-motor was driven by a computer running a LabVIEW (National Instruments) control program. A data acquisition card (National Instruments PCI-6221) in the computer was used to output the motor control signals. The high-speed schlieren system operated at a framing rate of 8 kHz and consisted of a high-brightness pulsed LED light source (ISSI, Inc.), two 318 mm (12.5 *in*) diameter mirrors with focal lengths of 152 mm (72 *in*), and a high-framing rate CMOS camera (Photron FastCam-Ultima APX) fitted with a 105 mm f/2.8 lens (Nikon AF Micro-Nikkor). The camera was shuttered to 10 μs and the image resolution was 1024 × 128 pixels. A row of 7 fast-response pressure transducers were flush mounted in a row near the spanwise centerline of the inlet / isolator model. The transducer locations are labeled T1 – T7 on the schematic of Fig. 2.8a. The locations were the same for each of the 6 inlet / isolator models tested. T1 (Kulite XCQ-062-15A) had a range of 0-100 kPa (0-15 psia) and T2-T7 (Kulite XCQ-062-50A) had ranges of 0-350 kPa (0-50 psia). T1 and T2-T7 had effective frequency responses of about 30 kHz and 50 kHz, respectively. T7 was on the spanwise centerline of the model whereas transducers 1 - 6 were shifted slightly off center by 4.1 mm (0.16 *in*) in the starboard direction to accommodate a laser-exit window (used in side-view PIV experiments). The transducer signals were each sent through a wideband differential DC amplifier (Dynamics Model 7525) and then low pass filtered depending on the sampling rate at 50 kHz or 12.5 kHz using an active filter (DL model 4302 or Ithaco S30). The filtered signals were digitized at a rate of 192 kHz or 25 kHz with two A/D cards (National Instruments DAQ PCI-6110E) mounted in a personal computer. The A/D cards were controlled by a Labview code developed in house. The timing electronics, which were used to synchronize the schlieren imaging, pressure measurement and motor drive control systems, consisted of three pulse/delay generators (Stanford Research Systems

DG535) and an in-house built divide-by circuit. The pressure data and imaging systems were synchronized in such a way that two pressure measurements were recorded during the 10 μs exposure time of each schlieren image.

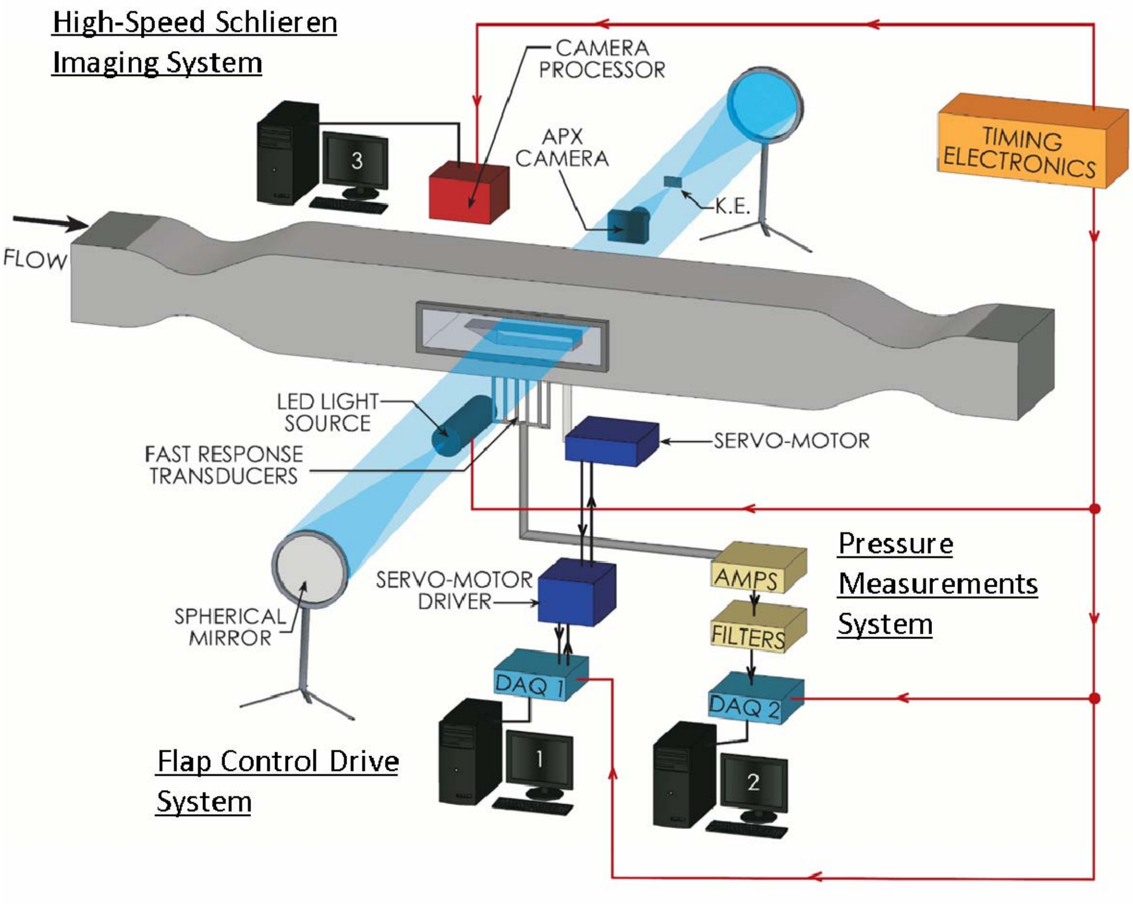

Figure 2.11 Schematic of an inlet / isolator model in the Mach 5 Wind Tunnel along with the schlieren imaging, instantaneous pressure measurements and flap control drive systems.

2.3.1 Pressure Uncertainty Analysis

The total noise band of the electronics added an uncertainty of about ± 0.55 kPa (± 0.08 psi) to instantaneous pressure values reported herein. The transducers were calibrated using least squares linear regression fits and a factory-calibrated precision dial gage (Heise Model CMM). All pressure values used to generate the calibration lines fell within 1% of the corresponding linear fit values. Prior to a calibration and to a wind-tunnel run, each transducer was zeroed at the ambient pressure. The ambient pressure was then read from a manometer. Some drift from the zero occurred during a run and during a calibration. Certain channels were seen to drift and have more uncertainty than others as will be quantified below. In order to account for this drift as well as other sources of uncertainty (i.e., human error reading the manometer, variations in tunnel and model flow, hysteresis, non-repeatability and non-linearity of the Kulites, etc.) tests were conducted to gage the repeatability of the pressure measurements. These tests involved recording the mean inlet / isolator pressure distributions with the flap fully down on six different runs of the wind-tunnel with the same flow condition settings (same plenum pressure and same inlet / isolator model). In addition to run-to-run non-repeatability, there was also calibration non-repeatability. The calibration uncertainty estimate was based on variations in three different calibrations that were nominally the same. Assuming the calibration non-repeatability and run-to-run non-repeatability to be independent, the uncertainty due to non-repeatability is the root-sum-square value of these two sources. The root-sum-square of the *RMS* uncertainties due to calibration and run-to-run variations is given for each transducer location in Table 2.2. Unless otherwise specified, mean pressure distributions were generated using only data from one wind-tunnel run. Therefore, using the standard error (i.e., $\varepsilon = 2\sigma / \sqrt{n}$) the uncertainty in the mean flap-fully-down data due to run-to-run and calibration-to-calibration variations is estimated to be $\pm 2\sigma$ at a given transducer location. Thus, the total uncertainty in each pressure value is estimated to be the root-sum-square of the 1% calibration non-linearity error and the non-repeatability uncertainty seen in Table 2.2.

In addition, similar repeatability tests were conducted for which a high-compression shock system existed within the isolator. For these tests, five different wind tunnel runs with the same flow conditions were made to provide an estimate for run-to-run variations. The calibration uncertainty estimate was based on variations in three different calibrations that were nominally the same. The root-sum-square of the *RMS* uncertainties due to the calibration and the run-to-run variations is given for a high-compression shock system at each transducer location in Table 2.2.

Table 2.2 Standard deviations to provide uncertainty ranges that are due to run-to-run and calibration-to-calibration variations.

Transducer	σ(psi) Flap-down	2σ Flap-down.	σ High-Comp.	2σ High-Comp.
T1	0.071	0.14	0.071	0.14
T2	0.056	0.11	0.056	0.11
T3	0.155	0.31	0.152	0.30
T4	0.064	0.13	0.068	0.14
T5	0.060	0.12	0.053	0.11
T6	0.195	0.39	0.123	0.25
T7	0.056	0.11	0.165	0.33
Average	0.094	0.19	0.112	0.22

Tests were also conducted to see whether or not the fast-response measurements were capable of providing useful *RMS* pressures. A particular concern was that noise fluctuations might be greater than or comparable to fluctuations in an actual run. The lowest fluctuations in a run were seen to occur in cases when the model flow was fully supersonic and the flap was in the fully-down position. Therefore, pre-run pressure fluctuations (i.e., noise) were compared to those given at each transducer during a run. An example of such a test is given in Fig. 2.12, which shows the *RMS* pressure distributions in the 6-degree inlet / long-isolator model prior to and during a run where the flow in the model was fully supersonic and the flap was fully-down. The characteristics of the actual run data are not important at this time. What is highlighted here is the comparison of the pre-run (noise) and actual run *RMS* pressures. As is seen in Fig. 2.12, the fully supersonic *RMS* pressure at T1 (*x/h* = -0.4) upstream of the model is exactly the same as the pre-run noise. However, the other six *RMS* values are above their pre-run counterparts. Therefore, it is evident that the pressure fluctuations in the undisturbed boundary layer are not resolvable. For this reason, *RMS* pressures are not given in the results sections corresponding to the 0-degree inlet cases where the inlet ingests undisturbed boundary layer flow.

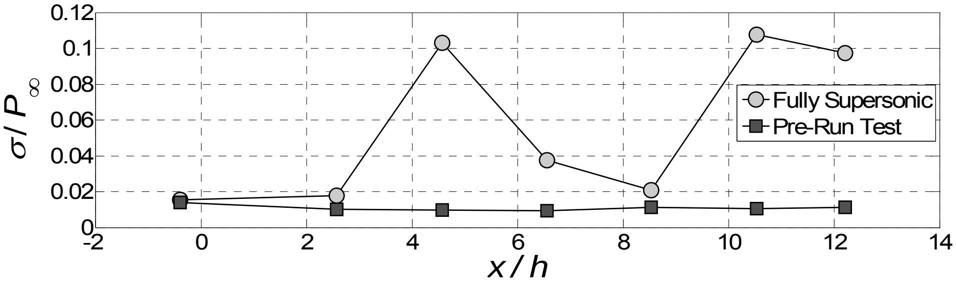

Figure 2.12 A comparison of no-flow noise in the pressure transducer signals to *RMS* pressures measured in the fully supersonic started flow of the 6-degree inlet / long-isolator model.

2.3.2 Schlieren Fields of View

The entire length of the inlet / long-isolator models was 333 mm (13.1 *in*), but the maximum schlieren field of view obtainable was 318 mm (12.5 *in*) owing to the size of the schlieren mirrors. Therefore, in some cases to image the entire flow field including about 25 mm upstream of the inlet, two overlapping fields of view were used. The two fields of view are referred to as the “upstream-view” and “downstream-view.” As shown with the dashed-line rectangle in Fig. 2.8a, the upstream-view extended from outside the inlet at *x/h* = -0.7 to inside the isolator at *x/h* = 10.8. As shown in Fig. 2.8b, the downstream-view imaged the entire isolator section where the flow was visible. These two fields of view were not acquired simultaneously but on different runs of the wind tunnel. Note that the two fields of view just described were used primarily in the 6-degree inlet / long-isolator tests. For experiments using other models, the fields of view predominantly covered only the isolator sections of the models where the flow was visible.

2.4 PIV SYSTEM AND MEASUREMENT CONSIDERATIONS

2.4.1 PIV System Details

Figure 2.13 shows a schematic of the PIV system setup for plan-view measurements. Note that the pressure measurements and flap drive control systems seen in Fig. 2.11 were used simultaneously with the PIV system seen in Fig. 2.13. The seeding system can be seen on the left of the figure. The PIV seed-particles were titanium dioxide (TiO_2) with a manufacturer specified nominal diameter of 0.02 μm. Compressed nitrogen drove the seeding system. The particles were seeded upstream of the stagnation chamber using a two-stage fluidized-bed seeder followed by a cyclone separator. For further details of the seeder system see Hou (2003). Note that in previous Mach 2 studies at this facility, it was possible to get high seeding densities by seeding into the wind tunnel plenum (e.g., Hou, 2003, Bueno et al., 2006 and Ganapathisubramani et al. 2007). However, this has not been the case in Mach 5 PIV experiments where it has proven difficult to get adequate seeding densities. For example, in order get a high enough seed density, Beresh (1999) was forced to inject particles directly into the test section boundary layer upstream of the compression ramp shock wave / boundary layer interaction he was investigating. In the current work it was desired to avoid disturbing the flow upstream of the inlet. Therefore, in order to allow for seeding injection into the plenum, the seeding mass flow rate was increased. This was achieved primarily by using a high flow rate dome loaded pressure regulator (Grove Powreacter 202F) to control the flow of nitrogen into the seeder. The set pressure of the regulator was typically near 8.3 MPa (1200 psi). In order to cope with the high volumes of nitrogen that were required to drive the seeding system, a manifold connected six pack of K bottles was used. The seeding system was effective as it provided good particle densities for PIV correlations. However, use of the system proved quite tedious. For example, the high pressures required to give adequate seeding resulted in the compaction or "caking" of particles in the seeder beds, seeder tubing and in the system's check valve. This required that the seeder system had to be disassembled and thoroughly cleaned after each PIV run.

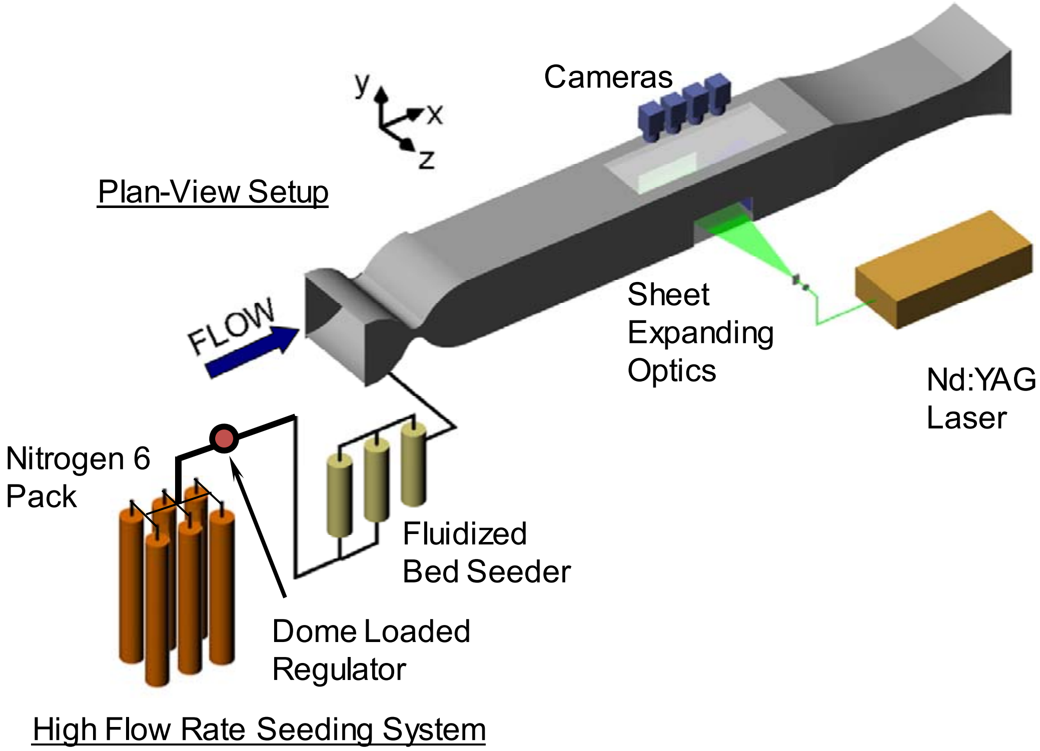

Figure 2.13 Schematic showing the wide-field PIV system setup for plan-view measurements.

The wide field PIV system utilized pulsed laser sheets from a dual-cavity flashlamp pumped Nd:YAG laser (Spectra Physics PIV 400) separated in time by 2.00 μs. The laser repetition rate was 10 Hz. The fields of view corresponding to the plan- and side-view measurements are given in Figs. 2.14a and 2.14b respectively.

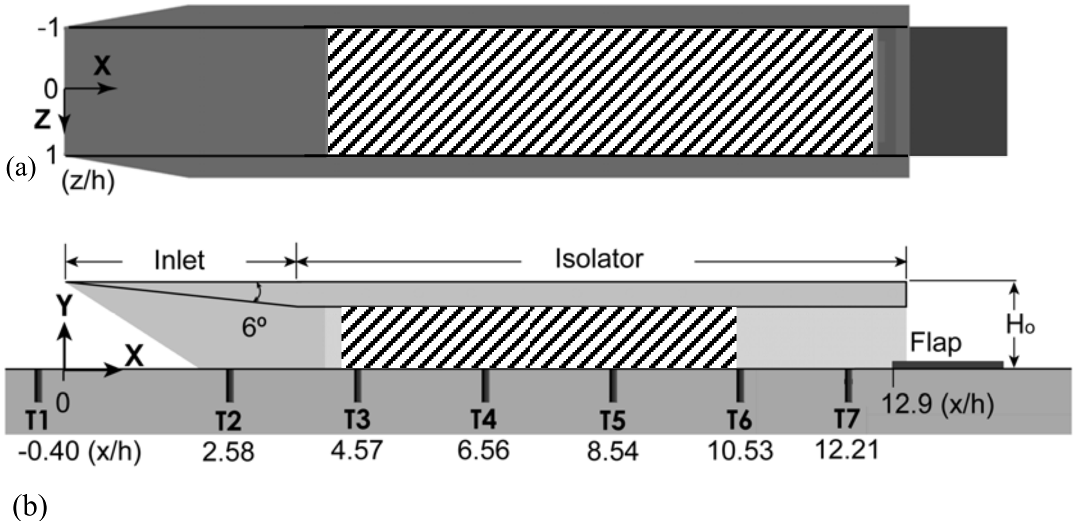

Figure 2.14 PIV fields of view: a) The hatched rectangle indicates the plan-view PIV field of view, and b) side-view PIV field of view.

For the plan-view, the sheets entered and exited the wind tunnel test section through the fused-silica side windows and passed through the acrylic isolator sidewalls. The sheets were at the wall-normal center of the model (y/h = 0.5). The laser energy of each pulse was set to about 140 mJ and the thickness of each sheet was approximately 1.4 mm. Digital image pairs were acquired with four Kodak MegaPlus ES 1.0 cameras (1024 × 1024 pixels) which imaged the flow through a fused-silica test section window and the acrylic isolator ceiling. The cameras were fit with fitted with 105 mm lenses (Nikon AF Micro-Nikkor) and arranged side-by-side to capture a field of view that extended in the streamwise direction from x/h = 4.0 to 12.5 for a total length of 216 mm. The lens aperture setting (*f* – number) was 16 for the plan-view experiments. The entire internal span of the isolator from *z/h* = -1.0 to + 1.0 (51 mm) was imaged.

For the side-view, the laser sheets entered the wind tunnel test section through a fused-silica top window, passed through an acrylic isolator ceiling and exited through an acrylic isolator/test-section floor window. The sheets were offset 3.2 mm to the port side of the spanwise center of the model isolator. The laser energy of each pulse was set to about 100 mJ and the thickness of each sheet was approximately 1.4 mm. Digital image pairs were acquired with three Kodak MegaPlus ES 1.0 cameras. The cameras were arranged side-by-side to capture a field of view of 150 mm (5.9 *h*) long by 25.4 mm (1.0 *h*) high. The *f* – number was 8 for the side-view experiments. The field of view covered a portion of the visible isolator as shown in Fig. 2.14b.

PIV images were processed with LaVision's DaVis 7.21 software. Prior to correlation computations, each image was background subtracted using the sliding minimum background subtraction function built into the software. This function searched a given image and one to four of its preceding and subsequent images for the minimum intensity at each pixel location. The minimum intensity corresponding to each pixel location was then subtracted from each pixel location. This served to remove some of the background noise due to particles sticking to the tunnel and isolator walls. To illustrate this, Fig. 2.15 shows an example side-view PIV image taken while the flow throughout the model was fully supersonic. Figure 2.15a is the image unprocessed and Fig. 2.15b shows the sliding minimum background subtracted image. In comparison, the processed image is seen to have far less background reflections and less of a background haze. Not surprisingly, image pairs that were subjected to the sliding minimum background technique tended to provide higher quality data. For example, it is estimated that the amount of valid vectors was increased by about 3-5% by using this technique.

After the background subtraction, correlations were then computed using the normalized cross correlation function with a Gaussian weighted interrogation window. The interrogation window size was 32 × 32 pixels which corresponded to linear resolutions of 1.95 × 1.95 mm and 1.78 × 1.78 mm for the plan- and side-views respectively. An overlap of 50 % was used resulting in final fields of 219 × 51 vectors and 173 × 28 vectors for the plan- and side-views respectively. Four passes (three adaptive passes) were used to calculate the final vector field. On each pass, a signal-to-noise filter removed vectors with a ratio of highest correlation peak to second highest correlation peak ratio less than 1.2. In addition, the velocity data were filtered with a standard 3 × 3 median filter. In the median filter, the components of the velocity vector in question were compared to the median velocity components of the neighboring vectors. Vectors having a velocity component with a deviation outside the range of $\pm 2\sigma$ (where σ is the standard deviation) from the median were removed. Missing vectors were interpolated using a 3 × 3 local average technique. The percentage of valid vectors in the PIV data was seen to vary according to the flowfield being measured. Further details are given in the results sections.

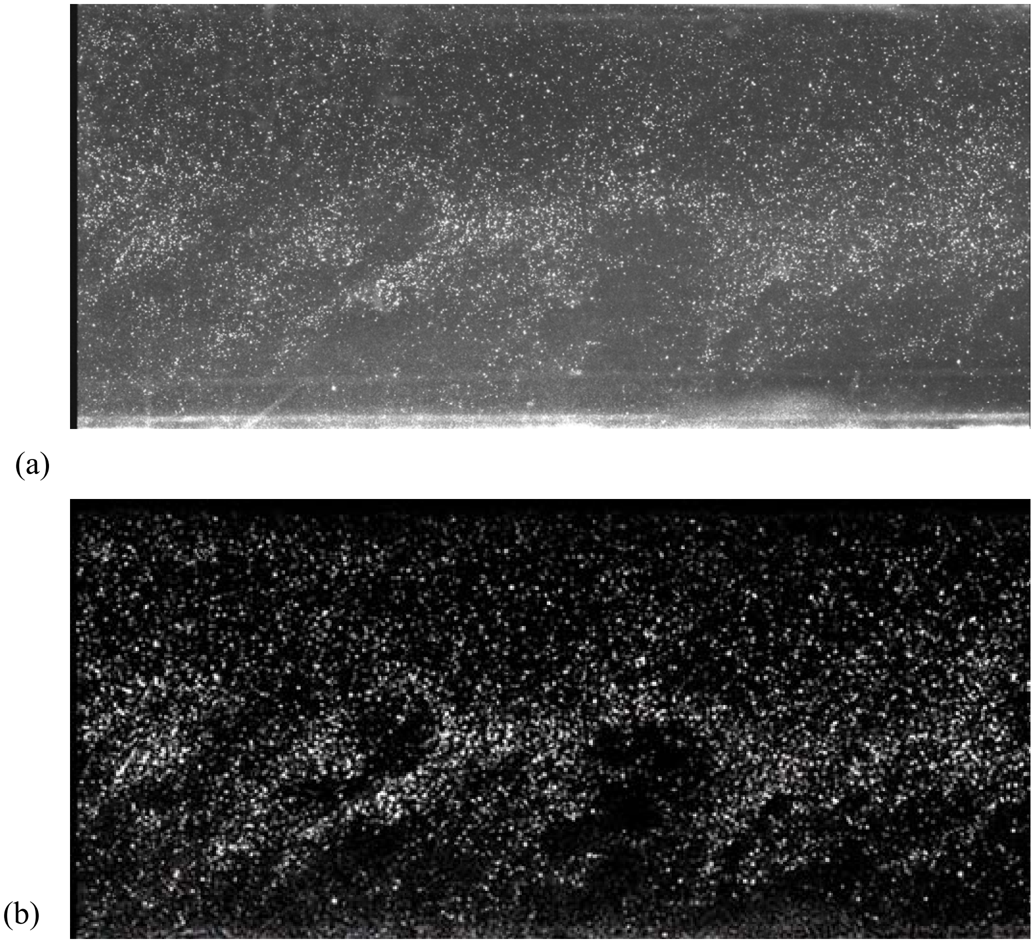

Figure 2.15 Example of the sliding minimum background subtraction technique of LaVision Davis 7.2: a) example raw image, and b) same image processed with the technique.

2.4.2 Particle Flow Tracking Considerations

A source of bias error can arise in PIV if the particles do not faithfully track flow velocity changes. A measure of the particles' ability to track velocity changes in the flow is the particle time constant τ_p (Melling, 1997). By definition a particle experiencing a step change in velocity will take a time τ_p to change 63% of the velocity step change. Hou (2003) investigated the response time of the same TiO_2 particles used in this study.

His measurements were based on the relaxation distance of particles as they passed through a shock wave. For example, the response time τ_p of particles traveling through a Mach 2 normal shock was measured to be about 2.6 μs. From this response time the effective agglomerated diameter of the particles was estimated to be about 0.26 μm. However, for the flow conditions reported herein, the particle response time due to a sudden velocity change is expected to differ from that at Mach 2. This is clear upon inspection of the relation for τ_p given by Erbland (2000)

$$\tau_p = \frac{\rho_p d_p^2}{18\mu}\left[1 + Kn(2.492 + 0.84\exp(-0.435/Kn)\right] \qquad (2.1)$$

where μ is dynamic viscosity of the gas (calculate herein with Sutherland's formula), ρ_p is the particle density, d_p is the particle density and Kn is the Knudsen number which is equal to the mean free path (Λ) divided by the particle diameter. The mean free path, Λ is given by

$$\Lambda = \frac{k_B T}{\sqrt{2}\pi\sigma_{coll}^2 P} \qquad (2.2)$$

where k_B is equal to the Boltzmann constant and σ_{coll} is equal to the molecular collision diameter which is about 0.75 nm for air. Note that in Equation 2.1, the term outside of the brackets is based on the assumption that the particles experience a Stokes drag and the term inside the brackets accounts for rarefied-flow effects. This work includes PIV measurements of fully supersonic flow where the flap is fully down, of the unstart process, of unstarted flows and of high-compression shock systems. To get an estimate of the particles' ability to track velocity fluctuations within these flows, three particle response times were calculated using Equation 2.1 and the particle diameter measured by Hou (2003) of 0.26 μm. These response times correspond to particles in the freestream flow, particles processed by a 6-degree (flow deflection angle) oblique shock and particles processed by a normal shock. In addition to particle response times, the distances over which the particles travel in the particle response times are also given. According to Melling (1997), the particle velocity, $u_p(t)$ after a velocity step change is

$$u_p(t) = u_2 + (u_1 - u_2)e^{-t/\tau_p} \tag{2.3}$$

where u_1 and u_2 are the velocities upstream and downstream of the step change, respectively. Upon integration of Equation 2.3 (e.g., Hou, 2003), the distance (X_p) that a particle travels to reach the velocity $u_p(t)$ is

$$X_p = \tau_p \left[u_1 - u_p(t) - u_2 \ln\left(\frac{u_p(t) - u_2}{u_1 - u_2} \right) \right] \tag{2.4}$$

Finally, when $t = \tau_p$, the difference between the particle velocity and that of the velocity after the step change ($u_p(t) - u_2$) is 36.8% of the velocity step change ($u_1 - u_2$). Equation 2.4 then reduces to

$$X_p = \tau_p \left(u_1 - u_p(t) - u_2 \right) \tag{2.5}$$

To estimate flow tracking in the started flow, time constants for freestream particles and those behind a 6-degree oblique shock were calculated. For the freestream flow, the particle $Kn = 0.27$ and τ_p computes to be 7.1 μs. Note that in this case, the rarefied-flow term of Equation 2.1 substantially increases the calculated particle response time to 1.7 times the value that would correspond to pure Stokes drag. The freestream τ_p was used to estimate particle tracking in the turbulent floor boundary layer of the started flow which was seen to be very similar to the floor boundary layer in the test section outside of the isolator. Samimy and Lele (1991) reported that for particles to faithfully track velocity fluctuations in a turbulent shear layer, the Stokes number, which is defined as $St = \tau_p / \tau_f$, where τ_f is the characteristic flow timescale, must be less than about 0.5. In the turbulent boundary layer, the characteristic timescale based on outer-scale or large-scale structures is taken to be $\tau_f = \delta / \Delta U$, where ΔU is the characteristic velocity difference. The minimum velocity measurements made in the floor boundary layer were about 400 m/s. Taking the characteristic velocity difference to be the difference between this minimum and the freestream velocity gives $\tau_f = 55$ μs and $St = 0.13$. Therefore, the particles should faithfully track large-scale velocity fluctuations within the turbulent floor boundary layer of the started flow. When the flap was in the fully down position, the flow consisted of a series of oblique shock and expansion wave reflections. To get an idea of the particles' ability to follow the started flow, the particle response time after a 6-degree oblique shock ($Kn = 0.16$) was calculated using Equation 2.1. Based on this particle time constant of 4.5 μs and Equation 2.5, particles will travel a distance of about 3.5 mm to reach 63% of the velocity induced by a 6-degree oblique shock. Therefore, the started flow velocity data in regions corresponding to oblique shocks is expected to appear smoothed.

During unstart a strong shock-system was seen to propagate upstream through the inlet / isolator model. To estimate the ability of particles to track the flow behind this unstart shock system, the unstart shock system was modeled as a Mach 5 normal shock and the response time of particles with flow conditions behind this shock was calculated. Using the flow conditions behind a Mach 5 normal shock ($Kn = 0.06$) and Equation 2.1 gives a response time τ_p of 0.75 μs. Using Equation 2.5, this corresponds to a distance of 0.4 mm that the particles will travel to reach 63% of the velocity step change. This suggests that the ability to resolve the unstart shock system will be limited by the spatial resolution of the data and not the particle response time. It is also important to estimate the particles ability to faithfully track the flow behind the unstart shock system. As will be discussed, the flow behind the unstart shock system was seen to contain prominent shear layers with velocity differences across the layers being as high 1000 m/s. The particle response time at flow conditions behind a Mach 5 normal shock was used to estimate particle tracking capabilities in these shear layers. The requirement of Samimy and Lele (1991) that St should be less than 0.5 was used to estimate the characteristic flow widths over which particles may be expected to track velocities. The characteristic flow width corresponding to $St = 0.5$, $\tau_p = 0.75$ μs and $\Delta U = 1000$ m/s is 1.5 mm. This estimate suggests that the particles should be able to faithfully track large scale velocity fluctuations of large-scale flow structures within the shear layers that exist during unstart.

The PIV processing correlation algorithm introduces additional sources of error. The ability of an algorithm to accurately find a correlation in an interrogation window depends in part on the seeding density, velocity gradients and out of plane motion within the window (Keane and Adrian, 1992, and Westerweel, 1997). In classical algorithms, velocity gradients have been shown to degrade the detection probability for correlations as well as to introduce bias towards low velocities (Keane and Adrian, 1992, and Westerweel, 1997). However, advanced algorithms (such as those used by LaVision 7.2) that incorporate fractional window shifting and deformation have been shown to substantially increase detection probabilities as well as to significantly reduce bias error in flow regions of high shear (Scarano and Riethmuller, 2000). As will be discussed, the flowfields during unstart were seen to contain regions of high velocity gradients. The effects of these gradients on the vector detection capability as well the errors they induce are discussed quantitatively in Appendix C. Uncertainties in the mean flowfields presented herein are also discussed in Appendix C.

CHAPTER 3

3. Baseline Case: 6-degree Inlet / Long-Isolator Flows

3.1 FULLY SUPERSONIC STARTED FLOW (FLAP-FULLY DOWN)

3.1.1 Started Flow Schlieren Imaging and Pressure Measurements

Figure 3.1 shows upstream- and downstream-view schlieren images for the started fully supersonic inlet / isolator. White lines mark the floor, 6-degree compression ramp and the isolator ceiling. The inlet section, with its swept sidewalls, are seen in shadow since they are made of aluminum. The upstream-view (Fig. 3.1a) was obtained using a horizontal knife edge in order to reveal vertical density gradients such as those due to boundary layers. As labeled, the thick (δ = 19.3mm) floor boundary layer entering the inlet is visualized as a bright region, whereas the thin ceiling boundary layer is seen as a dark region (arrow A). The initial oblique shock from the inlet ramp is visually blocked by the inlet's aluminum sidewalls, but the first reflected shock is seen near the isolator entrance as a dark line (arrow 1). The first reflected shock impinges on the isolator ceiling, which results in an increase in boundary layer thickness downstream of the impingement point. The subsequent reflected shock is seen as a bright line (arrow 2), which then reflects again from the isolator floor (arrow 3). The expansion fan originating at the inlet shoulder (i.e., the junction of the inlet and isolator) can also be seen as a dark region that enters the field of view in the upper left hand portion of the isolator (arrow B). Figure 3.1b shows a downstream-view schlieren image of the started flow. The image was acquired using a vertical knife edge to highlight horizontal density gradients. All three reflected shocks are captured in this field of view (arrows 1-3). The final reflected shock intersects the isolator ceiling near the exit of the model. A detached shock (arrow C) is seen to form just upstream of the flap (arrow D).

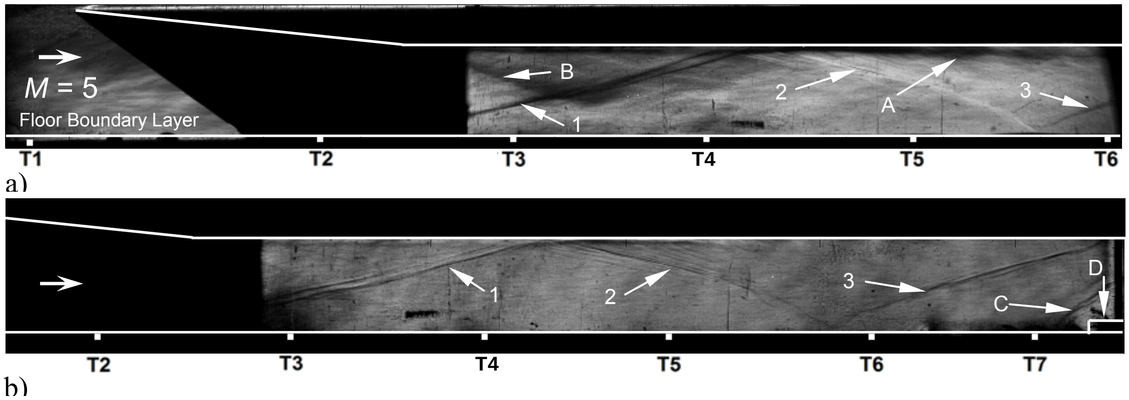

Figure 3.1 Schlieren images of started flow a) upstream-view obtained with a horizontal knife edge and b) downstream-view obtained with a vertical knife edge. (All figures in chapter 3 correspond to flows in the 6-degree inlet / long-isolator model).

The mean (P_m) and *RMS* (σ) pressure distributions are shown in Fig. 3.2. The pressures of Fig. 2 are normalized by that measured at T1, which is assumed to equal the freestream pressure P_∞. The pressure at T1 was measured to be 5.38 kPa (0.78 psia). For all pressure plots, the distributions are normalized by the T1 pressure. This pressure for each figure can be looked up in Appendix A using Tables A.1 and A.2 Figure 3.2a shows that the mean pressure remains nearly constant from T1 (x/h = -0.40) upstream of the inlet to T2 (x/h = 2.58) within the inlet portion of the model. A pressure increase is then seen at T3 (x/h = 4.57). At T3, the flow has been processed by the 6-degree ramp shock as well as the first reflected oblique shock. Using inviscid oblique shock theory, the pressure ratio of the freestream to that processed by two oblique shocks with flow deflection angles of 6-degrees is computed to be 3.7. The pressure ratio P_3/P_1 is measured to be 3.6, which is in good agreement. Moving downstream the pressure then decreases across T4 (x/h = 6.56) and T5 (x/h = 8.54) as the flow passes through reflections of the inlet shoulder expansion fan. The maximum mean pressure for the started case occurs at T6 (x/h = 10.53) just behind the second reflected oblique shock.

Just upstream of the flap shock, the pressure at T7 (*x/h* = 12.21) is slightly lower than that at T6, which is most likely a result of the flow passing through additional reflected expansions. The *RMS* pressure distribution of Fig. 3.2b shows T3, T6 and T7 to have the highest fluctuations. T3 and T6 are just downstream of impinging shocks, whereas T7 is just upstream of the flap shock. It therefore appears that shockwave / turbulent boundary layer interactions are responsible for the increased pressure fluctuations.

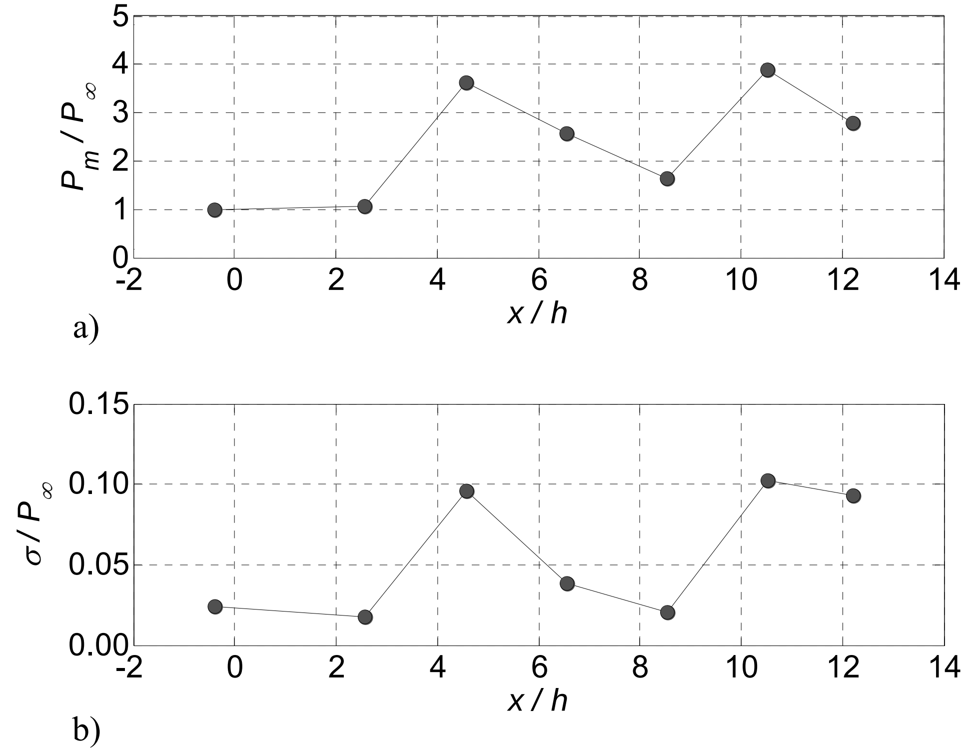

Figure 3.2 Fully supersonic started flow: a) mean pressure distribution and b) pressure standard deviation distribution.

3.1.2 Fully Supersonic Started Flow PIV Measurements

Mean velocity fields of the fully supersonic started isolator were acquired in a field of view covering nearly 2/3 of the isolator as seen in Fig. 2.14b. Ninety PIV images from one wind tunnel test were used to calculate the mean. The percentage of valid (noninterpolated) vectors is about 93% for the dataset. The majority of invalid vectors occurred near the floor where the seeding density was lower due the thick turbulent boundary layer (compressibility effects). Only valid vectors were used to calculate the mean. This means the data are biased to regions with higher particle density. The three cameras were aligned in a way such that the upstream field of view sufficiently overlapped the middle field of view to produce two independent measurements of the column of vectors at $x/h = 6.5$. Similarly the middle field of view sufficiently overlapped the downstream field of view to produce two independent measurements of the column of vectors at $x/h = 8.4$. The comparison of vectors given by the two independent measurements allowed for the uncertainties associated with the PIV data reduction process (i.e., processing uncertainty) and camera noise to be approximated. Uncertainty analysis for the PIV data is given in Appendix C. In short, uncertainties associated with laser pulse time variations, calibration (image registration), precision uncertainty, camera noise, and the data reduction process were considered. The maximum uncertainties occur near the wall and are about ±17 m/s. Outside of the floor boundary layer at about $y/h = 0.8$, the uncertainties decrease to about ± 6 m/s. Further details can be found in Appendix C.

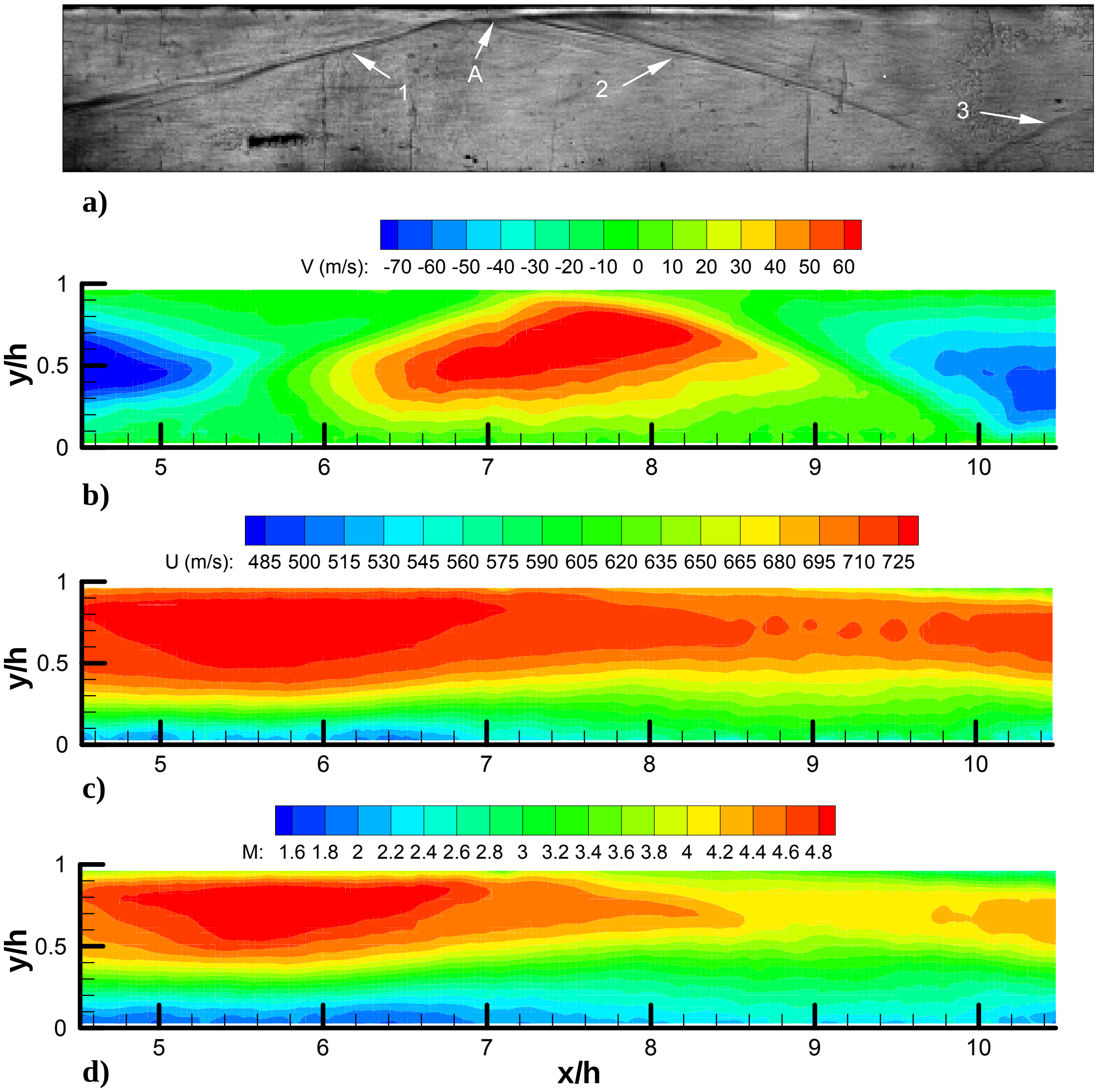

Figure 3.3 Flowfield structure for the fully supersonic long isolator: a) representative schlieren image in the PIV field of view, and b) mean (based on the 90 vector fields) wall-normal velocity contours, and c) mean streamwise velocity contours, d) Mach number contours.

The mean velocity fields of the fully supersonic started isolator are shown in Fig. 3.3. For comparison, a schlieren image, taken at the same steady-state condition, but not simultaneously, is shown in Fig. 3.3a. The three ramp shock reflections are seen in the image (Arrows 1-3). The mean wall-normal velocity contour and streamwise velocity contour plots are shown in Figs. 3.3b and 3.3c, respectively. The wall-normal contour plot of Fig. 3.3b shows the presence of the system of reflected shocks and expansions within the isolator. Flow at the far left of the image is turned downward by the oblique shock due to the 6-degree compression ramp. Proceeding downstream, the flow in the upper portion of the isolator is then turned parallel to the ceiling by the inlet shoulder expansion fan. The first reflected oblique shock turns the flow in the lower portion of the isolator parallel to the floor. From about x/h = 6 to 9 the flow is predominantly inclined upward due to the system of reflected shock and expansion waves. The flow then turns parallel to the floor and then downward due to continued reflections of this system. The streamwise velocity contour plot of Fig. 3.3c shows the thick floor boundary layer in the isolator exhibits a nearly constant thickness until a streamwise coordinate of about x/h = 6. From this streamwise location to about x/h = 8 a noticeable growth in boundary layer thickness is evident. This is probably due to upward transport of low momentum fluid due to expansion waves. The boundary layer thickness then appears to remain nearly constant until about x/h = 10. This is due to the return to wall-parallel flow seen in wall-normal velocity contour plot. In addition, the streamwise velocity plot also shows the presence of the thin isolator ceiling boundary layer. After x/h = 7, the ceiling boundary layer grows at a substantially higher rate. The representative schlieren image of Fig. 3.3a shows this growth occurs after the impingement point of the first reflected oblique shock (arrow A).

Figure 3.3d gives the mean Mach number distribution for the fully supersonic flow. Mach numbers were calculated by first approximating the temperature field based on velocity measurements. It can be shown (e.g., White, 1991) that the energy equation simplifies to the Crocco-Busemann relation if the following approximations are made: (*i*), steady flow, (*ii*) $Pr = 1$, (*iii*) adiabatic flow, (*iv*) two-dimensional flow, and (*v*) boundary layer approximations hold ($V << U$ and $\partial / \partial x << \partial / \partial y$). With the above approximations the energy equation reduces to the familiar form:

$$C_p T_0 = C_p T + \frac{U^2}{2} + \frac{V^2}{2} \tag{3.1}$$

from which the temperature and therefore Mach number were calculated. The Mach number plot shows the flow expands to near the freestream Mach number in the upper half of the isolator between $x/h = 5$ and 6. This is expected since in this region, the flow has passed through the compression ramp oblique shock and then through the inlet shoulder expansion fan. The theoretical Mach number for this sequence from shock-expansion theory is 4.87. The Mach number in the lower portion of the isolator entrance is seen to decrease to less than 2 near the floor. Proceeding downstream, the Mach number decreases along the duct centerline to about 3.5 as the floor boundary layer thickness increases downstream of $x/h = 6$. A similar decrease in Mach number is seen near the ceiling after the increased ceiling boundary layer growth downstream of $x/h = 7$. Finally, the Mach number in between these regions of increased boundary layer growth is seen to decrease to about 4 from about $y/h = 0.6$ to 0.8.

3.2 T7 PRESSURE TIME HISTORY DURING UNSTART AND UNSTARTED FLOWS

Figure 3.4, shows a time history of the wall pressure measured by transducer number 7 (T7 in Fig. 1) during a rather complex sequence of flap positions. During this sequence the flap began in the fully down (undeflected) position, and was then raised to about 27 degrees to initiate unstart. Note the flap angle seen to cause unstart was 26.6 ± 0.6 degrees (For details on the flap angle uncertainty range see Appendix B). Once the flow was unstarted the flap was then lowered slightly, raised and then lowered again. The purpose of performing this complex sequence is to show the differing flow behaviors that can be achieved with different flap positions. The time-record is two seconds long and includes regions with different distinct pressure signatures. The specific sequence is as follows. From 0 to about 0.05 s, the downstream flap (throttle) is in the fully down position and the inlet / isolator is started with supersonic flow throughout. After 0.05 s the flap is raised and at about 0.19 s, the pressure rises rapidly as unstart begins. From 0.20 to 0.45 s high-amplitude pressure oscillations are seen. This region is termed "high-amplitude oscillatory unstarted flow." At about 0.5 s the flap is lowered slightly such that the flow is still unstarted but the pressure fluctuations are less intense. This region of unstarted flow is seen to have non-periodic pressure fluctuations and is termed "non-oscillatory unstarted flow." At about 0.95 s the flap is again raised, which leads to an increase in the unstarted flow pressure fluctuations, but not to values as high as observed after the initial unstart pressure rise. These pressure fluctuations are also seen to exhibit strong periodicity. This region of unstarted flow is termed "lower-amplitude oscillatory unstarted-flow." Finally, the fall in pressure at about 1.4 s corresponds to a lowering of the flap and the subsequent restart of the inlet / isolator.

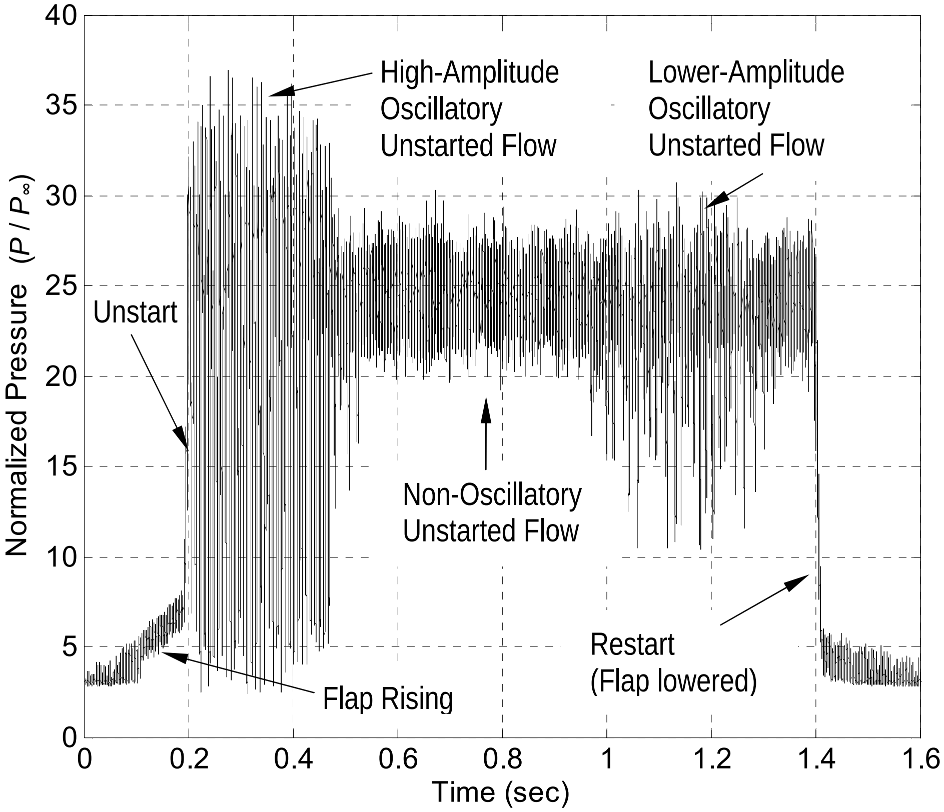

Figure 3.4 Pressure time history corresponding to inlet unstart, unstarted flows and restart processes obtained at T7.

3.3 INITIATION OF UNSTART

Figure 3.5 shows the pressure time-history at pressure transducer T7 with a smaller time window than used in Fig. 3.4 that emphasizes the beginning of the unstart event. During the unstart process, the pressure at T7 rises by about 500%, from 0.19 to 0.2 s. Similar pressure increases were observed in all other unstart events examined.

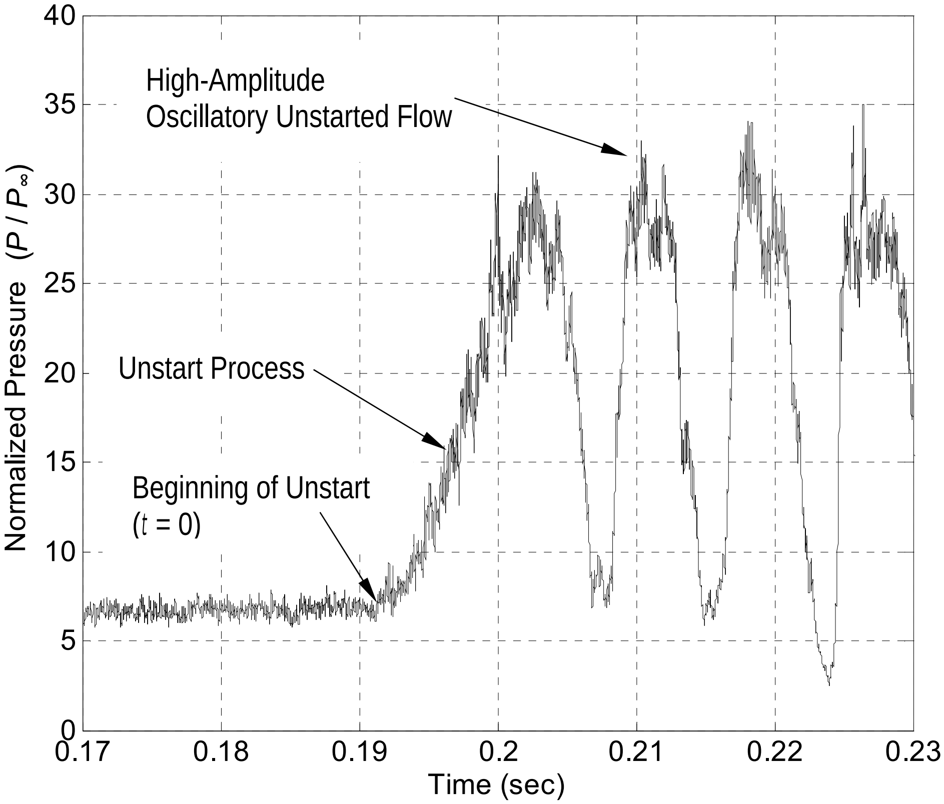

Figure 3.5 T7 pressure time history of the unstart process followed by high-amplitude oscillatory unstarted flow cycles.

Figure 3.6 shows a schlieren image (emphasizing vertical gradients) for the case where the flap (arrow A) has been raised to an angle of about 27 degrees to induce unstart. Again, the shape of the flap is a result of the 3.2 mm step as well as the upstream displacement of the flap's leading edge that occurs when it is raised. The detached flap shock (arrow B) and third reflected shock (arrow C) are impinging in close proximity to one another on the isolator ceiling near the exit. Near the impingement point of these shocks, the upper boundary layer of the isolator has separated forming a separation shock (arrow D). Although not visible with this schlieren image, there are also interactions between these shocks and the isolator sidewall boundary layers (these are termed glancing shock interactions). The semi-empirical correlation by Korkegi (1975), suggests that it is very likely that the sidewall boundary layers have also separated due to interactions with the flap shock. These separated flows are expected to lead to large viscous blockage effects that combine with the blockage of the flap. As will be discussed later, unstart seems to be associated with the presence of this severe separation at the downstream end of the isolator. Owing to these strong shock / boundary layer interactions, it was not possible to set up a strong stable shock system, analogous to that found in a ramjet isolator, by raising the flap. It is noted that in the model scramjet computational study of McDaniel and Edwards (2001), unstart appeared to be initiated by sidewall boundary layer separation due to combustion. In the current work it cannot be stated for certain that separation directly causes unstart, but what is clear is that the upstream propagation of unstart is highly associated with shock-induced separation.

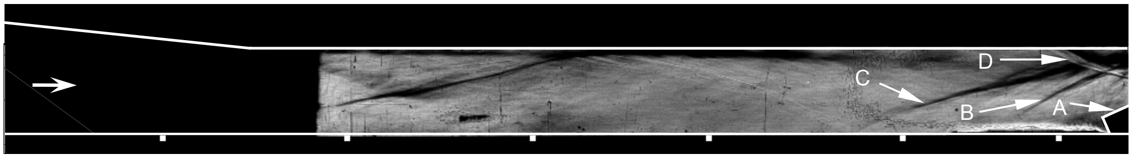

Figure 3.6 Downstream-view schlieren image showing the flow just before the onset of unstart ($\theta_F \approx 27$ degrees).

The ceiling separation shock (arrow D) in combination with the flap shock (arrow B) form what is termed the "unstart shock system." As will be shown, the unstart process involves the upstream propagation of the unstart shock system through the model which results in significant changes to the flow structure.

3.4 UNSTART TIME-SCALES VS. FLAP RISE-TIME

The effect of flap rise-time on unstart was investigated. The fast-response pressure measurements were used to calculate the time-scales involved in the unstart process. As the unstart shock system crossed over T6 to T1, a clear rise in pressure was recognized which allowed the times that the unstart shock system spent between transducers to be determined. The crossing time was defined to be the time that corresponded to the pressure at a given transducer becoming greater than a threshold value. The threshold pressure was chosen for each transducer to be just above those caused by pre-unstart pressure fluctuations. The times for ten different unstart events are shown in Fig. 3.7. For all of the unstart events shown in Fig. 3.7a, the flap was brought to a final angle between about 27 and 30 degrees. The minimum achievable rise time (due to flap drive mechanical limitations) was about 140 ms. The “fast-flap” data correspond to unstart events induced during upward motion of the flap at the maximum possible flap speed (minimum flap rise time). The “slow-flap” data correspond to an unstart event induced during a flap rise time of about 530 ms. Obviously, neither of these times are nearly as short as flow transit times within the inlet and so the flow for both cases is probably quasi-steady. High-speed schlieren imaging showed unstart began when the flap was near its final angle for both the fast-flap and slow-flap data of Fig. 3.7(a). In some cases the flap was brought to the final angle of about 27 degrees and unstart did not occur during the rise time of the flap nor immediately thereafter. Rather, the model remained started and would then unstart at an unpredictable later time while the flap remained at its terminal angle. Two of these unstart events are shown in Fig. 3.7a and are termed “natural” unstarts. Collectively, the ten unstart events of Fig. 3.7a do not show any discernible influence of flap speed on the time-scales of the unstart process. Also, schlieren imaging did not show distinguishable differences in the flow structure of unstart that was initiated at the different flap speeds or naturally. Finally, it is noted that Wieting (1973) reported similar results, where unstart was initiated with the insertion of a cylindrical pin and it was noted that the pin insertion velocity did not affect the unstart propagation velocities.

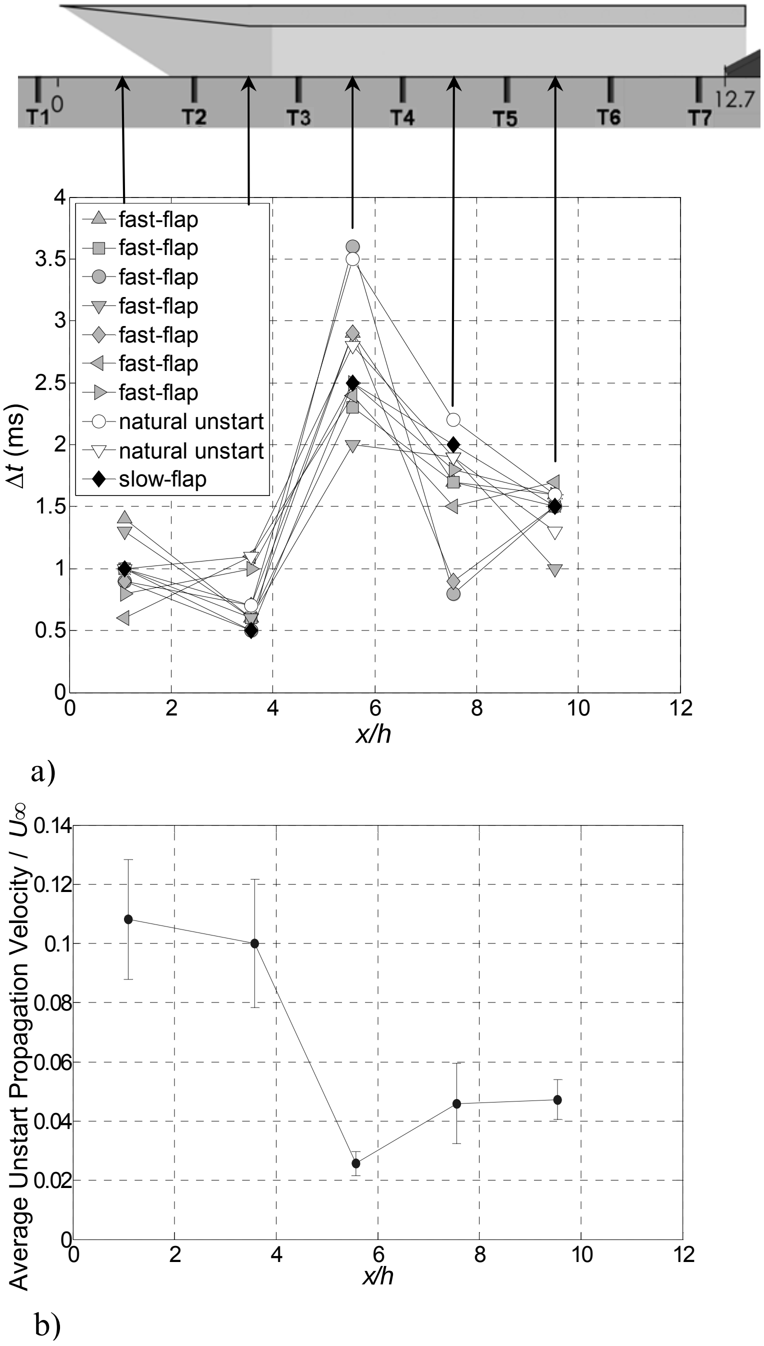

Figure 3.7 a) Unstart time-scales for ten runs (Δt is defined as the time spent between consecutive transducers) and b) average unstart shock-system velocities (normalized by $U_\infty = 740$ m/s), based on the ten runs.

3.5 UNSTART DYNAMICS AND FLOW STRUCTURE

3.5.1 High-Speed Schlieren Imaging and Pressure Measurements

To aid in the characterization of the unstart dynamics, the onset of unstart was defined by using either the downstream-view schlieren imaging or the pressure time history of T7. In this work, $t = 0$ refers to the time at the onset of unstart. An example of a $t = 0$ schlieren image is shown in Fig. 3.8a ($t = 0$). Near the onset of unstart, the shock system created by the flap and final reflected shock (arrows A and C) was seen to go from relatively stationary to having significant upstream motion. The frame just before this upstream motion was observed was defined as the $t = 0$ of the unstart process. This definition of the onset of unstart is termed the "schlieren-determined" onset of unstart. Using this definition for a number of repeated runs, unstart onset could be determined with an uncertainty of ±0.4 ms. As an alternative technique, the onset of unstart was determined by using the pressure time history of T7. As illustrated in Fig. 3.5, the beginning of unstart was arbitrarily chosen to be the point in time where the pressure increases above the background fluctuations. This definition of the beginning of unstart is termed the "pressure-determined" onset of unstart. For this particular unstart event, it so happened that the time of the pressure-determined onset of unstart (0.1911 s) coincided closely with the schlieren-determined onset of unstart time (0.1913 s). However, for some unstart events, the rise in the pressure at T7 was less pronounced than seen in Fig. 3.5. This lack of a clear rise in pressure made it difficult to pick the onset of unstart from the T7 pressure time history alone. For the ten unstart events of Fig. 3.7a, both the schlieren-determined and pressure-determined onset times of unstart were estimated. On average the pressure-determined onset time was 1.0 ms earlier than the schlieren-determined onset time. The standard deviation of the difference between these times was 1.2 ms, which shows the two could differ significantly. In general, the schlieren-determined onset was found to be much more identifiable (and therefore reliable) than the pressure-determined onset of unstart. Therefore, the schlieren-determined onset of unstart is used in this work wherever downstream-view imaging is available.

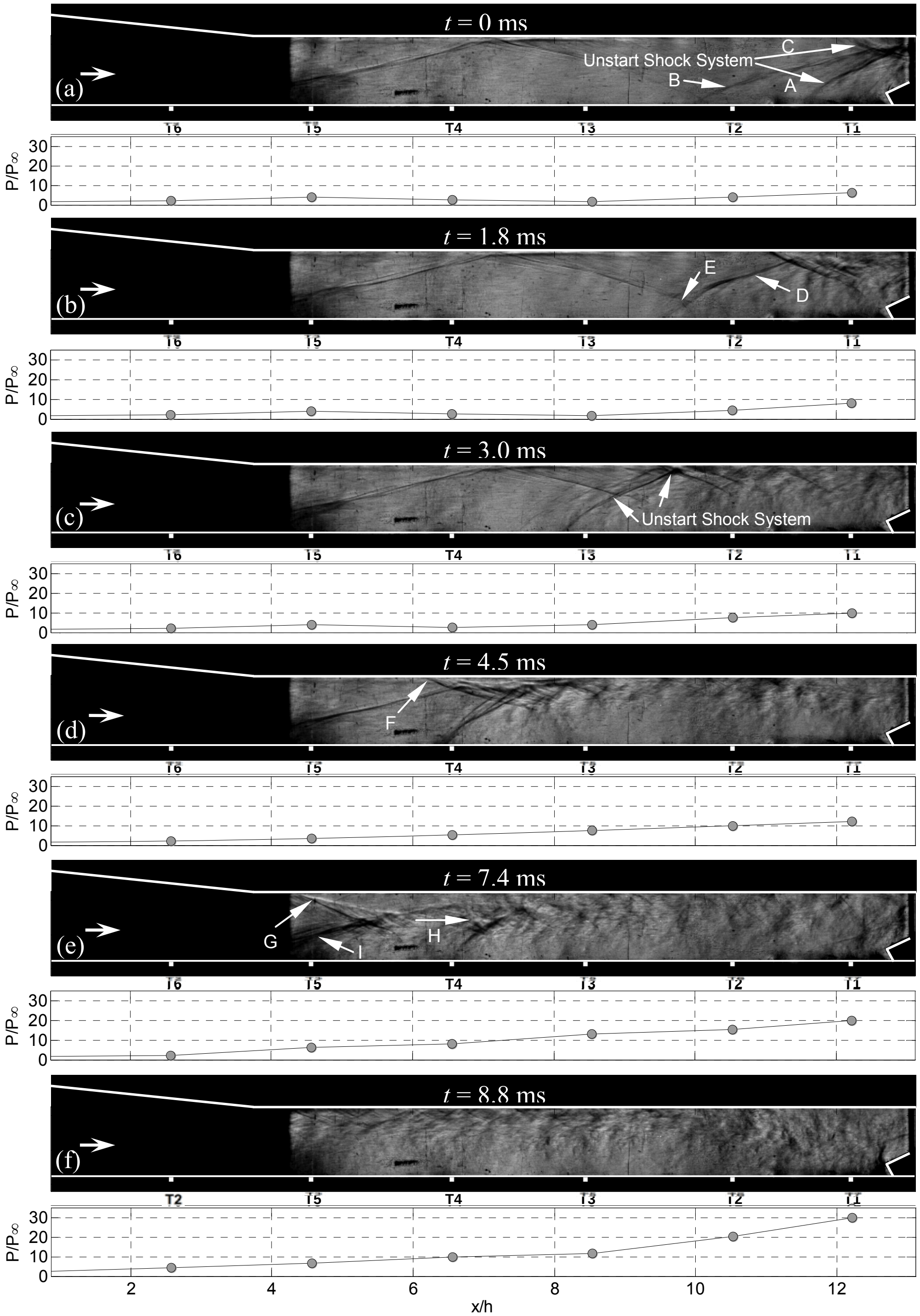

Figure 3.8 Sequence of downstream-view schlieren images and corresponding instantaneous pressure distributions showing the unstart process at times: a) *t* = *0*, b) *t* = 1.8 ms, c) *t* = 3 ms, d) *t* = 4.5 ms, e) *t* = 7.4 ms, and f) *t* = 8.8 ms

The total time for the model to unstart was determined by using the schlieren imaging and the T1 pressure time history. As explained above, when the unstart shock system reached T1 upstream of the inlet, an increase in pressure was observed. The inlet / isolator was defined to be unstarted at the time of this pressure increase. This definition of unstart applies for all other models tested as well. Based on the ten unstart events of Fig. 3.7a the average unstart total time is 8.2 ms (±0.6 ms). The standard deviation, maximum and minimum of the ten unstart times are 0.7, 9.9 and 7.3 ms respectively.

Upstream propagation velocities of the unstart shock system were computed using the times spent between transducers for the ten unstart events of Fig. 3.7a. The velocities of the ten unstart events were averaged to produce the velocity distribution shown in Fig. 3.7b. The velocities have been normalized by the freestream velocity of 740 m/s and are plotted at streamwise positions corresponding to the midpoints between consecutive transducers. The uncertainty ranges are 95% confidence intervals based on the student-t analysis. The relatively large uncertainties in time (±0.4 ms) associated with the schlieren-determined onset of unstart combined with uncertainties in identifying the initial position of the unstart shock system made it difficult to determine meaningful unstart propagation velocities downstream of T6. Therefore, only propagation velocities upstream of T6 are shown. Figure 3.7b shows the average propagation velocity of the unstart shock system to be about 0.047 U_∞ (35 m/s) in the middle portion of the isolator. The average velocity then slows to about 0.026 U_∞ (19 m/s) in the upstream portion of the isolator. The unstart shock system then accelerates upstream through the inlet. In order to compare to Wieting (1973) and Rodi et al. (1996), the freestream velocities in their experiments were estimated assuming isentropic nozzle expansion processes and using their given M_∞ and T_0 values. The result was an isentropic U_∞ of 703 m/s for Weiting and 672 m/s for Rodi et al. (1996). The average propagation velocity in the inlet (between T3 and T1) is 0.10 ±0.01 U_∞ (74 ±7 m/s) which is close to the maximum velocity of 0.10 U_∞ (70 m/s) reported by Rodi et al. (1996). In comparison, the average unstart propagation velocity in the isolator (between T6 and T3) is much slower at 0.035 ±0.003 U_∞ (26 ±2 m/s). Weiting reported a similar velocity of 0.038 U_∞ (27 m/s) in a constant area section of a model scramjet. The average unstart propagation velocity through the entire inlet / isolator model is 0.05 ±0.003 U_∞ (37 ±2 m/s). The observed average velocity range in this experiment of 19 to 80 m/s is broader than those measured experimentally by Weiting (10 to 27 m/s) or Rodi et al. (55 to 70 m/s).

The flow structure of the unstart process as seen in the downstream-view and with a vertical knife edge (which is sensitive to streamwise density gradients) is shown in Fig. 3.8. Six images and their corresponding pressure distributions at times of 0, 1.8, 3.0, 4.5, 7.4 and 8.8 ms are shown. The onset of unstart, seen at $t = 0$ ms (Fig. 3.8a) corresponds to the absolute time of 0.191 seconds in Fig. 3.5. Note that some of the observations made in this section were made with high speed movies and may not be readily seen in the time-sequences shown. Looking to the rear of the isolator at the onset of unstart, the flap shock (arrow A) and final reflected shock (arrow B) remain separate entities. These shocks interact at their impingement location on the isolator ceiling where the flow separates and another shock forms in response to this separated flow (arrow C). This separation shock in combination with the flap shock mark the unstart shock system (arrows A and C). As time progresses, the unstart shock system moves upstream and the flap shock appears to coalesce with the final reflected oblique shock. The unstart shock system is seen to be asymmetric with respect to the isolator horizontal centerline probably owing to the thicker boundary layer on the floor as compared to the ceiling. As this shock system moves upstream the pressure at T7 ($x/h = 12.21$) rises. In Fig. 3.8b at $t = 1.8$ ms, the lower upstream leg of the unstart shock system has now replaced what was initially the third reflected shock of the started flow (arrow D). During this process the pressure at T6 (*x/h* = 10.53) rises in response to this stronger shock. Also, between 0 and 1.8 ms, the shock angle of the lower upstream leg of the unstart shock system increases near its intersection with the floor. In addition, this lower upstream leg becomes increasingly more bifurcated with unstart progression (arrow E), which indicates an increase in the degree of separation of the lower-wall boundary layer. Similar observations were made by Neaves et al. (2001). From *t* = 1.8 ms to *t* = 3.0 ms (Fig. 3.8c) the pressure at T5 (*x/h* = 8.54) increases as the unstart shock system moves upstream through the region initially containing the second reflected shock. Between 3.0 and 4.5 ms (Fig. 3.8d) the unstart shock system continues to move upstream and the pressure at T7 to T5 continues to rise. At *t* = 4.5 ms, the presence of the unstart shock system has caused separation of the isolator ceiling boundary layer (arrow F). This separation was seen to begin at the impingement point of the first reflected shock of the initial oblique shock system. Also, the pressure has risen at T4 (*x/h* = 6.56) as the lower upstream leg of the unstart shock system has passed over it. Between 4.5 and 7.4 ms (Fig. 3.8e) the unstart shock system continues to propagate upstream with increasing separation of the ceiling boundary layer. The *t* = 7.4 ms image shows propagation of the unstart shock system has resulted in the formation of a prominent shear layer (arrows G and H) that originates at the separation point of the isolator ceiling boundary layer (arrow G). Figure 3.7b shows that the propagation velocity of the unstart shock system tends to slow down between *x/h* = 6.56 and 3.57. However, it should be noted that the unstart shock system velocity is determined by the pressures measured on the floor of the isolator. Therefore, this result only shows propagation along the floor of the isolator slows as the ceiling boundary layer separates. Another feature of the *t* = 7.4 ms image is the first reflected shock of the initial reflected oblique shock system has "lifted" slightly (arrow I). As a result, the pressure at T3 (x/h = 4.57) increases by about a factor of 2 over that at the previous time. Finally, at 8.8 ms (Fig. 3.8f), which corresponds to the absolute time of 0.20 s of Fig. 3.5, the unstart shock system has moved farther upstream into the converging inlet section and increases the pressure at T2 (x/h = 2.58). The pressures at T7 through T3 have further increased and the resulting isolator flow is seen to be highly separated.

A time-sequence of upstream-view schlieren images is shown in Fig. 3.9. Eight images taken with a horizontal knife edge (to highlight vertical gradients) are shown for the times of 0, 2.9, 3.9, 7.6, 8.5, 9.3, 10.1 and 15.4 ms from the onset of unstart. In addition, the pressure time history of each transducer during this unstart event is given in Fig. 3.10. Since the upstream-view does not show the onset of unstart, the pressure-determined onset of unstart based on the T7 time history is used. At t = 0 ms (Fig. 3.9a) the flow in the inlet / isolator field of view is fully supersonic. At 2.9 ms (Fig. 3.9b), the unstart shock system has moved upstream intersecting the floor between T5 and T4 at an approximate location of x/h = 7.5 (arrow A). As shown in Fig. 3.10, the pressure at T6 and T5 has risen with the passage of the unstart shock system. Looking to Fig. 3.9c at t = 3.9 ms, the unstart shock system is far enough upstream to induce significant boundary layer separation on the ceiling of the isolator (arrow B). As demonstrated in the t = 7.6 ms image (Fig. 3.9d), as time progresses, the upper boundary layer separates further and the unstart shock system moves upstream with the upstream motion of the ceiling boundary layer separation point (arrow C). At this time the pressure at T4 and T3 has risen due to the passage of the unstart shock system. Also, the first reflected shock of the initial started flow field appears to be “lifted” (arrow D) in response to the propagating unstart shock system. Neaves et al. (2001) reported a similar lifting effect due to unstart. At t = 8.5 ms (Fig. 3.9e), the unstart shock system has propagated upstream of the inlet

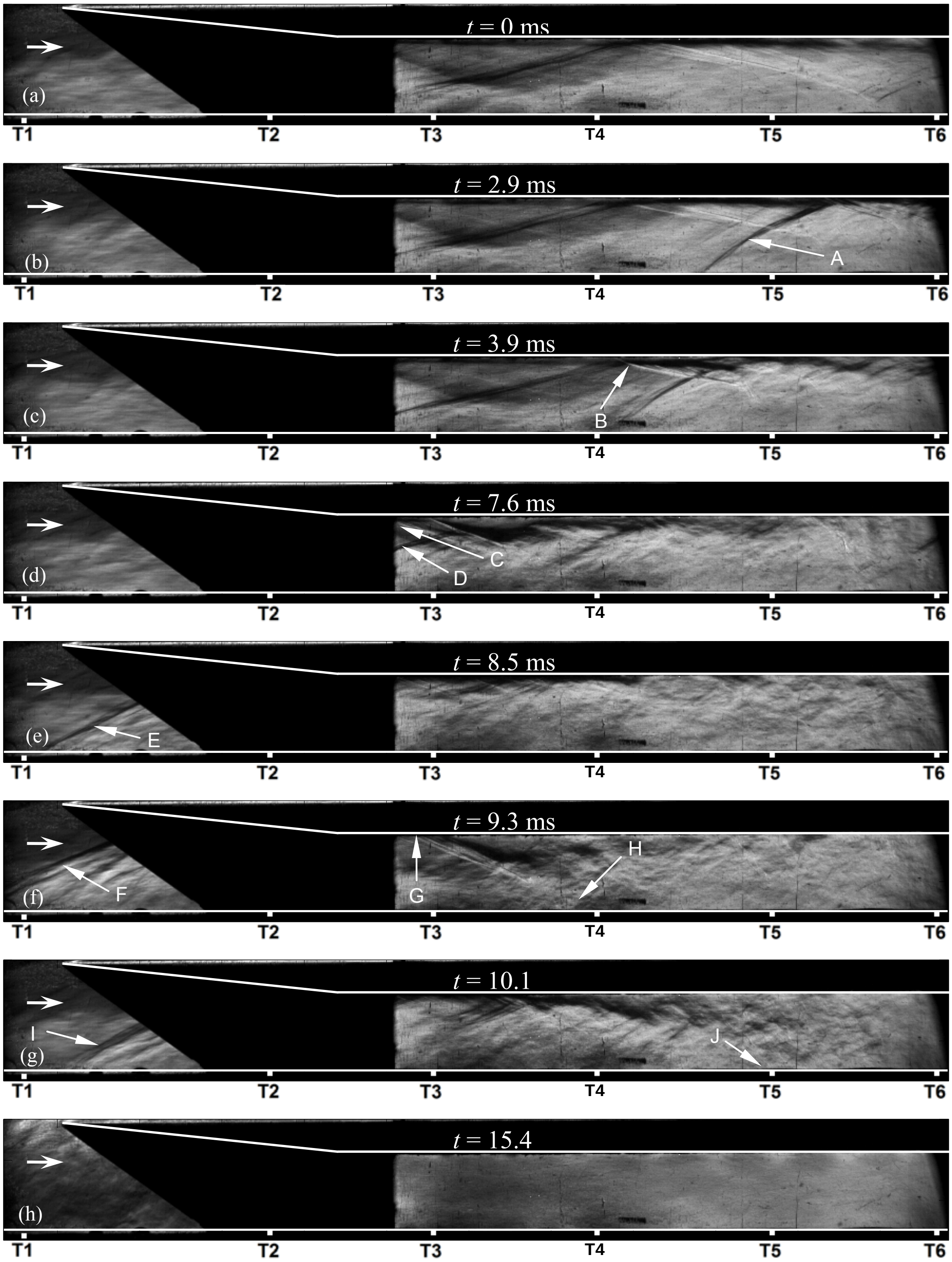

Figure 3.9 Sequence of upstream-view schlieren images showing the unstart process at times: a) $t = 0$, b) $t = 2.9$ ms, c) $t = 3.9$ ms, d) $t = 7.6$ ms, e) $t = 8.5$ ms, f) $t = 9.3$ ms, g) $t = 10.1$ ms, and h) $t = 15.4$ ms.

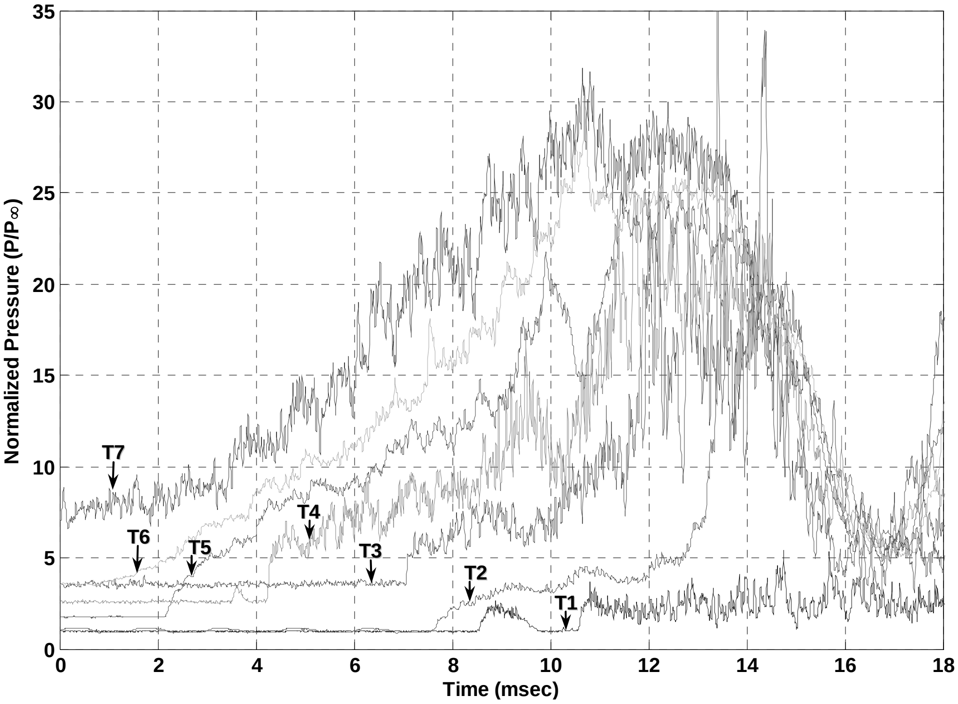

Figure 3.10 Pressure time histories obtained at T1 – T7 for the unstart event of Fig. 3.9.

entrance (arrow E). However, the unstart shock system has not yet crossed over the T1 location. Figure 3.10 shows the pressure rise at T1 due to the crossing of the unstart shock system occurs at about *t* = 8.6 ms. At *t* = 9.3 ms (Fig. 3.9f), the unstart shock system has crossed upstream over T1 (arrow F). A separated flow appears to be emanating from the ceiling (arrow G) and impinging on the isolator floor (arrow H). Up until 9.3 ms, the unstart shock system has undergone only upstream motion; however, from *t*= 9.3 ms to 10.1 ms (Fig. 3.9g), the leading shock (arrow I) of the unstart shock system moves downstream. Fig. 3.10 shows that this results in a decrease in the T1 pressure to the pre-unstart level. The *t* = 10.1 ms image also shows that the floor impingement point of the separated flow has moved downstream (arrow J). As demonstrated in Fig. 3.10, the isolator pressure distribution (T7-T3) decreases with the downstream propagation of the unstart shock system. The pressure decrease is first seen at T3 (*t* = 9.3 ms), followed by T4 (*t* = 9.5 ms), T5 (*t* = 9.9 ms), T6 (*t* = 10.7 ms) and finally T7 (*t* = 10.9 ms). Similar pressure time histories were seen during each of the ten unstart events of Fig. 3.7a. This indicates that the momentary downstream propagation of the unstart shock system described in this section is typical of the unstart process in the current model. It is possible that this momentary downstream motion is part of an acoustic resonator oscillation. For instance at *t* = 9.3 ms, the leading shock (arrow I) is most likely strong enough to induce significant separation and therefore some subsonic flow. With some subsonic flow entering the inlet entrance, it can now act as an open end for an acoustic resonator. If the period of this oscillation is approximated as the time spent between the first (*t* = 8.6 ms) and second crossing of T1 (*t* = 10.6 ms), the oscillation frequency then computes to be 500 Hz. As will be discussed, this frequency is near that of an ideal half-wave resonator. Figure 3.10 shows that following local minima, the pressures at T1-T7 increase. This increase was seen in simultaneous schlieren imaging (not shown here) to be associated with the unstart shock system reverting back to upstream propagation. It was also observed from the schlieren images that after about 13 ms, the leading oblique shock of the unstart shock system no longer intersected the inlet ceiling. Rather, it had moved far enough upstream to be considered a bow shock that passes over the inlet. Without the impingement of the leading oblique shock on the inlet ceiling, there was no longer a separated flow emanating from the ceiling. With increasing time, the unstart bow shock continued to move upstream. Figure 3.10 shows that as the bow shock moves upstream, the pressure within the model decreases rapidly ($t \approx 14-17$ ms) and becomes much more uniform indicating the flow in the model is subsonic. The *t* = 15.4 ms image of Fig. 3.9h demonstrates this point. The unstart bow shock is out of the field of view and estimated to be near a maximum upstream location. The lack of waves and strong gradients within the entire visible portion of the isolator suggests the isolator flow is subsonic. Up until 17.25 ms, where the model pressure decreases to a minimum, the flowfield looks very similar to that of the t = 15.4 ms image. The fact that the pressure distribution decreases as the unstart bow shock moves upstream may be attributed to increased spillage over the top and around the sides of the inlet entrance.

3.5.2 Unstart Process Side-View PIV

A "pseudo-sequence" of the unstart process is presented in Fig. 3.11. With the 10 Hz PIV system of this study, one image pair could be captured every 100 ms. However as described above, the unstart process occurred in a period of about 10 ms. Therefore, it was not possible to capture more than one wide-field image pair per unstart event. In fact, the onset of unstart (t = 0) was not repeatable enough to guarantee that a given unstart event could be captured at the time of the PIV acquisition. Thus, in order to increase the likelihood for acquiring PIV data during unstart, the model was unstarted and restarted up to thirty times during a given wind-tunnel run. Most data acquired during such a run consisted of either started or unstarted flow. However, usually at least one acquisition time during a run corresponded to the unstart process. Since the flow structure during the unstart process as seen with schlieren imaging is quite consistent, the PIV data from different unstart events were pieced together to form a pseudo-sequence of the process. The repeatability of the unstart flow structure as seen with the schlieren imaging is shown in detail in Appendix E. In addition, further justification for the pseudo-sequence will be presented with the data corresponding to a stationary high-compression shock system in section 3.9. Since this shock system was stationary, 90 vector fields were acquired to compute its mean flowfield. As will be seen, the flow structure of the mean flowfield is similar to the instances of unstart seen in the pseudo-

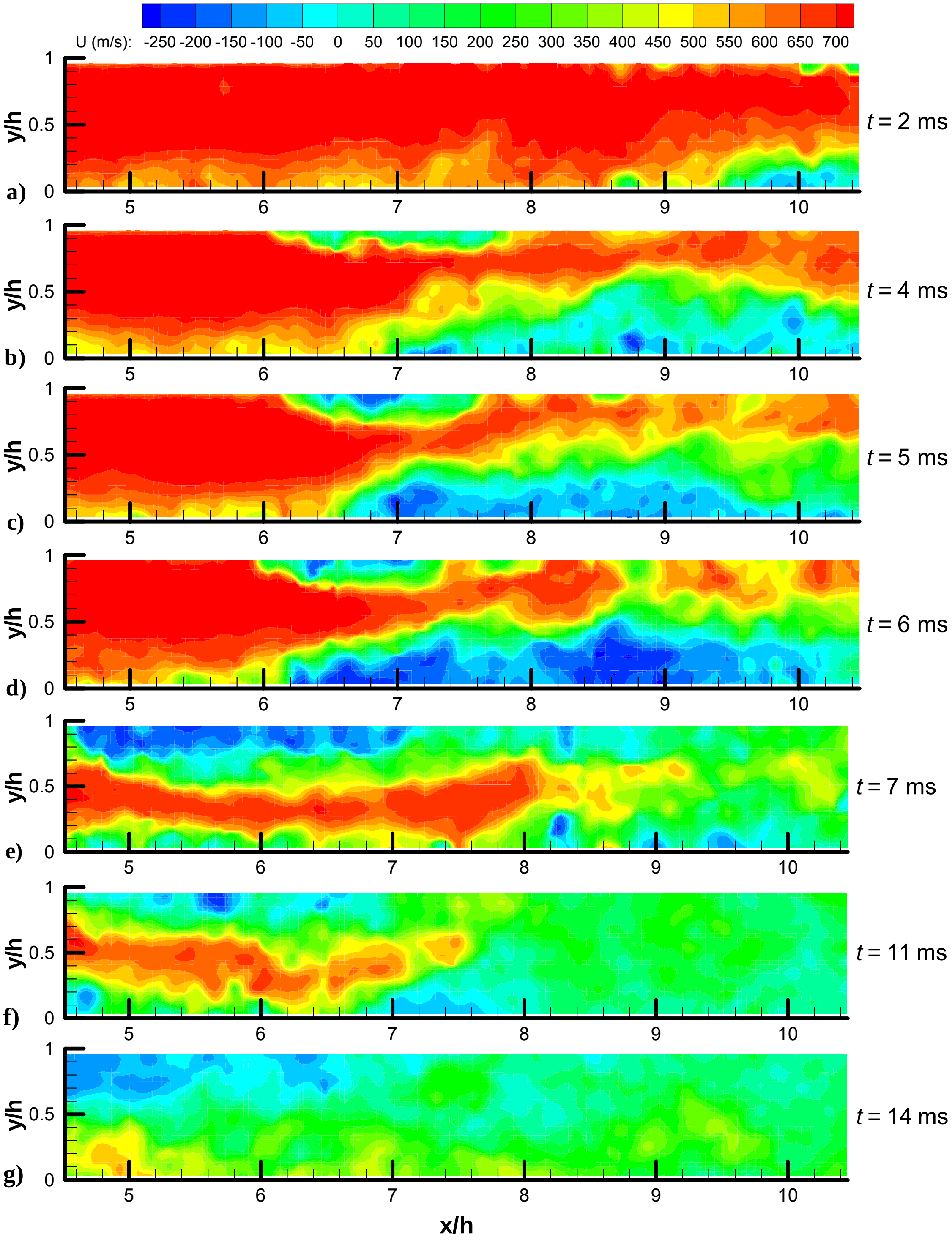

Figure 3.11 Unstart pseudo-sequence side-view PIV: a) 2 ms, b) 4 ms, c) 5 ms, d) 6 ms, e) 7 ms, f) 11 ms, and g) 14 ms into the unstart process.

sequence at t = 4, 5 and 6 ms. Furthermore, schlieren images of the stationary high-compression shock system will also be shown to be very similar to those seen when the unstart shock system is at a similar streamwise location. Since both the instantaneous PIV data and schlieren imaging of the unstart process show similar flow structure to the stationary shock system case for which a significant number of vector fields were acquired, and since the flow structure as seen by the schlieren imaging of the unstart process was seen to be very repeatable (Appendix E), it therefore appears to be justifiable to piece the PIV data together to form a pseudo-sequence. Data from seven different unstart events are shown in figures 3.11a to 3.11g to form the pseudo-sequence of streamwise velocity contours at estimated times of 2, 4, 5, 6, 7, 11 and 14 ms during the unstart process. As illustrated in Fig. 3.5, the onset of unstart (t = 0) is estimated from the T7 pressure time history. As described in the previous section, the timescales do vary from event to event. Therefore it should be emphasized that the times given in Figs. 3.11a to 3.11g serve to give an order to the sequence but are not expected to be repeatable to within ±0.6 ms.

The number of valid vectors for the unstart pseudo-sequence dataset is 82%. With upstream propagation, the unstart shock system created high velocity gradients as well as seeding non-uniformities which were responsible for correlation degradations. It is interesting to note how the PIV data quality changes with the upstream progression of the unstart shock system. From Figs. 3.11a to 3.11e the head of the unstart shock system is seen to move upstream through the field of view. In order from Figs. 3.11a to 3.11e, the percentages of valid vectors are 90, 85, 87, 78 and 65. These percentages are significantly lower than that of the started flow which had 93% valid vectors. Therefore, the unstart shock system seriously degrades the PIV data. Inspection of the PIV image pairs showed this is a result of a redistribution of seeding due to the unstart shock system.

The seeding upstream of the unstart shock system was seen to be fairly uniform considering the thick floor boundary layer. However, flow downstream of the system was seen to be very non-uniform consisting of regions of high and low seeding densities. Seeding in the separated ceiling boundary layer was seen to be especially low. The separation of the ceiling boundary layer creates a region of low seeding density during unstart. Besides seeding non-uniformities, another cause of correlation degradations in the unstart PIV data is the high gradients as seen in Fig. 3.11. High gradients tend to broaden the correlation peaks making them less detectable (Keane and Adrian 1992 and Westerweel 1997), although advanced algorithms that utilize interrogation window deformation in response to velocity gradients (e.g, Scarano 1999), significantly reduce this bias error. The PIV processing software used for the current work (LaVision 7.2) utilizes similar advanced algorithms. The dominant source of uncertainty in the unstart process PIV data was that which occurred in the data reduction process. The uncertainty in the PIV processing stemmed from regions of high velocity gradients and seeding non-uniformities. A detailed PIV uncertainty discussion is given in Appendix C.

This section uses the sequence of streamwise velocity contours shown in Fig. 3.11 to show how the isolator flow structure evolves as the unstart shock system moves upstream. In addition, Figs. 3.12 through 3.15 and 3.17 provide further details of this process at the selected times of 2, 5, 7, 11 and 14 ms, respectively. Included in these figures are representative schlieren images, representative wall pressure distributions, velocity vector plots, streamwise velocity contour plots, wall-normal velocity contour plots and Mach number contour plots. The representative schlieren images and PIV data were not acquired simultaneously, but rather during different unstart events. The schlieren images were picked by comparing the T7 pressure values recorded at the time of the schlieren image acquisition to the T7 pressure values recorded at time of the PIV data acquisition. However, due to T7 pressure fluctuations, there were seen to be several times for which the T7 pressures were equal. Therefore, the representative schlieren image was then picked on the further requirement that it have the most similar flow structure to that which could be inferred from the PIV data. The pressure distributions given in the Figs. 3.12 through 3.15 and 3.17 correspond to those taken at the time of the schlieren image not the PIV data. The Mach number plots were generated using the simplified energy equation given in section 3.1.2 above. This can be justified as follows. First, since the unstart process times are much larger than flow transit times (the unstart propagation velocity is 3.5% U_∞), the flow can be considered quasi-steady. Second, as will be seen in the velocity plots, the flow behind the unstart shock system is seen to be dominated by shear layers. Therefore, it is expected that assumptions *i*) through *v*) of section 3.1.2 are reasonable enough to provide approximate Mach number distributions.

Figure 3.12 shows the flow structure where the unstart shock system has propagated to near the downstream edge of the field of view. Recall that the unstart shock system was seen to propagate to this position first with a separation of the isolator ceiling boundary layer that occurred near the ceiling impingement point of the third ramp shock reflection (e.g., See Figs. 3.8a and 3.8b). Further upstream propagation was seen to occur with an increase in separation of the floor boundary layer. The floor boundary layer separation was seen to occur near the floor impingement location of the second ramp shock reflection (e.g., See Fig. 3.8b). This separation of the floor boundary layer is also seen in the schlieren image of Fig. 8a (arrow A). The velocity vector plot of Fig. 3.12b and streamwise velocity contour plot of Fig. 3.12c suggest unstart has progressed to about x/h = 9 along the isolator floor. Furthermore, the Mach number plot of Fig. 3.12e shows the flow to be subsonic near the floor downstream of the unstart shock system.

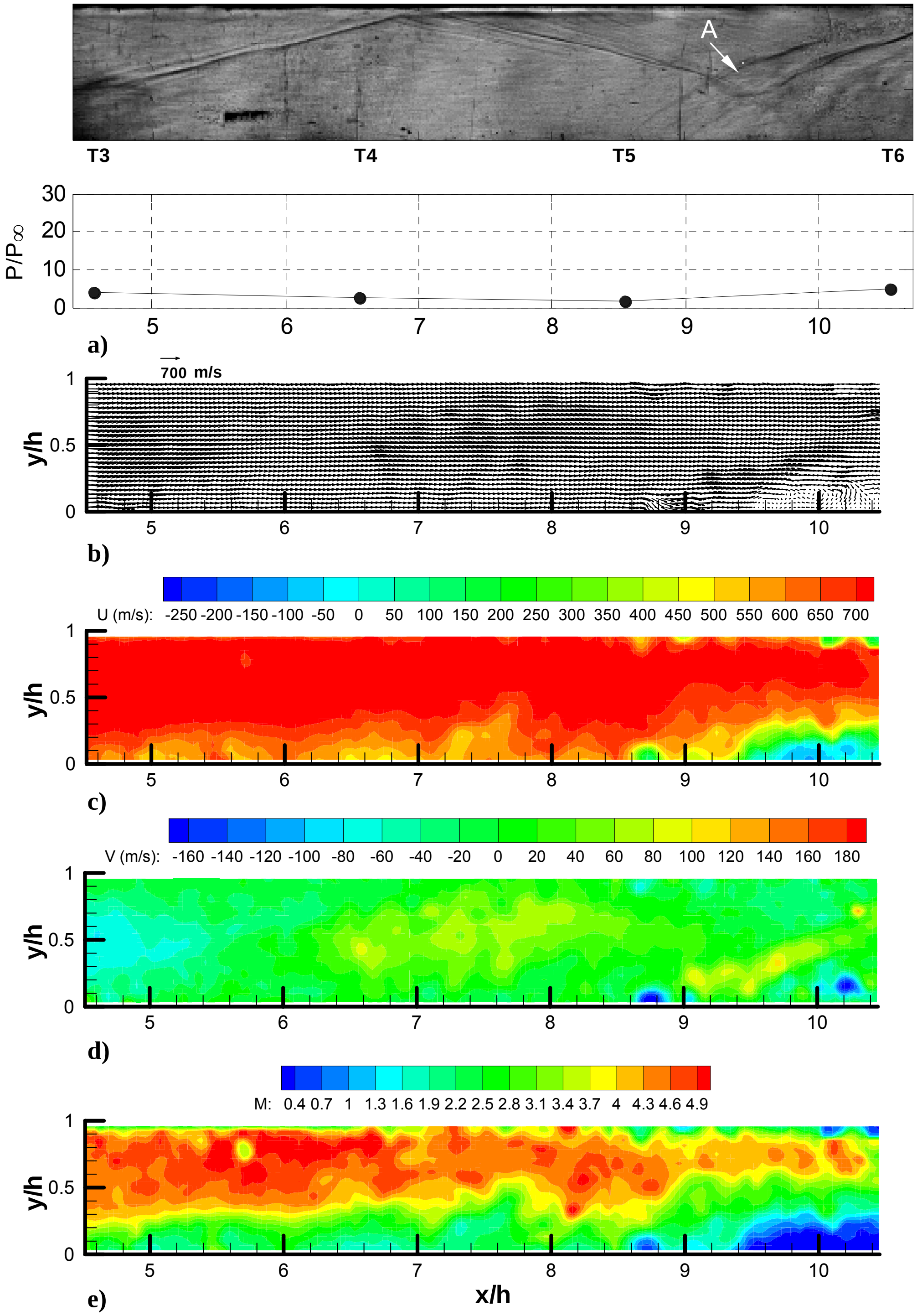

Figure 3.12 Instantaneous flow structure during unstart at $t = 2$ ms: a) representative schlieren image and corresponding pressure distribution, b) velocity vectors, c) U contours, d) V contours, e) M contours.

Figure 3.11b at t = 4 ms, shows that unstart has progressed upstream to the floor location of about x/h = 6.5. In addition, low momentum fluid indicates the unstart shock system intersects the isolator ceiling at the approximate location of x/h = 6.

Figure 3.11c at t = 5ms, shows the strength of reverse flow near the ceiling and floor has increased compared to t = 4 ms. Figure 3.13 provides additional flowfield information at this time during unstart. The representative schlieren image of Fig. 3.13a shows that the ceiling boundary layer has separated (arrow A) with the upstream propagation of the unstart shock system. This ceiling separation was seen to occur near the impingement location of the first reflection of the compression ramp shock (e.g., See Fig. 3.3, arrow A). Fig. 3.13a also shows that the wall pressure at T4 to T6 has increased in response to the crossing of the unstart shock system. The velocity vector plot of Fig. 3.13b shows that the unstart shock system has taken the form of two separation shocks with one shock intersecting the floor near x/h = 6.5 and the other intersecting the ceiling near x/h = 6. Both the vector and streamwise velocity velocity plot of Fig. 3.13c show that unstart has induced regions of reversed flow near the ceiling and floor. The velocity magnitude of this reversed flow is between 100 and 200 m/s. The PIV data show that the current PIV system is successfully able to resolve the unstart flow structure even in the presence of high velocity gradients. In addition, the PIV data provide flow structure information in low speed regions where the density gradients are not high enough to show structure in the schlieren image of Fig. 3.13a. The Mach number contour plot at t = 5ms is shown in Fig. 3.13e. At the left of the figure, the Mach number is close to the freestream value of 4.9 at the top of the isolator and it decreases to about 2 in the thick floor boundary layer. Regions of predominantly subsonic flow are seen downstream of the floor and ceiling separation shocks. The floor subsonic region extends from about the floor separation shock location to the right edge of the image. It is likely that this

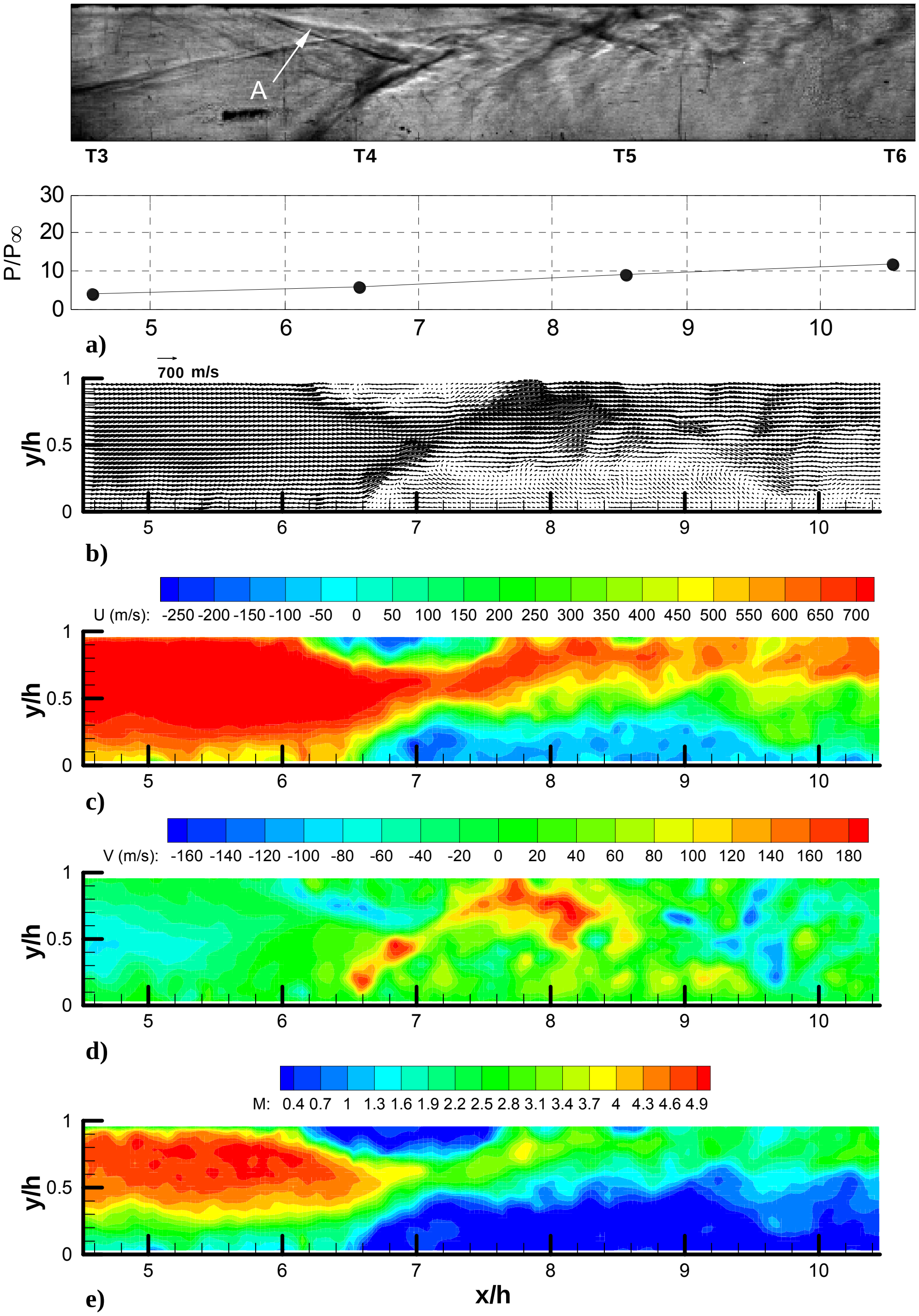

Figure 3.13 Instantaneous flow structure during unstart at *t* = 5 ms: a) representative schlieren image and corresponding pressure distribution, b) velocity vectors, c) *U* contours, d) *V* contours, e) *M* contours.

subsonic region continues until the isolator exit. If this is the case, then the exit area decrease imposed by the flap is “communicated” through this subsonic region.

Moving on to the streamwise velocity contour plot of Fig. 3.11d at *t* = 6 ms, the extent of floor and ceiling separation is seen to increase. In addition, the magnitude of reverse flow has increased compared to Fig. 3.11c and the maximum reverse velocities have reached nearly 300 m/s. The shear layers seen in Fig. 3.11d create very high velocity gradients. For example, at $x/h = 6.6$ and from the floor to $y/h = 0.5$, the streamwise velocity goes from near -300 m/s to 700 m/s in only about 12 mm.

Proceeding to Fig.3.11e taken 7 ms into unstart, the flow structure is seen to have been substantially altered. The corresponding detailed flow information given in Fig. 3.14, shows that unstart has progressed through the upstream portion of the isolator with increased separation of the ceiling boundary layer. The ceiling separation point has progressed out of the field of view of the representative schlieren image of Fig. 3.14a (arrow A). Figure 3.14a also shows that the isolator pressure distribution has increased further compared to that in Fig. 3.13a. In addition, the increased pressure at T3 indicates that the unstart shock system has crossed this transducer location ($x/h = 4.57$). The velocity vector and streamwise velocity plots of Figs. 3.14b and 3.14c show a region of reverse flow spanning the ceiling from the field of view entrance to about $x/h = 7.2$. The maximum measured reverse streamwise velocity is about 250 m/s in this region. The relatively large V components of about -150 m/s at the isolator entrance near the wall-normal center portion of the isolator are due to the strong separation shock associated with the ceiling separation. This separation shock is also seen in the representative schlieren image (arrow B). Near the floor around $x/h = 6$, the vector and wall normal plots show the flow direction to return to parallel to the wall. Although altered, the

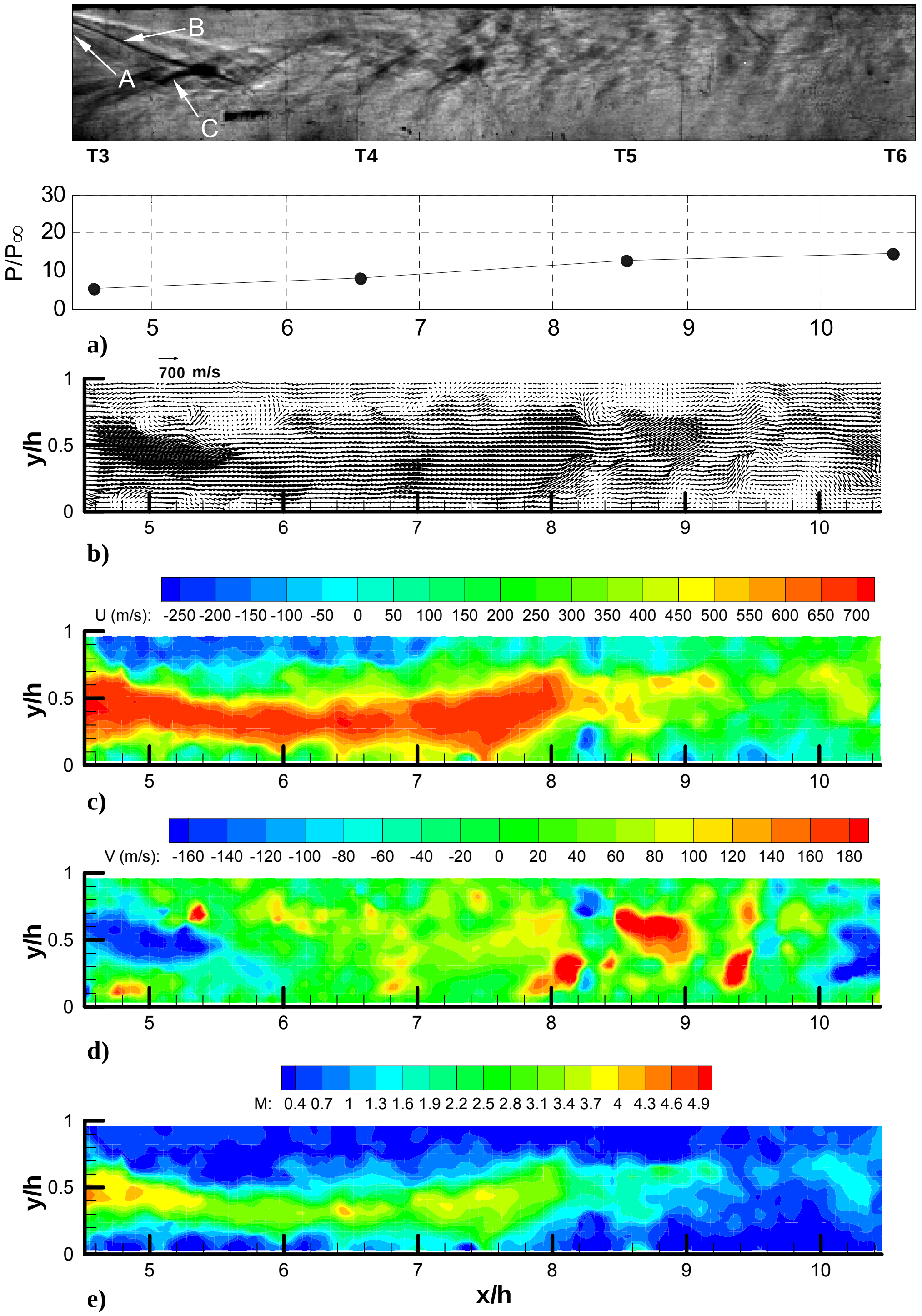

Figure 3.14 Instantaneous flow structure during unstart at $t = 7$ ms: a) representative schlieren image and corresponding pressure distribution, b) velocity vectors, c) U contours, d) V contours, e) M contours

schlieren image shows the first reflected shock remains in the field of view (arrow C). This shock may be partly responsible for this parallel flow. Progressing downstream, the flow becomes more uniform likely due to the high levels of mixing created by the strong shear layers. Downstream of $x/h = 9$, the streamwise velocity is more uniform at about 300 m/s over most of the isolator height. Fig. 3.14e shows the flow to be subsonic along the length of the isolator ceiling and mostly subsonic along the length of the isolator floor. High momentum fluid enters the field of view near the wall-normal center with a Mach number near 4. With increasing streamwise distance the Mach number in the high momentum region decreases to about 3 by $x/h = 8$. Finally, the downstream portion of the field of view is seen to contain a more uniform distribution at a Mach number near unity.

Figure 3.11f shows the streamwise velocity plot at $t = 11$ ms where the unstart shock system has progressed further upstream. In addition, Fig. 3.15 provides more flow structure details at this unstart time. Also, Figure 3.16a shows the T1 and T7 pressure time histories for the unstart event corresponding to the data of Figs. 3.11f and 3.15. At the time of the PIV image pair acquisition, the unstart shock system has crossed T1 ($x/h = -0.4$), which is upstream of the inlet entrance. This is evident by the distinct pressure increase at about $t = 9.8$ ms. Recall that the unstart shock system was seen to leave the inlet in the form of a strong oblique shock (e.g., See Figs. 3.9e to 3.9g). This oblique shock is referred to herein as the "unstart oblique shock." At the time of the PIV data acquistion, Fig. 3.16a shows the T7 pressure to be in the middle of a peak pressure "plateau." The schlieren image of Fig. 3.15a shows what appears to be separated flow entering the isolator entrance (arrow A). Recall the previous section suggested that this separated flow originates in the inlet section at the ceiling, due to the impingement of the unstart oblique shock (e.g., See Figs. 3.9e to 3.9g). The separated flow appears to

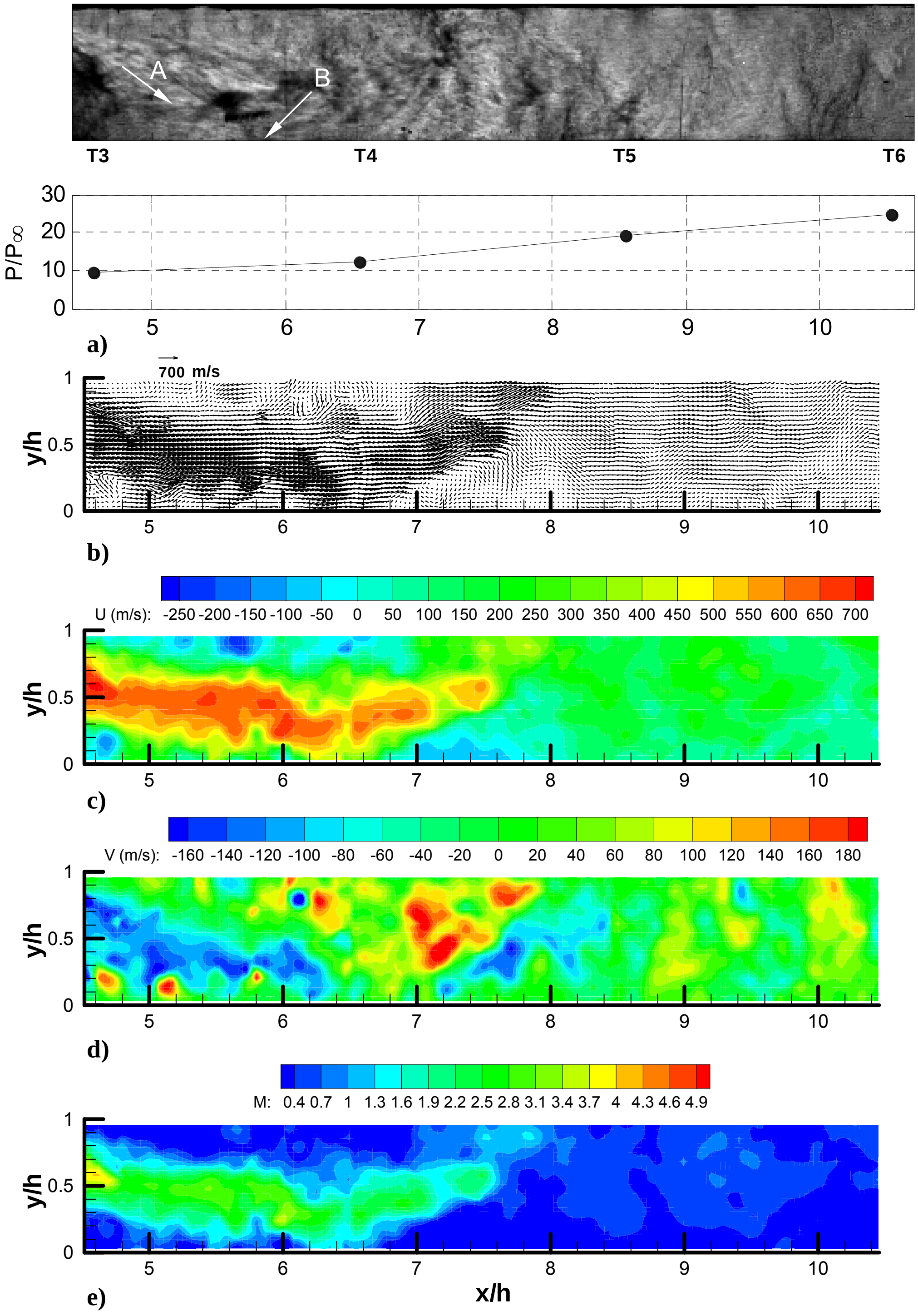

Figure 3.15 Instantaneous flow structure during unstart at $t = 11$ ms: a) representative schlieren image and corresponding pressure distribution, b) velocity vectors, c) *U* contours, d) *V* contours, e) *M* contours.

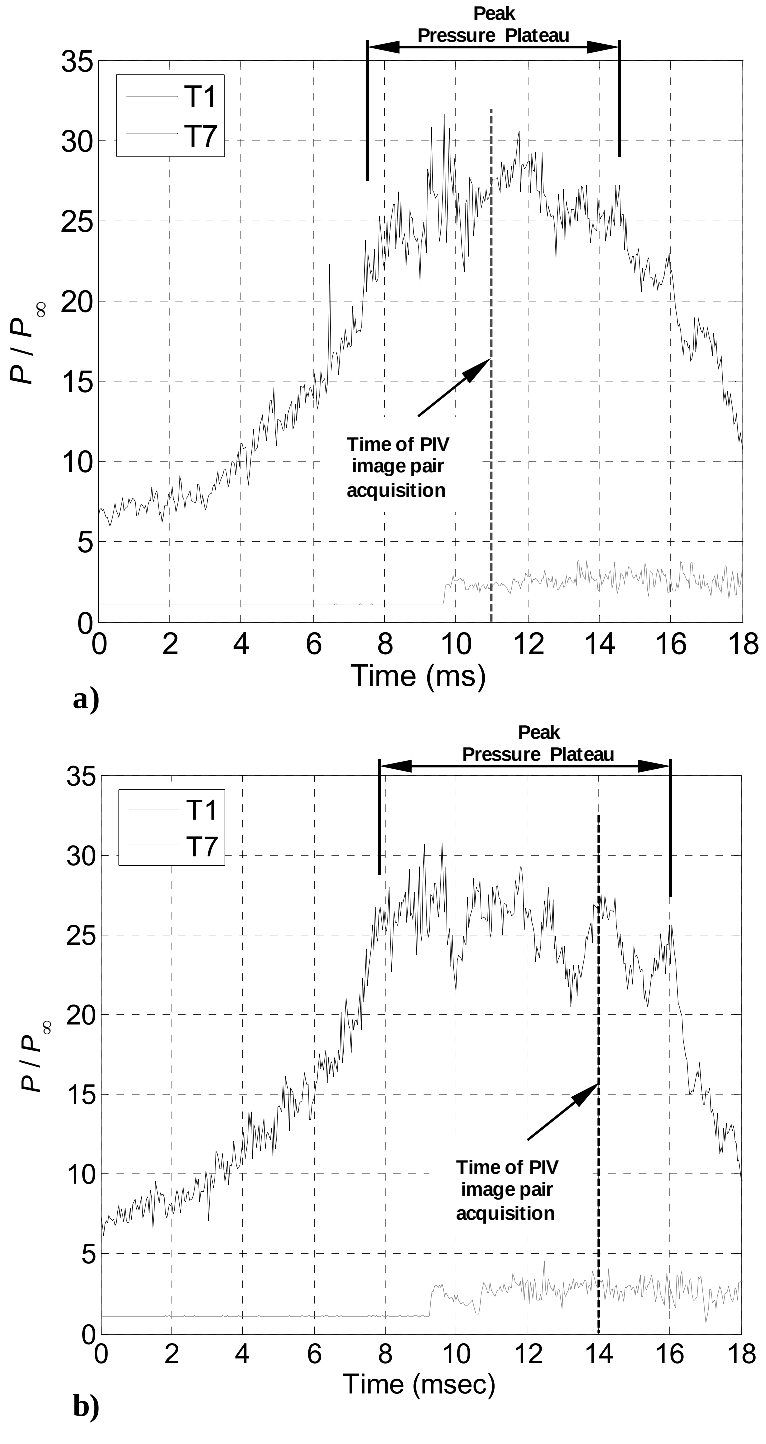

Figure 3.16 Pressure histories showing the time of PIV image pair acquisition for the unstart process pseudo-sequence at pressure plateau: a) *t* = 11 ms, and b) *t* = 14 ms.

impinge on the isolator floor at a location of about *x/h* = 6 (arrow B). In Fig. 3.15a), the isolator pressure distribution has increased compared to Fig. 3.14a. The velocity vector plot of Fig. 3.15b also shows the separated downward turned flow entering the isolator entrance. Consistent with the schlieren image, the vector plot and streamwise velocity plot of Fig. 3.15c show the separated flow appears to impinge on the floor at about *x/h* = 6.4. Fig. 3.15b shows the separated flow then appears to reflect off of the floor near *x/h* = 6.8. Downstream of this reflection a flow recirculation region from about *x/h* = 7 to 8 is seen to exist. Downstream of *x/h* = 8, the streamwise velocity and wall-normal velocity (Fig. 3.15d) distributions are seen to be much more uniform. At *t* = 11 ms, Fig. 3.15e shows the Mach number to be predominantly subsonic downstream of *x/h* = 8. The Mach number in this region is near 0.4. At the isolator exit, the flap angle of about 30 degrees results in an area decrease of about 27% (Recall that the flap height at the isolator exit can be found with Fig. B.3 of Appendix B.). Interestingly, quasi-one-dimensional flow theory predicts that the Mach number of a uniform Mach 0.4 flow will be brought to unity with a decrease in area of 37%. However, a uniform Mach 0.5 flow would choke with only a 25% area decrease. Therefore, it is possible that at this time the flow is choked at the isolator exit. Note that this is purely speculative since there is no optical access at the isolator exit to verify this hypothesis.

Figure 3.11g shows the streamwise velocity distribution for the unstart time of *t* = 14 ms and Fig. 3.17 provides additional flowfield information at this time. Also, Fig. 3.16b shows the T7 pressure to be near the end of a pressure plateau. Inspection of pressure time histories has shown that the rest of the isolator pressure distribution increases with increasing duration of the T7 plateau. Fig. 3.17a shows the isolator pressure distribution has increased further compared to the *t* = 11 ms distribution of Fig. 3.15a. The velocity data of Figs. 3.17b to 3.17d show a much more uniform flow in the isolator compared to the previous figures of the pseudo-sequence. Still, a region of reverse flow is seen in the upper portion of the field of view from x/h = 4.5 to 6.5. The peak streamwise reverse velocity in this region is measured to be about 150 m/s. Figure 3.17e shows that downstream of x/h = 5.6, the flow is predominantly subsonic intermixed with near sonic regions. Recall from the results above, that near the end of the T7 pressure plateau, the unstart oblique shock tends to propagate far enough upstream to become a bow shock that passes over the inlet ceiling. The results also showed, that as the bow shock propagated upstream, the isolator pressure distribution decreased to a minimum. As will be discussed further, following this minimum a periodic unstarted flow with high pressure fluctuations was seen to exist.

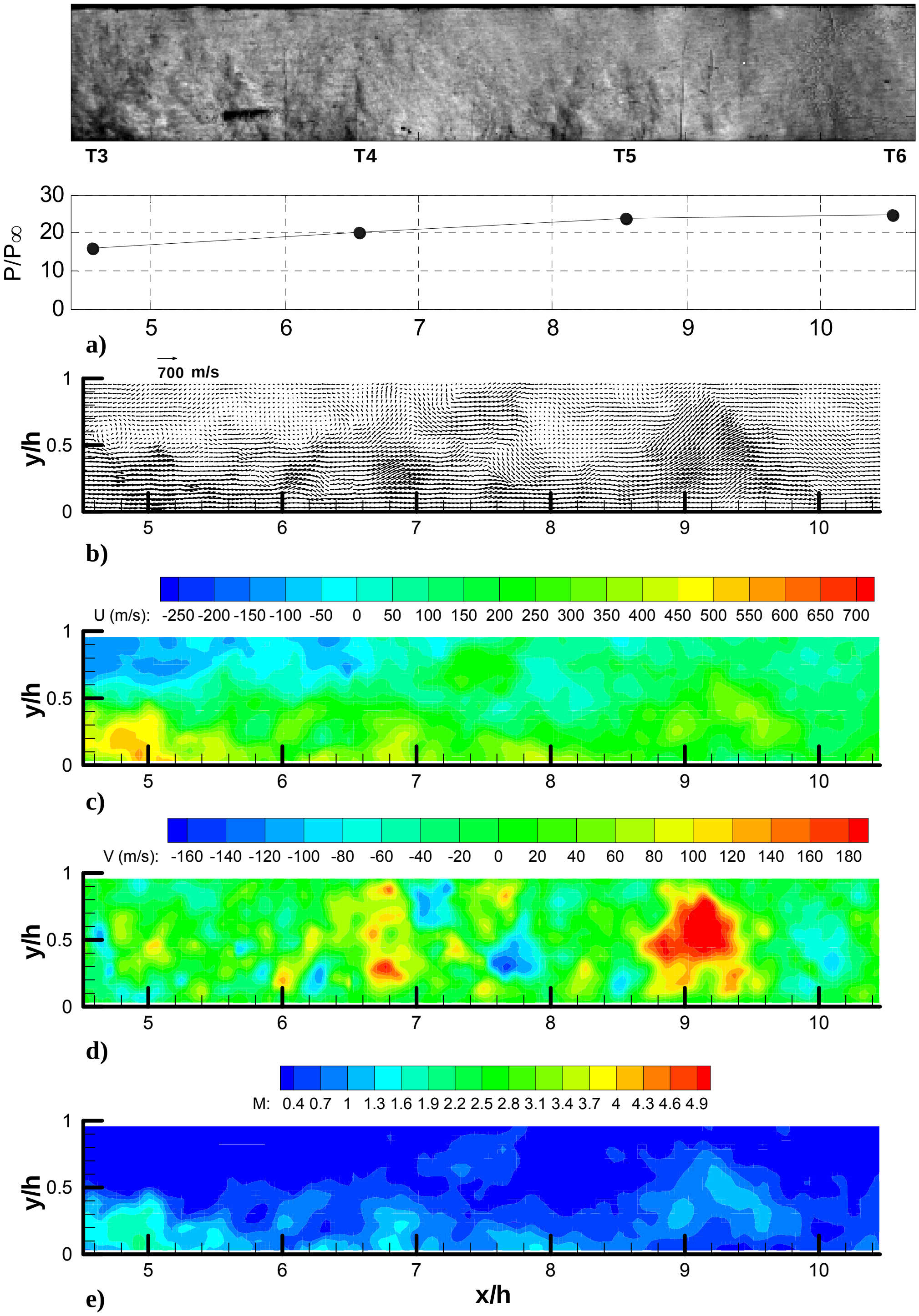

Figure 3.17 Instantaneous flow structure during unstart at $t = 14$ ms: a) representative schlieren image and corresponding pressure distribution, b) velocity vectors, c) U contours, d) V contours, e) M contours.

The PIV results confirm that the propagation of the unstart shock system in the model of the current study is highly dependent on flow separation. The high-speed schlieren imaging results suggested that unstart began with strong shock-induced separation of the isolator ceiling boundary layer (e.g., See Fig. 3.8a). This separation was seen to occur near the impingement point of the third reflected shock of the initial oblique shock system. At t = 2 ms (Fig. 3.12), the upstream propagation of the unstart system into the PIV field of view is first noticed with separated flow near the floor impingement point of the second reflected shock of the initial oblique shock system. From 2 to 4 ms (Fig. 3.11b), the unstart shock system is then seen to propagate further upstream with an increased strengthening of shock-induced separation that induces large reverse flow velocities up to about 250 m/s. Proceeding to t = 5 ms (Figs. 3.11c and 3.13), the unstart system is seen to induce significant separation of the ceiling boundary layer. This ceiling boundary layer separation seems to begin near the ceiling impingement point of the first reflected shock of the initial oblique shock system. Progressing to t = 7 ms (Figs. 3.11e and 3.14), the unstart system is seen to have propagated upstream to near the isolator entrance. This propagation is seen to be associated with increasing separation of the ceiling boundary layer. At this time, reverse flow velocities up to 250 m/s were measured. These observations suggest the flow structure of the unstart process to be dependent on the impingement locations of the initial reflected oblique shocks. The wide-field PIV pseudo-sequence indicates that the unstart system propagates through the inlet / isolator as strong shock-induced separation occurs first near the floor and then near the ceiling. This shift from the floor to ceiling of the shock-induced separation appears to be related to the location of the impingement points of the initial reflected shocks. Therefore, it appears that unstart progresses upstream taking the “path of least resistance,” as the flow separates in regions of pre-existing adverse pressure gradients.

3.5.3 Unstart Process Plan-View PIV

Figure 3.18 shows a plan-view pseudo sequence of streamwise velocity contour plots during the unstart process. Figs. 3.18a to 3.18f correspond to times of t = 0, 2, 3, 6, 8 and 10 ms respectively. Again, these times are provided to give an approximate order to the sequence and are not meant to imply that they are entirely repeatable (e.g., See section 3.5.1). The field of view plane is at the wall normal center height of $y/h = 0.5$ and it covers nearly the entire isolator (see Fig. 2a). Similar to the side-view unstart PIV data, the plan-view data are arranged to form a pseudo-sequence.

The percentage of valid vectors in the data set is 87%. The plan-view PIV correlations were also seen to degrade with upstream progression of the unstart shock system. For example, the percentages of valid vectors in order from Fig. 3.18a to Fig. 3.18f are 100, 95, 90, 82, 82 and 76. The reasons for the weaker correlations are similar to those given for the side-view data. Similar to the side-view, the dominant source of uncertainty was seen to occur in the PIV processing or the data reduction process. Again, further details are given in Appendix C. Note the uncertainties in U are less than that for the side-view. In addition, the plan-view measurements contain more valid vectors than the side-view. There are two reasons for this: (*i*) seeding particles tended to stick to the model walls and the side-view measurements required imaging through the two acrylic isolator sidewalls, whereas the plan-view measurements required imaging only through the acrylic isolator ceiling and (*ii*) the plan-view measurements tended to have higher seeding levels since they were made along the wall-normal center plane which was out of the lower portion of the floor boundary layer at a height of about $y = 0.66\ \delta$. This was not the case for the side-view PIV data that included the entire floor boundary layer which tended to contain regions of lower seeding densities which therefore decreased the correlation detection probability.

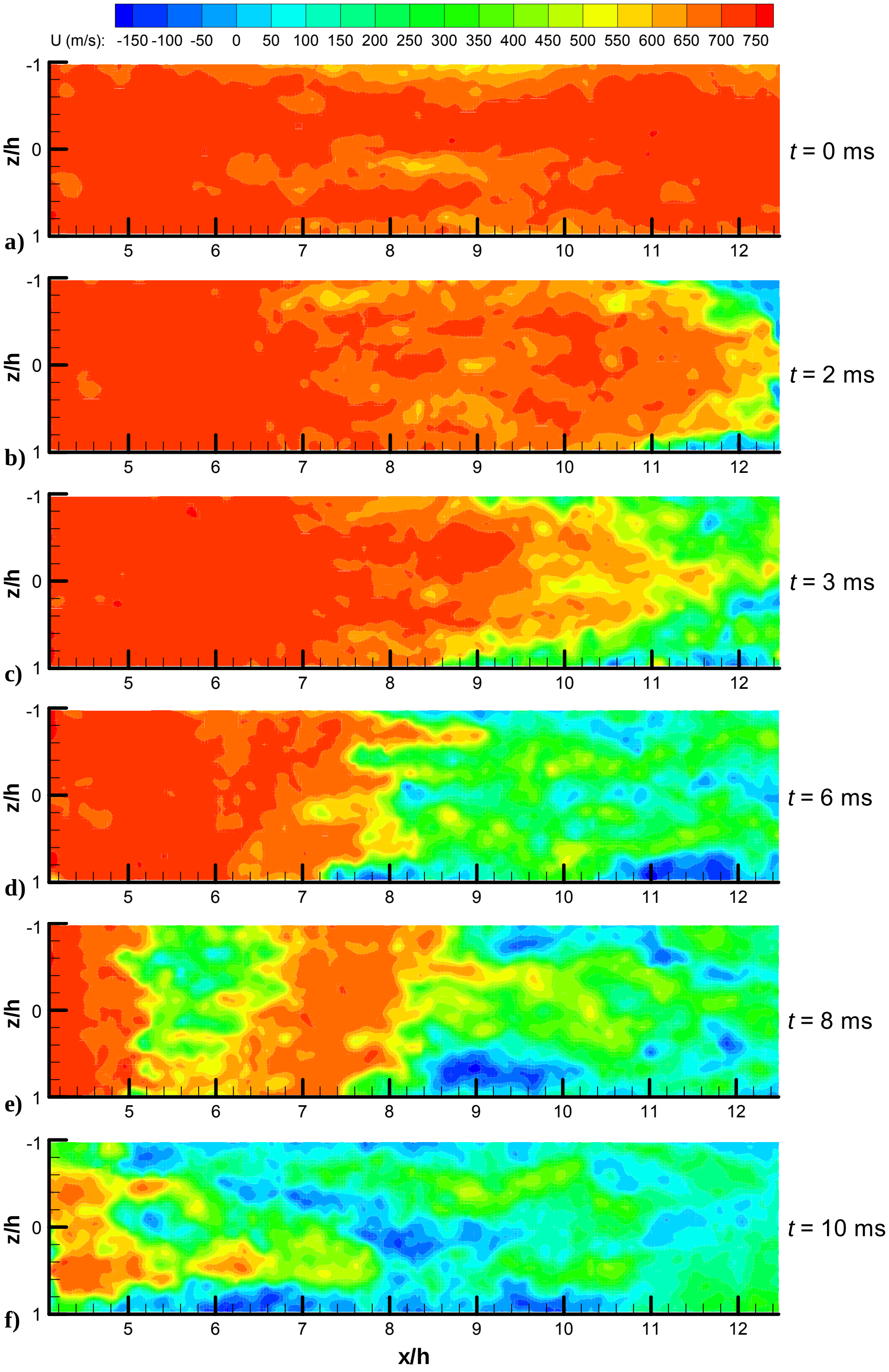

Figure 3.18 Unstart pseudo-sequence plan-view PIV: a) 0 ms, b) 2 ms, c) 3 ms, d) 6 ms, e) 8 ms, and f) 10 ms into the unstart process.

Fig. 3.18a shows the wall-normal center plane flow for the flap in the fully-down position or for the fully supersonic flow. Most of the entire flow-field in Fig. 3.18a consists of high speed fluid with velocities near 700 m/s. A few regions of lower speed fluid are observed and are attributed to the fact that measurements were taken within the turbulent floor boundary layer ($y \approx 0.66\ \delta$). In Fig. 3.18b at $t = 2$ ms, the unstart shock system has propagated into the field of view resulting in a separation of the sidewall boundary layers. At this time, unstart is clearly seen to be three-dimensional. In Fig. 3.18c at $t = 3$ ms, unstart has progressed further upstream along the isolator sidewalls to about $x/h = 8.5$. In comparison, the spanwise centerline flow is seen to be high-speed until the streamwise location of about $x/h = 10$. Fig. 3.19 shows the velocity vector plot corresponding to Fig. 3.18c. The separation of the sidewall boundary layers is demonstrated further in this plot. These data indicate that at the wall-normal center plane, the unstart shock system tends to move upstream first with side-wall boundary layer separation. In Fig. 3.18d at $t = 6$ ms, a shock is seen to mark the head of the unstart system at the streamwise location of about $x/h = 7.5$. While unstart is three-dimensional, there is not the clear pattern like in Figs. 3.18b and 3.18c where unstart progressed first along the isolator sidewalls. Rather, the unstart shock appears undulated along the spanwise direction. Ganapatisubramani et al. (2007) observed similar undulations in a ramp-induced shock-wave boundary layer interaction in a Mach 2 flow. The undulated shock shape was seen to conform to long, streamwise regions of high and low momentum fluid found in the floor boundary layer. Noting the approximate location of $x/h = 7.5$ of the undulated shock in Fig. 3.18d and looking to Fig. 3.11d of the side-view pseudo-sequence, it is apparent in Fig. 3.18d that the flow in the wall-normal center plane goes only through the shock that is associated with separation of the floor boundary layer. At $t = 8$ms, Fig. 3.18e shows that the isolator entrance flow has a velocity near 700 m/s up

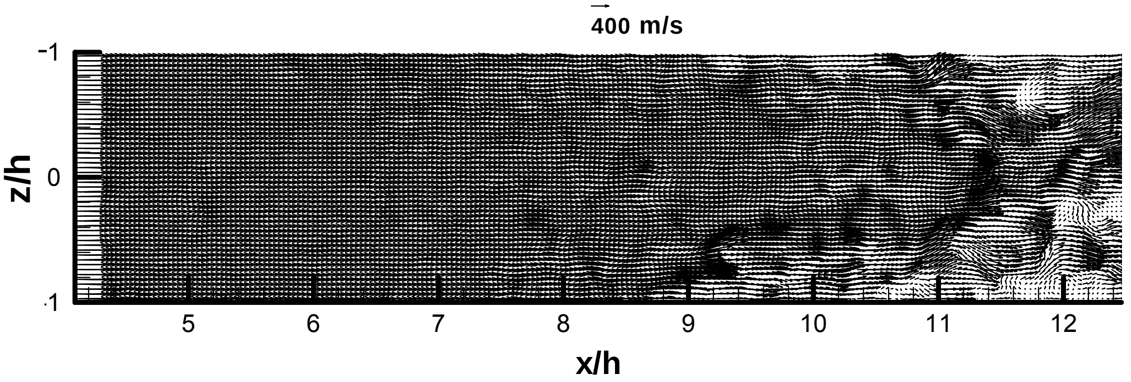

Figure 3.19 Unstart plan-view PIV vector field at t = 3 ms into the unstart process.

until the streamwise location of x/h = 5 where the velocity then decreases to about 300 m/s. Proceeding downstream along the spanwise centerline, the velocity then increases to about 650 m/s at x/h = 7 and then decreases back to about 300 m/s at x/h = 8.4. Comparing the streamwise velocity of Fig. 3.18e to that at y/h = 0.5 in Fig. 3.11e, shows similar streamwise velocities at similar streamwise locations. This indicates that the flowfield seen in Fig. 3.18e is a result of the prominent shear layer seen in Fig. 3.11e. A similar velocity decrease to that seen at about x/h = 8 in Fig. 3.18e, is seen at a similar streamwise location in Fig. 3.11e. As was mentioned, this decrease in velocity is possibly due to the high levels of mixing within the shear layer. Figure 3.18e shows that downstream of x/h = 8, the flow is three-dimensional with low speed and reversed flow occurring at the sidewalls around x/h = 8.5 along the port sidewall and around x/h = 9.0 along the starboard sidewall. The vector plot of Fig. 3.20 corresponding to Fig. 3.18e shows the flow to be separated near these locations. Finally, Fig. 3.18f shows the isolator flow at a time just after the unstart shock system has crossed T1 upstream of the inlet (x/h = -0.40). The isolator entrance still has regions of fast fluid with velocities of about 700 m/s near the spanwise center, whereas the flow near the sidewalls contains predominantly reverse flow. This is similar to the three-dimensional flowfield observed during unstart in the computational study of McDaniel and Edwards (2001).

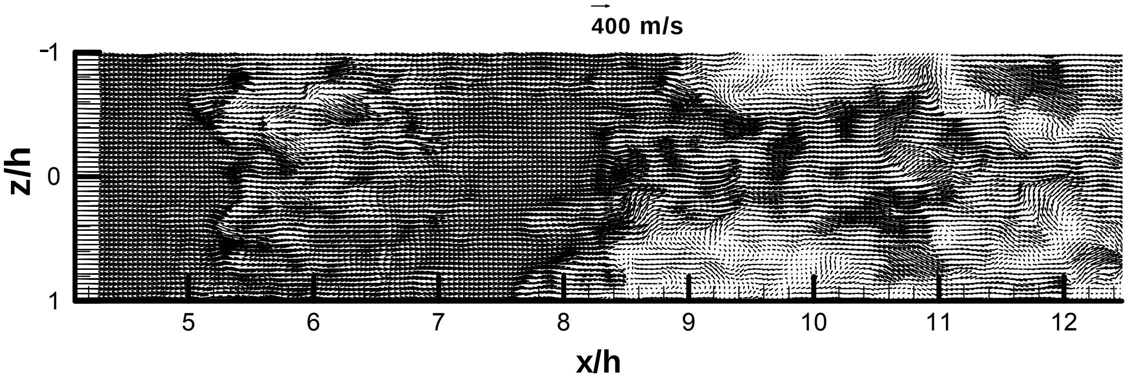

Figure 3.20 Unstart plan-view PIV vector field at $t = 8$ ms into the unstart process.

3.6 HIGH-AMPLITUDE OSCILLATORY UNSTARTED FLOW

3.6.1 High-Speed Schlieren Imaging and Pressure Measurements

Once the inlet / isolator model unstarted, high-amplitude periodic pressure fluctuations at T7 as high as 35 P_{∞}, occurred as seen in Fig. 3.4 from 0.19 to 0.45 seconds. A few cycles of these oscillations at T7 can also be seen in Fig. 3.5. The previous section described the first pressure increase and decrease during unstart. This section focuses on the pressure oscillations that follow unstart. Figure 3.21 is a series of representative downstream-view schlieren images and the corresponding wall pressure distributions for this process. The knife edge was in a vertical position to highlight horizontal gradients such as those due to normal shocks and compression waves. In this section, observations made of other high-amplitude oscillatory unstarted flow cycles using the upstream-view will also be discussed. The first image in Fig. 3.21 corresponds to the absolute time of 0.31 seconds in Fig. 3.4. The sequence is labeled with times, ϕ, that are normalized by the period of the oscillation shown in Fig. 3.21, which is equal to

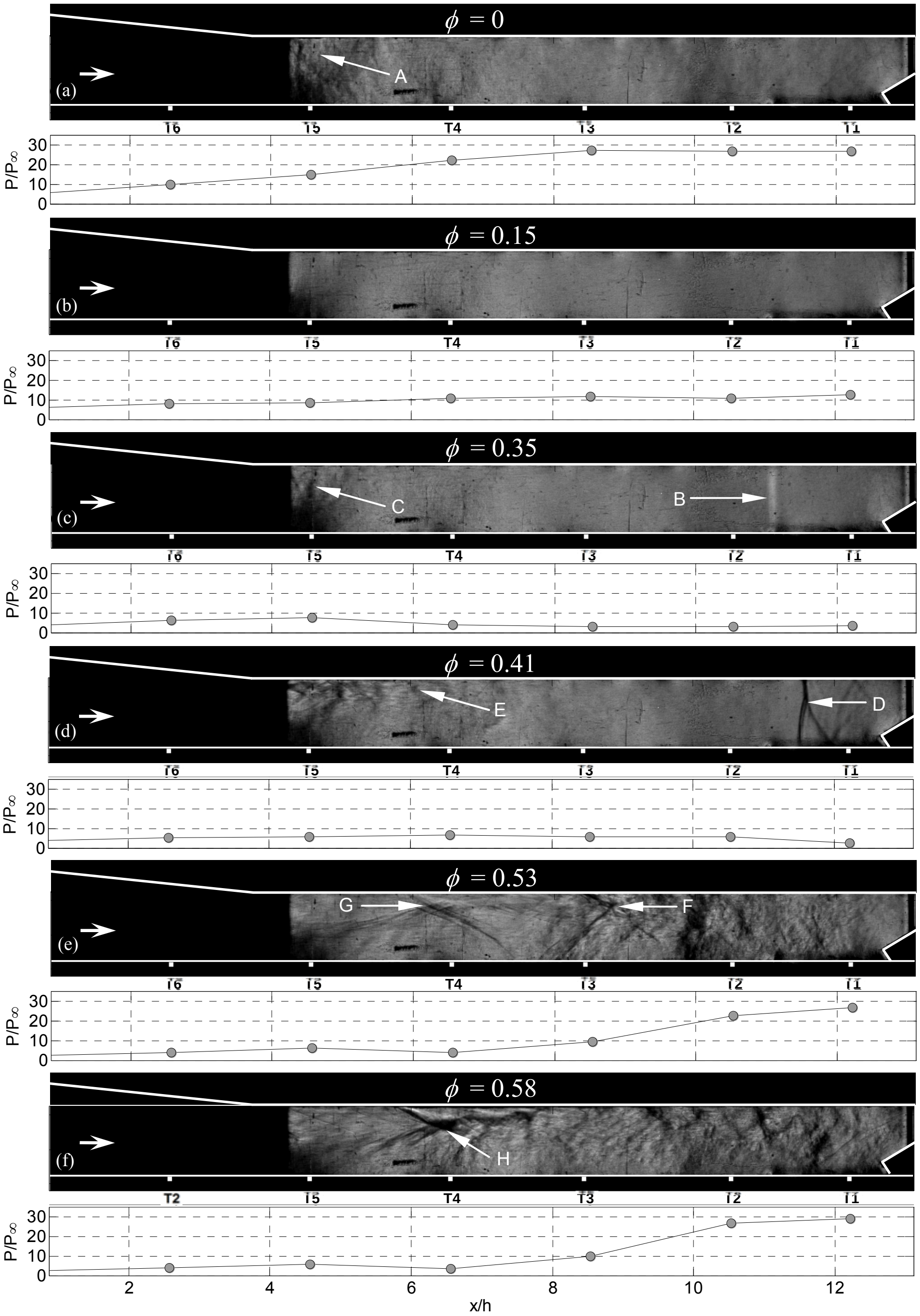

Figure 3.21 Sequence of downstream-view schlieren images and corresponding instantaneous pressure distributions showing high-amplitude oscillatory unstarted flow at times normalized by the oscillation period of 7.4 ms: a) ϕ = 0, b) ϕ = 0.15, c) ϕ = 0.35, d) ϕ = 0.41, e) ϕ = 0.53 , and f) ϕ = 0.58.

7.4 ms. The sequence is for the relative normalized times of $\phi = 0$, 0.15, 0.35, 0.41, 0.53 and 0.58, which represents part of an oscillation cycle. In this section, the time $\phi = 0$ is chosen to be when overall, the inlet / isolator pressure distribution is near a cycle-maximum. In the $\phi = 0$ image of Fig. 3.21a, visible flow features are apparent near the isolator entrance (arrow A). The featureless flow in the downstream section of the isolator indicates that the flow is largely subsonic. Upstream-view schlieren images for other high-amplitude oscillatory unstarted flow cycles (not shown here) were used to determine the flow structure near the inlet entrance. The images indicated that at cycle times when overall, the inlet / isolator pressure distribution was near a maximum (such as at $\phi = 0$ of Fig. 3.21a), an oblique shock sat upstream of the inlet floor and intersected the inlet ceiling just downstream of $x/h = 0$. The $\phi = 0.15$ image (Fig. 3.21b) shows that the flow within the entire isolator is quiescent and most likely subsonic. Upstream-view images of other cycles showed that unlike at $\phi = 0$, where an oblique shock is upstream of the inlet, the quiescent flow at $\phi = 0.15$ is the result of a bow shock that is upstream of the inlet. The bow shock is near its most upstream location of the cycle. The pressure distribution at $\phi = 0.15$ indicates the isolator pressure is lower than that at $\phi = 0$. During the decreasing-pressure part of the cycle, downstream propagating compression waves were observed. These compression waves became more distinct in the schlieren images when the isolator pressure distribution was near a minimum. In Fig. 3.21c at $\phi = 0.35$, the isolator pressure distribution has further decreased and a compression wave has propagated to near the downstream end of the isolator. The compression wave, which appears to be an acoustic wave, is seen as a vertical white line (arrow B) at the approximate streamwise location of $x/h = 11$. From the schlieren time-sequence, the velocity of the compression wave was estimated to be about 350 m/s near the downstream section of the isolator. This propagation velocity is near the stagnation speed of sound, which suggests the compression wave is in fact an acoustic wave. Similar compression wave velocities were observed in other high-amplitude oscillatory unstarted flow cycles. Another key feature of the $\phi = 0.35$ image is that the visible flow features (arrow C) have re-entered the entrance of the isolator. Upstream-view images revealed that as these visible flow features moved back within the isolator, the bow shock upstream of the inlet moved downstream to once again intersect the inlet ceiling as an oblique shock. The $\phi = 0.41$ image (Fig. 3.21d) shows an upstream propagating strong bifurcated normal shock is near the exit of the isolator (arrow D). This normal shock appears to be related to the acoustic-compression waves that reflect off the flap at the end of the isolator. Also, note in the $\phi = 0.41$ image that the visible flow features (arrow E) have moved even further downstream into the isolator. The upstream-view schlieren images showed that as the visible flow features moved further downstream, the oblique shock upstream of the inlet also moved further downstream. As time progresses between $\phi = 0.41$ and 0.53 (Fig. 3.21e), the visible flow features at the isolator entrance continue to move downstream as the flow becomes supersonic, while the strong-compression system generated at the exit of the isolator continues to move upstream. As a result two distinct shock systems (arrows F and G) form within the isolator as seen in the $\phi = 0.53$ image. The pressure in the downstream half of the isolator has increased as the strong shock generated at the rear of the isolator has moved upstream toward the center of the isolator. This upstream propagating shock system can be seen at the streamwise location of about the $x/h = 8.5$ (arrow F), followed by highly separated flow. The downstream propagating shock system can be seen near $x/h = 6$ (arrow G). This shock system is seen to be associated with a separated upper isolator boundary layer. As seen in the $\phi = 0.58$ image (Fig. 3.21f), the two shock systems interact and merge into a new single shock system (arrow H). Near the time of this merging, observations made with the upstream-view (of other cycles) suggest that the oblique shock upstream of the inlet has reached its most downstream location of the cycle. In subsequent images (not shown here), the shock system (of arrow H) then moves upstream until overall, the inlet / isolator pressure distribution is near a cycle maximum at $\phi = 1.0$ (about 7.4 ms). The flow field image and pressure distribution at this time (not shown here) are very similar to those seen at $\phi = 0$. Referring to Fig. 3.5, it can be seen that the rise time to peak pressure is noticeably smaller for high-amplitude oscillatory cycles as compared to the initial unstart transient. This faster isolator pressurization compared to the initial unstart pressurization may be related to the upstream and downstream propagating compression waves observed in the high-amplitude oscillatory unstarted flow schlieren images.

Figure 3.22 shows the power spectra of transducers T7, T2 and T1 for the high-amplitude oscillatory unstarted flow. For the spectra, the acquisition rate was 192 kHz and the number of samples taken was 48,000, which gives a maximum frequency of 96 kHz and a resolution of 4 Hz. However, the frequency information is only valid up to the low pass filter cutoff frequency of 50 kHz. Absolute frequencies as well as normalized frequencies are presented below. Unstarted flow frequencies were normalized as $f^* = f\,L\,/\,a_0$ (where a_0/L=1100 Hz), which would be appropriate for a purely acoustic oscillation. For example, use of these parameters would yield normalized frequencies of f^*= 0.25 and 0.5 for quarter and half-wave resonators, respectively. As seen in Fig. 3.22, the dominant frequency (f_1) for T7, T2 and T1 is about 124 Hz (f_1^*=0.11). The other four transducers also showed the same value of dominant frequency. The second and fourth highest peaks occur at the second and fourth harmonics of the dominant frequency (f_2 = 248 Hz, f_2^*=0.23 and f_4 = 496 Hz, f_4^*=0.45) and the third highest peaks occur near the third harmonic at about 364 Hz (f_3^*=0.33). The spectra for T6 through T3 (not shown here) within the isolator look very similar to that of T7, but the sound pressure levels (*SPL*)

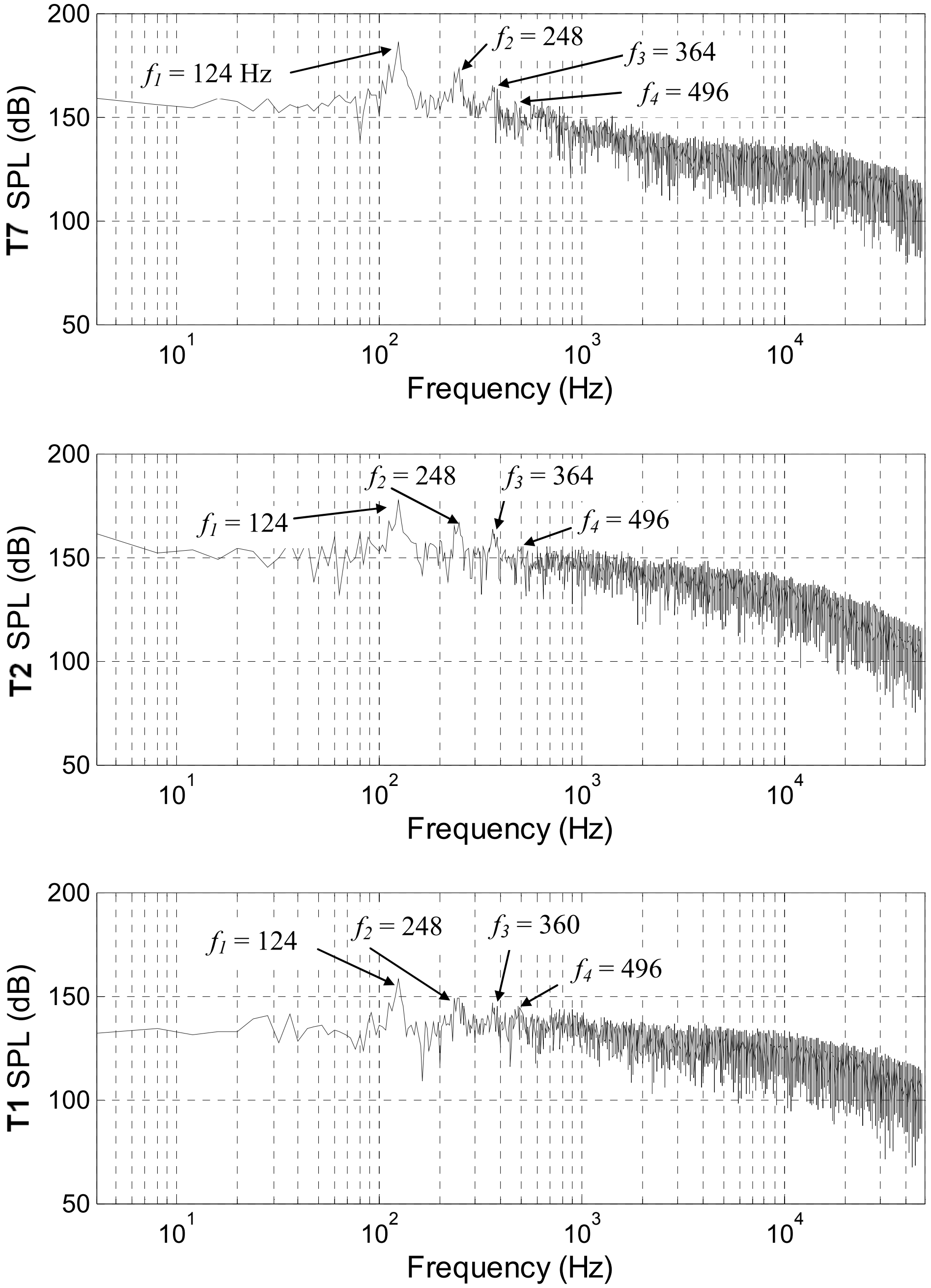

Figure 3.22 Power spectra of the pressure at T7, T2 and T1 for the high-amplitude oscillatory unstarted flow.

tend to decrease for the more upstream transducers. For example, the dominant peak occurs at 186 dB for T7 and 180 dB for T3. As seen in Fig. 3.22, the T2 (within the inlet) power spectrum looks similar to that of T7, but the dominant peak occurs at a lower *SPL* of 177 dB. The *SPL* distribution of T1 (upstream of the inlet) is seen to be much lower than those of T7 through T2. Such oscillatory unstarted flow pressure distributions have also been observed by other researchers (Hawkins and Marquart, 1995, Rodi et al., 1996 and Shimura et al., 1998). Rodi et al.[18] found the frequency of their oscillatory unstarted flow could be predicted by using linear acoustic theory for a half-wave resonator (i.e., the inlet / isolator is a resonator with two free boundaries). The speed of sound was calculated using the flow stagnation temperature. If in the current study the same is done, the calculation gives an oscillation frequency of 550 Hz ($f^* = 0.5$), which is more than four times the observed dominant frequency. As previously mentioned, since the traveling compression waves can be clearly seen to reflect as shocks, this means that the isolator exit acts more like a solid wall, and so treating the isolator as a quarter-wave resonator may be more appropriate. Doing so gives a resonant frequency of 275 Hz ($f^* = 0.25$), which is still more than twice the measured frequency. There do appear to be times in the oscillatory cycle for which acoustic theory may be appropriate. For instance, the compression wave of Fig. 3.21c at $\phi = 0.35$ propagates at a velocity of about 350 m/s which is near the stagnation speed of sound. However, there are other times in the oscillatory cycle where it is rather obvious that linear acoustic theory should not apply. For example, the Fig. 3.21 images at $\phi = 0.41$ and $\phi = 0.53$ show the isolator flow to be dominated by strong propagating shock systems (arrows F and G) that are associated with flow separation. In Fig. 3.21d at $\phi = 0.41$, the upstream propagating shock system (arrow D) is at the location of about $x/h = 11.5$. At $\phi = 0.53$ (Fig. 3.21e), the shock system (arrow F) has moved upstream to the approximate location of $x/h = 8$. Using the difference in approximate locations of the upstream propagating shock system between the $\phi = 0.41$ (3.0 ms) image and the $\phi = 0.53$ (3.9 ms) image gives an approximate shock system velocity of 100 m/s (≈0.3 a_0). This lower-than-acoustic velocity is likely because the upstream propagating shock system propagates against a supersonic flow. Owing to cycle times for which the isolator flow is dominated by propagating shock systems, frequencies lower than that predicted by linear acoustic theory are to be expected.

The mean pressure and mean *RMS* pressure distributions for the high-amplitude oscillatory unstarted flow are shown in Fig. 3.23. Both distributions are seen to increase in a nearly linear fashion with streamwise distance into the inlet / isolator model. Compared to the fully supersonic started flow of Fig. 3.2, this unstarted flow is seen to have much higher *RMS* and mean pressures.

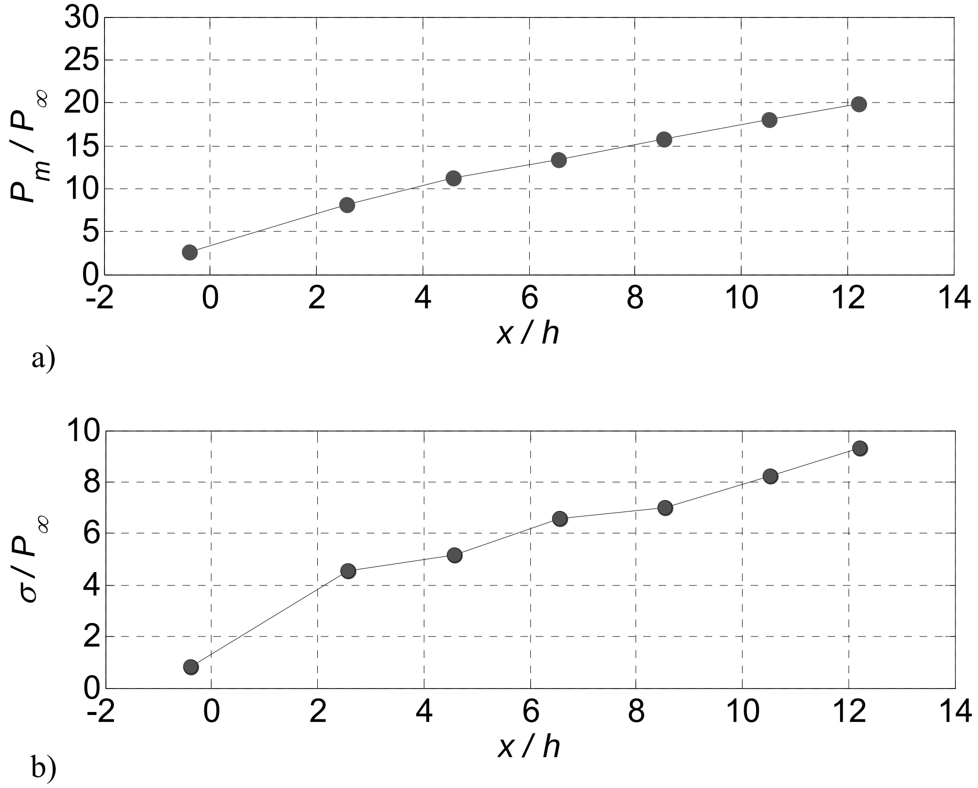

Figure 3.23 High-amplitude oscillatory unstarted flow: a) mean pressure distribution and b) pressure standard deviation distribution. (The distributions correspond to data acquired in the time range of 0.2 to 0.45 seconds in Fig. 3.4.)

3.6.2 Side-View PIV Measurements

This section focuses on side-view PIV and simultaneous pressure measurements made during high-amplitude oscillatory unstarted flow cycles. The measurements give insight into important features of this oscillatory unstarted flow. Figure 3.24 shows side-view streamwise velocity contours from three different unstarted flow cycles. Similar to the unstart process, it was not possible to acquire unstarted flow PIV from the same cycle due to the repetition rate of the PIV system. Figures 3.24a and 3.24b show velocity data corresponding to cycle times for which the isolator pressure distribution is at a near maximum and minimum respectively. Figure 3.24c corresponds to a time for which the isolator pressure distribution is increasing. The percentages of valid vectors for Figs. 3.24a, 3.24b and 3.24c are 88%, 99% and 78%, respectively. In addition, Figs. 3.25a to 3.25c show the isolator pressure time-histories corresponding to a few cycles of unstarted flow near the time of the PIV data acquisition of Figs. 3.24a to 3.24c. Note the time axes of Figs. 3.25a to 3.25c start at an arbitrary zero such that the middle of the plot of corresponds to the time of the PIV data acquisition. Fig 3.25a shows that at the time of the PIV data acquisition the isolator pressure distribution is near a maximum. The corresponding streamwise velocity plot of Fig. 3.24a shows the isolator entrance flow to be about 600 m/s near the floor and about -200 m/s near the ceiling. Moving downstream the velocity decreases and becomes more uniform. Downstream of x/h = 7, the streamwise velocities are seen to range from 0 to 300 m/s. Moreover, although not shown here, the Mach number downstream of x/h = 7 was seen to be predominantly subsonic. Figure 3.25b shows that at the time corresponding to the PIV data of Fig. 3.24b, the pressure within the isolator is near a minimum and very uniform. This indicates a subsonic isolator flow. Recall that the results above indicated that when the isolator pressure distribution was near a minimum such as in Fig. 3.25b, a bow shock sat

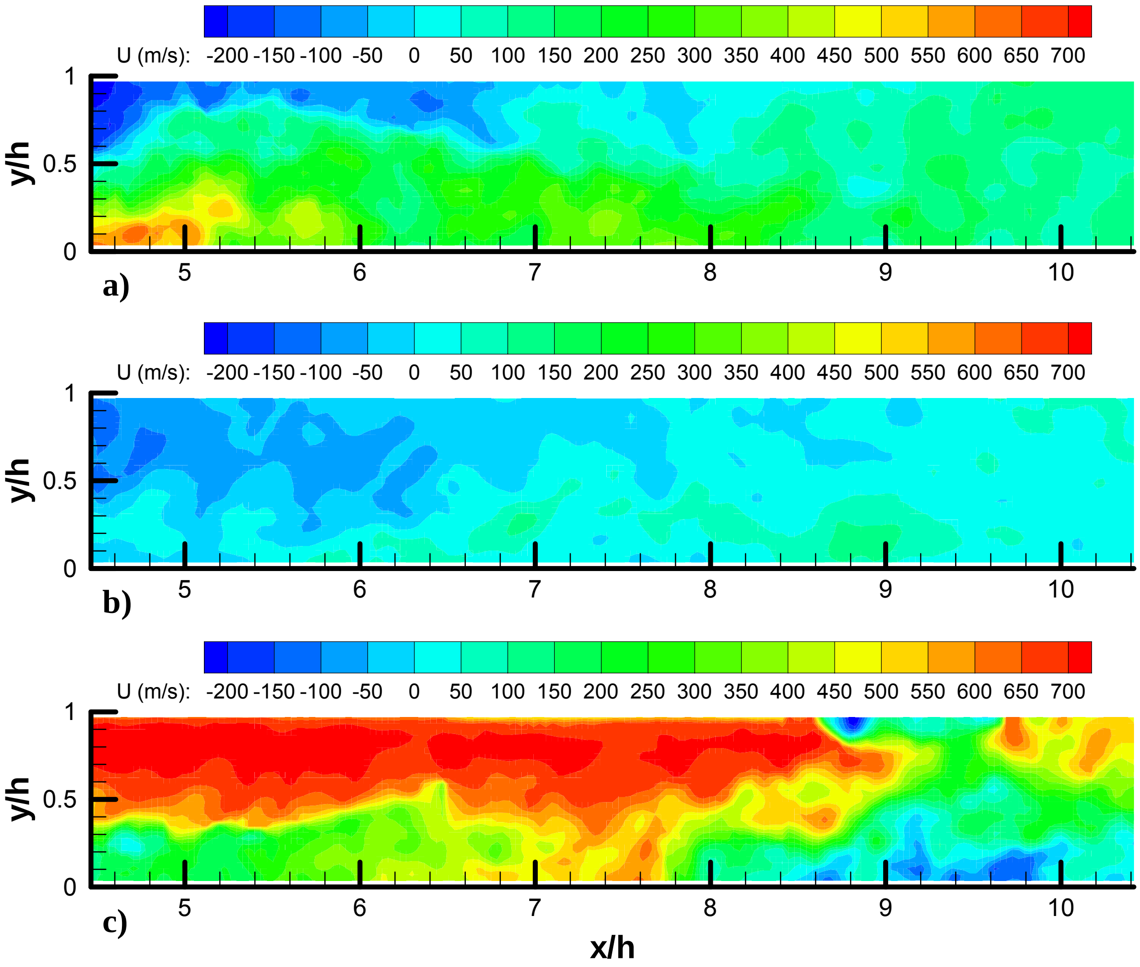

Figure 3.24 High-amplitude oscillatory unstarted flow PIV for selected times during the flow cycle: a) near the peak pressure of the cycle, b) near the trough in pressure of the cycle, and c) rising from pressure trough to the peak of the cycle.

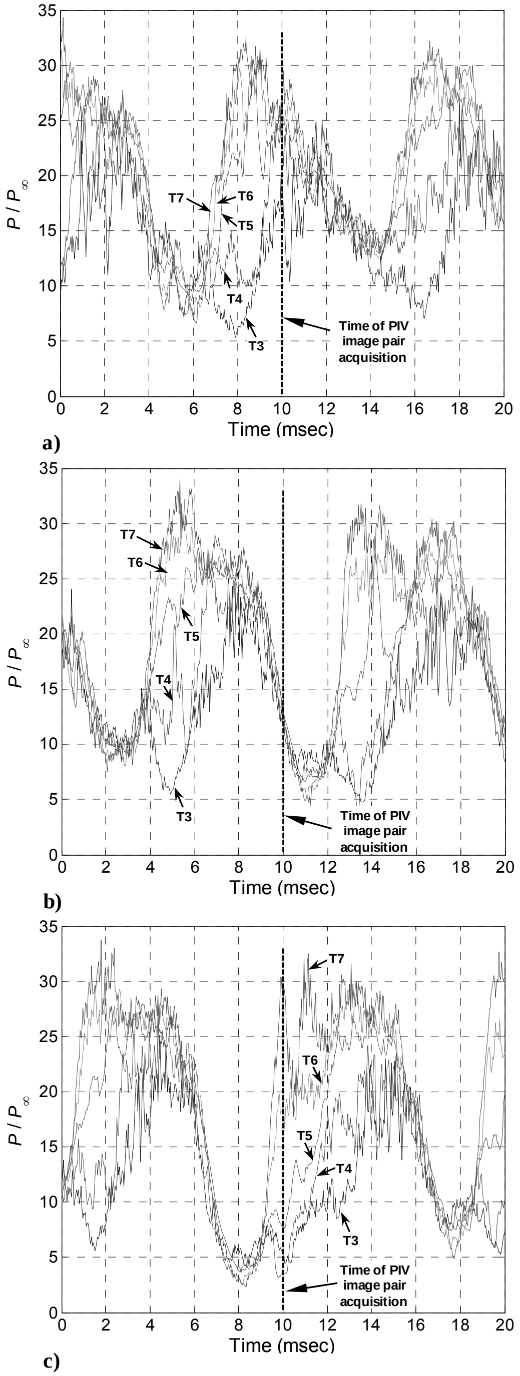

Figure 3.25 Pressure histories showing the location of PIV image pair acquisition for selected times during high-amplitude oscillatory unstarted flow cycles: a) near the peak isolator pressure distribution of the cycle, b) near the trough of the cycle, and c) rising from the trough to the peak of the cycle.

upstream of the model at its most upstream location of the cycle. The streamwise velocities of Fig. 3.24b confirm the flow not only to be subsonic but nearly completely stagnant. Finally, Figs. 3.24c and 3.25c correspond to a cycle time at which the isolator pressure distribution as a whole is increasing. Note in Fig. 3.25c that the pressures at the more downstream T7 (x/h = 12.21) and T6 (x/h = 10.53) have increased to near cycle maximums, the pressure at T5 (x/h = 8.54) has increased slightly and the pressures at the more upstream, T4 (x/h = 6.56) and T3 (x/h = 4.57) remain at near cycle minimums. The explanation of this pressure distribution is clear upon inspection of the streamwise velocity plot of Fig. 3.24c. Figure 3.24c shows that high-speed supersonic flow enters the isolator above y/h = 0.5. Farther downstream, a shock system is seen that intersects the floor at about x/h = 7.8 and the ceiling at about x/h = 8.6. This shock system is the aforementioned upstream traveling shock system that was a result of compression wave reflections near the isolator exit. Figure 3.26 presents additional flow information to help show the flow structure corresponding to this upstream traveling shock system. Figure 3.26a displays a representative schlieren image corresponding to the PIV data of Fig. 3.24c. The schlieren image was taken from another unstarted flow cycle, not simultaneously. The schlieren image was picked with the requirement that its corresponding isolator pressure distribution closely match that of the PIV data. Both the pressure distributions corresponding to the PIV and schlieren data are also shown in Fig. 3.26a. To make comparison to the schlieren image easier, the streamwise velocity contour plot of Fig. 3.24c is shown again in Fig. 3.26b along with its corresponding vector plot in Fig. 3.26c. The schlieren image of Fig. 3.26a clearly shows the upstream traveling shock system (arrow A) that was a result of compression wave reflections. The location of this shock is seen to be similar to that given in the streamwise velocity and vector plots of Figs. 3.26b and 3.26c, respectively. In addition, the velocity vector plot shows a high level of flow separation downstream of this shock system which is also seen in the schlieren image. The schlieren image of Fig. 3.26a also shows another shock system (arrow B). This is the shock system mentioned in the previous section that was seen to form and propagate downstream while simultaneously, the upstream propagating shock system (arrow A) moved upstream (e.g., See arrow G of Fig. 3.21e). The formation of the downstream propagating shock system (arrow B) in the upper portion of the isolator indicates that the flow entering the upper portion of the isolator is supersonic. This is seen to be the case upon inspection of the streamwise velocities in Fig. 3.26b. Recall from the previous section that continuation of the oscillatory cycle was seen to occur with continuing upstream motion of the upstream propagating shock system (arrow A).

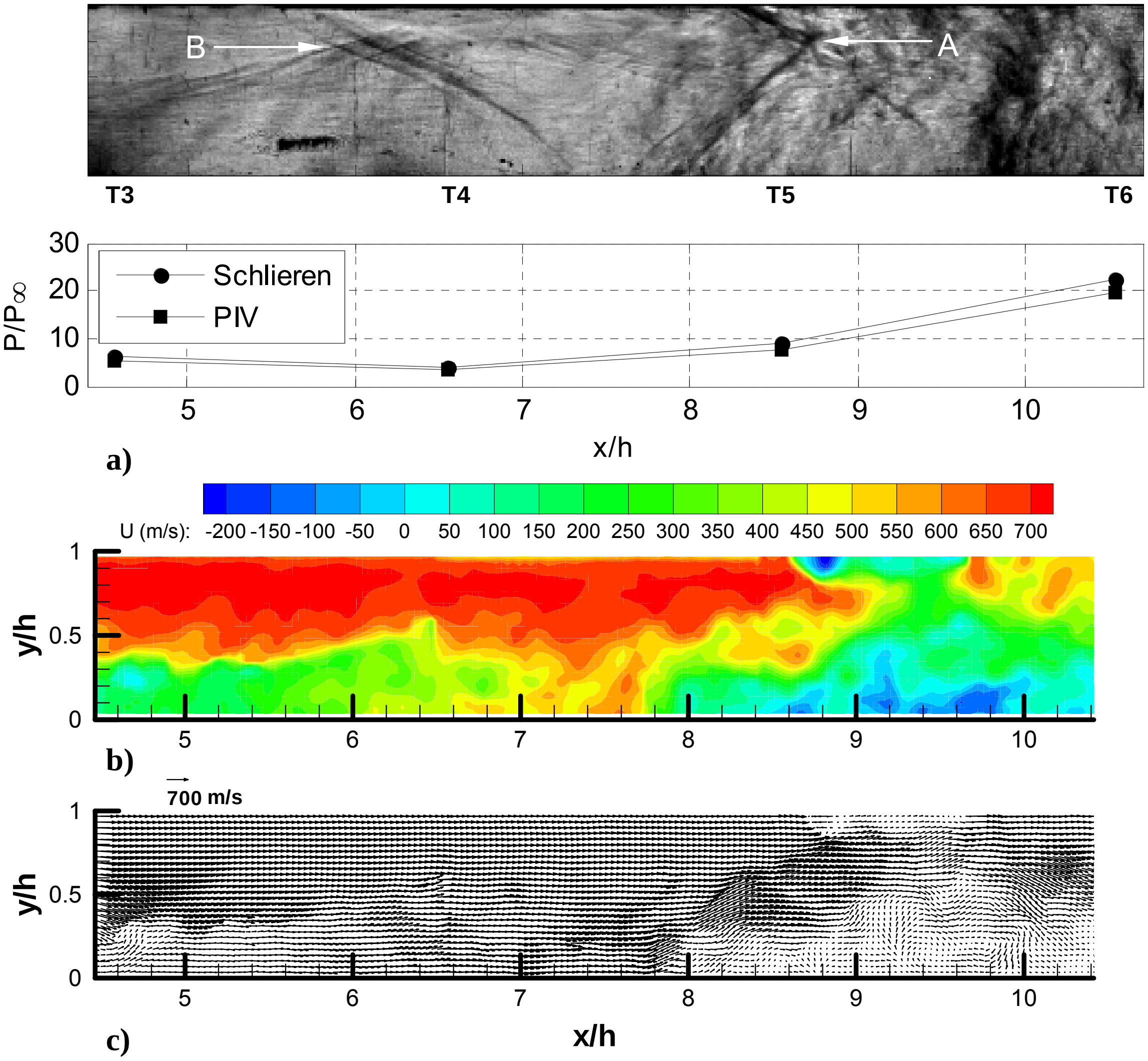

Figure 3.26 Instantaneous flow structure during high-amplitude oscillatory unstarted flow corresponding to increasing pressure portions of the cycles. a) representative schlieren image and corresponding pressure distributions, b) *U* contours, c) velocity vectors.

The combined results of the schlieren imaging, fast-response pressure and PIV measurements help to give an explanation for the lower than acoustic frequencies measured. The pressure time-histories in Fig. 3.25 show distinct patterns. During the falling pressure portions of the cycles, the pressure decreases uniformly throughout the isolator flow which is seen to contain subsonic flow. It appears that during the decreasing pressure portions of the cycle, the isolator acts as a quarter-wave resonator (i.e., one free-boundary, one solid boundary). On the contrary during the increasing pressure portions of the oscillations, the isolator flow is dominated by supersonic entrance flow and the pressure rises through an upstream traveling shock system, not acoustic mechanisms. Inspection of the rising pressure portions of Fig. 3.25, shows a phase difference in the pressures during the increasing pressure portions of the oscillations. The pressure at T7 is seen to increase followed by T6, then T5, then T4 and finally the pressure at T3 increases. This is consistent with the upstream traveling shock system that originates near the isolator exit. Although the previously mentioned results explain the lower than acoustic frequencies, they do not explain what drives the isolator entrance flow to go from subsonic to supersonic flow in the decreasing and increasing portions of the oscillations respectively. From the schlieren results it was observed that this was related to an oscillating “leading shock” upstream of the inlet. When the flow in the isolator was seen to be subsonic, the leading shock was a bow shock located near its most upstream location of the cycle. However, when the isolator entrance flow was supersonic, the leading shock was seen to be an oblique shock that intersected the inlet ceiling. The reasons behind the oscillations of the leading shock and therefore oscillations of the isolator entrance flow between supersonic and subsonic currently remain unclear. Better measurements in the vicinity of the oscillating leading shock could prove useful in providing answers.

3.7 NON-OSCILLATORY UNSTARTED FLOW

After unstart and the high-amplitude oscillatory unstarted flow, it was possible to drastically change the characteristics of the unstarted flow by lowering the flap. Note that following unstart, the flow mode was always seen to be the previously discussed high-amplitude oscillatory unstarted flow. However, the oscillations could be reduced and in the case of the current section removed, with a subsequent lowering of the flap. This section focuses on what is defined to be non-oscillatory unstarted flow. This mode of unstarted flow was seen to lack the periodic oscillations of the previously discussed unstarted flow.

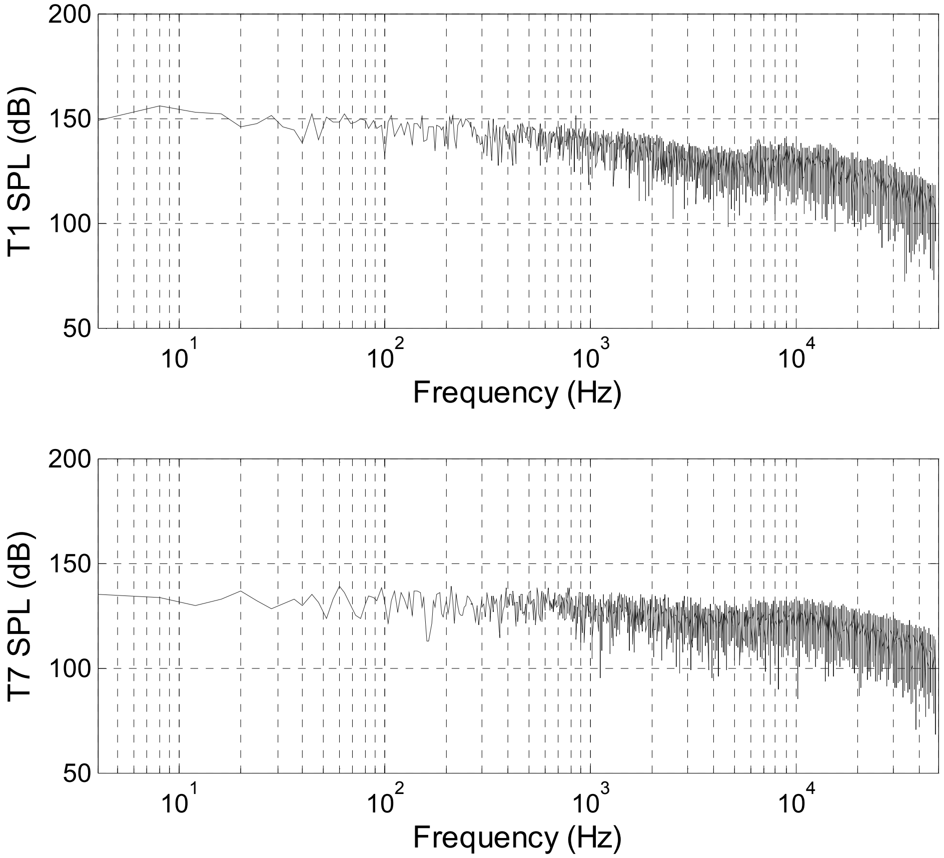

Figure 3.27 Power spectra of the pressure at T7 and T1 for non-oscillatory unstarted flow.

3.7.1 Schlieren and Pressure Measurements

As seen in Fig. 3.4, at a time of about 0.5 seconds the flap was brought to a slightly lower position maintaining an unstarted inlet / isolator. However, this unstarted flow had much smaller pressure fluctuations at T7 (about 10 P_∞). The pressure power spectra at each transducer during this time reveal that the fluctuations are more broadband and do not exhibit the dominant peaks seen in the oscillatory unstarted flow described above. For example, the pressure power spectra for T7 and T1 are shown in Fig. 3.27 and demonstrate the broadband nature of the fluctuations. Furthermore, compared to the high-amplitude oscillatory unstarted flow, the non-oscillatory unstarted flow is seen to have lower *SPL* levels. An example of an upstream-view schlieren image from the non-oscillatory unstarted flow is shown in Fig. 3.28. This image was taken from another non-oscillatory unstarted flow similar to that shown in Fig. 3.4. During this unstarted flow mode an oblique shock (arrow A) is always seen to sit upstream of the inlet entrance. A shear layer (arrow B) that appears to be the result of ceiling boundary layer separation is also always seen during this mode. The mean pressure distribution plot of Fig. 3.29a shows the mean pressure near the end of the isolator (at T7) to be 23.9 P_∞, which is 86 % of the pressure computed for a Mach 4.9 normal shock of 27.8 P_∞. Furthermore, Fig. 3.29b shows that the pressures of this unstarted flow mode are much steadier than that for the high-amplitude oscillatory unstarted flow (compare to Fig. 3.23b).

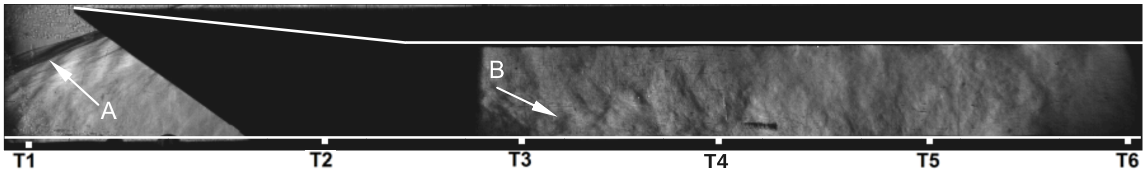

Figure 3.28 Upstream-view schlieren image showing non-oscillatory unstarted flow.

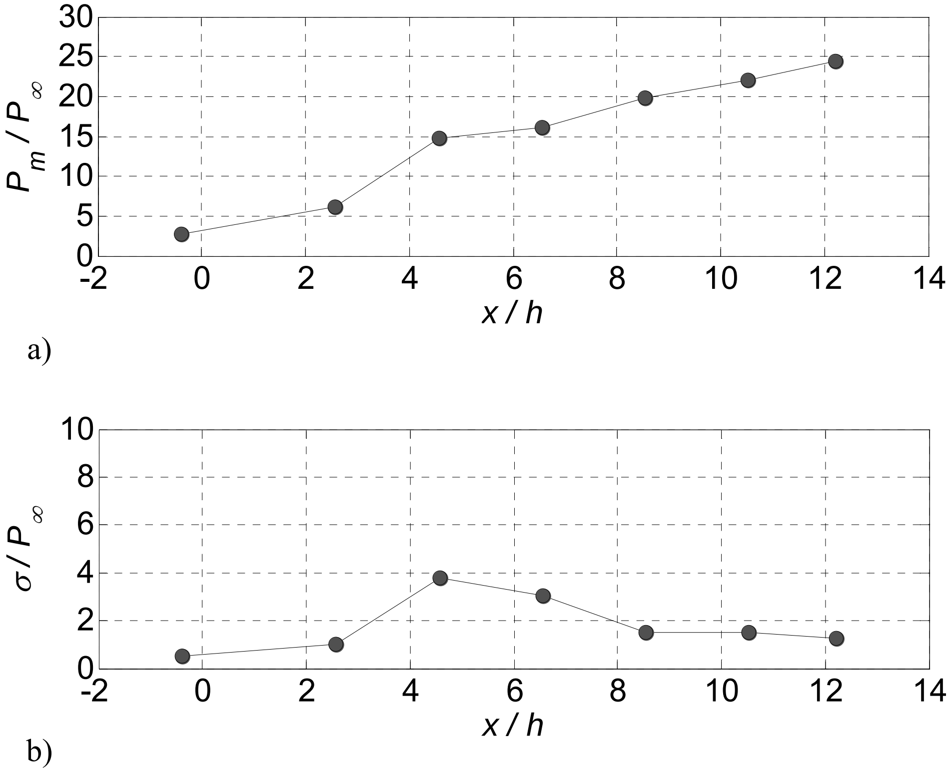

Figure 3.29 Non-oscillatory unstarted flow: a) mean pressure distribution and b) pressure standard deviation distribution.

3.7.2 Side-View PIV Measurements

This section presents mean side-view PIV data corresponding to the non-oscillatory unstarted flow. Forty vector fields were used to calculate the mean. The dataset was seen to contain about 78% valid vectors. Only valid vectors were used to calculate the mean. The PIV and pressure data corresponding to the non-oscillatory flow discussed below were acquired on a different run than those discussed above. However, based on the observed flow structure and pressure distributions, the unstarted flows are similar enough to make comparisons.

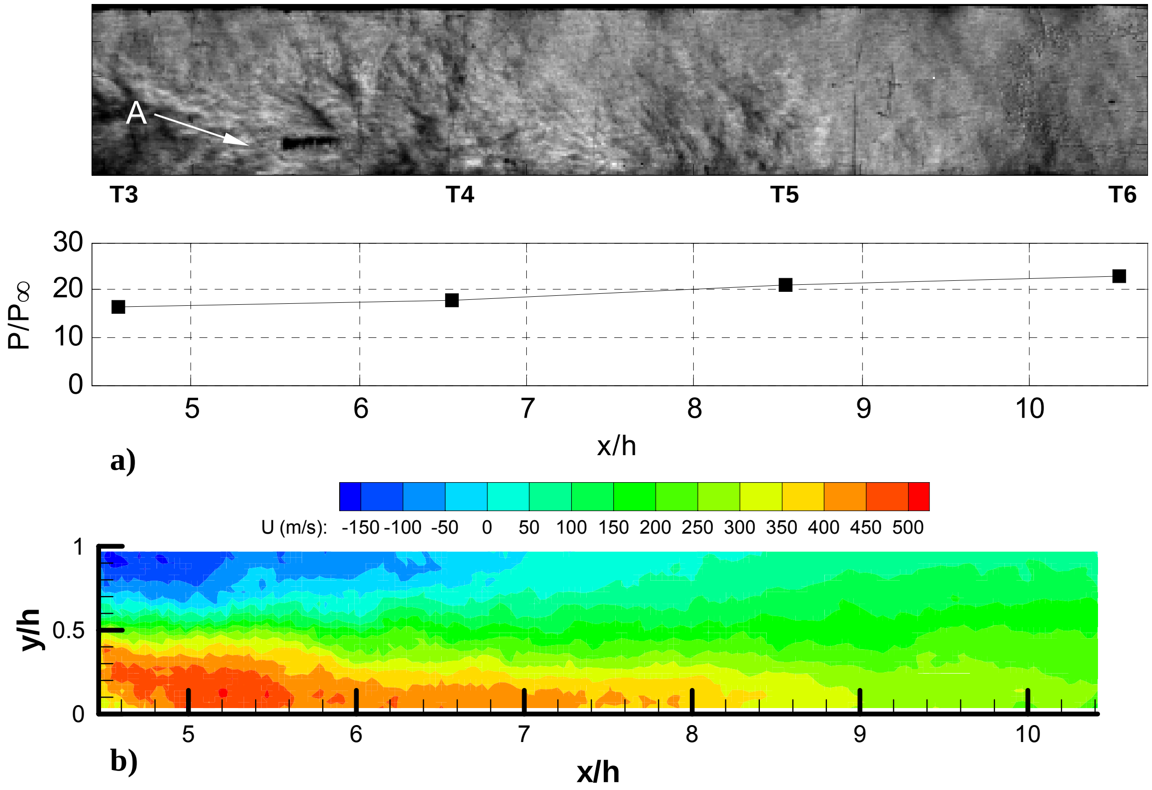

Figure 3.30 Non-oscillatory unstarted flow PIV a) representative schlieren image and pressure distribution corresponding to the PIV data, b) mean *U* contours.

Figure 3.30 shows flowfield data corresponding to the non-oscillatory unstarted flow. Fig. 3.30a gives a representative schlieren image of this unstarted flow. As discussed above, a strong oblique shock was always seen to exist upstream of the inlet entrance which appears to result in ceiling boundary layer separation. The schlieren image of Fig. 3.30a shows the separated ceiling flow entering the isolator (arrow A). In addition, the isolator mean wall pressure corresponding to the PIV data is also given in Fig. 3.30a. Again, the non-oscillatory unstarted flow is seen to result in significant compression. Although not shown here, the pressure at T7 was 25.2 P_∞, which is 91% of the pressure increase computed for a Mach 4.9 normal shock of 27.8 P_∞. Finally, Fig. 3.30 shows the mean streamwise velocity contours for this unstarted flow. The nonsmooth contours are an artifact of only having forty vector fields to compute the mean. However, some interesting observations can still be made. Separation of the ceiling boundary layer is evident near the isolator entrance. In fact, the mean flow is actually seen to be reversed with velocities up to -150 m/s. Near the floor, high speed flow is seen to enter the isolator. This is most likely due to the separation of the ceiling boundary which causes high-speed fluid to be turned downward upon entering the isolator as seen in the schlieren image (arrow A). Near the isolator entrance, the high-speed fluid near the floor and reverse flow near the ceiling create a prominent shear layer near the transverse centerline. Proceeding downstream, the velocity field becomes much more uniform due to the high levels of mixing in this prominent shear layer.

3.8 LOWER-AMPLITUDE OSCILLATORY UNSTARTED FLOW

Another type of oscillatory unstarted flow was observed in the current model. As shown in Fig. 3.4, at a time of about 1.0 second the flap was slightly raised resulting in what is termed lower-amplitude oscillatory unstarted flow. The T7 pressure fluctuations of about 20 P_∞ that occur from about 1.0 to 1.3 seconds are lower than those observed during the high-amplitude oscillatory unstarted flow. Observations of downstream-view schlieren images (not shown here) appear to show downstream and upstream propagating compression waves. However, compared to the high-amplitude oscillatory unstarted flow, these waves appear much less frequently in the schlieren images. In addition, the waves are far less pronounced indicating they are weaker than in the high-amplitude case. Figure 3.31 shows the power spectra for T7, T2 and T1 for this unstarted flow mode. The highest peak and second highest peaks are seen to occur at f_1 = 84 Hz (f_1^*=0.076) and f_2 = 68 Hz (f_2^*=0.062) for both T7 and T2. To summarize, Table 1 gives the dominant frequencies for T7 and the corresponding *SPL* values for both oscillatory unstarted flow modes.

Table 3.1 Dominant frequencies and SPL for oscillatory unstarted flows at transducer T7

Amplitude	f_1, Hz	f_1^*, Normalized	*SPL*, dB
High-	124	0.11	186
Lower-	84	0.076	174

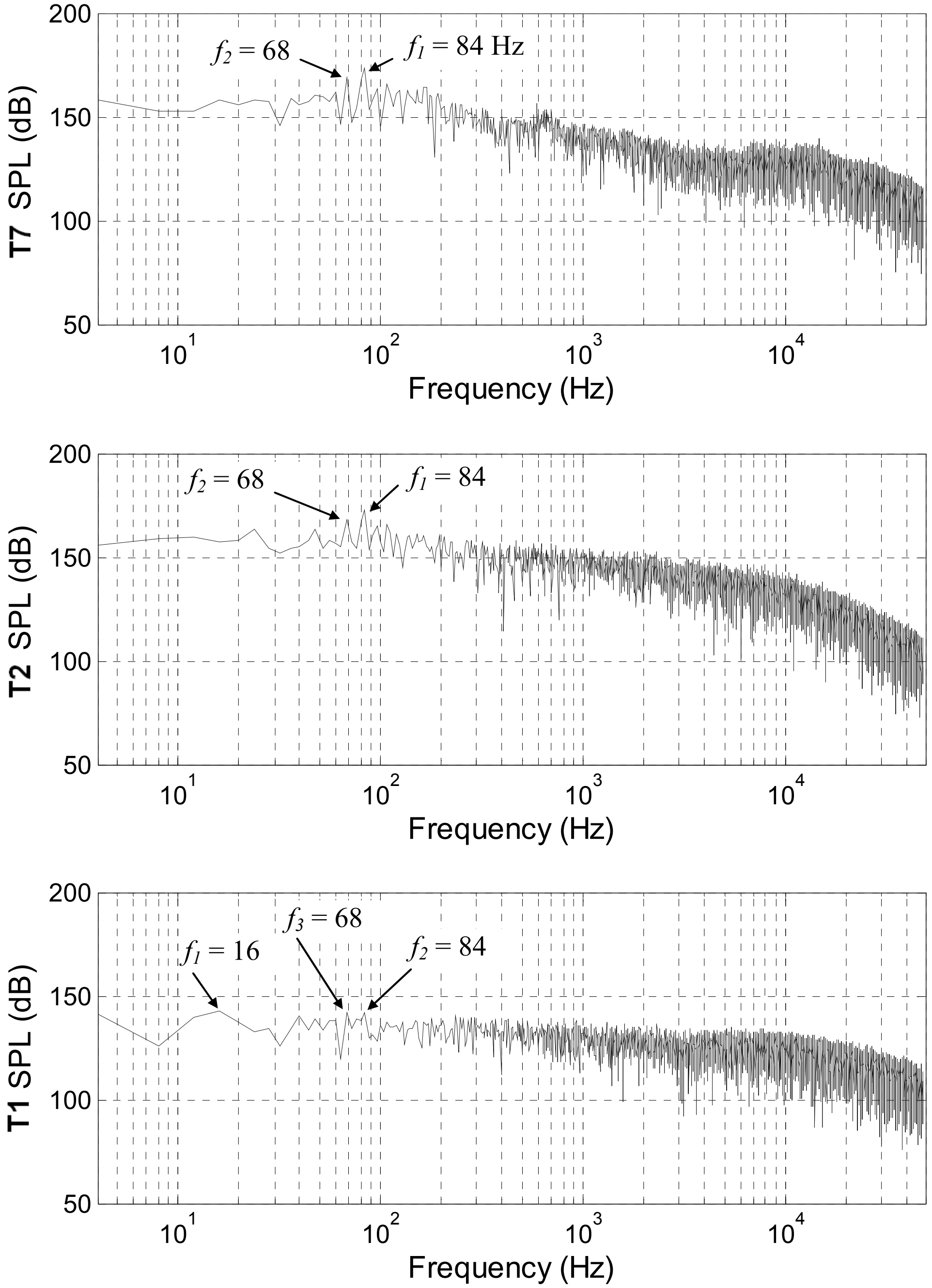

Figure 3.31 Power spectra of the pressure at T7, T2 and T1 for the lower-amplitude oscillatory unstarted flow.

For the lower-amplitude flow, the same frequency values were seen to correspond to the highest and second highest peaks for the spectra of T6-T3 (not shown here) as well. The spectra for T6-T3 are similar to that of T7, but the *SPL* level decreases for upstream transducers. For example, the highest peak *SPL* value is 174 dB for T7 and 164 dB for T3. As seen in Fig. 3.31, the T2 *SPL* peak of 173 dB is close to that of T7. (This was not the case in the high-amplitude oscillatory unstarted flow for which the T2 *SPL* peak was lower than those of T7-T3.) T1 has a peak *SPL* value at f_1 = 16 Hz (f_1^*= 0.015). The second and third highest peaks occur at f_2 = 84 Hz (f_2^*=0.076) and f_3 = 68 Hz (f_3^*=0.062). The mean pressure and *RMS* pressure distributions for this flow are shown in Fig. 3.32.

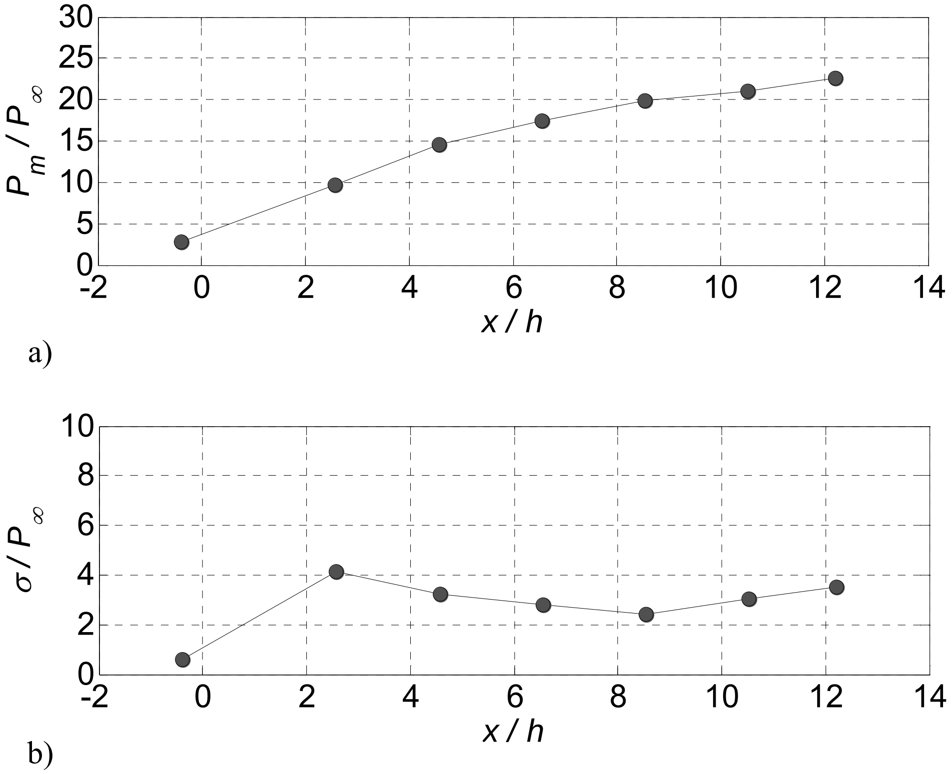

Figure 3.32 Lower-amplitude oscillatory unstarted flow: a) mean pressure distribution and b) pressure standard deviation distribution.

The mean isolator pressure distribution for the lower-amplitude unstarted flow is higher than that of the high-amplitude case shown in Fig. 3.23. The *RMS* pressure distribution exhibits a maximum at T2 located just inside the inlet portion of the model. This indicates that streamwise oscillations of the unstarted shock system occur close to T2 near the inlet entrance. Although not shown here, schlieren images for this flow did not contain entirely quiescent flowfields like that seen in Fig. 3.21b. Rather, some visible flow structures were always present at the isolator entrance, even at times when the isolator pressure distribution was near a minimum. This indicates that the shock upstream of the inlet (the leading shock) did not propagate as far upstream as in the high-amplitude case. In addition, since the schlieren images of this unstarted flow always showed the presence of visible flow structures at the isolator entrance, this indicates that the flow within the isolator may be on average faster than for the high-amplitude case. This could perhaps be an explanation of the lower frequency observed for this unstarted flow. Of course, further clarification would be given with PIV data. However, PIV data of this flow was not acquired in this study.

3.9 HIGH-COMPRESSION SHOCK SYSTEMS

3.9.1 T7 Pressure Time History during the Formation of Weak and Strong-compression Shock Systems

As previously discussed in section 3.2, it was not possible to set up (form) a stationary high-compression system in the isolator analogous to that which may be found in a dual-mode engine isolator by raising the flap alone. Rather, the only non-transient flow that could be generated by raising the flap in the current model of discussion was a fully supersonic flow in most of the isolator with a detached shock upstream of the raised flap (e.g, section 3.1). Near the flap position of 27 degrees, unstart would occur and was suggested to be due to strong shock-induced separation near the isolator exit in the vicinity of the flap. However, it was possible to lower the flap and set up a stationary high-compression shock system within the isolator. This amounted to restarting the model, but not to the fully supersonic condition discussed above.

Figure 3.33 shows the T7 pressure time history corresponding to a run in which the flap was lowered to form high-compression shock systems in the isolator. At about 0.25 seconds, unstart is seen to occur followed by high-amplitude oscillatory unstarted flow. The flap is then instructed to begin lowering at the time of about 0.35 seconds. The lowering of the flap can be seen to alter the characteristics of the unstarted flow. In particular, note the high-amplitude oscillations disappear as the flap is lowered. Then at a time near 0.55 seconds the flap reaches a constant angle, θ_F of about 17.4 degrees. Near this time, the inlet / isolator restarts, but to an elevated T7 pressure compared to that when the flap is fully down. This flow is termed to be the "weak-compression shock system." Note that the flap angle required to set up this compression system was not entirely repeatable. On some runs for the same angle, the flow was seen to restart to the fully supersonic started flow and on other runs it was seen to remain unstarted. On other runs which will be discussed, the angle required to set up a weak-compression system was seen to vary by over a degree. After the inlet / isolator restarted to the weak-compression shock system mode, the strength of the compression shock system could be increased by raising the flap. This is seen in Fig. 3.33 at the time of about 0.75 seconds. At this time, the flap is raised to an angle of about 20.6 degrees which results in an increase in T7 pressure to about 12.5 P_∞. This flow is termed to be the "strong-compression shock system." Furthermore, Figure 3.33 shows that about 1.7 seconds, the flow unstarts. This is the result of the flap being raised to the angle of about 21.0

degrees. The time for the flap angle θ_F to go from 20.6 to 21.0 degrees is about 40 ms. It is interesting to note the lack of high-amplitude oscillations after unstart in comparison to those that were always seen after an unstart event from the fully supersonic flow.

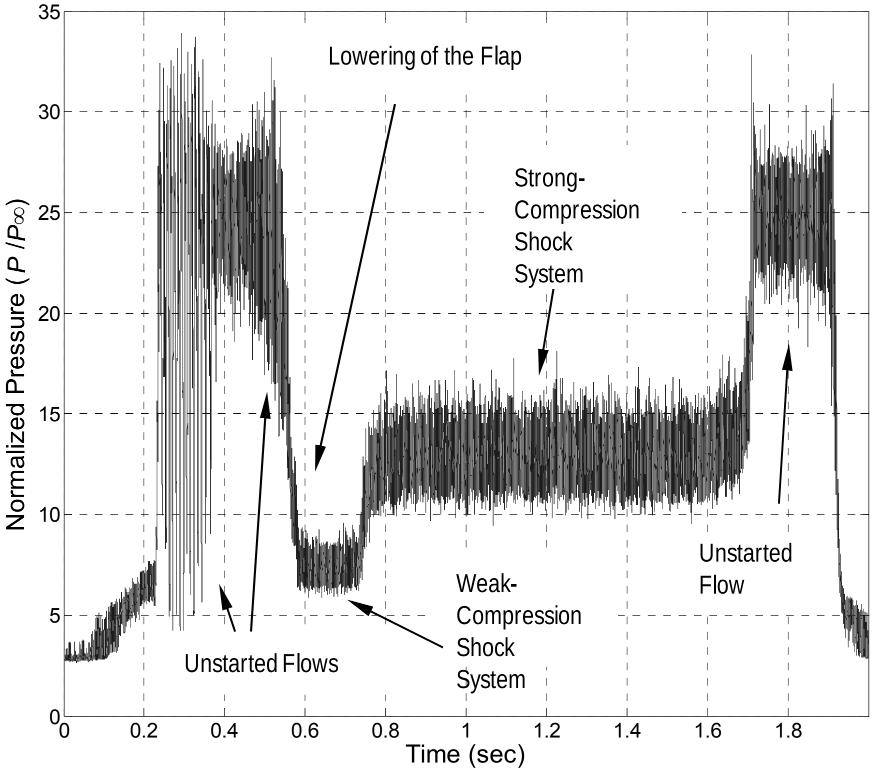

Figure 3.33 T7 Pressure time history demonstrating the lowering of the flap to obtain high-compression shock systems within the isolator.

3.9.2 Schlieren and Pressure Measurements

Figure 3.34 shows a schlieren image corresponding to the weak-compression shock system labeled in Fig. 3.33. The head of this system consists of a strong leading shock (arrow A) that is seen to intersect the floor at about $x/h = 8$. Note the lack of an obvious reflection of this shock off of the ceiling indicates that the flow behind the shock is predominantly subsonic. Moreover, note that the flow structure of this compression system is very similar to that seen at the unstart time of $t = 2.9$ ms in Fig. 3.9b. This observation suggests that at certain times in the process, the flow structure of unstart might be consistent with that seen in high-compression shock system flows. The obvious difference here is that during unstart, the compression system is transient in response to flap.

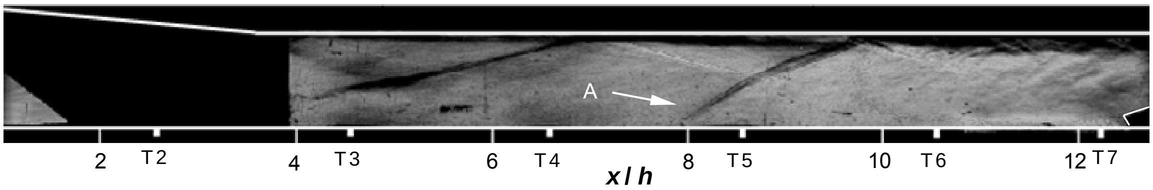

Figure 3.34 Schlieren image, obtained with a horizontal knife edge, showing the weak-compression shock system ($\theta_F = 17.4$ degrees).

Figure 3.35a gives the mean pressure distribution corresponding to the weak-compression shock system. In comparison to the started flow, the pressure at T5 (x/h = 8.54) through T7 (x/h = 12.21) has increased. The T7 pressure of about 7.5 P_∞ is nearly double that of the fully supersonic started flow. In addition, the *RMS* pressure plot of Fig. 3.35b, shows the compression system significantly increases the pressure fluctuations. Furthermore, although not shown here, power spectra did not show any dominant frequency peaks that would be indicative of an oscillatory flow.

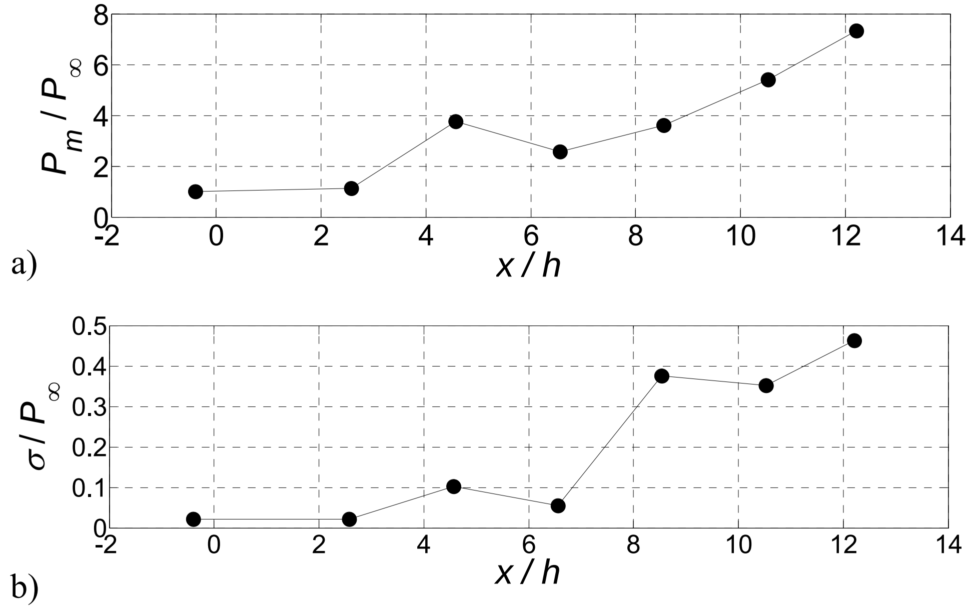

Figure 3.35 Weak-compression shock system: a) mean pressure distribution and b) pressure standard deviation distribution (θ_F = 17.4 degrees).

A schlieren image corresponding to the strong-compression shock system is shown in Figure 3.36. This system consists of two strong shocks. One shock (arrow A) intersects the floor at about *x/h* = 6.5 near T4. The second shock (arrow B) is associated with the high level of ceiling boundary layer separation seen in the image. Moreover, note that the first reflection of the compression ramp shock (arrow C) is unaltered in the upstream portion of the isolator. Note that the flow structure of this high-compression shock system is similar to that seen during unstart (Fig. 3.8d). The separation of the ceiling boundary layer due to the strong-compression shock system highly resembles that seen at times when the unstart shock system in near a similar location. Finally, as will be discussed in section 3.10, a further increase in flap angle results in unstart.

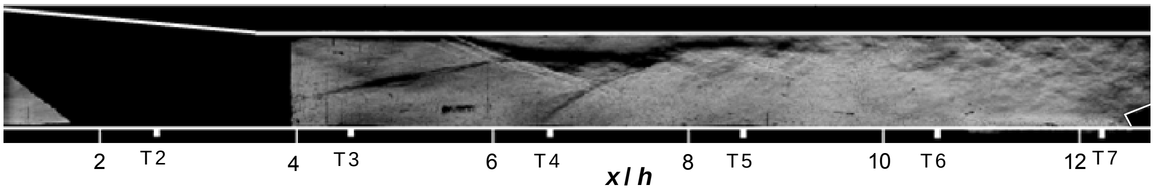

Figure 3.36 Schlieren image, obtained with a horizontal knife edge, showing the strong-compression shock system (θ_F = 19.2 degrees).

Figure 3.37 shows the mean (P_m) and *RMS* (σ) pressure distributions corresponding to the strong-compression shock system. In comparison to the started flow, the pressure at T3 (x/h = 4.57) through T7 (x/h = 12.21) is seen to have increased. Note the pressure at T7 of about 13 P_∞ is nearly double that of the weak-compression shock system. Figure 3.37b shows that other than at T4 (x/h = 6.56), the pressure fluctuations increase with distance. This is likely due to the fact that the pressure also increases with distance. To demonstrate this, Fig. 3.37c shows the σ / P_m distribution. The relatively constant values of σ / P_m at T5 (x/h = 8.54) through T7 suggest that the increased pressures at the more downstream transducer locations are partly responsible for the increase in pressure fluctuations. Figures 3.37b and 3.37c show the pressure fluctuations to be significantly higher at T4 compared to T5. This goes against the overall trend of increasing *RMS* pressures with increasing distance. The reason for the increased T4 fluctuations is as follows. Inspection of the schlieren image of Fig. 3.36 shows that the floor separation shock (arrow A) resides near the T4 location. Although not shown here, the high speed imaging showed the floor separation shock to be unsteady with streamwise excursions occurring near T4. It is likely that these streamwise fluctuations near T4 resulted in an increase in pressure fluctuations. This assertion is supported by the experimental work of Le et al. (2006 and 2008). They also reported an increase in *RMS* pressure when the leading edge of a high-compression shock system (in their case a shock-train) was near a given pressure transducer location. Finally, it is noted that similar to the weak-compression case, dominant frequency peaks consistent with an oscillatory flow were not measured for this strong-compression shock system.

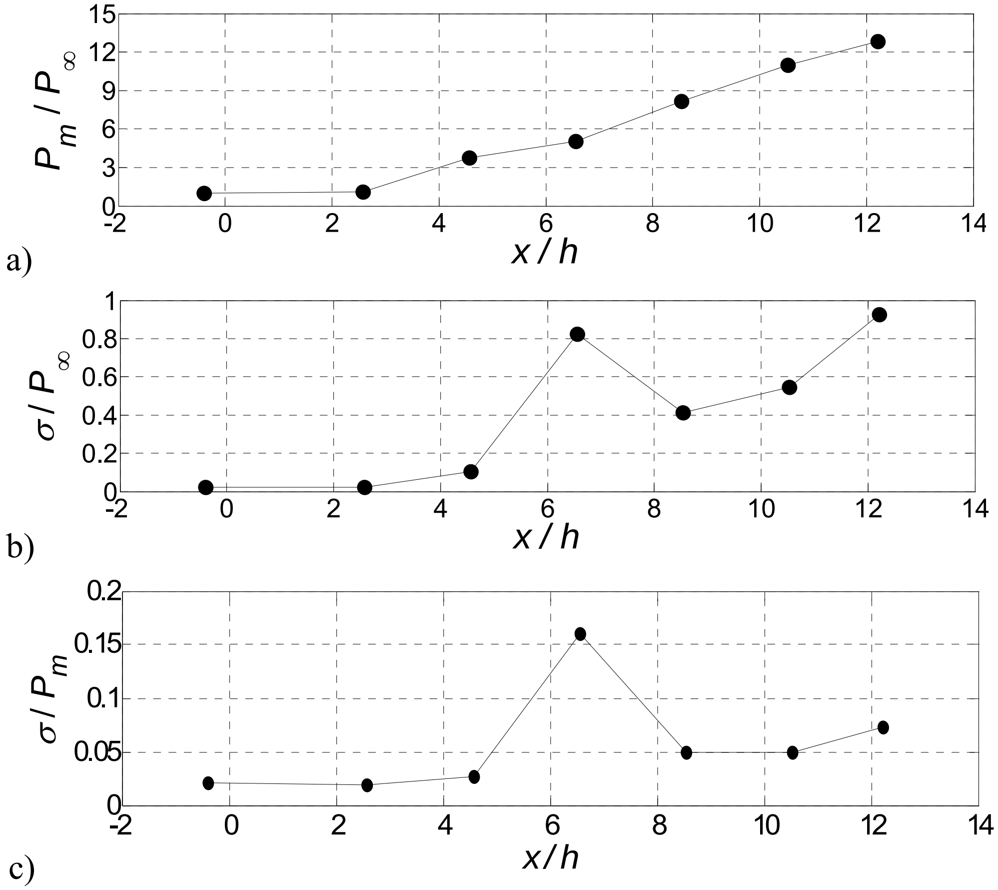

Figure 3.37 Strong-compression shock system: a) mean pressure distribution (P_m), b) pressure standard deviation distribution (σ), and c) σ / P_m distribution (θ_F = 19.2 degrees).

3.9.3 Side-View PIV Measurements

In this section, PIV results are presented for the strong-compression shock system. Similar to the unstart shock system (e.g., See appendix C), the strong-compression system was seen to dramatically change the seeding downstream of the floor and ceiling separation shocks that march the upstream boundary of the system. Particle accumulation was a problem in all PIV tests of this work due to the fact that the isolator sidewalls contained four surfaces for potential accumulation and the tunnel sidewalls contained two more. However this particle accumulation was especially prevalent on the inner sidewall surfaces during the strong-compression shock system experiments. The reason for this is the fact that a stationary shock system remained in the isolator and induced significant flow recirculation regions. In these separation regions, particles tended to accumulate relatively rapidly compared to the image acquisition rate of 10 Hz. The accumulation of too many particles resulted in sections of images being completely saturated, which obviously could not be remedied by sliding background subtraction techniques. In addition, accumulation in the recirculation regions adjacent to the ceiling was seen to attenuate the incoming laser sheet. To get adequate data for this flow, various seeding densities were tried. Recall that the PIV field of view was generated with three cameras. The upstream camera contained the floor and ceiling separation shocks of the strong-compression shock system and therefore the most significant flow separation and particle accumulation. For this field of view, a lower seeding level was used, which allowed for adequate correlations to be obtained without significant particle accumulation. However, using this same seeding level, the other two fields of view had particle densities too low for adequate correlation detection. Therefore, two other runs were used with higher seeding levels to obtain vectors in the fields of view corresponding to the middle and downstream cameras. On these two runs, the seeding level was increased to a point where the upstream camera field of view became unusable due to high levels of particle accumulation. The three different runs were then combined to produce the mean velocity fields shown in Fig. 3.38. The total number of image pairs

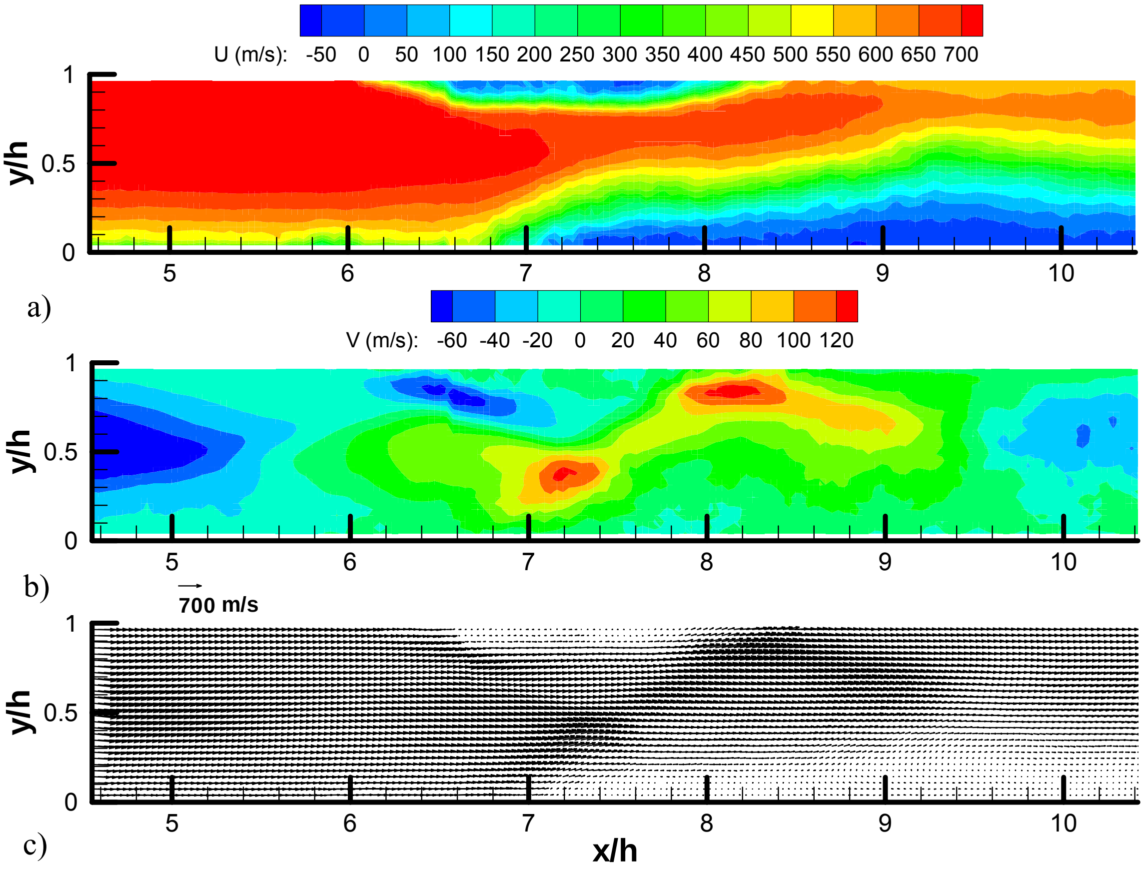

Figure 3.38 Strong-compression shock system PIV: a) mean (based on 90 vector fields) U contours, b) mean V contours, and c) mean vector field ($\theta_F = 22.0$ degrees).

used per field of view was about 90. The percentage of valid vectors for the dataset is about 75%. Uncertainties for the mean data can be found in Appendix C (e.g., Fig. C.6). Figure 3.39 shows the mean and *RMS* isolator pressure distributions for the strong-compression shock systems corresponding to the PIV data of Fig. 3.38. This figure includes both the pressure data corresponding to the PIV data used to generate the upstream portion of the flowfield in Fig. 3.38, as well as the pressure data corresponding

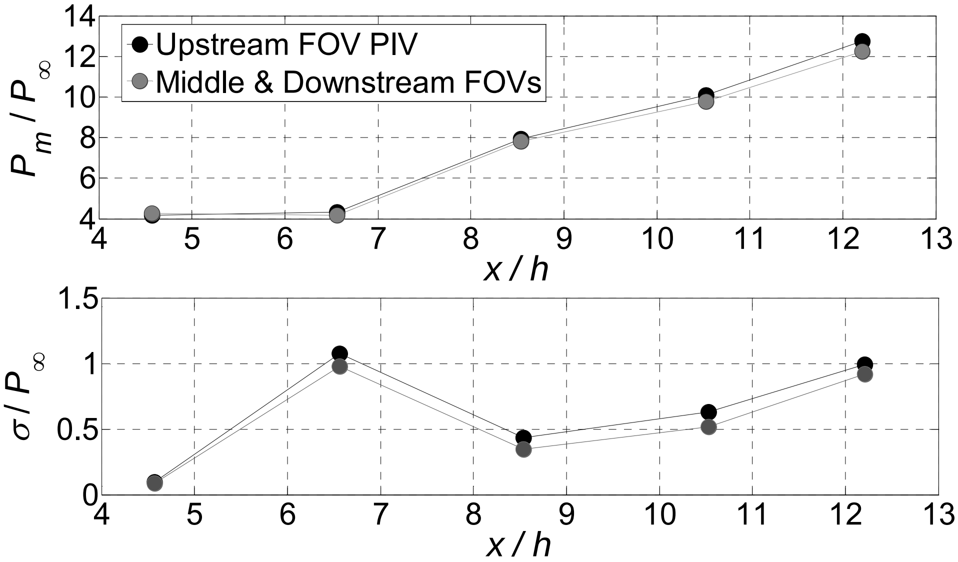

Figure 3.39 Strong-compression shock systems corresponding to the PIV data of Fig. 3.38: a) mean pressure distributions and b) pressure standard deviation distributions (θ_F = 22.0 degrees).

to the PIV data used to generate the middle and downstream portions of the flowfield in Fig. 3.38. Note that while small differences are seen between the mean pressure distributions, they fall within the uncertainty ranges given in Table 2.1. In order to form this compression system within the isolator, the model was first unstarted and the flap was then lowered to the angle of 19.2 degrees to obtain a weak-compression shock system. The angle to form the weak-compression system was seen to be nearly 2 degrees higher than that corresponding to the weak-compression system discussed in the section above. It was found for these PIV runs that lowering the flap to the same angle as in section 3.9.1 above, would result in a complete restart to the fully supersonic flow mode. This illustrates that the flap angles to obtain the high-compression systems were not entirely repeatable. In order to get the high-compression shock system corresponding to the current PIV data of discussion, the flap was next raised to an angle of 22.0 degrees. The same flap angle settings were used for each of the three runs used to generate the mean field of Fig. 3.38. Figure 3.38 shows the mean streamwise velocity, wall-normal velocity and velocity vectors corresponding to the strong-compression shock system. From the upstream edge of the field of view to the streamwise location of about *x/h* = 6, the flowfield is seen to be the same as that corresponding to the fully supersonic flow (e.g, compare to Fig. 3.3). Similar to the flow structure observed in the schlieren image of Fig. 3.36a, the presence of the high-compression shock system is first noticed in Fig. 3.38a at the isolator ceiling. Shortly downstream of the ceiling shock, the mean flow is seen to have velocities near 0 m/s and is clearly separated. Proceeding downstream, at the ceiling location of about *x/h* = 8.6 the boundary layer appears to reattach. The strong-compression shock system is seen to intersect the floor at the streamwise location of about *x/h* = 6.6. Shortly downstream of the floor shock, the mean flow is seen to be separated. Note this separation is strong enough to induce mean reverse flow with velocities of about -50 m/s near the floor. Again, note that the flow structure that can be inferred from the mean PIV data is consistent with that seen in the schlieren image of Fig. 3.36a.

Finally, the similarity in the flow structure seen in the mean strong-compression shock system to that seen during unstart at *t* = 4, 5, and 6 ms (Figs. 3.11b to 3.11d) is reemphasized here. This similarity of PIV data, in combination with the similarity of schlieren imaging, strengthens further the argument that the pseudo-sequences do in fact provide an accurate depiction of the flow structure during unstart.

3.9.4 Shock-Train (Pseudo-Shock) or Separation-Shock?

The flow structure of the high-compression shock systems do not appear to be consistent with that observed in previous studies of shock-trains (pseudo-shocks). For example, again refer to Fig. 1.4 taken from Matsuo et al. (1999). Note that this figure corresponds to a normal shock-train which tends to occur for isolator Mach numbers less than about 2 to 3 (Heiser and Pratt, 1994). At higher entrance Mach numbers, the isolator is typically seen to be that of an oblique shock-train (Heiser and Pratt, 1994 and Matsuo et al., 1999). However, the oblique shock-train is similar to that of Fig. 1.4, except a series of crossing oblique shocks forms the shock-train instead of a series of normal shocks. Upon inspection of Figs. 3.36 and 3.38, this series of shocks is clearly not present. Rather only two leading oblique shocks consisting of a ceiling separation and floor separation shock are present. This can hardly be called a shock-train. Perhaps, the fact that roughly 75% of the isolator entrance flow is boundary layer significantly alters the flow structure of the compression system. Although on the contrary, the experiments of Carrol and Dutton (1992) do not support this assertion. In their experiments, schlieren images showed a prevalent shock-train to exist even when the thickness of the ceiling and floor boundary layers added to be 50% of the total isolator height. However, it should be noted that this result was seen at an isolator entrance Mach number of 1.6. Furthermore, the boundary layers in their duct were symmetric, whereas in the current study this is not the case. The asymmetry of the incoming boundary layers does appear to affect the structure of the leading shocks of the high-compression shock system, but it does not explain why the isolator does not contain a series of shocks or a shock-train.

To resolve the questions of whether the strong-compression shock system could be considered a shock-train (pseudo-shock), the wall pressures were compared to equation 1.8, the well known correlation of Waltrup and Billig (1973 and 1993). Following the studies of Sullins and McLafferty (1992), Reinartz et al. (2003) and Wang et al. (2006), the upstream Mach number (M_1) was taken to be the stream-thrust-averaged Mach number, M_{sta}. The stream-thrust-averaged Mach number at the inlet entrance was computed using equations 1.9 to 1.11, the freestream conditions given in section 2.1.2

(M_∞ = 4.9 conditions) and the floor boundary layer properties given in section 2.2. The stream-thrust-averaged Mach number at the inlet entrance then computed to be 4.3, which was then used in equation 1.8. Note the possible effects of approximating M_{sta} upstream of the strong-compression system to be equal to that at the inlet entrance are addressed below. Figure 3.40 shows the average isolator pressure distribution corresponding to the three runs used for the mean PIV results. The uncertainties included in the plot were calculated based on the *RMS* values given in table 2.1 and the standard error (i.e., $\varepsilon = 2\sigma / \sqrt{n}$). The coarse placement of the pressure transducers did not allow for the exact location of the upstream boundary of the strong-compression shock system to be measured. In addition, since the upstream boundary did not coincide with a transducer location, the exact pressure just upstream of the compression system could not be determined. The following approach was therefore used to estimate the location and pressure just upstream of the compression system. The pressure measured at T4 (x/h = 6.56) was seen to be elevated due to the strong-compression shock system. However, note from Fig. 3.36 and Fig. 3.38 that the intersection of the floor separation shock appears to occur near the T4 location. It was therefore decided that the best option for estimating the pressure just upstream of the floor separation shock was to use the value that corresponded to the mean T4 pressure measured when the isolator flow was fully supersonic. In order to estimate the upstream boundary, the mean fully supersonic T4 pressure was then set to P_1 in equation 1.8. Finally, the pressure was plotted according to equation 1.8 with the origin at various streamwise locations in an iterative fashion. The upstream boundary location was then defined to be that at which the pressure predicted by equation 1.8 matched that measured at T4 in the case of the strong-compression shock system. In other words the origin of the correlation curve was translated iteratively until the measure T4 pressure matched the correlation-predicted-pressure. The approach just

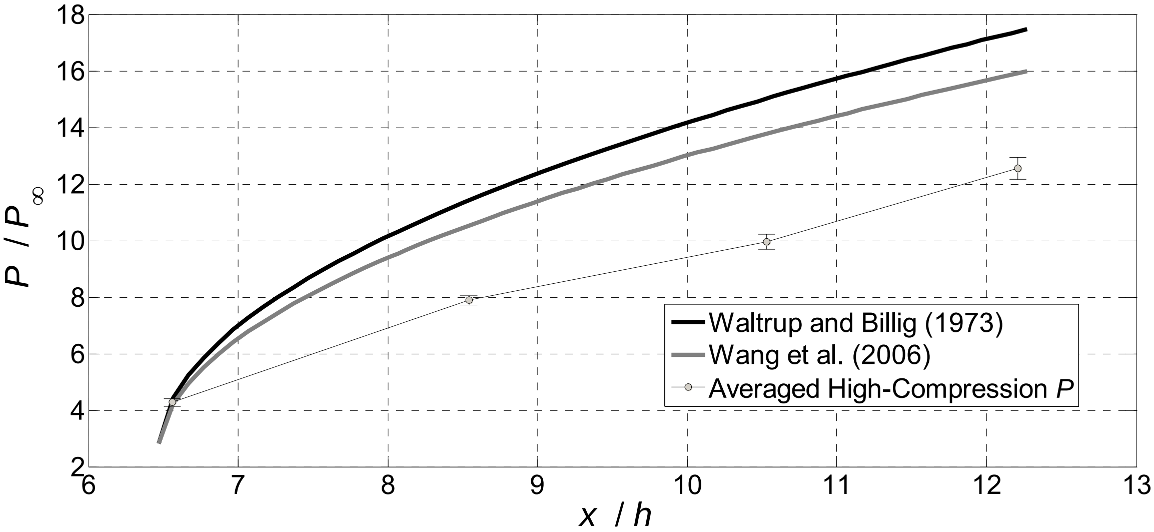

Figure 3.40 Comparison of the strong-compression shock system pressure distribution to that predicted by the pseudo-shock (shock-train) correlations of Waltrup and Billig (1973) and Wang et al (2006).

described forces the measured and correlation-predicted pressures to agree at *x/h* = 6.56. However, this allows for the measured mean pressure values downstream of T4 to be compared to the correlation. From inspection of Fig. 3.40, it is evident that equation 1.8 over predicts the pressures of the strong-compression shock system by about 40%. As mentioned above, the M_{sta} at the inlet entrance was used rather than that at the upstream boundary of the strong-compression shock system. However, around the approximate upstream boundary location, the upstream flow is seen to be similar to that observed in PIV of the test section flow with no model. Therefore, this approximation is not expected to be too far off. Still as a test and to get a more concrete answer, M_{sta} was varied until the point where equation 1.8 most closely matched the measured wall pressure distribution. It was seen that this corresponded to a stream thrust average Mach number of about 3 which is significantly lower than 4.3. Therefore, it is unlikely that the approximation for M_{sta} is responsible for the disagreement between the measured wall pressures and those predicted by equation 1.8.

As previously mentioned, Wang et al. (2006) also reported lower wall pressures than those predicted by the Waltrup and Billig correlation. They suggested that using equations 1.12 and 1.13 in combination with $\alpha = 0.3$, would give better agreement than equation 1.8. In the limit of the ceiling boundary layer momentum thickness going to zero in equation 1.12, the asymmetry parameter, D_θ, equals unity. This limit is appropriate in the current case, where the floor boundary layer is much thicker than the ceiling boundary layer. Using D_θ equal to unity and equation 1.13, the predicted pressure distribution was then calculated and plotted as seen in Fig. 3.40. Although this suggested correlation gives better agreement than equation 1.8, the measured pressure at T7 is still seen to be over predicted by about 30%.

The combination of the flow structure and pressure distributions measured in the strong-compression shock system suggests that this flow is not the classical shock-train (pseudo-shock). It is possible that the strong-compression shock system is the separation-shock mode described by Penzin (1998). This would be consistent with the lower pressure distribution of Fig. 3.40, since the separation-shock mode is known to require longer ducts for an equivalent pressure increase. However, according to Equation 1.14 and taking M_1 to be M_{sta}, the separation-shock mode should occur for an isolator aspect ratio greater than three. In the current work the aspect ratio is two. On the other hand, the computational study of Nedungadi and Van Wie (2004) suggested that the separation-shock occurred for Mach number and aspect ratio combinations that were supposed to give the pseudo-shock mode according to Penzin. In addition, it is interesting to note that some similarities are seen between the current work and in the separation-shock mode computed by Nedungadi and Van Wie for an inflow Mach number of 4 and an aspect ratio of 2.5. For these flow conditions, a region corner flow separation occurred that did not reattach. The corner separation was seen to occur near the surface containing a thick boundary layer that was 25% of the duct height. The PIV data of Fig. 3.38 also show a separated floor boundary layer that does not reattach. While the above discussion suggests that the strong-compression shock system does not contain the classical shock-train, it can only be suggested that the mode is instead that of the separation-shock. Since the pressure at a given streamwise location has been measured to vary along the cross-section in a distinct fashion (Penzin, 1998), wall pressure measurements along the other four walls could help prove or disprove this possibility. However, further evidence that the strong-compression shock system may be of the separation-shock form is given if the displacement thickness of the thick floor boundary layer is considered. Specifically, if the floor boundary layer displacement thickness, δ^* of 9.1 mm (Barter, 1996) is subtracted from the isolator height, the aspect ratio becomes 3.1. Recall that in comparison to an incompressible boundary layer, in a compressible boundary layer, the displacement thickness can be a much larger fraction of the boundary layer thickness owing to the fact that the density decreases as the distance away from the wall decreases. Using the aspect ratio of 3.1, which accounts for displacement thickness effects, Equation 1.14 predicts that the high-compression system should be of the separation-shock form.

3.10 UNSTART FROM THE HIGH-COMPRESSION SHOCK SYSTEM MODE

This section discusses unstart of the inlet / isolator model from the high-compression shock system mode. Again, the T7 pressure increase during unstart can be seen at about t = 1.7 seconds in Fig. 3.33. Similar to that observed in unstart from the fully supersonic started flow, unstart was seen to progress upstream with increasing separation of the isolator ceiling boundary layer. However, both the schlieren imaging and pressure measurements showed this unstart process to contain oscillations. The schlieren images showed streamwise oscillations of the unstart shock system occurred with the oscillation of the separation point of the ceiling boundary layer. Recall that during all of the unstart events of Fig. 3.7a, one oscillation was seen to occur. Again, in Fig. 3.10, an example of this oscillation is clearly seen in the T1 time history from 8.4 to 10.4 ms. Similar oscillations in T1 pressure were also observed for the unstart events from the strong-compression shock system mode. However, more oscillations occurred during unstarts from this mode. The number of oscillations seen in the T1 time histories for these unstart events varied from about 2 to 4. Figure 3.41 shows the pressure time histories of all seven transducers during unstart from the strong-compression shock system flow. The unstart event of Fig. 3.41 is the same as in Fig. 3.33. The $t = 0$ point of the plot was chosen to correspond to the time when the T7 pressure increased above the fluctuations of the strong-compression shock system. At about $t = 16$ ms, the unstart shock system causes a distinct increase in pressure at T3 ($x/h = 4.57$) near the isolator entrance. As part of an oscillation, the pressure then decreases back to the level prior to unstart at about $t = 17.5$ ms. At about 19 ms, the pressure at T3 once again increases which indicates the unstart shock system is once again propagating upstream. Similar oscillations can be seen in the inlet pressure time histories of T2 and T1. Note that two oscillations about T1 are clearly evident. T1 is first crossed at $t = 21.5$ ms, but oscillations in T1 occur until the time of about 26 ms. After this time, the unstart shock system is seen to remain upstream of T1 ($x/h = 0.4$). Furthermore, it is interesting to note that the unstarted flow does not contain the high-amplitude oscillatory fluctuations that were always seen to occur after unstart from the fully supersonic flow mode. From the T1 time history of Fig. 3.41, it is estimated that the T1 oscillations occur with a period of 2.4 ms, which corresponds to a frequency of about 420 Hz. Using the period of the T1 oscillations for other unstart events showed T1 oscillation frequencies to lie in

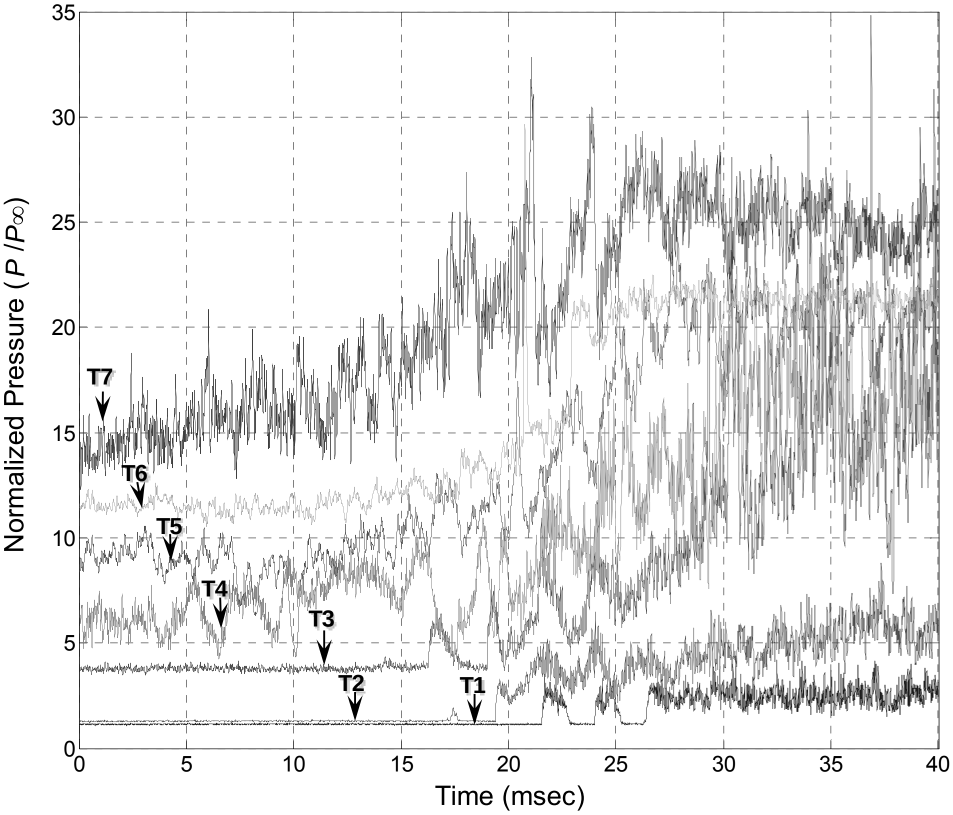

Figure 3.41 Pressure time histories obtained at T1 – T7 during the unstart event from the high-compression shock system mode of Fig. 3.33.

between 330 and 430 Hz (f^{*}= 0.30 to 0.39). Note that this range of oscillation frequencies lies in between the frequency of an ideal quarter- and half-wave resonator. Therefore, unstart from this mode could be dependent on acoustic mechanisms. In addition, the propagation velocity of the unstart shock system was seen to be significantly lower for this type of unstart. Table 3.2 gives a comparison of average unstart propagation velocities in the inlet for the two different types of unstart discussed thus far. The timescales and velocities for unstart from the high-compression mode are based on 7 samples. Again, the transducer crossing time that was used to get the time spent between transducers was defined as the time for which the pressure first increased above pre-unstart fluctuation levels. Table 3.2 shows that unstart in the inlet occurs about three times slower from the high-compression mode (compared to unstart from the fully-supersonic mode). Differences in the unstart propagation velocities are attributed to the fact that unstart was initiated in different ways for the two different flow modes. In the fully supersonic started flow case, unstart occurred after the flap reached an angle of 26.6 ± 0.6 degrees and was seen to be associated with a high amount of shock-induced separation near the isolator exit. In the current case, the flap is brought to the angle of 20.6 degrees prior to unstart. Unstart then occurs while the flap is being raised slightly to the angle of 21.0 ± 0.6 degrees. Thus, the lower unstart propagation in the current case may be related to the fact that the flap creates a smaller disturbance compared to that created during the unstart from the fully supersonic flow case. Specifically, the amount of flap blockage is lower.

Table 3.2 Comparison of average unstart propagation velocities in the inlet for unstart events from the fully-supersonic mode and for unstart events from the high-compression mode

Flow Type Prior to Unstart	Δt (T3-T1), ms	$V_{\text{T3-T1}}$
Unstart from the fully supersonic started flow mode	1.7 ± 0.2	74 ± 7
Unstart from the high-compression shock system mode	5.3 ± 2.1	24 ± 12

3.11 TRIPPED INLET BOUNDARY LAYER EXPERIMENTS

For the previous experiments reported, the sidewall and ceiling boundary layers developed and transitioned naturally. The current section focuses on unstart events in the

6-degree inlet / long-isolator where the sidewall and inlet ceiling boundary layers were tripped. Sand was used as the roughness element that induced transition. The sand was filtered through a wire mesh screen filter until it was determined to be close to the size of that adhered to 60 grade sandpaper. The filtered "60 grade sand" was then mixed with epoxy and applied to the internal inlet walls. The strips were applied to have a streamwise width of about 6.4 mm (0.25 in). The strips spanned the entire width of the ceiling and the entire height of the sidewalls. The trip leading edges were placed 12.7 mm (0.5 in) downstream of the leading edges of each inlet wall. The trips were placed parallel to the leading edges of their corresponding walls. The last row shows the average unstart propagation velocity in the model corresponding to a tripped inlet. The results show that the adding the trips to the inlet lowers the unstart propagation velocity further by about 40%.

Table 3.3 Comparison of average unstart propagation velocities showing the effects of boundary layer trips and paint in the 6-degree inlet / long-isolator model

Inlet Conditions	$V_{\mathrm{T6\text{-}T1}}$, m/s	$V_{\mathrm{T6\text{-}T1}}$, normalized
6-degree baseline	37.8 ± 2.3	0.0511 ± 0.0031
6-degree with trips	22.3 ± 1.0	0.0297 ± 0.0013

In order to understand better how the boundary layer trips affect the unstart process, the average velocity distributions corresponding to the two different inlet conditions above are plotted below in Fig. 3.42. The velocity reported in the downstream section of the isolator at $x/h = 9.54$ (between T6 and T5) is lower for the case of the inlet with boundary layer trips. However, it is noted that the uncertainty bands at this location are close to overlapping. At $x/h = 7.55$ (between T5 and T4), the velocities of both cases are similar to within the uncertainty bands. In contrast, clear differences in the upstream portions of the model can be observed. For example the velocity reported at $x/h = 4.57$

(between T4 and T2) is 50% lower in the case of the tripped and painted inlet. In addition, the velocity reported at x/h = 1.09 (between T2 and T1) is about 35% lower for the case with tripped boundary layers. This shows that the boundary layer trips result in a slower unstart process in the upstream portion of the isolator as well as in the inlet. This decreased unstart velocity is likely related to the fact that the tripped, turbulent boundary layers have fuller velocity profiles, which means that the unstart shock system has to propagate against an overall higher speed flow compared to the non-tripped case. This idea will be discussed further in the comparison of the unstart process in configurations with different inlet geometries.

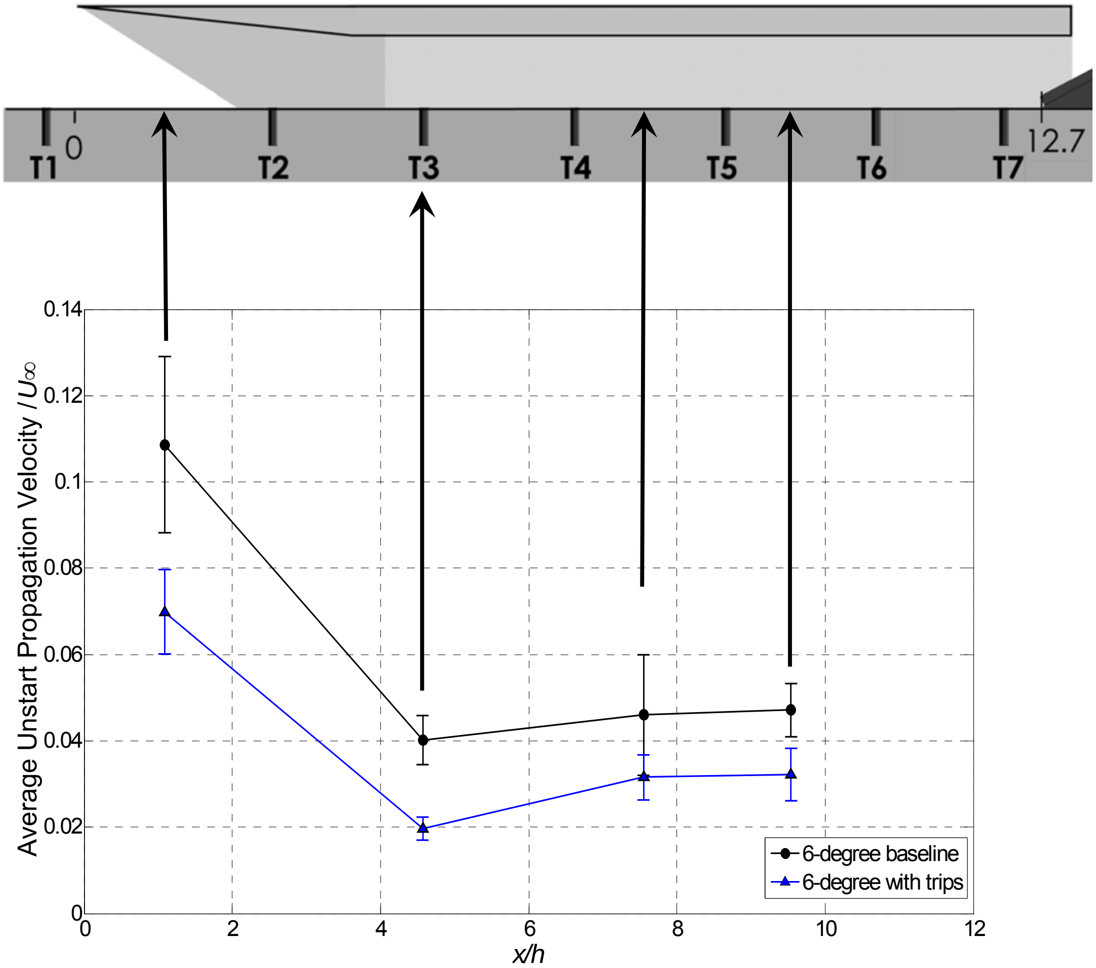

Figure 3.42 Comparison of the average unstart propagation velocities (normalized by U_∞) in the baseline 6-degree inlet / long-isolator to those in the 6-degree inlet / long-isolator containing inlet trips.

CHAPTER 4

4. Inlet Geometry Variations (0- and 8-degree Inlets)

Since the baseline case suggested that the flow structure and dynamics of the unstart process were dependent on inlet geometry, two different inlets were tested using the same isolator as that of the previous chapter. One of the new inlets tested contained an eight-degree compression ramp (e.g., See Fig. 2.9a) and the other contained no compression ramp (e.g., See Fig. 2.9b). Again, the no-compression ramp case is referred to as the zero-degree inlet. As will be discussed below, varying the inlet geometry was seen to change the unstart process, the resulting unstarted flow, and the capability of the model to contain a high-compression shock system (by lowering the flap). This chapter first presents results obtained with the zero-degree inlet, which is followed by results obtained with the eight-degree inlet. The flows in these models were characterized using fast-response pressure measurements and high-speed schlieren imaging. Finally, a discussion summarizing all three inlet / isolator combinations presented so far follows.

4.1 0-DEGREE INLET / LONG-ISOLATOR RESULTS

This model was studied to decouple the effects of inlet geometry on the unstart process and unstarted flows. More specifically, without an inlet, the fully supersonic started flow lacked the oblique shock and expansion reflections that existed in the 6-degree inlet / long-isolator model. Therefore, it was desired to study this model to compare results of a model without an inlet to the results obtained in models containing inlets.

4.1.1 Fully Supersonic Started Flow (flap fully-down)

Figure 4.1 shows the mean (P_m) wall pressure distribution with the flap fully-down. Again all pressures reported herein are normalized by that measured at T1 which is taken to be P_∞. Again, the T1 pressure corresponding to each figure, as well as the other selected run conditions are given in Tables A.1 and A.2. In addition, note that in the results reported in this chapter, the T3 pressure fluctuations are not given. This is due to the fact that this transducer lost its frequency response. This was most likely a result of an accumulation of PIV particles clogging the transducer during the runs corresponding to the data of the previous chapter. The mean pressures at T3 are reported since with enough time, the pressure was seen to reach a constant value. Also, note the T6 signal was seen to give non-physical negative pressure values for the 0-degree inlet model fully supersonic flow. The reason behind these non-physical values was suspected to be a voltage zero shift that occurred during the run possibly due to loose electrical connections. Owing to this zero shift, the mean pressures at T6 are not reported in this chapter. However, the T6 fluctuations were not affected by the shift and are therefore reported. The mean distribution for the 0-degree inlet model of Fig. 4.1 shows that the wall pressure increases with streamwise distance into the isolator. This increase in pressure is likely due to viscous effects (i.e., boundary layer growth).

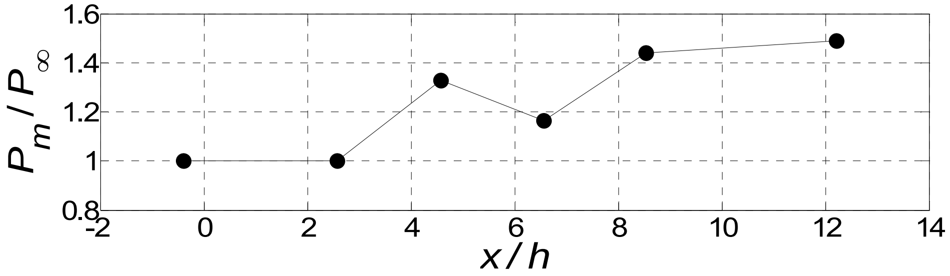

Figure 4.1 0-degree / long isolator fully supersonic started flow mean pressure distribution.

4.1.2 T7 Time History During Unstart and Unstarted Flow

Figure 4.2 shows the pressure time history measured at T7 for a flap sequence that resulted in unstart, unstarted flow and restart. As seen in Fig. 4.2, from 0 to about 0.35 seconds, the flap is down and the pressure is constant. At about 0.35 seconds, the flap begins to rise. Next, at about 0.46 seconds, a rapid increase in pressure is observed which corresponds to the unstart of the model. The angle seen to induce unstart 24.3 degrees. However, for the particular run shown, the flap was brought to a final angle of about 27 degrees. Following unstart, T7 pressure fluctuations up to about 15 P_∞ are observed. As will be shown, this unstarted flow was seen to be non-oscillatory. Finally, at about 0.9 seconds, the flap is lowered resulting in a full restart of the model.

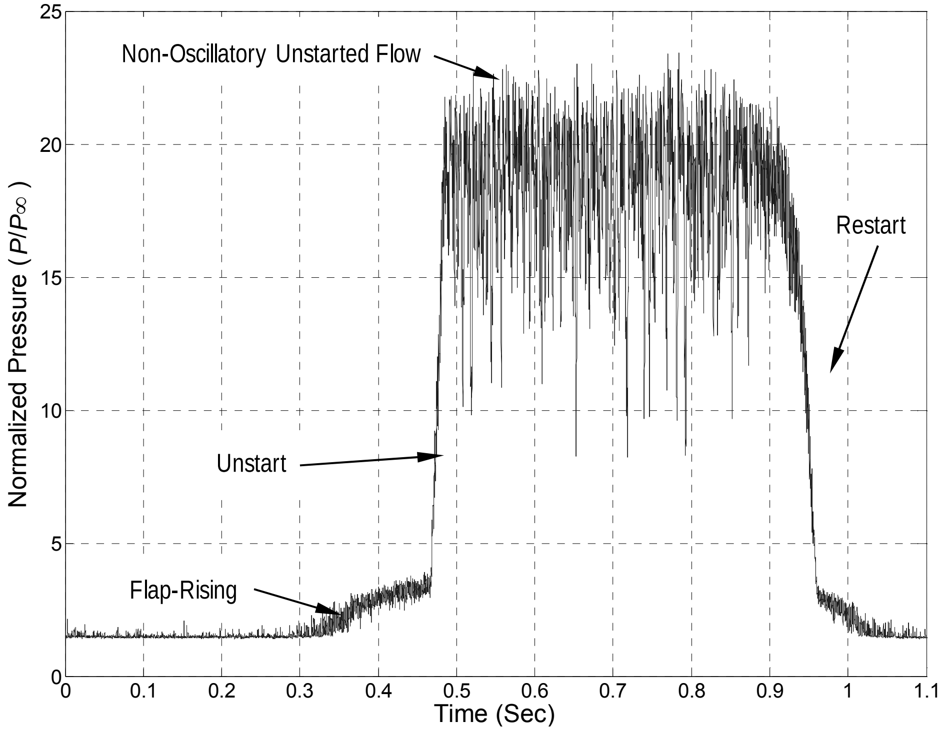

Figure 4.2 0-degree inlet / long isolator pressure time history corresponding to inlet unstart, unstarted flows and restart processes obtained at T7.

4.1.3 Unstart Dynamics and Flow Structure

4.1.3.1 High-Speed Schlieren and Simultaneous Pressure Measurements

This section focuses on the unstart process in the zero-degree inlet / long-isolator model. Figure 4.3 gives a series of schlieren images (obtained using a horizontal knife edge) corresponding to the same unstart event seen in Fig. 4.2. In the same fashion of that of the previous chapter (e.g., see section 3.5.1), the schlieren imaging was used to determine the onset of unstart (t = 0). In addition, Fig. 4.4 gives the accompanying pressure time histories at T7-T4, T2 and T1. T3 is not included due to the lack of frequency response mentioned above. The schlieren image of Fig. 4.3a was acquired at a time prior to the onset of unstart. Up until the streamwise location of x/h = 4, the image is seen in shadow which is a result of the aluminum inlet. At this location, a wave (arrow A) is seen to emanate from the ceiling. This wave is a result of a slight step between the inlet and isolator junction. The inclination angle of the wave indicates it is a Mach wave. In addition, the development of the ceiling boundary layer (arrow B) is apparent in the image. At the exit of the isolator, the raised flap is seen to result in the detached flap shock (arrow C). Note that the flap shock appears to be exiting the isolator without ceiling impingement. The unstart process is seen to occur when flap is raised to an angle great enough to result in an impingement of the flap shock on the isolator ceiling. When this occurs, the boundary layer separates and unstart ensues. Recall that the initiation of unstart with ceiling boundary layer separation was also observed in the 6-degree inlet case. It is interesting to note that the flap angle required to induce unstart for the no-inlet case of 24.3 degrees is lower than the corresponding 6-degree angle of 26.6 degrees. This means that the contraction ratios required to induce unstart in the 0- and 6-degree models are 1.27 and 1.81, respectively. (Recall that the exit blockage can be found using Fig. B.3 and that the 6-degree model has contraction in the inlet as well as the isolator

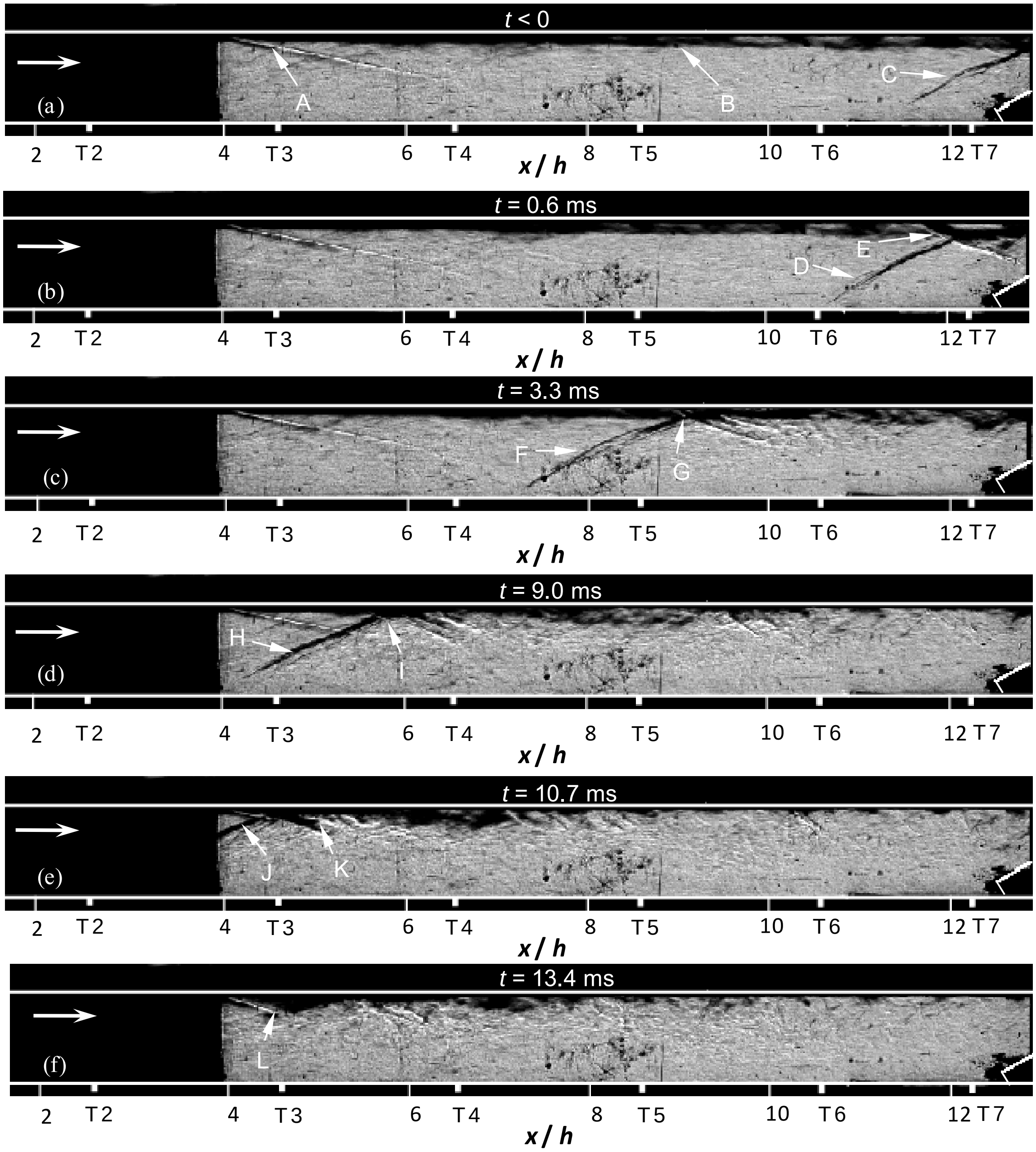

Figure 4.3 Schlieren of the unstart process in the 0-degree inlet / long-isolator at times: a) $t < 0$, b) $t = 0.6$ ms, c) $t = 3.3$ ms, d) $t = 9.0$ ms, e) $t = 10.7$ ms, and f) $t = 13.4$ ms, ($\theta_F \approx 27$ degrees).

exit.) Compared to the 0-degree model, the contraction ratio required to induce unstart is about 40% higher in the 6-degree model. Since the flow at the isolator exit is expected to have a higher Mach number for the 0-degree inlet / isolator, this also means that the flap shock wave boundary / layer interactions should be stronger in this case. If the interactions are stronger this implies separation (viscous blockage) will occur for lower flap angles, which may then explain the lower unstart contraction ratio of the 0-degree case. Figure 4.3b, taken at *t* = 0.6 ms, shows the beginning of the unstart process. The unstart shock system is seen to be a combination of the detached flap shock (arrow D) and the separation shock created by its ceiling impingement (arrow E). Between *t* = 0.6 and 3.3 ms (Fig. 4.3c), the unstart shock system propagates upstream maintaining a relatively constant flow structure. The unstart shock system is still seen to consist of a "leading shock" that resembles the detached flap shock (arrow F) and a separation of the ceiling boundary layer due to the impingement of this shock (arrow G). Note that downstream of the impingement point, visible flow structures (apparently eddy shocklets) are observed which indicate that the flow near the ceiling remains supersonic. Furthermore, Fig. 4.4 shows the pressure has increased at T5-T7 with the upstream propagation of the unstart shock system. At *t* = 9.0 ms (Fig. 4.3d), the unstart shock system has propagated to near *x/h* = 4. Its flow structure is seen to remain the same with the leading shock (arrow H) intersecting the ceiling at about *x/h* = 6 (arrow I). Again, downstream of the ceiling impingement point the flow appears to be separated. Also, there still appears to be supersonic flow near the ceiling downstream of the impingement point as indicated by visible flow structures. Figure 4.4 shows that the pressure at T4 has more than tripled as a result of the propagation of the unstart shock system. The next schlieren image of Fig. 4.3e, is at a time when the unstart shock system has propagated into the aluminum "inlet" section. The leading shock (arrow J) is still seen to impinge on the ceiling (arrow K). Moreover, Fig. 4.4 indicates that the unstart shock system has passed the T2 location as seen by the pressure increase at *t* = 10.4 seconds. Finally, the

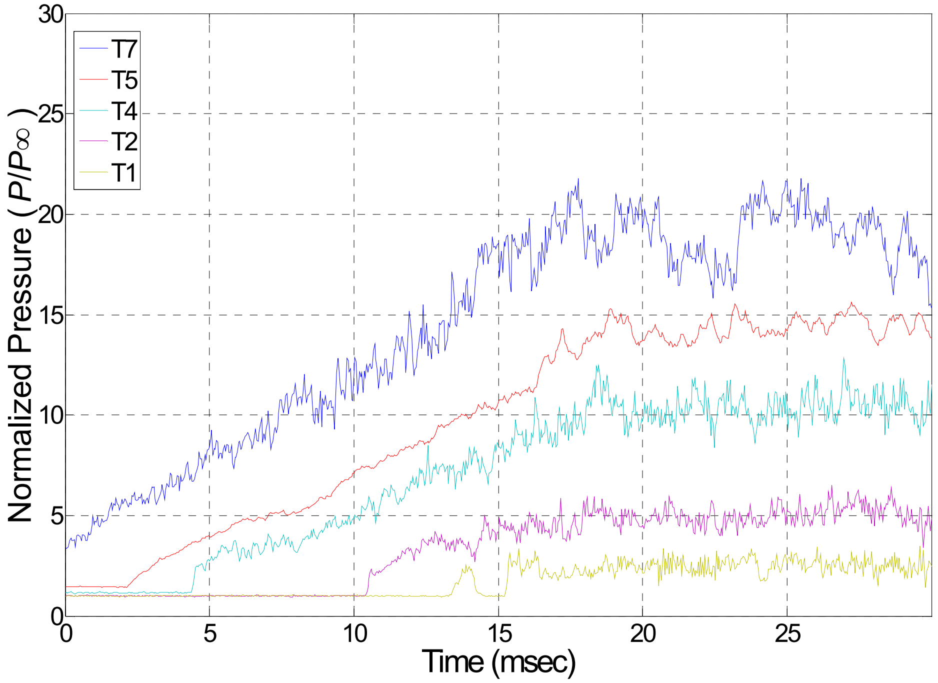

Figure 4.4 Pressure time histories obtained at T1 – T7 for the unstart event of Fig. 4.2.

image of Fig. 4.3f, taken t = 13.4 ms into unstart, shows the leading shock has propagated out of the visible portion of the field of view. The T1 pressure time history in Fig. 4.4 indicates that the leading shock has just reached the T1 location. Separated ceiling flow (arrow L) is still seen to enter the visible portion of the field of view and the appearance of visible flow structures indicates the flow to be supersonic near the ceiling. The preceding discussion demonstrates that the shock structure of the unstart shock system remains relatively constant as it propagates upstream through the model. In other words, the unstart shock system consists of a lower separation shock that impinges on the isolator resulting in separation of the ceiling boundary layer. As the unstart shock system moves upstream this shock structure remains. In contrast, the shock structure of the unstart shock system in the 6-degree case varied much more as a function of time. Specifically, it was seen to be dependent on the initial reflected oblique shock system that was generated by the compression ramp. Specifically, recall that as the unstart shock system propagated upstream in the 6-degree model, boundary layer separation was seen to increase at the impingement locations of the ramp shock reflections (e.g., Fig. 3.8, Fig. 3.9, and Fig. 3.11). Note that Fig. 4.4 shows that T1 pressure decreases to the pre-unstart value at a time of t = 14.6 seconds. This is due to a change to a downstream propagation of the unstart shock system. Then at t = 15.2 seconds, the pressure once again increases as the unstart shock system reverts back to upstream propagation. Recall that similar behavior near T1 was seen to occur during the unstart of the 6-degree inlet / long-isolator (e.g., section 3.5.1 and Fig. 3.10). As previously discussed, perhaps these observations are the result of an acoustic oscillation. Recall that in the 6-degree unstart event, the frequency of this oscillation is about 500 Hz (f^* = 0.45), which is near that of an ideal half-wave resonator. Similarly, if the time spent between the first (t = 13.28 ms) and second (t = 15.24 ms) crossings of T1 is assumed to be the oscillation period, the frequency then computes to be about 510 Hz (f^* = 0.44) in the 0-degree case. Therefore, the oscillations that occur near the end of the unstart processes in the 0-, and 6-degree inlet / long-isolator models may be part of an acoustic half-wave resonator oscillation. Also, note that the slopes of the isolator pressure time histories (T4-T7) show that the unstart process occurs at more gradual rate than in the 6-degree inlet case (e.g., See Fig. 3.10). Another interesting observation is that the peak pressures of about 20 P_∞ are about 40% lower than those reached during the unstart of the 6-degree inlet model. This is likely due to the fact that the leading shock of the unstart shock system propagated further upstream during unstart in the 6-degree case compared to unstart in the 0-degree case.

4.1.3.2 Unstart Timescales and Velocities

The timescales of the unstart process in the 0-degree inlet / long-isolator model for ten different unstart events are given in Fig. 4.5a. In a similar to fashion to the 6-degree, case, the effect of flap rise time on the unstart timescales was investigated. Figure 4.5a gives the times spent between consecutive transducers for unstart events during which the flap was raised in about 140 ms, 350 ms and 500 ms. The arrows intersecting the floor of the model schematic show the streamwise midpoints between the consecutive transducers. Note that since T3 lacked the frequency response to determine the unstart shock system crossing time, the velocity from T4 to T2 is given instead. Also, similar to the 6-degree unstart events (e.g., Section 3.4), it was not possible to obtain statistically meaningful times spent between T7 and T6. Therefore, these times are not given. Note the rise times are large compared to flow transit times, so the flow is likely quasi-steady for all three speeds tested. Similar to that in the 6-degree events, there is no discernable difference in unstart timescales with varying flap speeds. The timescales corresponding to the ten unstart events in Fig. 4.5a were averaged to produce the average unstart propagation velocities given in Fig. 4.5b. Compared to the 6-degree case seen in Fig. 3.7b, the propagation velocity in the 0-degree case is lower and varies less with streamwise location. This will be discussed further in the upcoming comparison section.

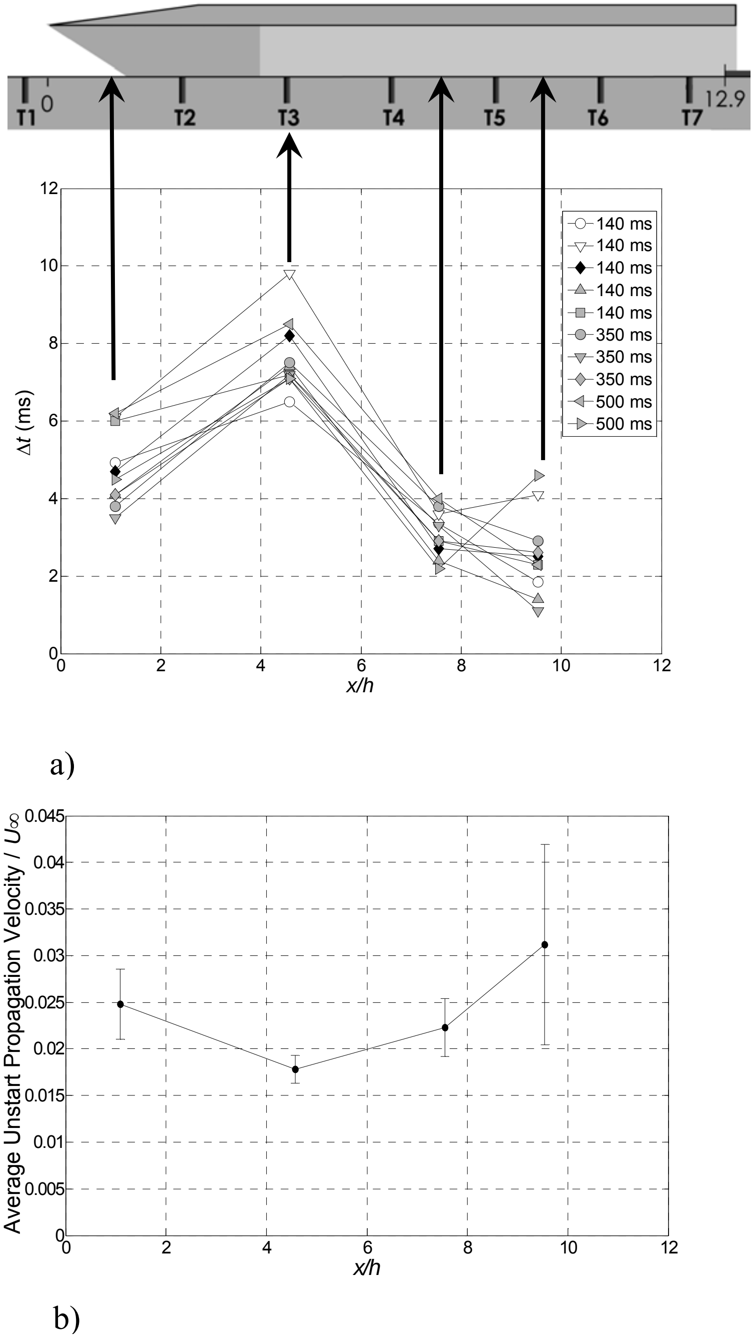

a)

b)

Figure 4.5 a) 0-degree / long-isolator unstart time-scales for ten runs (times spent between consecutive transducers) and b) average unstart shock-system velocities (normalized by U_∞ = 750 m/s), based on the ten runs.

4.1.4 Non-Oscillatory Unstarted Flow

Figure 4.4 shows the unstarted flow in the 0-degree inlet / long isolator to be substantially different than after unstart in 6-degree inlet / long isolator. For example in Fig. 4.4, after about 18 ms, the pressures at each transducer are relatively constant. This is in stark contrast to the unstarted flow of the 6-degree case where high-amplitude oscillations were always seen to follow unstart (e.g., See Fig. 3.10). Although not shown here, schlieren images of the 0-degree non-oscillatory unstarted flow suggest that the leading shock of the unstart shock system did not propagate upstream far enough to become a bow shock. Rather, the images suggest that the leading shock impinged on the inlet ceiling, which resulted in separation of the ceiling boundary layer.

Figure 4.6 presents pressure power spectra for T1, T2 and T7 of the flow following unstart in the current model of discussion. For the spectra, the acquisition rate was 25 kHz and the number of samples taken was 8,750, which gives a maximum frequency of 12.5 kHz and a resolution of 2.9 Hz. The spectra correspond to the same run as that in Fig. 4.2 and were acquired over the time span of 0.5 to 0.85 seconds. The broadband nature of the spectra indicate this unstarted flow is not oscillatory.

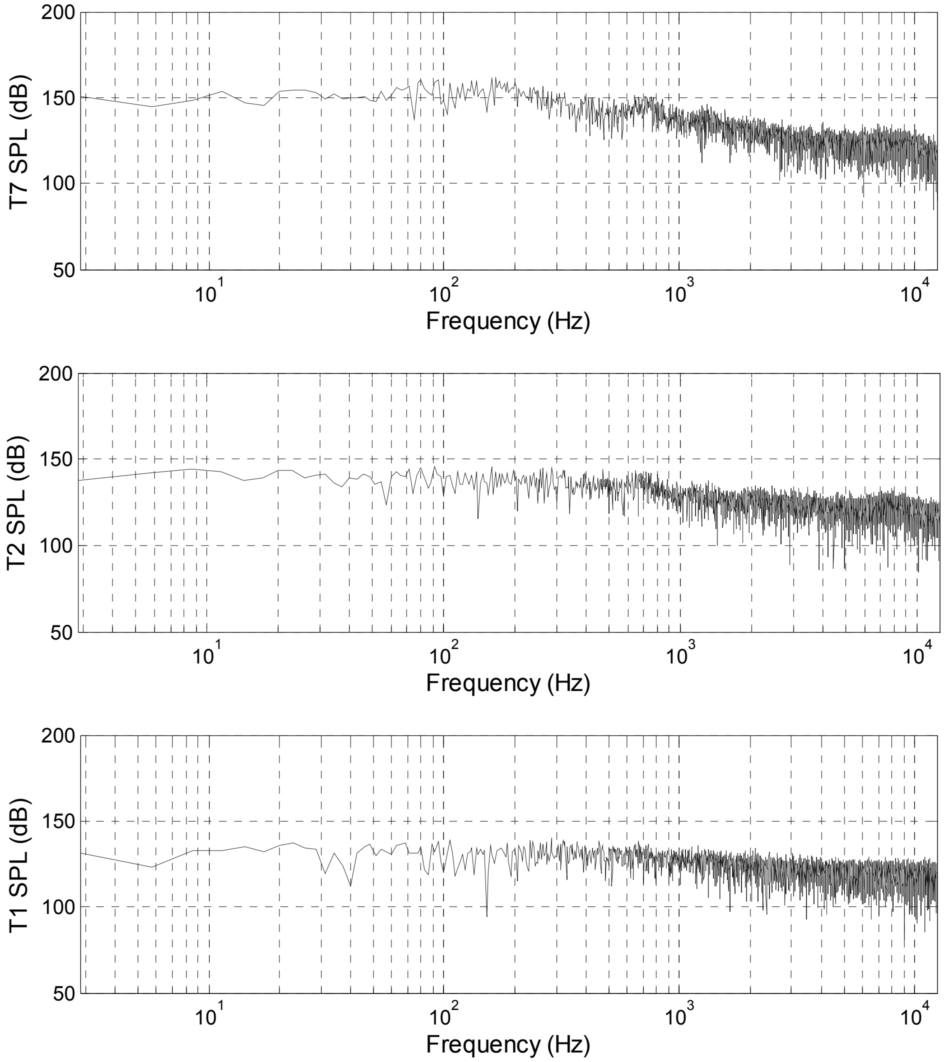

Figure 4.6 Power spectra of the pressure at T7, T2 and T1 for the 0-degree inlet / long-isolator non-oscillatory unstarted flow.

Figure 4.7 presents the mean (P_m) and *RMS* (σ) wall pressure distributions corresponding to this unstarted flow. The mean distribution of Fig. 4.7a shows the pressure to increase with streamwise distance in a nearly linear fashion. The pressure measured at T7 is 18.2 P_∞, which corresponds to 60% of the pressure increase that would be seen downstream of a Mach 5.1 normal shock. In addition, Fig. 4.7b shows that the pressure fluctuations tend to increase with streamwise distance. Note this was not the case in the non-oscillatory unstarted flow corresponding to the 6-degree inlet / long-isolator case. For example, Fig. 3.29b shows the highest *RMS* pressures measured were at T3 and T4. Furthermore, although not shown here, it was possible to alter the characteristics of the unstarted flow in the 0-degree inlet / long-isolator model by raising the flap. For instance, raising the flap to an angle of 31 degrees was seen to result in increased pressure fluctuations that were seen to be oscillatory.

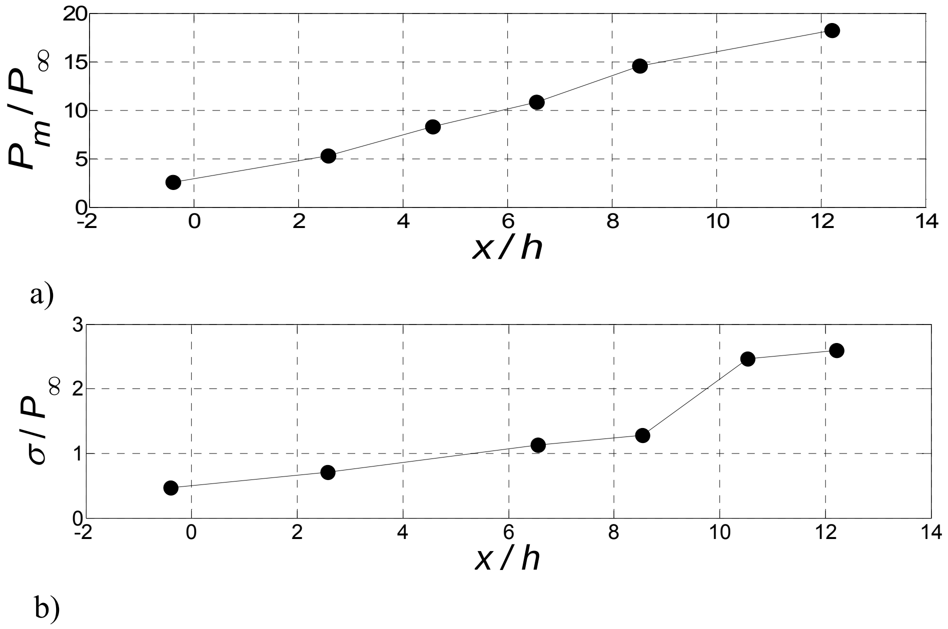

Figure 4.7 Non-oscillatory unstarted flow in the 0-degree inlet / long-isolator model: a) mean pressure distribution and b) pressure standard deviation distribution.

Finally, it is noted that unlike the 6-degree case, it was not possible to set up a high-compression shock system within the 0-degree inlet / long-isolator model. After unstart, lowering of the flap resulted in maintaining non-oscillatory unstarted flow or a complete restart of the model. This was not due to a significant lack in resolution of the flap drive system. For example in a particular test, at a flap angle of 19.4 degrees the flow remained unstarted, but at an angle of 19.2 degrees the flow restarted to a state similar to that seen in Fig. 4.3a.

4.2 8-DEGREE INLET / LONG-ISOLATOR RESULTS

4.2.1 Fully Supersonic Started Flow (Flap fully-down)

Figure 4.8 shows a schlieren image of the fully supersonic started flow in the 8-degree inlet / long-isolator model obtained using a horizontal knife edge. At the location of $x/h = 4$, two reflected oblique shocks are seen (arrows A and B). The presence of two shock reflections suggests that the initial 8-degree compression ramp shock and its subsequent reflection are strong enough to separate the floor boundary layer. This is supported by Equation 1.5 given by Love (1955). Note that oblique shock theory predicts that at the freestream Mach number of 5.1, the Mach number behind an eight-degree oblique shock and a subsequent reflection will be equal to 3.64. Therefore, M_d / M_u is equal to 0.71, which according to equation 1.5 should result in separation of the turbulent floor boundary layer. Thus, it appears the upstream reflection (arrow A) corresponds to the separation shock and the downstream reflection (arrow B) corresponds to the re-attachment shock. The two shock reflections begin to coalesce before they intersect the ceiling at about $x/h = 6.2$. The shocks then reflect and coalesce into a single shock (arrow C) which intersects the floor near $x/h = 9$. The resulting third shock reflection (arrow D) is seen to intersect the ceiling at about $x/h = 12$. Next, a fourth reflection off of the ceiling is seen (arrow E) that exits the isolator. Finally, a detached shock (arrow F) exists upstream of the flap.

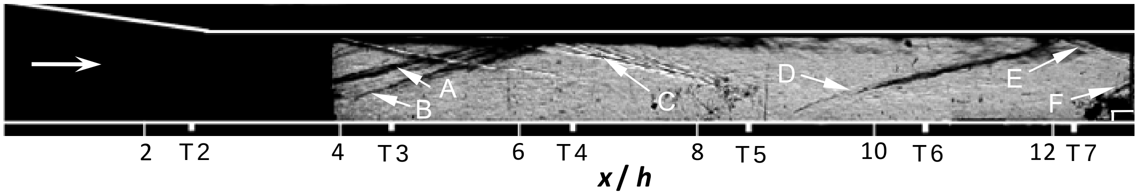

Figure 4.8 Schlieren images of fully supersonic started flow in the 8-degree inlet / isolator model obtained with a horizontal knife edge

Figure 4.9 shows the mean and *RMS* pressures corresponding to the 8-degree inlet / long-isolator fully supersonic started flow. Fig. 4.9a shows that the mean pressure remains nearly constant from T1 (*x/h* = -0.4) to within the inlet at T2 (*x/h* = 2.58). At T3 (*x/h* = 4.57), the flow has passed through the leading edge 8-degree compression ramp shock as well as its subsequent reflection. As a result the pressure has increased to about 5.2 P_∞. Oblique shock theory predicts for the current M_∞ of 5.1 that the pressure behind an 8-degree oblique shock and subsequent reflection will be 5.6 P_∞, which is greater than that measured at T3. However, this is to be expected as the flow has also been processed by expansion waves that originate at the inlet shoulder (i.e., the ceiling location corresponding to the junction of the inlet and isolator). Next the pressure is seen to decrease at T4 (*x/h* = 6.56) and T5 (*x/h* = 8.54) as the flow has passed through expansion waves that originate at the inlet shoulder and then reflect off of the isolator floor. Finally, the pressure near the isolator exit at T7 is seen to be about 3 P_∞. The *RMS* pressures shown in Fig. 4.9b follow a similar trend to that observed in the 6-degree inlet case (e.g., Fig. 3.2b). Namely, the pressure fluctuations are seen to be elevated at T6 and T7 which are in the vicinity of shock wave / boundary layer interactions. Recall that in the 6-degree case, the *RMS* pressure at T3 was also elevated which was similarly attributed to shock wave / boundary layer interactions. Unfortunately, for the experiment currently being reported on, T3 had lost its frequency response and therefore was unable to faithfully measure fluctuations.

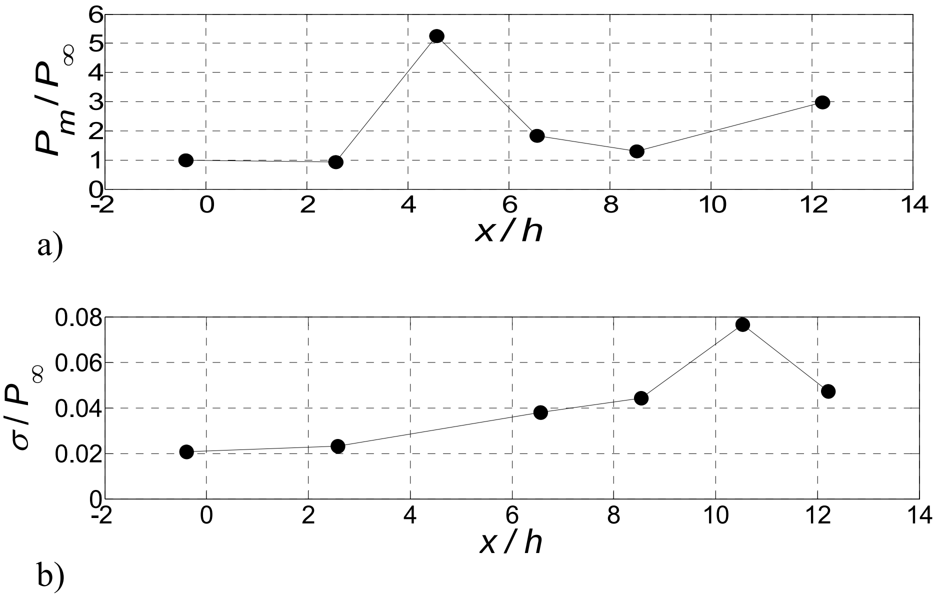

Figure 4.9 8-degree inlet / long-isolator fully supersonic started flow: a) mean pressure distribution and b) pressure standard deviation distribution.

4.2.2 T7 Time History During Unstart and Unstarted Flow

Figure 4.10 shows the pressure time history measured at T7 for a flap sequence that resulted in unstart, unstarted flow and restart. From 0 to about 0.43 seconds, the flap is fully-down and the flow in the inlet / isolator is started and fully supersonic. From about 0.43 to 0.63 seconds the flap is raised, which increases the pressure at T7. During this time the strength of the flap shock increases, but not to a point great enough to induce unstart. For this model, the angle at which unstart occurred was seen to be 26.6 degrees which was the same angle seen to induce unstart in the 6-degree inlet model. (Therefore the contraction ratio required to induce unstart is 1.81 for both 6- and 8-degree models.) However, for the unstart event described in this section, the flap was raised to the angle of 27.5 degrees to ensure that unstart would occur. Figure 4.10 shows a rapid T7 pressure increase at about 0.63 seconds, which corresponds to the unstart of the model. From about 0.63 to 1.0 seconds an oscillatory unstarted flow is seen to occur. The T7 pressure fluctuations of about 20 P_∞ are similar in magnitude to those observed in the lower-amplitude oscillatory unstarted flow of the 6-degree inlet / long-isolator model (e.g, See Fig. 3.4). Therefore, this unstarted flow is also termed lower-amplitude oscillatory unstarted flow. Finally at the time of about 1.0 second, the flap is lowered which results in a restart of the model to the fully supersonic started flow.

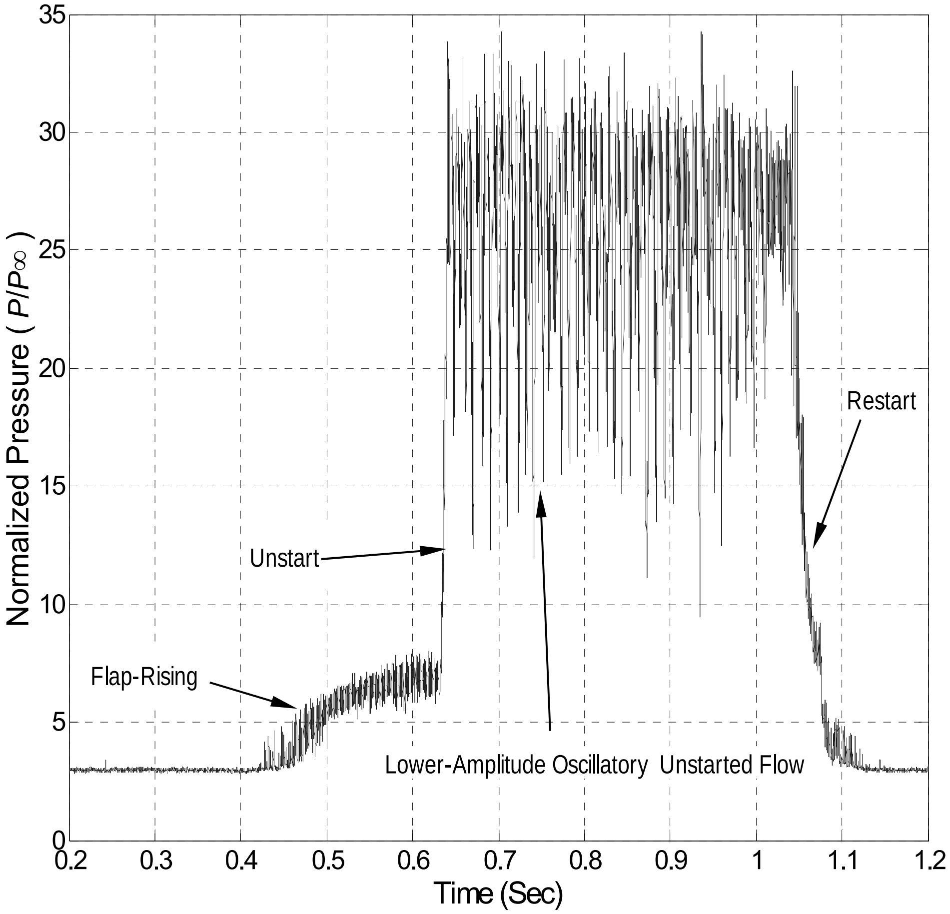

Figure 4.10 8-degree inlet / long isolator pressure time history corresponding to inlet unstart, unstarted flows and restart processes obtained at T7.

4.2.3 Unstart Dynamics and Flow Structure

4.2.3.1 High-Speed Schlieren and Simultaneous Pressure Measurements

Figure 4.11 shows a sequence of schlieren images acquired during the unstart of the 8-degree inlet / long-isolator model. Figures 10a through 10h correspond to unstart times of t = 0, 0.6, 2.3, 3.3, 4.4, 5.5, 6.8 and 8.0 ms, respectively. The images were obtained using a horizontal knife edge as to highlight vertical density gradients. Also, Fig. 4.12 provides the pressure time histories of T1, T2 and T4-T7 corresponding to the

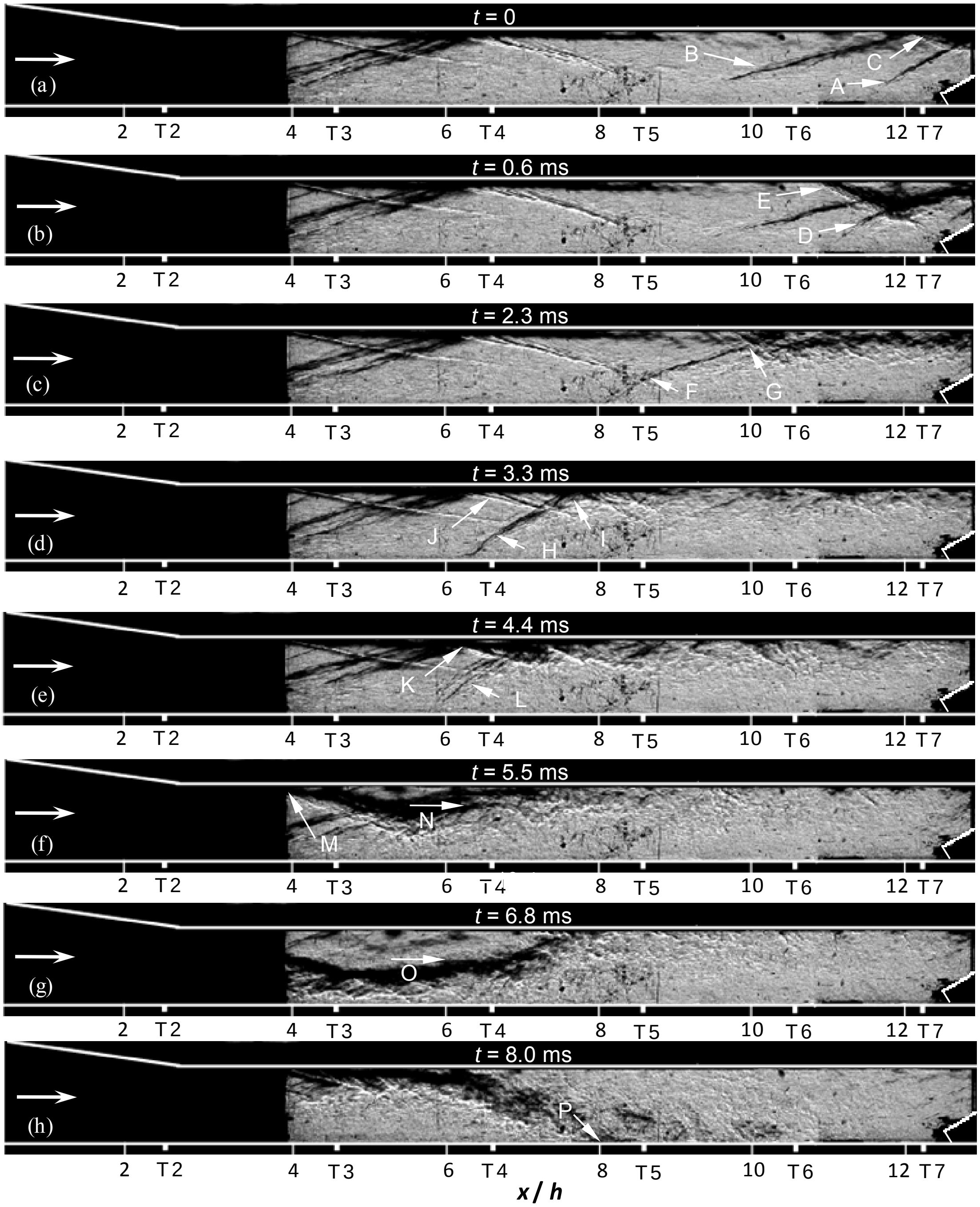

Figure 4.11 Schlieren of the unstart process in the 8-degree inlet / long isolator at times: a) $t = 0$, b) $t = 0.6$ ms, c) $t = 2.3$ ms, d) $t = 3.3$ ms, e) $t = 4.4$ ms, f) $t = 5.5$ ms, g) $t = 6.8$ ms, and g) $t = 8.0$ ms ($\theta_F \approx 27$ degrees).

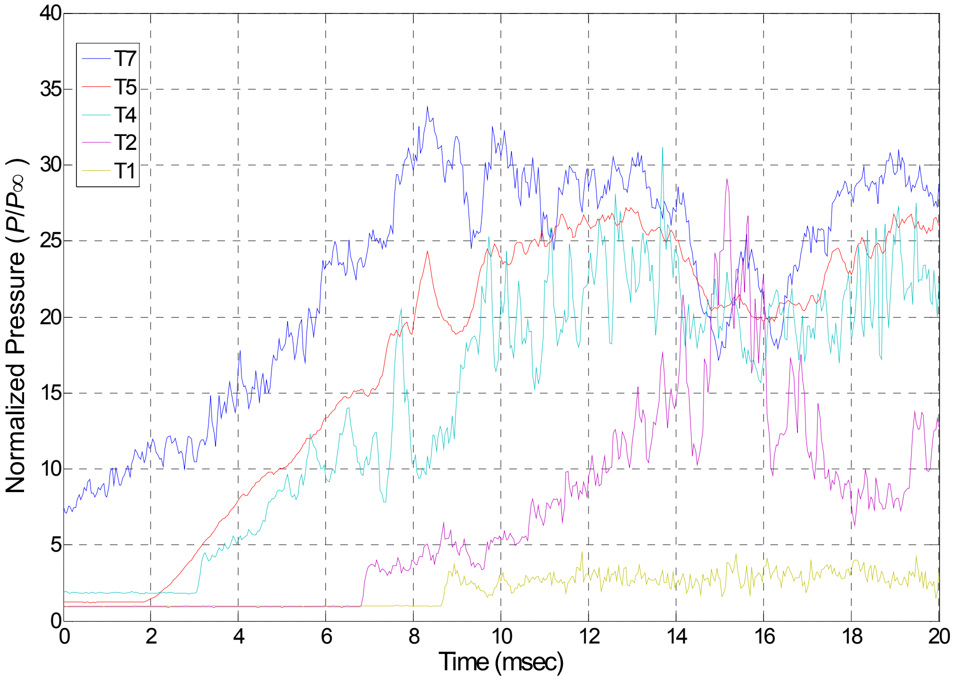

Figure 4.12 Pressure time histories obtained at T1 – T7 for the unstart event of Fig. 4.10.

unstart event of Fig. 4.10. Once again, T3 was not available for these tests. Figure 4.11a corresponds to the onset of unstart or $t = 0$. The onset was defined using the schlieren images in the same way as for the 6-degree case (e.g., See section 3.5.1). In Fig. 4.11a, the flap is at an angle of about 27.5 degrees, which is great enough to induce unstart. Both the detached flap shock (arrow A) and the third ramp shock reflection (arrow B) are seen to impinge on the ceiling near the isolator exit. In addition, the fourth reflection of the compression ramp shock (arrow C) is also present near the isolator exit. These three shocks lead to both impinging and glancing SWBLI along the ceiling and sidewalls at the isolator exit. Similar to the 0- and 6-degree inlet models, unstart is seen to progress with an increased separation of the ceiling boundary layer which is first observed at the impingement location of the third shock reflection. The image of Fig. 4.11a corresponds to the frame acquired just before the ceiling separation became great enough to cause unstart. Figure 4.11b, taken 0.6 ms later shows unstart has propagated upstream with a significant increase in separation of the ceiling boundary layer. Two shocks are seen to mark the unstart shock system at this time. The first shock (arrow D) is similar in structure to that of the detached flap shock and the second (arrow E) is a ceiling separation shock. At t = 2.3 ms, Fig. 4.11c shows that unstart has propagated to the floor streamwise location of about x/h = 8. Furthermore, Fig. 4.12 shows that the unstart shock system has increased the pressure at transducers T5 and T7. Note in Fig. 4.11c that the third oblique shock and detached flap shock can no longer be identified separately. Rather, unstart has resulted in the formation of the shock marked by arrow F. In between the times corresponding to Figs. 4.11b and 4.11c, the second oblique shock reflection (arrow C in Fig. 4.8) was seen to “lift” and become more bifurcated near its intersection with the floor. These observations indicate that the propagation of unstart results in an increase in floor boundary layer separation near the impingement point of the second reflection. Also, while the extent of floor boundary layer separation has increased from t =0.6 to 2.3 ms, the extent of ceiling boundary layer has decreased (arrow G). The next image schlieren image of Fig. 4.11d, corresponds to t = 3.3 ms. The leading shock of the unstart shock system (arrow H) has grown substantially stronger as evidenced by its increase in inclination angle. In addition, note the extent of ceiling boundary separation (arrow I) has decreased. Figure 4.11d also shows that the second reflection of the compression ramp shock (arrow J) remains unaltered near the ceiling. This is not the case in the t = 4.4 ms image of Fig. 4.11e, which shows that the propagation of the unstart shock system results in separation of the ceiling boundary layer (arrow K). In this image the floor separation shock (arrow L) is still apparent; however, Fig. 4.11f taken at t = 5.5 ms no longer shows a floor separation shock. Rather, the flow structure has been dramatically altered due to an increase in ceiling separation. The separation ceiling separation point (arrow M) is seen near $x/h = 4$. The high amount of ceiling separation results in the formation of the prominent shear layer labeled by arrow N. These observations are consistent with those observed in the baseline 6-degree inlet / long-isolator case. Recall in the 6-degree case, that as the unstart shock system progressed upstream, the flow became highly separated in regions corresponding to the impingement locations of the initial reflected oblique shock system. Similarly, the currents results demonstrate that the flow structure of the unstart shock system depends on the impingement locations of the initial reflected oblique shock system. In addition, Fig. 4.12 shows the pressure within the isolator has increased substantially with the upstream propagation of the unstart shock system. Figure 4.11g shows as time progresses to $t = 6.8$ ms, the unstart shock system moves into the inlet piece of the model. The prominent shear layer (arrow O) is still visualized from about $x/h = 4$ to about $x/h = 8$ where it appears to impinge on the ceiling. Note that the shear layer is now closer to the floor, which suggests that the magnitude of ceiling separation has grown with upstream propagation of the unstart shock system. Moreover, Fig. 4.12 indicates that the unstart system has just reached T2. Finally, at $t = 8.0$ ms (Fig. 4.11h) the shear layer now enters the acrylic portion of the isolator near the ceiling and appears to impinge on the floor (arrow P) at about $x/h = 8$. Although, it is not evident from this image sequence alone, the schlieren images show that as the unstart shock system progressed upstream through the inlet, the shear layer moved throughout the isolator with an up and down “whip like” motion. Figures 4.11g and 4.11h show instances where the shear layer appears to impinge on the floor and ceiling, respectively. The time history of T1 in Fig. 4.12 indicates that the unstart shock system reaches the streamwise location of $x/h = 0.4$ at about 8.6 seconds. Similar to the criteria for the other models, at this time the model is said to be unstarted. Figure 4.12 also shows that the maximum pressures reached at each transducer during unstart are similar to those seen in the 6-degree case (e.g., See Fig. 3.10).

4.2.3.2 Unstart Velocities

Figure 4.13 presents the average unstart propagation velocities in the 8-degree inlet / long-isolator model. The velocities are based on six different unstart events and the 95% uncertainty levels are based on a student-t analysis. The plot shows that the unstart shock system accelerates as it moves upstream from T6 to T4. The unstart shock system then decelerates in the upstream streamwise half of the isolator between T4 and T2. Finally, as the unstart system moves upstream between T2 and T1, it maintains a velocity similar to that seen between T4 and T2. Note that the highest propagation velocity measured is in between T5 and T4. Recall that the schlieren image sequence of Fig. 4.11 suggested that unstart propagated upstream with floor boundary layer separation between the streamwise locations corresponding to T5 and T4. However, in between T4 and T2, the propagation of unstart was seen to be characterized by ceiling boundary layer separation. Therefore, the combined results of the schlieren imaging and unstart propagation velocities of Fig. 4.13, suggest that the unstart shock system travels at a greater velocity when it is associated with floor boundary layer separation than ceiling separation. However, as mentioned with the similar occurrence seen in the 6-degree case, this decrease in velocity is measured only along the floor. It is possible that the propagation velocity along the ceiling increases with ceiling separation. In fact, this possibility is supported by the schlieren images (not shown) recorded in between $t = 4.4$ ms (Fig. 4.11e) and $t = 5.5$ ms (Fig. 4.11f). Specifically, the images during this time span, show that the ceiling separation shock of the unstart shock system propagates upstream faster than the floor separation shock.

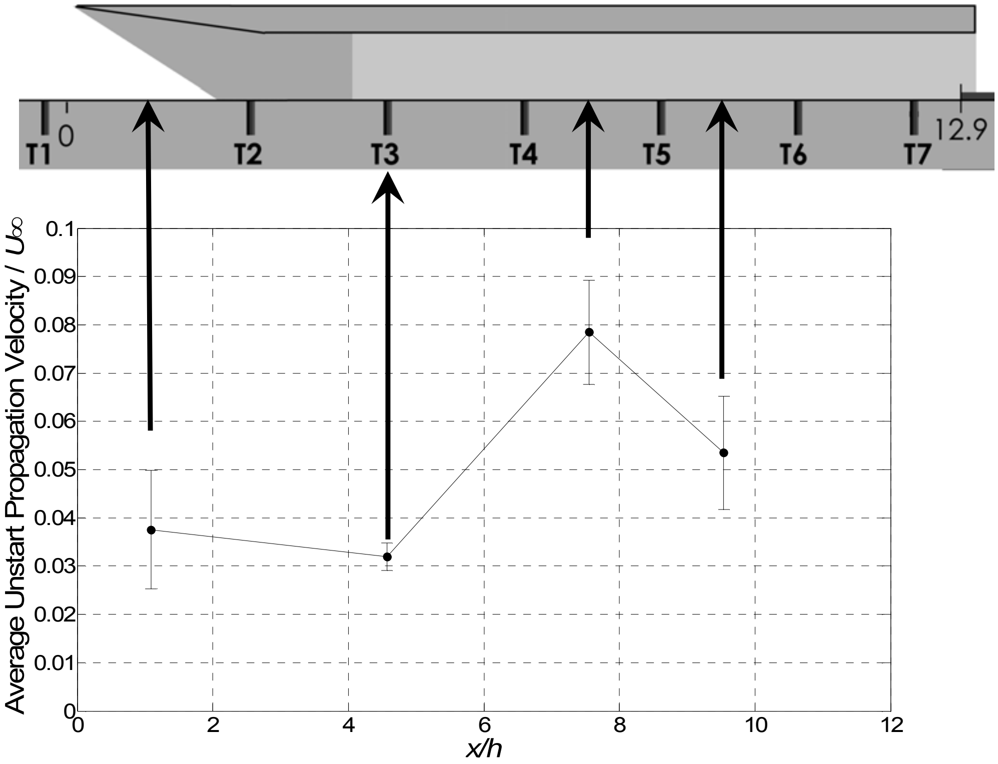

Figure 4.13 8-degree inlet / long-isolator average unstart shock-system velocities (normalized by U_∞ = 750 m/s), based on six unstart events.

4.2.4 Lower-Amplitude Oscillatory Unstarted Flow

Figure 4.12 shows that following unstart in the 8-degree inlet / long-isolator, the isolator pressure distribution remains relatively constant until the time of about t = 14 ms. After 14 ms, the isolator pressures at T4 to T7 decrease to minimum values and then begin to increase again around 16 ms. This cycle is the first of the lower-amplitude oscillatory unstarted flow labeled in Fig. 4.10. Also note that Fig. 4.12 shows that the oscillations first seen to follow unstart in the 8-degree inlet have much smaller amplitudes than those in the 6-degree case (e.g, compare to Fig. 3.10).

Figure 4.14 shows the pressure power spectra corresponding to the lower-amplitude oscillatory unstarted flow for T7, T2 and T1. For the spectra, the acquisition rate was 25 kHz and the number of samples taken was 8,750, which gives a maximum frequency of 12.5 kHz and a resolution of 2.9 Hz. The spectra correspond to the same run as that in Fig. 4.10 and were acquired over the time span of 0.65 to 1.0 seconds. As seen in Fig. 4.14, T7 (x/h =12.21) has an *SPL* peak of 169 dB at a frequency of 100 Hz (f *=0.090). In comparison, T2 (x/h = 2.58) within the inlet section has a greater *SPL* peak of 173 dB at a similar frequency of 97 Hz (f *= 0.087). The peak power at this transducer location was seen to be the highest in the model during this unstarted flow mode. The power spectrum for T1 (x/h = -0.4) upstream of the inlet also shows a peak at f = 97 Hz. However, the *SPL* value for this peak of 144 dB is much lower than all peak values within the model.

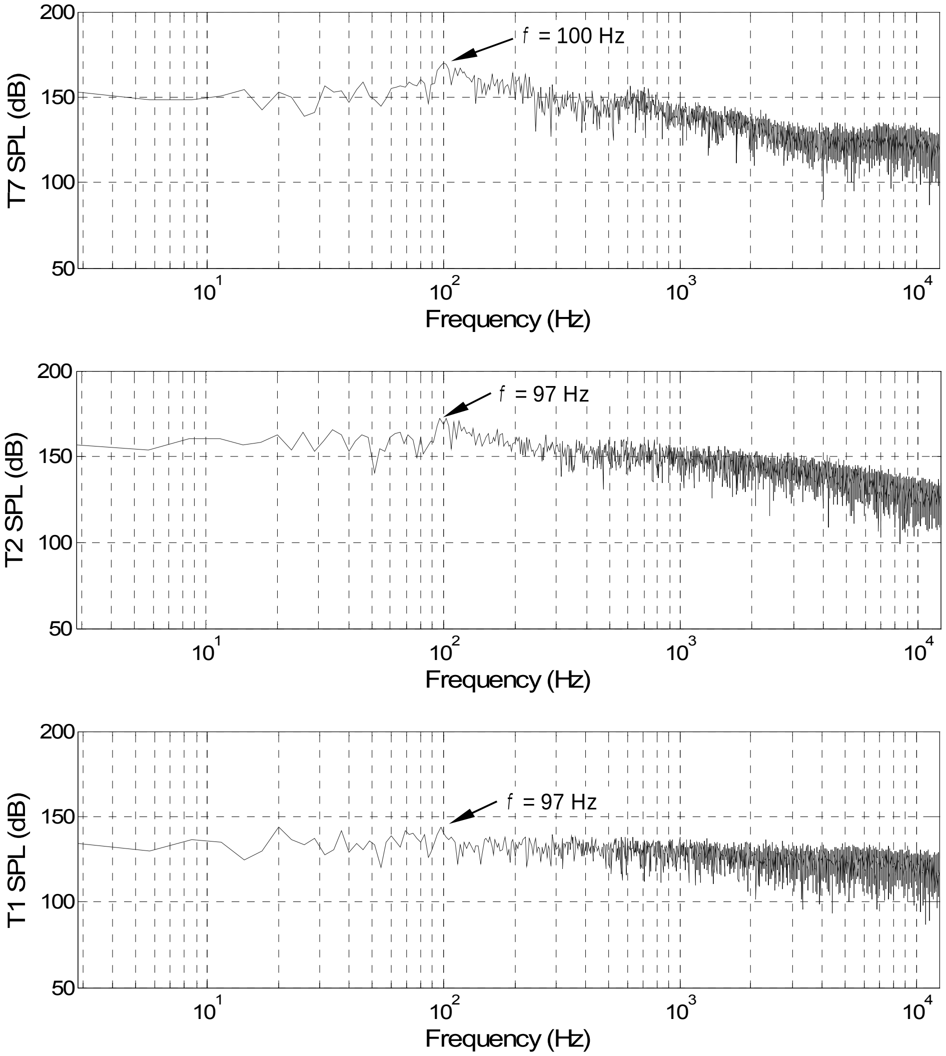

Figure 4.14 Power spectra of the pressure at T7, T2 and T1 for the 8-degree inlet / long-isolator lower-amplitude oscillatory unstarted flow.

Fig. 4.15 presents the mean (P_m) and *RMS* (σ) wall pressure distributions corresponding to the lower-amplitude oscillatory unstarted flow in the 8-degree inlet / long-isolator model. The mean distribution of Fig. 4.15a shows that the pressure increases with streamwise distance into the model. Compared to the high-amplitude oscillatory unstarted flow seen to follow unstart in the 6-degree inlet case (e.g., see Fig. 3.23), this lower-amplitude unstarted flow is seen to maintain a higher pressure distribution. Following unstart, interestingly, the mean pressure distribution of this lower-amplitude oscillatory unstarted flow is seen to be quite similar to that seen in the lower-amplitude oscillatory unstarted flow that could be set up by lowering the flap after unstart in the 6-degree case (e.g., see Fig. 3.32). The *RMS* wall pressure distribution of this unstarted flow is also similar to that seen in Fig. 3.32. For example, both distributions show the peak fluctuations occur within the inlet at T2. Figure 4.14b shows the *RMS* pressure at T2 to be nearly 7 P_∞. In comparison, the *RMS* pressure measured at T7 is about 40% lower at about 4 P_∞. These measurements suggest that although the pressure oscillations at T7 are lower for this unstarted flow mode compared to the high-amplitude oscillatory unstarted flow, high-amplitude oscillations still exist within the inlet. Figure 4.16 which gives the pressure time history at T2 for the same time span as the T7 time history of Fig. 4.10 further demonstrates this point. This inlet transducer time history shows the highest amplitude oscillations reported thus far. Note the pressure peak values are as great as 50 P_∞ and the minimum values decrease below 5 P_∞.

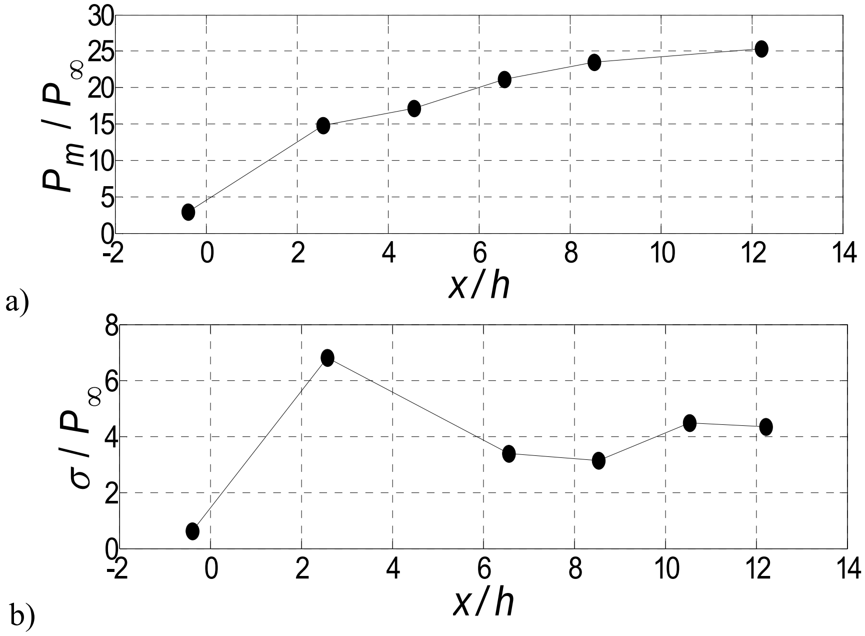

Figure 4.15 Lower-amplitude oscillatory unstarted flow in the 8-degree inlet / long-isolator model: a) mean pressure distribution and b) pressure standard deviation distribution.

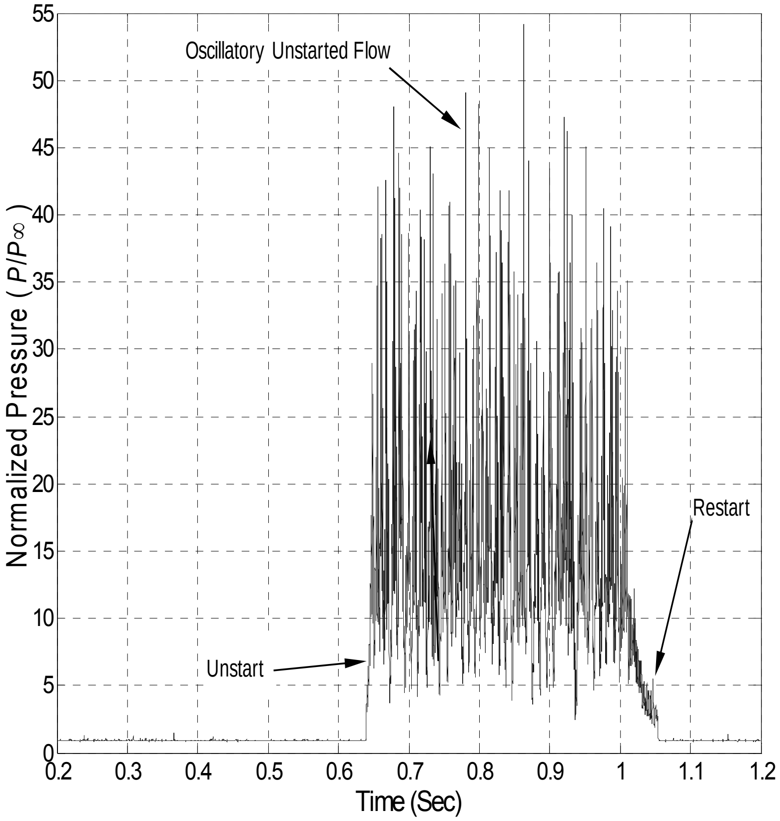

Figure 4.16 8-degree inlet / long isolator pressure time history corresponding to inlet unstart, unstarted flows and restart processes obtained at T2.

4.2.5 High-Compression Shock Systems

Like the 6- and 0-degree cases it was not possible to set up a high-compression shock system within the isolator by raising the flap in the fully supersonic started flow mode. However, like the 6-degree case, it was possible to first unstart the inlet and then lower the flap to set up a high-compression shock system within the inlet. The method to set up the high-compression system in the 8-degree inlet case is the same as described in the 6-degree case of section 3.9.1. Figure 4.17 shows the mean pressure distribution corresponding to a strong-compression shock system in the 8-degree inlet / long-isolator model. For the case shown in Fig. 4.17, a weak-compression shock system was set up in the isolator by lowering the flap to 18.3 degrees after unstart. The flap was then raised to an angle of 21.0 degrees, which resulted in the strong-compression system corresponding to the pressure distributions given in Fig. 4.17. Raising the flap to a higher angle of 21.9 degrees was seen to once again result in unstart. The mean pressure distribution plot of Fig. 4.17a is seen to quite similar to that of the strong-compression shock system in the 6-degree inlet (e.g., see Fig. 3.37). Note in both cases the T7 pressures are near 12 P_∞. Also, in both cases the peak *RMS* pressures occur at T7 and are near 0.9 P_∞. The similarities of pressure distributions suggests that like the 6-degree strong-compression system, the 8-degree strong-compression shock system is not a shock-train or pseudo-shock. As discussed in section 3.9.4, it is possible that this high-compression shock system is the separation-shock mode described by Penzin (1998).

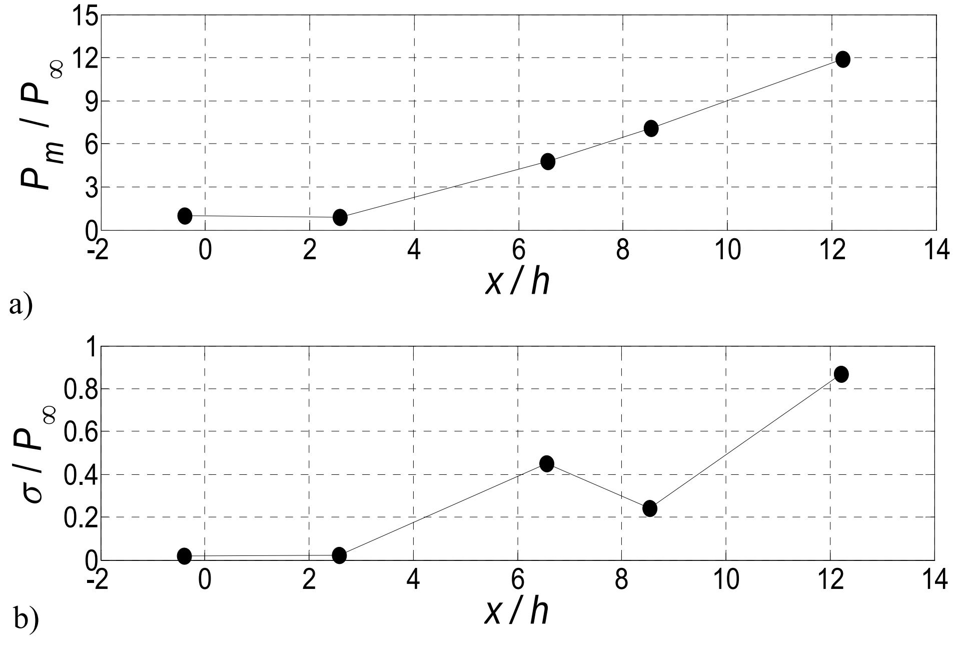

Figure 4.17 Strong-compression shock system in the 8-degree inlet / long-isolator model: a) mean pressure distribution and b) pressure standard deviation distribution (θ_F = 21.0 degrees).

4.3 COMPARISONS OF 0, 6 AND 8-DEGREE INLET / LONG-ISOLATOR RESULTS

The previous results indicate that the unstart process, unstarted flow and the ability to form a high-compression shock system within a given model are highly dependent on the geometry of the inlet. This section summarizes and discusses the effects of inlet geometry on the various inlet / long-isolator flows presented thus far.

The upstream propagation of unstart in all three cases was seen to be highly associated with shock-induced separation. The contraction ratio required to induce unstart was found to be 1.27 for the no-inlet case and 1.81 for both the 6- and 8-degree cases. A possible explanation is as follows. In the 0-degree model, it is expected that the Mach number near the isolator exit (upstream of the flap) is higher than that in the 6- and 8-degree inlet / isolators. Therefore, the flap shock wave / boundary layer interactions near the isolator exit are expected to be stronger in the 0-degree model. Stronger interactions imply increased separation or viscous blockage for a given flap angle. With an increased viscous blockage, the amount of physical area contraction required to induce unstart should be lower. In the 6-degree and 8-degree inlet cases, it was observed during unstart that the extent of boundary layer separation was dependent on the impingement locations of the oblique shock reflections. For example, when the unstart shock system reached a streamwise location close to a ceiling impingement point, the flow at that point became highly separated. As the extent of ceiling separation significantly increased, the extent of floor separation substantially decreased. Recall that examples of this alternation of floor to ceiling separation can clearly be seen in the PIV pseudo-sequence of Fig. 3.11 and in the schlieren sequences of Fig. 3.8, Fig. 3.9 and Fig. 4.11. Similarly, in the 6-degree and 8-degree experiments, an opposite alternation of ceiling to floor separation was also seen when the unstart shock system propagated to streamwise locations near floor impingement points. In comparison, the 0-degree (no inlet) case showed that the flow structure of the unstart shock system remained relatively constant taking the form of an upstream propagating shock similar to the detached flap shock seen prior to unstart (e.g., See Fig. 4.3). Thus, it is clear that the geometry of the inlet affects the flow structure seen during unstart.

Inlet geometry also influences the propagation velocity of the unstart shock system. Fig. 4.18 shows the normalized unstart propagation velocities for all three inlet cases. The 0-degree (no inlet) case is seen to have a much more constant unstart propagation velocity than either the 6-degree or 8-degree models. Also, note that the propagation velocity is significantly lower for the 0-degree case. This suggests that compression due to the presence of an inlet serves to increase the propagation velocity of unstart through the model. This is intuitive in the sense that increased compression means that the unstart shock system has to propagate against an overall slower and lower momentum fluid. Owing to the overlapping uncertainty levels, it is not possible to meaningfully compare propagation velocities within the isolator for the most downstream location of Fig. 4.18. Therefore, in order to compare isolator propagation velocities, the average velocities were computed for the isolator streamwise span in between T6 and T4. Note a more complete span would include T7 and T3. However, as mentioned T3 was not available for the 0-degree and 8-degree tests and as described in section 3.5.1, and the T7 time history was not able to meaningfully provide an estimation of the unstart shock system crossing time. Table 4.1 gives unstart propagation velocities normalized by U_∞ over three different streamwise sections for the three inlet geometry cases describe so far. The sections are: (i) nearly the entire model section from T6 (x/h = 10.53) to T1 (x/h = -0.4), (ii) within the isolator from T6 to T4 (x/h = 6.56) and (iii) within the inlet from T2 (x/h = 2.58) to T1. Table 4.1 shows that the average unstart propagation velocities over T6 to T1 for the 6-degree and 8-degree cases are over twice that of the 0-degree case.

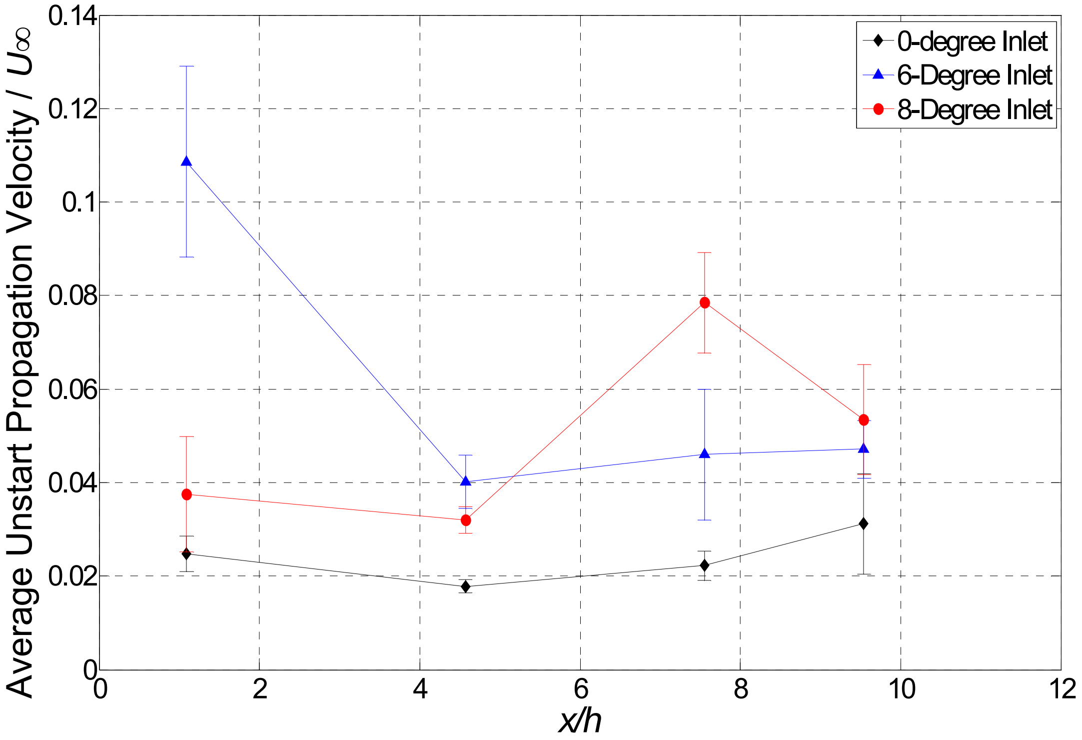

Figure 4.18 Comparisons of the average unstart shock-system velocities (normalized by U_∞) in the 0-, 6- and 8-degree inlet / long-isolator models.

Similarly, the average unstart propagation velocities in the isolator of the 6-degree and 8-degree inlet models are also seen to be substantially higher than that for the no inlet case. In addition, the velocities over this isolator span show that unstart tends to travel faster in the 8-degree inlet case than in the 6-degree case. The faster propagation velocity in the isolator of the 8-degree case could be due to the greater strength shocks and slower opposition flow velocities. However, as compared to the 6-degree case, the average velocity from T6 to T1, which extends over nearly the entire model is lower for the 8-degree case. Table 4.1 and Fig. 4.18 show the reason for this is the fact that the unstart shock system tended to travel much faster in the 6-degree inlet compared to the 8-degree inlet. However, the cause of the higher inlet propagation velocity in the 6-degree inlet is not currently understood. Even though the inlet velocities do not follow a clear trend, the isolator propagation velocities discussed suggest that the unstart propagation velocity tends to increase with increasing compression ramp angle. Again, this is possibly related to the fact that increasing the compression ramp angle, decreases the overall velocity of the flow the shock system propagates into.

Table 4.1 Comparisons of Unstart Propagation velocities normalized by U_∞ in the 0-degree, 6-degree and 8-degree inlet / long isolator models.

Inlet	$V_{\mathrm{T6\text{-}T1}}$	$V_{\mathrm{T6\text{-}T4}}$	$V_{\mathrm{T2\text{-}T1}}$
0-degree	0.019 ± 0.002	0.025 ± 0.004	0.025 ± 0.004
6-degree	0.051 ± 0.003	0.040 ± 0.005	0.109 ± 0.020
8-degree	0.045 ± 0.002	0.063 ± 0.007	0.038 ± 0.012

The peak pressures reached during unstart were seen to vary according with inlet geometry. For example, in the 6-degree and 8-degree experiments, peak pressures during unstart were seen to be about 30 to 35 P_∞. However, during unstart of the 0-degree inlet / long isolator, the peak pressure only reached about 20 P_∞. In addition, recall that Wieting (1973), stated that the transient pressures during unstart could be conservatively estimated using the pressure downstream of a stationary normal shock in the freestream flow. However, in the 6- and 8-degree inlet / long isolator models, unstart typically was associated with peak pressures somewhat greater than that which would found downstream of a freestream normal shock (Note that the pressure downstream of a Mach 5 normal shock is 29.9 P_∞). Moreover, in some unstart events of the 6-degree inlet / long isolator model, the inlet pressure at $x/h = 2.58$ were seen to spike as high as 45 P_∞. For example, a few of inlet (T2) pressure spikes can be seen in Fig. 3.10.

Following unstart, the unstarted flow in each inlet / long-isolator case was seen to have significantly different characteristics. It is reiterated here that the unstarted flows reported in this chapter corresponded to flap angles that were near (within 3 degrees) the angle that induced unstart. It was demonstrated in chapter 3, that for the 6-degree case, it was possible to change the unstarted flow characteristics by changing the flap position following an unstart event. Similarly, it was also possible to change the characteristics of the unstarted flows in the 0- and 8-degree inlet / long-isolator models. However, the unstarted flow data of this chapter were acquired at the flap angle that was used to induce unstart. Following unstart of the 6-degree inlet / long-isolator, the flow was seen to go into the high-amplitude oscillatory flow mode with a dominant frequency peak of 124 Hz (f^*=0.11). In contrast, following unstart of the 0-degree model, the unstarted flow was seen to be non-oscillatory with significantly lower pressure fluctuations. However, it was noted that an oscillatory unstarted flow could be formed in the 0-degree model by raising the flap from 27 to 31 degrees after the occurrence of unstart. Furthermore, a third unstarted flow mode was seen to follow unstart of the 8-degree model. This unstarted flow was said to be lower-amplitude oscillatory unstarted flow due to the fact that it had lower T7 oscillation amplitudes. However, it was noted that the oscillations at T2 within the inlet reached the highest peak pressures recorded in any of the flows reported on thus far. The lower-amplitude oscillatory unstarted flow that followed unstart in the 8-degree inlet case was similar to that which could be formed in the 6-degree case by a lowering of the flap after unstart (e.g., Fig. 3.4). The high pressure fluctuations in the inlet suggest that an unstarted shock system oscillated near the inlet transducer, T2 (x/h = 2.58). The dominant frequencies for the lower-amplitude oscillatory unstarted flow of the 8-degree inlet case were near 100 Hz (f^*=0.087) at each transducer. These results suggest that the inlet geometry strongly affects the flow that follows the unstart process.

Finally, it is noted that the inlet geometry also influenced the capability of a model to contain a high-compression shock system. Following unstart of the 6-degree and 8-degree cases, it was possible to set up (form) a high-compression shock system in the isolator by lowering the flap. The high-compression shock systems did not appear to be pseudo-shocks containing shock-trains. Rather, some evidence suggested that these high-compression shock systems could be of the separation-shock form described by Penzin (1998). In the case for the 0-degree inlet / isolator it was not possible to set up a high-compression shock. Following unstart of the 0-degree case the lowering the flap resulted in either a flow that remained unstarted or in a complete restart to fully supersonic flow.

CHAPTER 5

5. Isolator Geometry Variations (0-, 6- and 8-Degree Inlet / Short-Isolator Model Results)

For all three inlet / isolator combinations discussed thus far, it was not possible to set up a high-compression shock system within the model by raising the flap alone. In all three cases, raising the flap first resulted in the upstream propagation of a detached flap shock. Upon reaching a great enough flap angle, a significant increase in boundary layer separation at the isolator exit was seen to occur due to flap shock wave / boundary layer interactions. Following this boundary layer separation at the isolator exit, the unstart process began in the case of each inlet / long-isolator. Therefore, the blockage created by boundary layer separation in conjunction with the blockage of the flap itself was enough to always induce unstart. In attempts to mitigate this blockage effect, a shorter isolator as seen in Fig. 2.10 was tested with each of the three inlets. It was thought that shortening the isolator to place the flap downstream of the isolator exit would result in less severe shock induced-separation upon the raising of the flap. Specifically, it was thought that this would serve to mitigate the effects of glancing (sidewall) flap shock / boundary layer interactions. The idea was that with less separation, it would be possible to raise the flap and form a high-compression shock system within the isolator without unstarting it. As is discussed below, a significant amount of separation still ensued upon raising the flap. However, it was possible in all three inlet / short-isolator models to create a high-compression shock system within the isolator by raising the flap alone. The formation and characteristics of these high-compression shock systems are the focus of this chapter. Results using fast-response wall pressure measurements and high-speed schlieren imaging are presented for the 0-degree inlet, 6-degree inlet and 8-degree inlet in sections

5.1, 5.2 and 5.3, respectively. Finally, a summary of the high-compression shock systems in each of the 6 models tested is provided.

5.1 0-DEGREE INLET / SHORT-ISOLATOR RESULTS

5.1.1 Fully Supersonic Started Flow (flap-fully down)

The mean (P_m) pressure distribution for the fully supersonic flow is shown in Fig. 5.1. Again, all pressures in this chapter are normalized by that measured at T1, which is assumed to equal the freestream pressure P_∞. Similar to the previous chapter, for the 0- and 8-degree results in this chapter, T3 was able to measure mean pressure values, but not able to faithfully track fluctuations due to a decreased frequency response. Also, as discussed in section 4.1.1, the T6 signal was able to measure pressure fluctuations but not mean pressures. Note that the T3 and T6 channels were behaving normally for the 6-degree results of this chapter. The mean pressure distribution of Fig. 5.1a shows the pressure to increase with increasing streamwise distance which is likely the result of boundary layer growth effects.

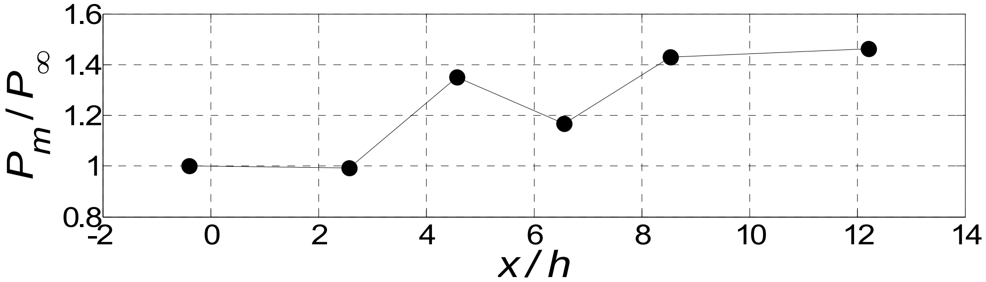

Figure 5.1 0-degree inlet / short-isolator fully supersonic started flow mean pressure distribution.

5.1.2 T7 Time History During High-Compression Shock Systems, Unstart and Unstarted Flows

Figure 5.2 shows the pressure time history recorded at T7 (x/h = 12.21) during a flap sequence resulting in the formation of high-compression shock systems, unstart and unstarted flow. In this section, various types of model flows are introduced. Futher discussion and details on these flows will follow in subsequent sections. In Fig. 5.2 from 0 to about 0.3 seconds, the flap is down and the flow is in the fully supersonic started mode. Next, the flap was raised to the angle of 39.4 degrees, which results in the gradual T7 pressure increase up until about 0.49 seconds. Following the gradual increase, a more rapid spike in pressure is seen in Fig. 5.2, which corresponds to the formation of a weak compression shock system in the isolator. Note that during both the gradual and rapid T7 pressure increases, the flap in not yet stationary, but still rising to the angle of 39.4 degrees. Following the rapid pressure increase, a relatively short lived T7 pressure plateau is seen to exist near 0.5 seconds. As will be shown with schlieren imaging, this short lived plateau corresponds to the formation of a weak compression system that remained stationary in the isolator for a time of about 25 ms. Following the weak compression system, the T7 pressure then increases once more until the time of about 0.51 seconds. At this time, the flap is stationary at the angle of 39.4 degrees, which results in the formation of what is termed the “stronger-compression shock system.” Then at 0.76 seconds the flap angle is increased to 40.4 degrees, which causes another step increase in T7 pressure. Next at 1.01 seconds, the flap angle is increased further to 41.3 degrees, which results in a more gradual T7 pressure increase. At 1.26 seconds, the flap is again raised to an angle of 41.7 degrees which results in another rise in T7 pressure. From about 1.26 to 1.51 seconds, the flow within the model is termed the “strongest-compression shock system,” since further increases in flap angle were seen to

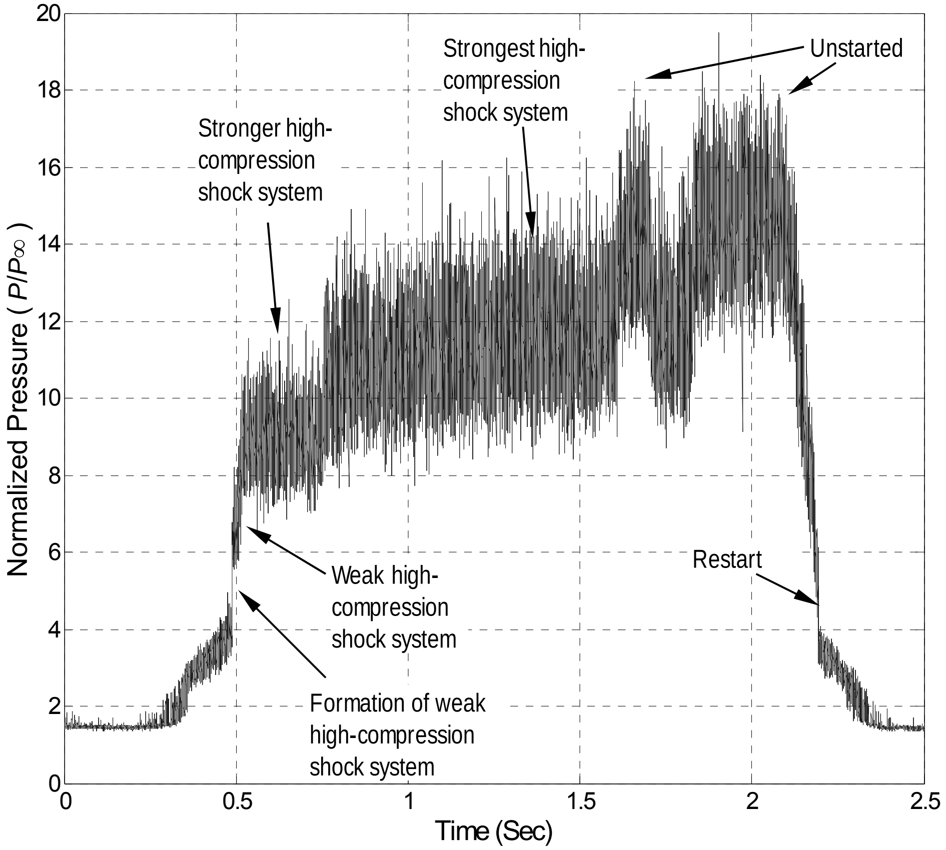

Figure 5.2 0-degree inlet / short-isolator T7 pressure time history corresponding to the formation of high-compression shock systems, unstarted flow and restart.

result in unstarted flow. For example at 1.51 seconds, the flap is raised to the angle of 42.2 degrees, where it remains until about 1.76 seconds. The step increase in pressure seen at about 1.6 seconds corresponds to the model unstarting. Again, the model is considered unstarted when an increase in T1 (x/h = 0.4) pressure is observed. A return to started high-compression shock system flow is then seen at about 1.7 seconds. This occurred "naturally" when the flap was stationary. Therefore, the flap angle of 42.2 degrees is a marginally stable position where either unstarted or high-compression shock system flow was possible. At 1.76 seconds the flap angle is again increased to the angle of 42.7 degrees which results in a return to unstarted flow. Finally, after 2 seconds the flap lowered to the fully-down position which eventually results in a complete restart of the inlet / isolator.

5.1.3 Schlieren Imaging and Pressure Measurements of High-Compression Shock Systems

Figure 5.3 presents a sequence of schlieren imgages (acquired with a horizontal knife-edge) showing the formation of high-compression shock systems as well as unstarted flow in the 0-degree inlet / short-isolator model. Figure 5.3a was taken at a time while the flap was raising to the angle θ_F of 39.4 degrees. In this image, the detached flap shock (arrow A) is seen to intersect the floor at the streamwise location x/h of about 11. Also, note that the flap shock appears to exit the isolator without impingement on the ceiling. The set up (formation) of a high-compression system in the 0-degree inlet / short-isolator model was similar to that seen at the beginning of unstart in the long isolator models. Namely, the formation process was seen to begin with separation of the ceiling boundary layer at the impingement location of the flap shock. An example of this is seen in Fig. 5.3b, which shows the flap angle is great enough to result in impingement of the flap shock (arrow B) on the isolator ceiling which results in the formation of a separation shock (arrow C). The combination of these two shocks marks the upstream boundary of the high-compression shock system. In subsequent images not shown here, the high-compression shock system propagates upstream in a similar manner to that seen in the case of unstart in the 0-degree inlet / long-isolator model (e.g., See Fig. 4.3). In fact, the upstream propagation velocity of the system in between T6 and T5 was measured to be 19.5 m/s (0.026 U_∞) which is also consistent with unstart in 0-degree / long-isolator model (e.g., See Fig. 4.18). The next schlieren image of Fig. 5.3c shows a weak compression shock system that remained in the isolator at a

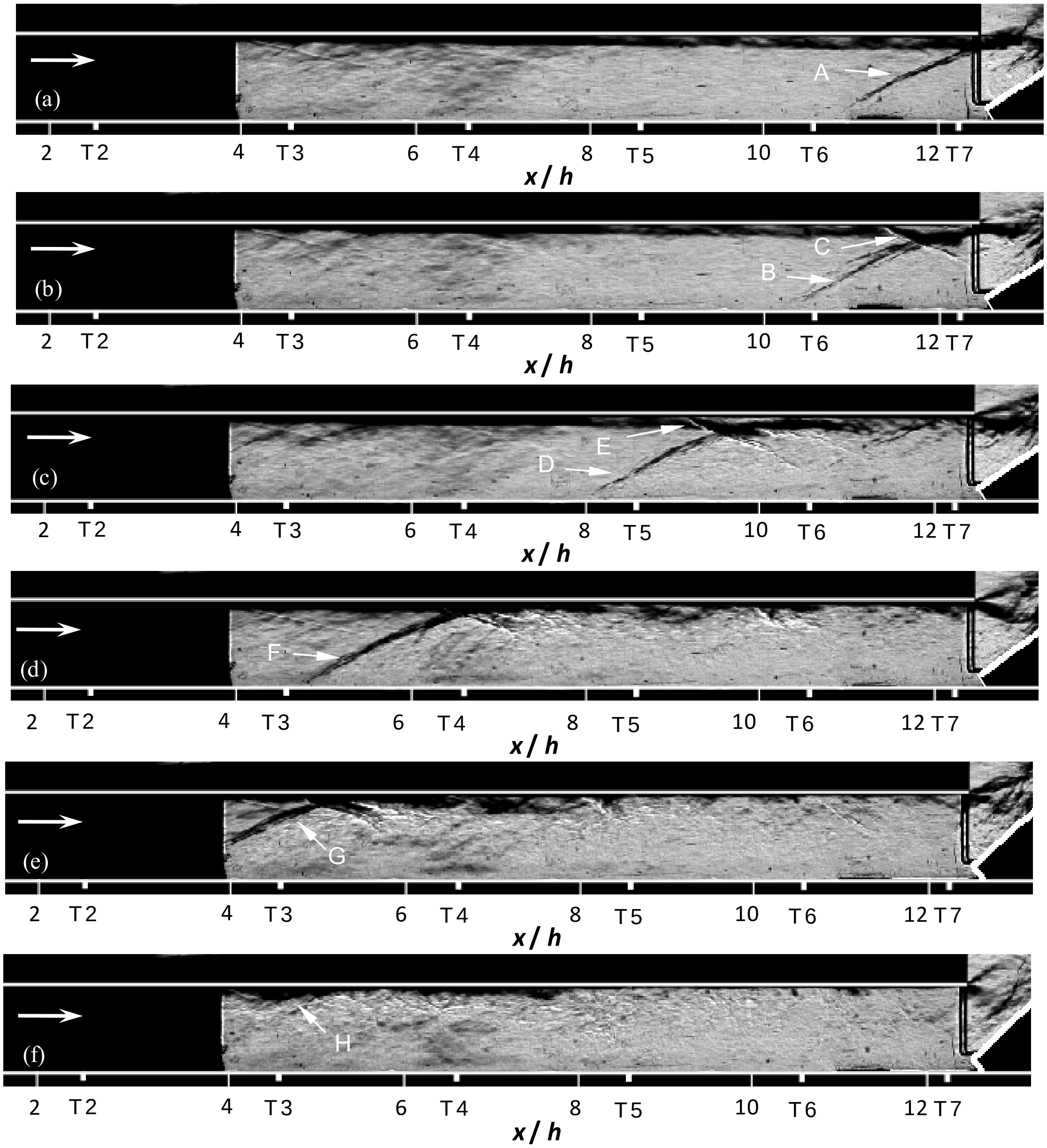

Figure 5.3 Schlieren images of high-compression shock systems in the 0-degree inlet / short-isolator model: a) prior to the set up of a high-compression system, b) set up of the weak system, c) flap rising, weak compression shock system, d) flap angle (θ_F = 39.4 degrees) stronger-compression shock system, e) θ_F = 41.7 degrees, strongest high-compression shock system, and f) θ_F = 42.7 degrees, unstarted flow.

near constant streamwise location for about 25 ms. This shock system is similar in structure to that observed in the unstart of 0-degree inlet / long-isolator model. The flow structure is the result of the upstream propagation of the flap shock (arrow D) and the boundary layer separation at its ceiling impingement location (arrow E). However, note that unlike the long-isolator unstart event, the high-compression shock system remains relatively stationary for about 25 ms. It is interesting to note that up until the formation of the short-lived weak compression shock system, the flow structure and propagation velocities are similar to those observed during unstart of the long isolator model. Recall, that the short isolator model was designed with the thought that a decreased amount of boundary layer separation at the isolator exit could allow for the formation of a stationary high-compression shock system in the model. However, the schlieren images show in both cases a very similar shock system to propagate upstream that is associated with similar levels of boundary layer separation. Therefore, the schlieren imaging does not suggest the extent of separation is lower in the short isolator model. Although, note that the side-view schlieren imaging is not expected to show sidewall separation. In the long isolators, the flap is partially enclosed by the isolator sidewalls, which should result in increased sidewall boundary layer interactions. In other words, in the long isolator, there is more sidewall surface area over which glancing interactions can occur, simply because it is longer than the short isolator. Thus, it is possible that glancing interactions near the exit of the long isolator are responsible for the fact that it was not possible to form a stationary high-compression system in the long isolator models by raising the flap alone. After the 25 ms short-lived weak compression shock system, and in between the times of images of 5.3c and 5.3d, the high-compression shock system was seen to propagate upstream maintaining a nearly constant flow structure as the flap angle continued to increase. In Fig. 5.3d, the flap has reached a stationary angle of 39.4 degrees, which results in the formation of the stronger-compression shock system labeled in Fig. 5.2. As seen in Fig. 5.3d, the leading shock (arrow F) of the stronger-compression shock system intersects the floor at about $x/h = 5$. The schlieren image in Fig. 5.3d corresponds to a time when the shock system was near its mean streamwise location. As will be shown, the high-compression systems discussed in this chapter were not seen to contain oscillatory (periodic) pressure fluctuations. However, the high-compression systems were observed to exhibit unsteady behavior. For example, the stronger-compression system of Fig. 5.3d fluctuated over a streamwise distance of about one isolator height, about the mean location.

Figure 5.4 shows the mean (P_m) and *RMS* (σ) pressures corresponding to the stronger-compression shock system of Figs. 5.2 and 5.3. Comparing the mean T3 ($x/h = 4.57$) pressure to that of the fully supersonic flow in Fig. 5.1, shows that the shock system remained downstream of T3. Figure 5.4a shows the mean pressure increases downstream of T3 in a nearly linear fashion. The pressure near the isolator exit at T7 is seen to be about 9 P_∞. In addition, Fig. 5.4b shows the pressure fluctuations are greatest at T6 ($x/h = 10.53$) and T7. Also, note that the *RMS* pressure at T4 ($x/h = 6.56$) is greater than that at T5 ($x/h = 8.54$). This is probably due to the fact that the leading shock (arrow F in Fig. 5.3d) fluctuates near the T4 location with downstream excursions of the stronger-compression shock system. Recall that Le et al. (2006 and 2008) also reported an increase in *RMS* pressure when the leading edge of a high-compression shock system (in their case a shock-train) was near a given pressure transducer location.

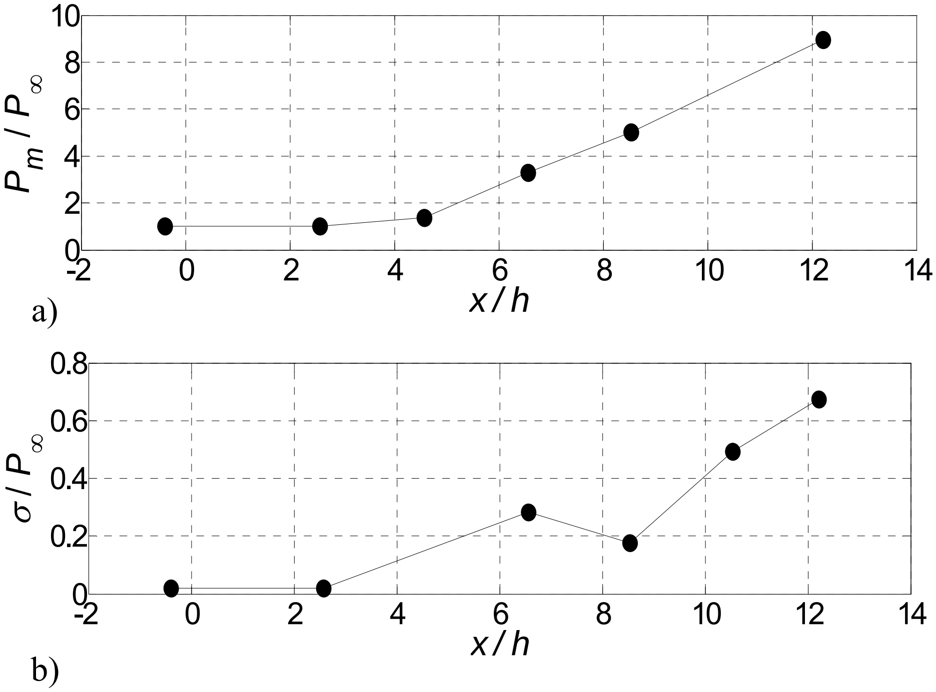

Figure 5.4 0-degree inlet / short-isolator stronger-compression system: a) mean pressure distribution and b) pressure standard deviation distribution (θ_F = 39.4 degrees).

Figure 5.5 compares the mean floor pressure distribution measured for the stronger-compression shock system to that predicted by the well known Waltrup and Billig correlation of Equation 1.8. The entrance pressure P_1 was taken to be the value measured at T3, which was the closest transducer still upstream of the high-compression shock system. The stream-thrust-averaged Mach number at the inlet entrance was calculated using equations 1.9 to 1.11, the freestream conditions given in section 2.1.1 ($M_\infty = 5.1$ conditions,) and the floor boundary layer properties given in section 2.2. The stream-thrust-averaged Mach number at the inlet entrance then computed to be 4.0, which was then used in equation 1.8. Note that the stream-thrust-averaged Mach number for the 0-degree case is lower than that computed for the 6-degree inlet which was found to be

4.3. This is because the 0-degree inlet ingested a greater proportion of boundary layer flow than the 6-degree inlet (75% compared to 55%). As previously discussed in section 3.9.4, the large spacing of the transducers made it impossible to definitively determine the leading edge location of the high-compression shock system. Therefore, a similar approach as described in section 3.9.4 was taken to approximate the leading edge location of the high-compression shock system. This approach involved assuming that the pressure at T4 could be predicted by the correlation. Therefore, the location of the upstream boundary of the high-compression system was determined in an iterative manner by varying its location such that the measured T4 pressure and T4 correlation-predicted-pressure were identical. Figure 5.5 shows that the semi-empirical Waltrup and Billig correlation gives reasonably good agreement with the measured pressure distribution. In addition, note that if the stream-thrust-averaged Mach number of 4.0 is used, Equation 1.14 predicts that an isolator aspect ratio greater than 3.17 should result in the separation-shock mode. Recall that if the displacement thickness of 9.1 mm is subtracted from the isolator height, the aspect ratio then computes to be 3.1. Therefore with this aspect ratio, the Penzin correlation of equation 1.14 predicts that the high-compression shock system in the 0-degree inlet / long-isolator should be a pseudo-shock. This is in agreement with the wall pressure distribution seen in Fig. 5.5. However, it is noted that there is a high level of uncertainty in generating the correlation curve itself. To show this, Fig. 5.5 also gives upper and lower correlation limits which form a correlation band. The upper limit curve was generated using the upper uncertainty pressure level at T3 ($P_m + 0.43P_\infty$). Similarly, the lower limit curve was generated with the lower uncertainty level pressure ($P_m - 0.43P_\infty$). Fig 5.5 shows that each measured pressure value is well within the uncertainty bands. However, the relatively wide spacing of the bands makes it difficult to say just how well the measured pressures agree with the correlation.

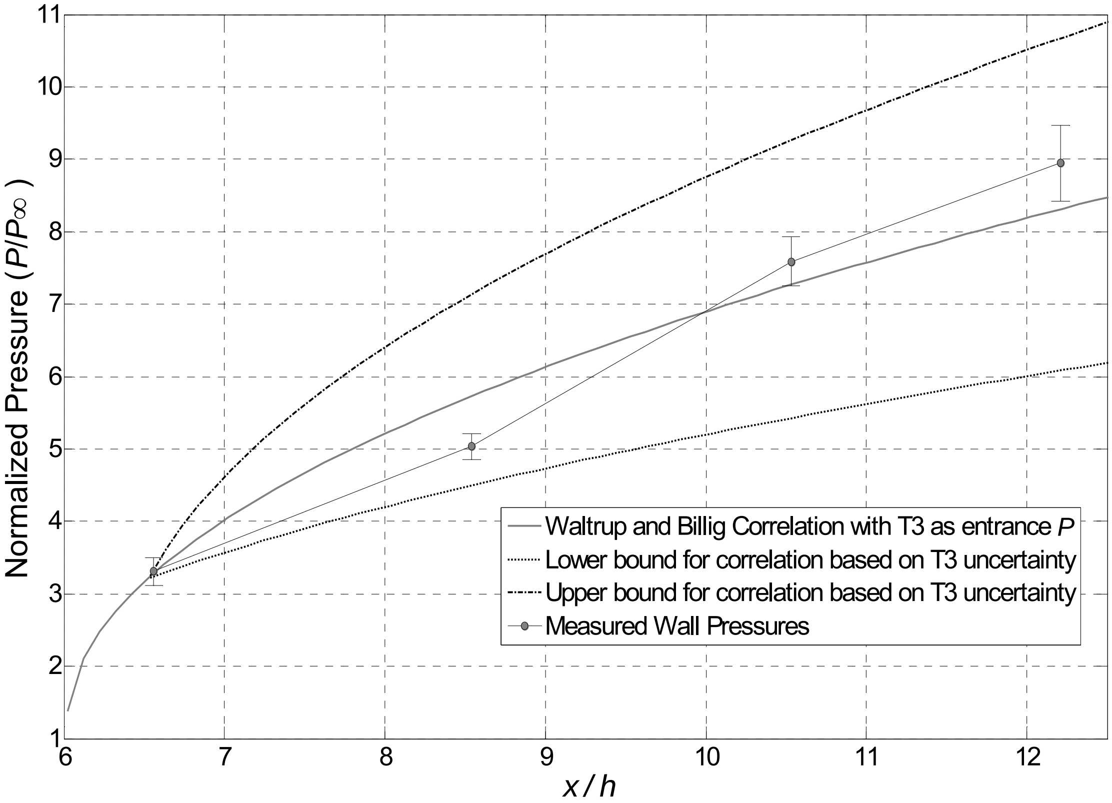

Figure 5.5 Comparison of the stronger-compression shock system pressure distribution in the 0-degree inlet / short-isolator to that predicted by the pseudo-shock (shock-train) correlations of Waltrup and Billig (1973).

Again as seen in Fig. 5.2, following the stronger-compression shock system flow, the flap was raised to the angle of 41.7 degrees to generate the strongest-compression shock system. Recall that this name was chosen as it was the maximum strength compression system that could be maintained in the model without unstart occurring. Figure 5.3e shows a schlieren image corresponding to this flow. The leading shock (arrow G) has propagated into the aluminum “inlet” section of the model. The structure of this leading shock is similar to that seen in the images of Fig. 5.3c and Fig. 5.3d. Although not shown here, the pressure time histories of T2 (*x/h* = 2.58) and T1 (*x/h* = -0.4) indicated that this high-compression system resided somewhere between the two transducers. Figure 5.6 presents the pressure power spectra for T1, T2 and T7 of the strongest-compression shock system flow. For the spectra, the acquisition rate was 25 kHz and the number of samples taken was 6,250, which gives a maximum frequency of 12.5 kHz and a resolution of 4 Hz. The spectra correspond to the same run as that in Figs. 5.2 and 5.3e and were acquired over the time span of 1.25 to 1.5 seconds. The broadband nature of the spectra suggest that this high-compression shock system is non-oscillatory. The peak seen in the T1 spectrum is due to 60 Hz noise. As was discussed in section 2.3.1, the noise floor of the pressure measurements system was too great to make meaningful measurements in the undisturbed boundary layer. However, this spectrum is included for later comparison to unstarted flows. Note that the inlet T2 peak *SPL* levels are greater than that at the isolator exit location of T7. Recall that Le et al. (2006 and 2008) reported an increase in power spectra peaks when the leading edge of a high-compression shock system (in their case a shock-train) was near a given pressure transducer location. Therefore, the greater T2 spectral levels are consistent with the leading shock being in close vicinity to T2. Note that this also appears to be the case upon inspection of the schlieren image of Fig. 5.3e.

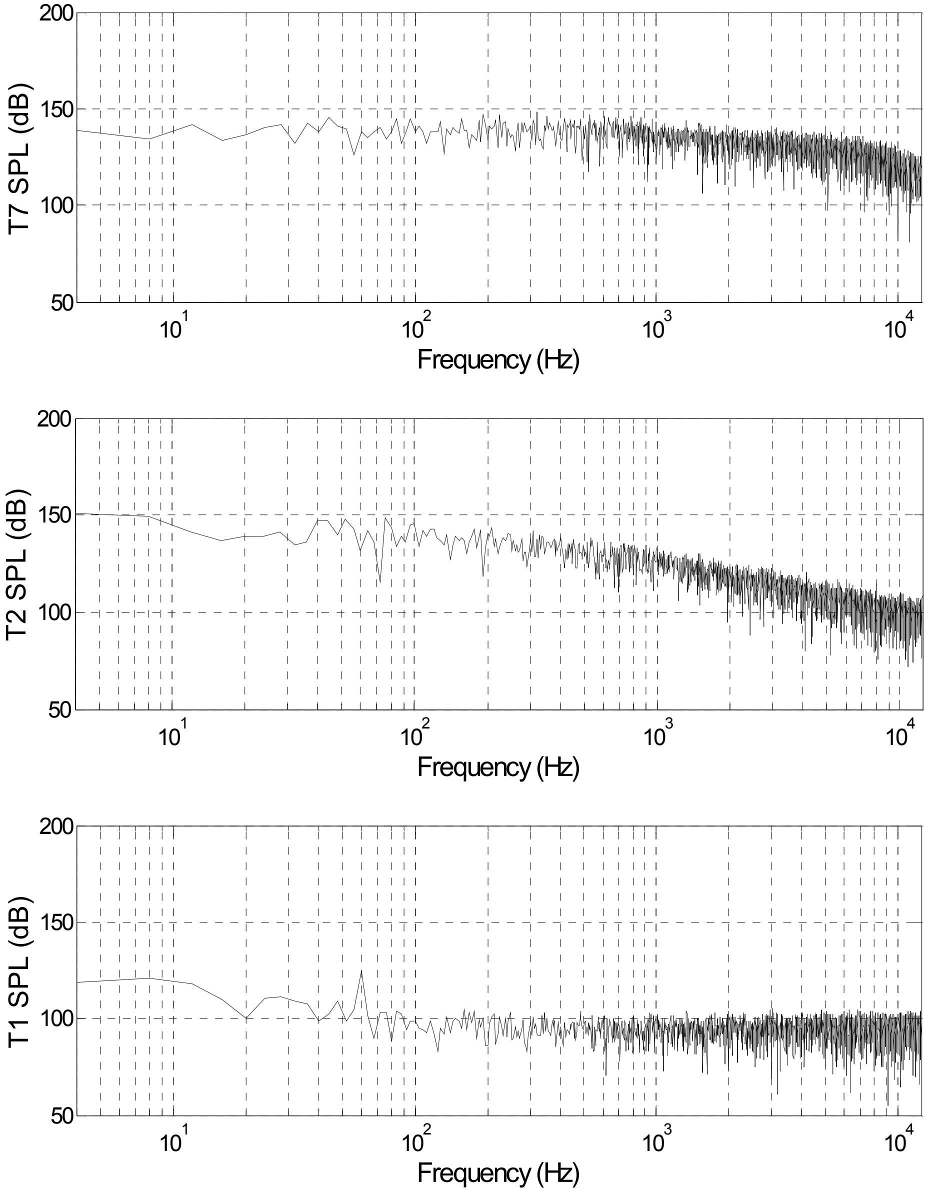

Figure 5.6 Power spectra of the pressure at T7, T2 and T1 for the 0-degree inlet / short-isolator stronger-compression shock system flow (θ_F = 39.4 degrees).

Figure 5.7 presents the mean and *RMS* pressure distributions for the strongest-compression shock system. The mean distribution of Fig. 5.7a shows the pressure at T2 to be slightly elevated compared to the started flow. Farther downstream, the pressure then increases in a nearly linear manner throughout the entire model and the exit (T7) pressure is nearly 12 P_∞. The *RMS* distribution of Fig. 5.7b shows T2 has elevated fluctuations, which is also consistent with the leading shock residing somewhere in the vicinity of the transducer. Note that the fluctuations are greater than those at the nearest downstream measurement location of T4. Finally, similar to the stronger-compression system, the maximum *RMS* pressures are seen to occur near the exit at T6 and T7.

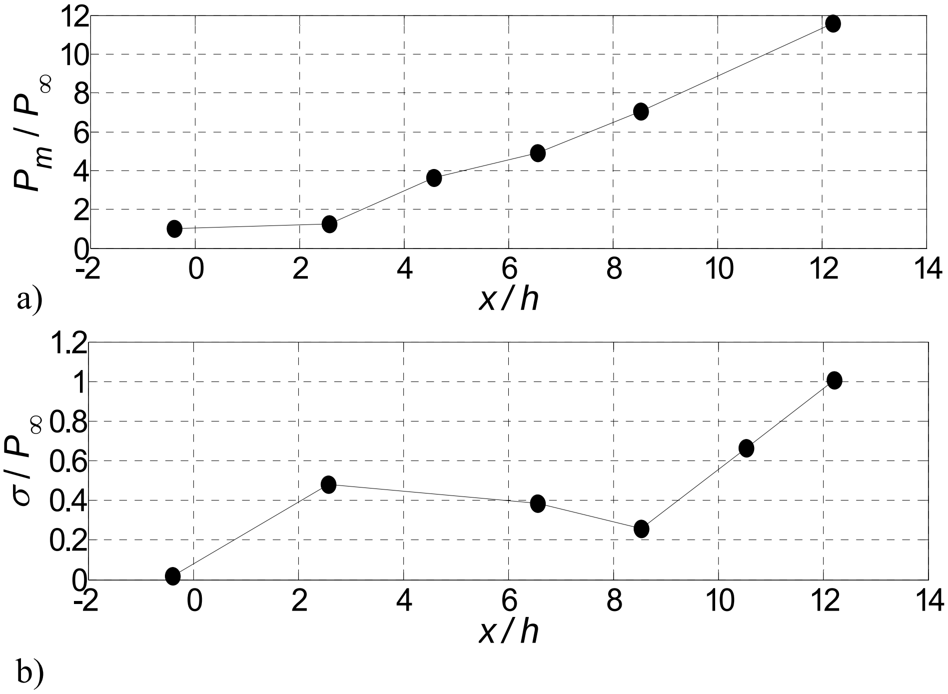

Figure 5.7 0-degree inlet / short-isolator strongest-compression system: a) mean pressure distribution and b) pressure standard deviation distribution (θ_F = 41.7 degrees).

Following the strongest-compression shock system, the flap was raised to unstart the model as was seen in Fig. 5.2. Again, the model is considered unstarted when the pressure at T1 (x/h = -0.4) is elevated with respect to the started pressure. Figure 5.3f show a schlieren image corresponding to the unstarted flow. The leading shock has moved upstream completely out of the visible isolator section. It is likely that the leading shock now impinges somewhere on the aluminum "inlet" ceiling. This is supported by the presence of a separated ceiling boundary layer (arrow H) near the entrance of the visible isolator section. The mean and *RMS* pressures are given in Fig. 5.8. Fig. 5.8a shows the mean pressure increases in a nearly linear fashion with increasing streamwise distance. The exit (T7) pressure is about 14 P_∞. The *RMS* pressure shows the trend of increasing fluctuations with increasing streamwise distance with the exception of that at T5 (x/h = 8.54).

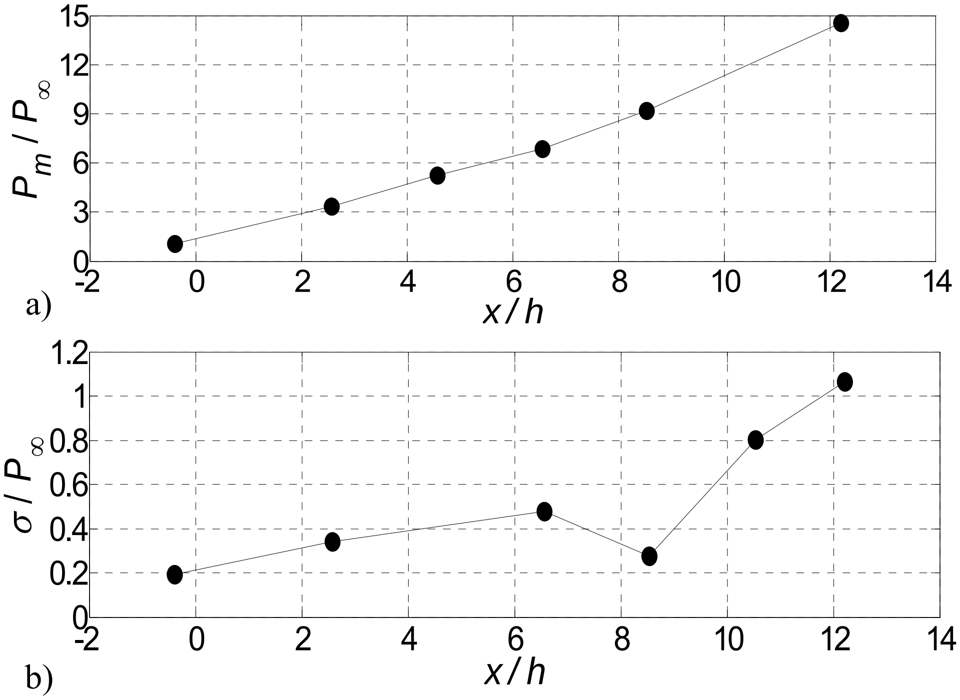

Figure 5.8 0-degree inlet / short-isolator non-oscillatory unstarted flow: a) mean pressure distribution and b) pressure standard deviation distribution.

Finally, in Fig. 5.9 the power spectra at T7, T2 and T1 are presented for the unstarted flow. For the spectra, the acquisition rate was 25 kHz and the number of samples taken was 5,000, which gives a maximum frequency of 12.5 kHz and a resolution of 5 Hz. The spectra correspond to the same run as that in Figs. 5.2 and 5.3f and were acquired over the time span of 1.9 to 2.1 seconds. The broadband nature of the spectra suggests that the unstarted flow is non-oscillatory. The highest *SPL* values occur at T7 near the isolator exit. Comparing the T1 spectrum of this unstarted flow to that in Fig. 5.6 where T1 was upstream of any shock system shows that the unstarted flow substantially increases the T1 *SPL* values.

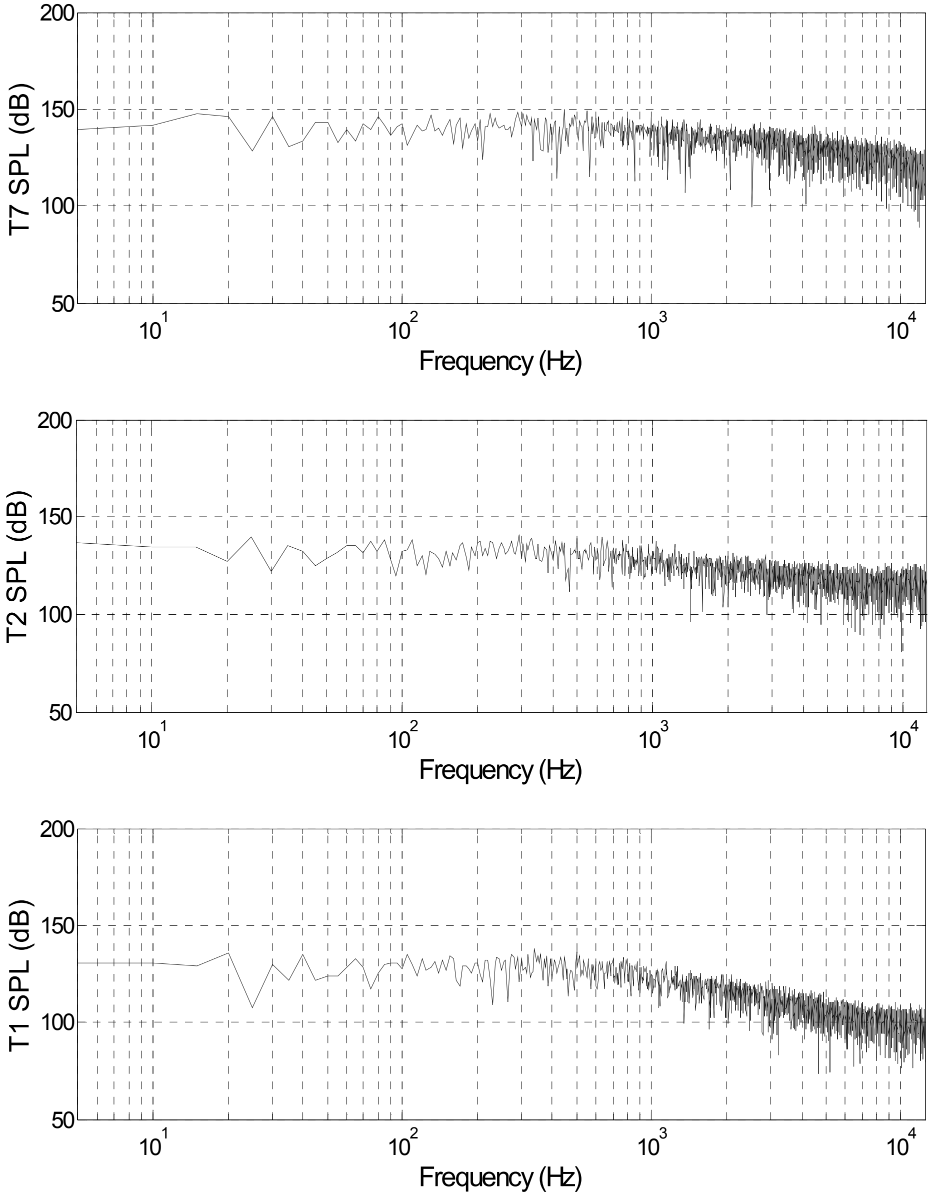

Figure 5.9 Power spectra of the pressure at T7, T2 and T1 for the 0-degree inlet / short-isolator non-oscillatory unstarted flow.

5.2 6-DEGREE INLET / SHORT-ISOLATOR RESULTS

5.2.1 Fully Supersonic Started Flow (flap-fully down)

The mean and *RMS* pressure distributions for the 6-degree inlet / short-isolator fully supersonic started flow are shown in Fig. 5.10. In addition, a schlieren image corresponding to this flap-fully down flow can be seen in 5.11a. All three compression ramp shock reflections can be seen in this image as labeled with arrows A, B and C. As is expected, both the schlieren image and the pressure distributions are very similar to those of the 6-degree / long-isolator case (e.g., See Figs. 3.1 and 3.2). Therefore, in the interest of brevity, a lengthy discussion of this flow will not be given here. More details on this flow are given in section 3.1, where the same reasoning should apply to the current section.

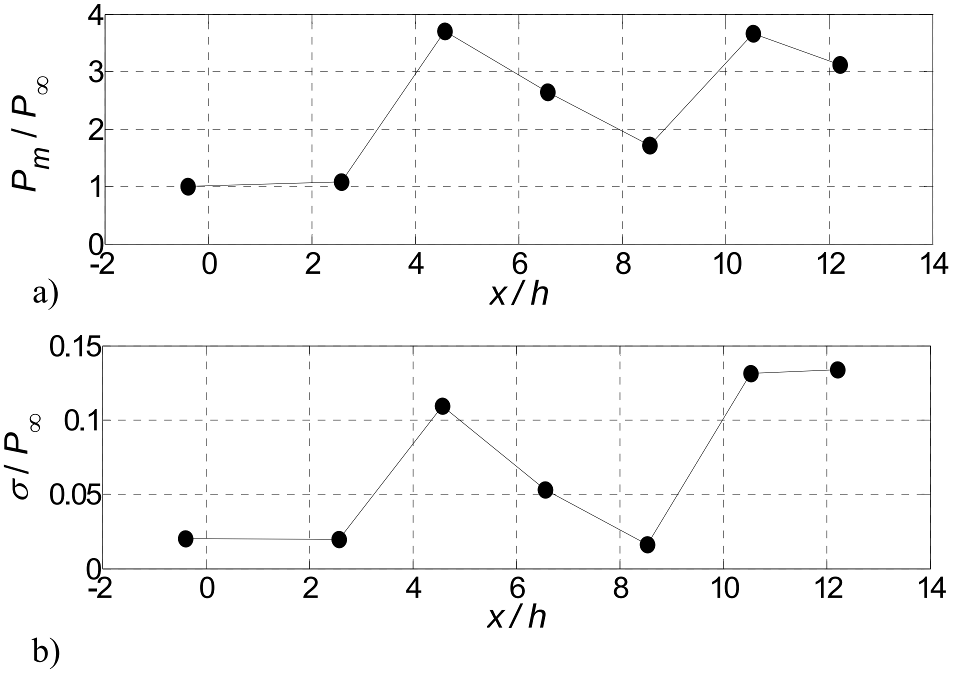

Figure 5.10 6-degree inlet / short-isolator fully supersonic started flow: a) mean pressure distribution and b) pressure standard deviation distribution.

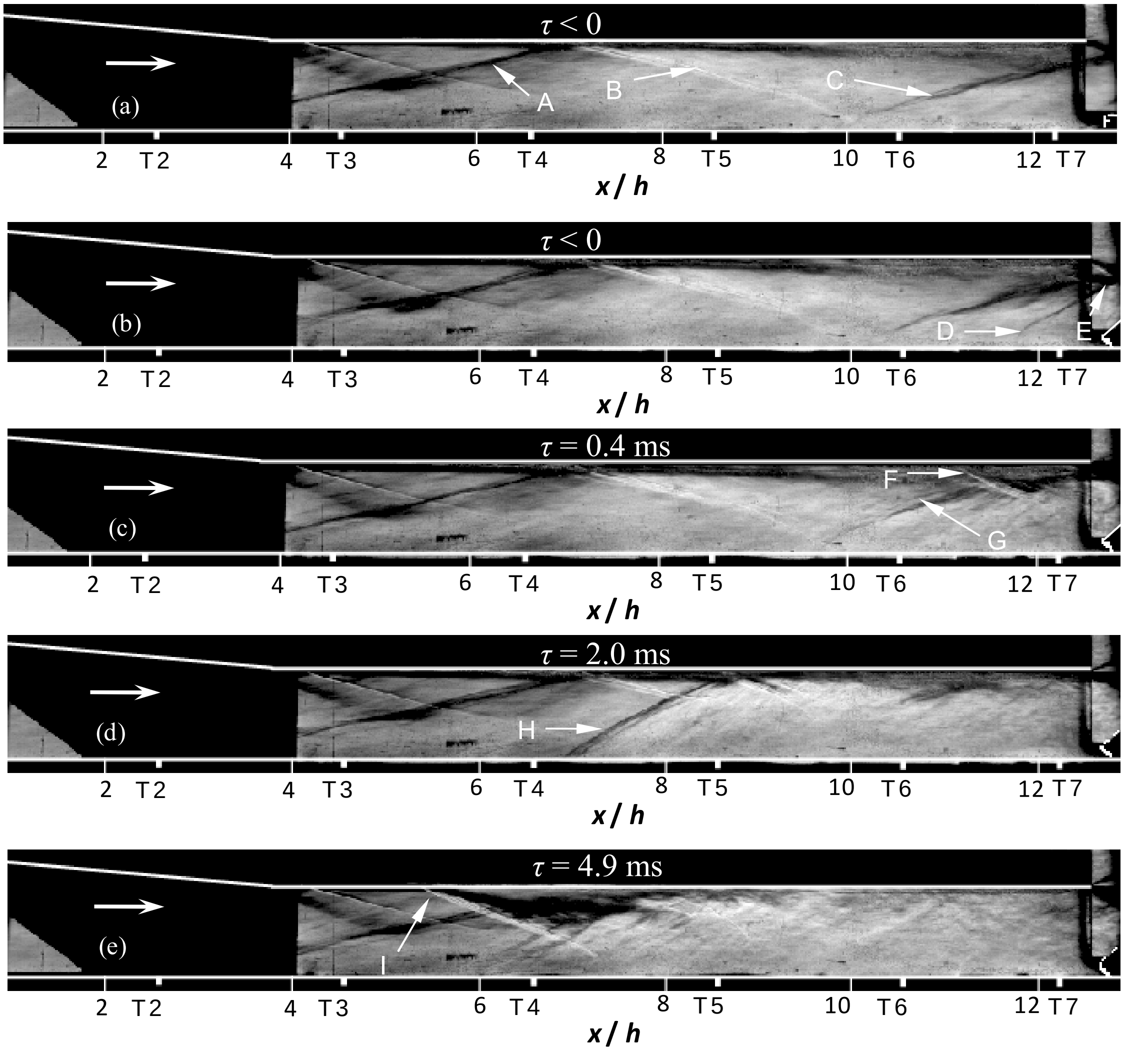

Figure 5.11 Schlieren images showing the set up of the oscillatory high-compression shock system in the 6-degree-inlet / short-isolator model: a) fully supersonic flow (flap-down), b) τ < 0, flap rising rising prior to the onset of the compression system set up process, c) τ = 0.4 ms into the set up of the compression system, d) τ = 2.0 ms into the set up of the compression system, and e) τ = 4.9 ms into the set up of the compression system (θ_F = 41.3 degrees).

5.2.2 T7 Time History During an Oscillatory High-Compression Shock System, Unstart and Unstarted Flows

Upon raising the flap, it was also possible in this short-isolator model to form a high-compression shock system without unstart occurring. Again, this was not possible in the long-isolator case. Figure 5.12 shows the pressure time history at T7 during the formation of a high-compression shock system, unstart and unstarted flow. Up until the time of about 0.1 seconds the flap is fully-down and the flow is in the fully supersonic started mode. From about 0.1 to 0.45 seconds, the flap angle is increased to 40.4 degrees which results in a gradual increase in T7 pressure. Next, at about 0.45 seconds, the flap is raised to 41.3 degrees. It takes about 100 ms for the flap to go from 40.4 to 41.3 degrees, which means the flap is stationary at about 0.55 seconds. Note that after the flap reaches 41.3 degrees at about 0.55 seconds, the flow within the isolator remains fully supersonic except behind the flap shock at the isolator exit. Next, at about 0.7 seconds a spike in pressure can be seen. This spike occurs when the flap is stationary. As will be discussed, this pressure increase corresponds to the formation of what is seen to be an "oscillatory high-compression shock system." Since the flap was stationary, this indicates that from about 0.55 to 0.7 seconds, the model flow was marginally stable. Therefore the formation of the high-compression system during this run is analogous to the "natural" unstart events discussed in section 3.4 (although in the current case the model does not unstart, rather a high-compression shock system is formed). The pressure fluctuations of about 15 P_∞ that exist from 0.7 to about 1.2 seconds correspond to the oscillatory high-compression shock system. Next, at a time of about 1.2 seconds the flap is instructed to increase its angle to 42.7 degrees. Inspection of the T1 pressure time history indicated that from about 1.2 to 1.65 seconds the flow was unstarted. This unstarted flow was also seen to be oscillatory and is termed "lower-amplitude oscillatory unstarted flow." Lastly, at a time of about 1.7 seconds the flap begins to lower and the flow eventually restarts.

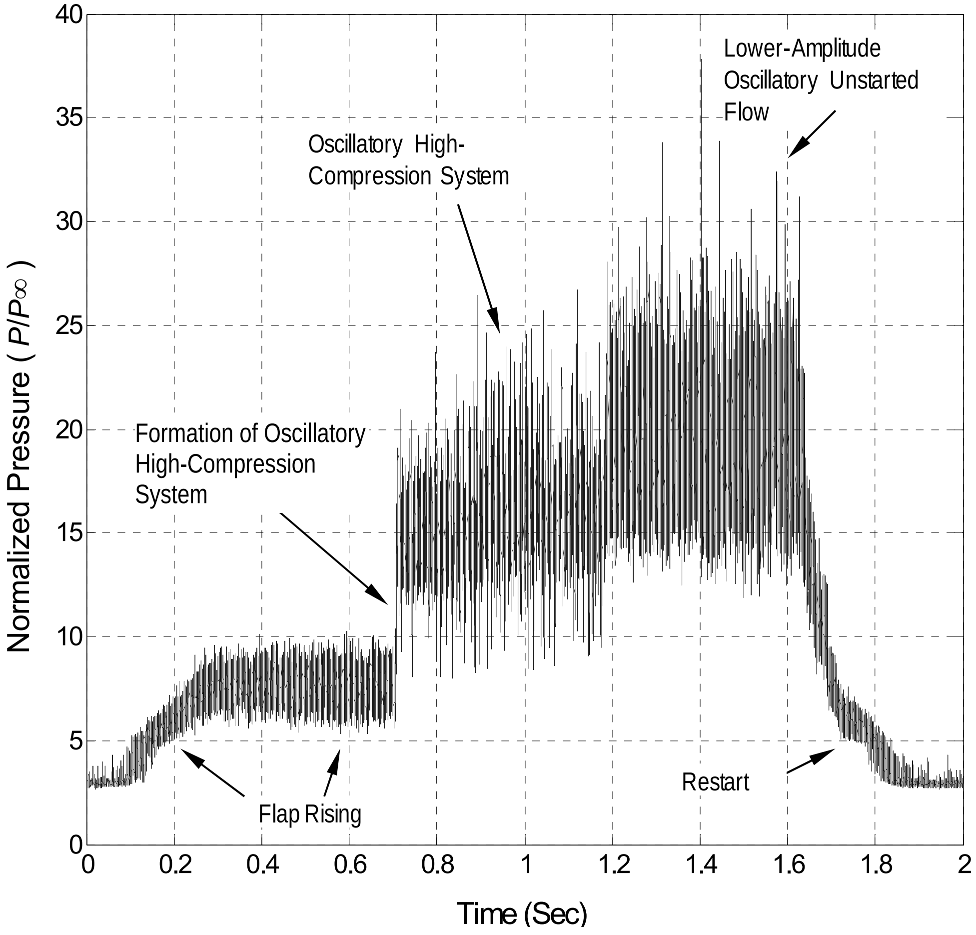

Figure 5.12 6-degree inlet / short-isolator T7 pressure time history corresponding to the formation of high-compression shock systems, unstarted flow and restart.

5.2.3 Schlieren Imaging and Pressure Measurements of the Oscillatory High-Compression Shock System and Lower-Amplitude Oscillatory Unstarted Flow

Figure 5.11 presents a schlieren image sequence (acquired with a horizontal knife-edge) showing the formation of the oscillatory high-compression shock system. Figure 5.11b shows the isolator flow when the flap is raised, but not to an angle great enough to induce the formation of the high-compression shock system. In this image a detached flap shock (arrow D) is seen. Note that this shock leaves the isolator without ceiling impingement. However, downstream of the isolator exit, the flap shock and fourth ramp shock reflection intersect and interact (arrow E). The next image of Fig. 5.11c was acquired at $\tau = 0.4$ ms into the formation of the compression system process. Note that $\tau = 0$ corresponds to the onset of the formation process. This onset was determined from the schlieren imaging in a fashion analogous to that discussed in section 3.5.1. Figure 5.11c shows that like the unstart process, the formation of the high-compression shock system begins with ceiling boundary layer separation (arrow F). This image also shows that the flap shock (arrow D in Fig. 4.11b) and third compression ramp shock reflection (arrow C in Fig. 4.11a) have coalesced into a single shock (arrow G). At $\tau = 2.0$ ms (Fig. 5.11d), the leading shock (arrow H) of the high-compression shock system has propagated to the floor location of about $x/h = 7$. Figure 5.11e acquired at at $\tau = 4.9$ ms, shows the high-compression shock system has moved upstream with separation of the ceiling boundary layer (arrow I). Note the flow structure in the current image sequence is nearly identical to that observed in the unstart process of the 6-degree inlet / long-isolator (e.g., see Fig. 3.8 and Fig. 3.9).

The propagation velocities of the high-compression shock system were computed in order to compare to those measured during unstart in the long-isolator model. Ten different runs involving the formation an oscillatory high-compression shock system were used to generate average propagation velocities between T6 (*x/h* = 10.53) and T5 (*x/h* = 8.54), as well as between T5 and T4 (*x/h* = 6.56). The velocities are summarized below in Table 5.1. The table shows that to within the 95 % uncertainty limits, the propagation velocity during unstart of the 6-degree / long-isolator model is identical to the propagation velocity during the formation of the 6-degree inlet / short-isolator high-compression system. This result in combination with the fact that the flow structure of both processes is nearly identical, suggests that similar physical mechanisms drive the dynamics and flow structure of both unstart and the formation of the high-compression shock system. Of course the main difference in the two processes is the fact that in the short-isolator case, the high-compression system remained in the isolator, whereas in the long-isolator case, the shock system always propagated upstream resulting in unstart. The similar flow structure suggests that the extent of shock-induced separation is similar in both processes. However, similar to the argument made in the comparison of the two 0-degree models above, the difference in the ability of the 6-degree models to contain internal high-compression shock systems by raising the flap alone might be explained by the fact that the flap is enclosed by the side walls of the long-isolator model. In other words, the flow at the exit of the longer isolator is subjected greater areas of glancing interactions.

Table 5.1 Comparison of average propagation velocities in the isolator of unstart in the 6-degree inlet / long-isolator and the formation of a high-compression system in the 6-degree inlet / short-isolator.

Transient Process and Model	$V_{T6\text{-}T5}$, m/s	$V_{T5\text{-}T4}$, m/s
6-degree / long-isolator unstart	35 ± 5	34 ± 10
6-degree / short-isolator set up of high-compression shock system	33 ± 7	36 ± 11

Figure 5.13 shows examples of oscillations of the high-compression shock system in the 6-degree inlet / long-isolator model. Note that the image of 5.11 corresponds to a time when the shock-system is near its mean streamwise location. Figures 5.13a and 5.13b give an example of an upstream streamwise excursion and of a downstream excursion seen during an oscillation of the shock system. Figure 5.13b was acquired 1.8 ms after Fig. 5.13a. It can be seen that the upstream oscillation is clearly associated with a significant increase in ceiling boundary layer separation, whereas the downstream oscillation is associated with a reattachment of the ceiling boundary layer. In Fig 5.13b, the leading shock has propagated downstream to intersect the floor near $x/h = 8$. In 5.13a the leading shock has propagated along the ceiling with separation at about $x/h = 4$. Therefore, oscillations of the high-compression shock system result in streamwise translations of about $4h$.

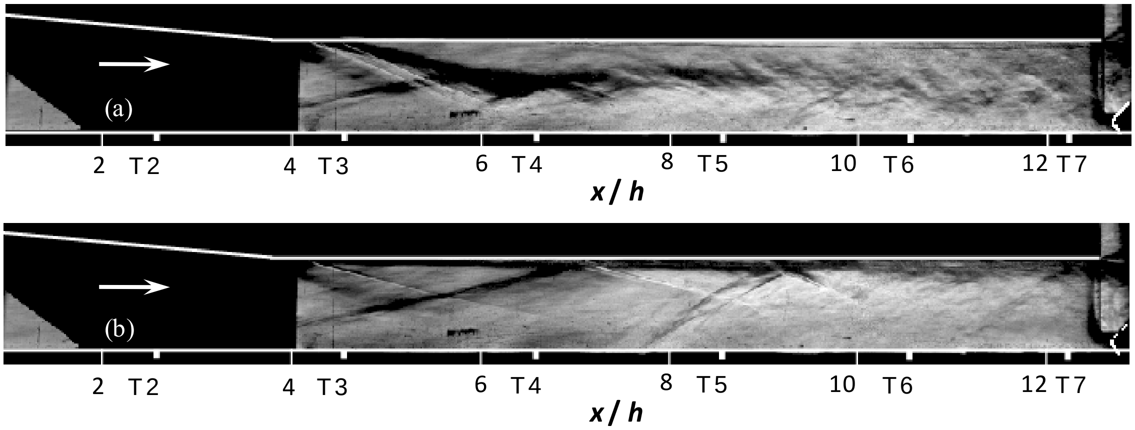

Figure 5.13 Schlieren images showing streamwise excursions of the oscillatory high-compression shock system: a) upstream excursion, and b) downstream excursion taken 1.8 ms after the image of Fig. 5.13a (θ_F = 41.3 degrees).

The mean and *RMS* pressures corresponding to the oscillatory high-compression shock system are given in Fig. 5.14. Figure 5.14a shows that the pressures at T1 (*x/h* = -0.4) to T3 (*x/h* = 4.57) are the same as the started flow pressures shown in Fig. 5.10. This indicates that the oscillatory high-compression system always resides downstream of *x/h* = 4.57. From T4 (*x/h* = 6.56) to the isolator exit, the pressure increases with a nearly linear trend. The pressure near the isolator exit at T7 is 15.6 P_∞. Figure 5.14b shows the pressure fluctuations downstream of *x/h* = 4.57 increase substantially due to the high-compression shock system. For example, the *RMS* pressures downstream of the compression system are all about 2 P_∞.

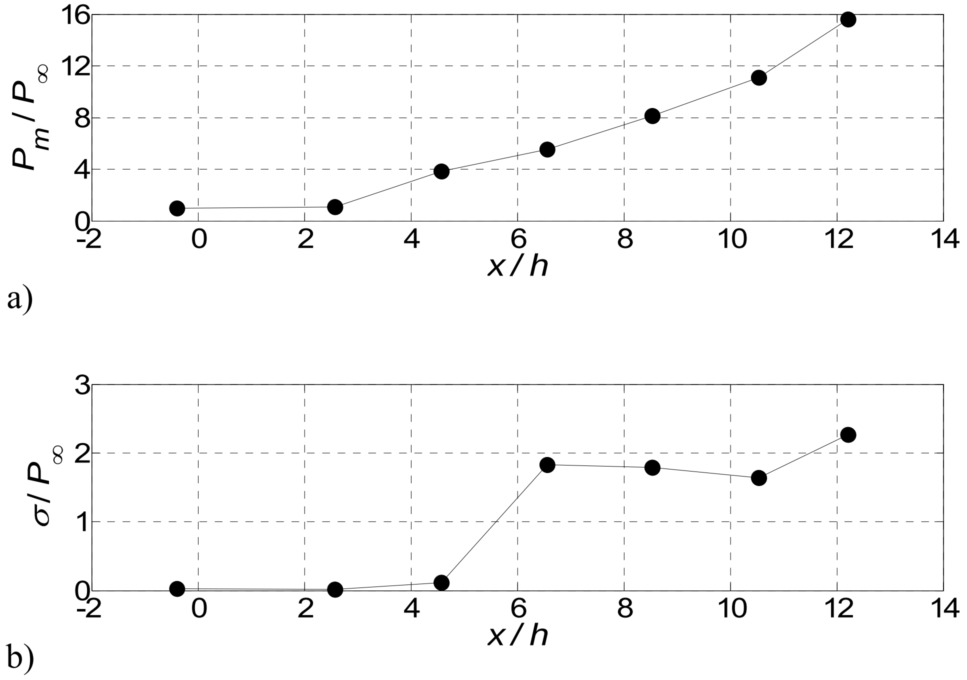

Figure 5.14 6-degree inlet / short-isolator oscillatory high-compression shock system: a) mean pressure distribution and b) pressure standard deviation distribution ($\theta_F = 41.3$ degrees).

In order to demonstrate the oscillatory nature of the 6-degree inlet / short-isolator high-compression system, power spectra for this flow at T7, T6 and T5 are given in Fig. 5.15. For the spectra, the acquisition rate was 25 kHz and the number of samples taken was 8,750, which gives a maximum frequency of 12.5 kHz and a resolution of 2.9 Hz. The spectra correspond to the same run as that in Figs. 5.12 to 5.14 and were acquired over the time span of 1.8 to 2.15 seconds. Each one of the isolator transducers shown has a peak *SPL* value at the dominant frequency of 89 Hz (f *=0.078). The *SPL* peaks corresponding to T7, T6 and T5 were measured to be 163.1, 160.2 and 162.8 dB respectively. Recall that the frequency is normalized as $f^* = f L / a_0$ (where $a_0 / L = 1154$ Hz), which would be appropriate for a purely acoustic oscillation. Similar to the discussion of unstarted flows in previous chapters, the fact that the dominant frequency of the oscillatory high-compression system is significantly lower than purely acoustic frequencies is to be expected since a supersonic flow always enters the inlet for this flow.

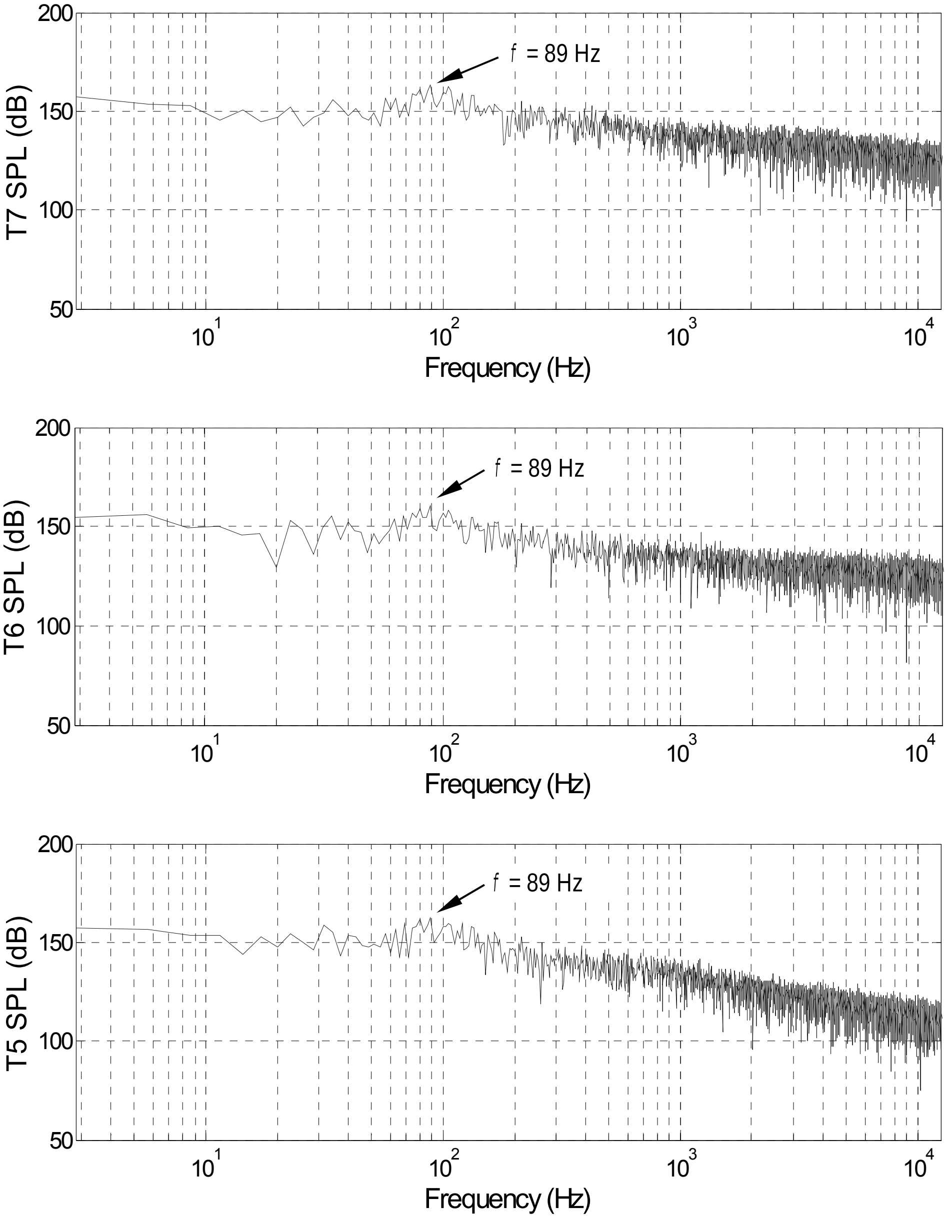

Figure 5.15 Power spectra of the pressure at T7, T6 and T5 for the 6-degree inlet / short-isolator oscillatory high-compression shock system flow.

Finally, as seen in Fig. 5.12, following the oscillatory high-compression shock system, the model was unstarted by raising the flap to the angle of 42.7 degrees. As will be discussed, pressure fluctuations during this unstarted flow were seen to be oscillatory. Figure 5.12 shows T7 oscillations up to about 20 P_∞ that are similar in magnitude to those observed in previously defined lower-amplitude oscillatory unstarted flows. Therefore, this unstarted flow is also termed lower-amplitude oscillatory unstarted flow. Figure 5.16 shows the mean and *RMS* pressures corresponding to this unstarted flow. In comparison to the started pressures of Fig. 5.10, Fig. 5.16a shows the pressure at each transducer is elevated. The mean pressure increases with increasing downstream distance to about 19 P_∞ near the isolator exit (T7). Figure 5.16b shows that the *RMS* pressure fluctuations are about 1 P_∞ at T2 to T5 (*x/h* = 4.57), and *RMS* about 2-3 P_∞ at T6 (*x/h* = 10.53) and T7 (*x/h* = 12.21).

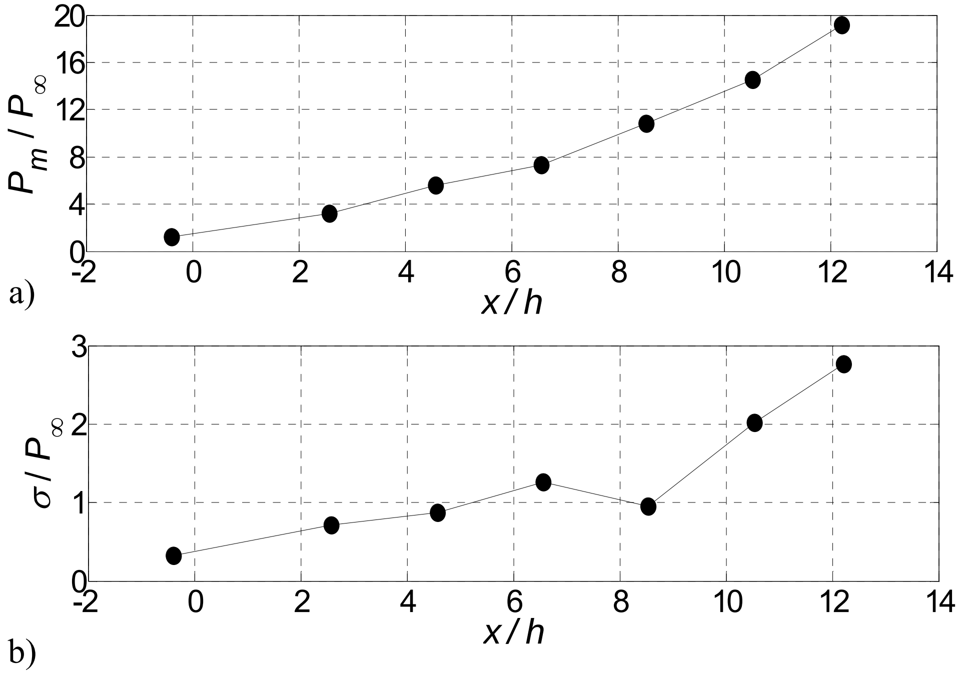

Figure 5.16 6-degree inlet / short-isolator lower-amplitude oscillatory unstarted flow: a) mean pressure distribution and b) pressure standard deviation distribution.

Figure 5.17 shows the pressure power spectra at T7, T2 and T1 for the lower-amplitude oscillatory unstarted flow. For the spectra, the acquisition rate was 25 kHz and the number of samples taken was 6,250, which gives a maximum frequency of 12.5 kHz and a resolution of 4 Hz. The spectra correspond to the same run as that in Figs 5.12 and were acquired over the time span of 1.35 to 1.6 seconds. The peak *SPL* values at T7, T2 and T1 are 165.4, 153.2 and 143.7, respectively. The dominant frequency at T7 and T2 is 284 Hz (f *=0.25) and the dominant frequency at T1 is 312 Hz (f *=0.27). Interestingly, for this unstarted flow, the dominant frequencies are near that corresponding to an ideal quarter-wave resonator. Note that experimental (Yuceil, 1995) and computational (Engblom, 1996, and Silton and Goldstien, 2005) studies have shown forward facing cavities in a supersonic flow to oscillate near f *=0.25 as well. In these studies, a bow shock upstream of the cavity entrance ensured that subsonic flow entered the cavity. Therefore, it was clear as to why the cavity should act as quarter-wave resonator. For the current unstarted flow the reasoning behind the near quarter-wave frequency does not appear to be as obvious. A possible explanation to explain the similarities between the current unstarted flow and the forward facing cavity flow frequencies is discussed below.

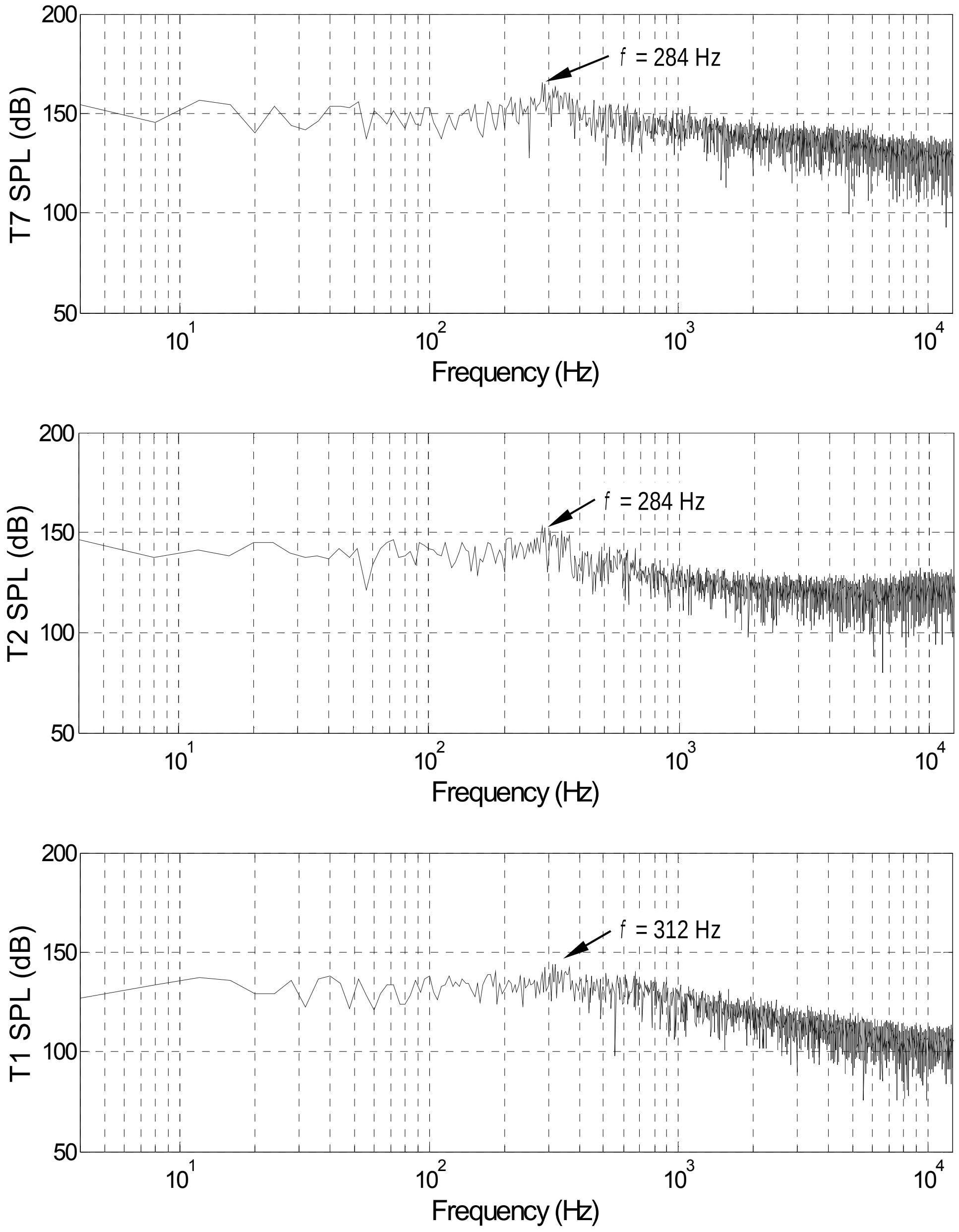

Figure 5.17 Power spectra of the pressure at T7, T2 and T1 for the 6-degree inlet / short-isolator lower-amplitude oscillatory unstarted flow.

Figure 5.18 shows a schlieren image (acquired with a horizontal knife edge) corresponding to the lower-amplitude oscillatory unstarted flow. During this unstarted flow, a strong oblique shock (arrow A) is seen to oscillate near the inlet entrance. This

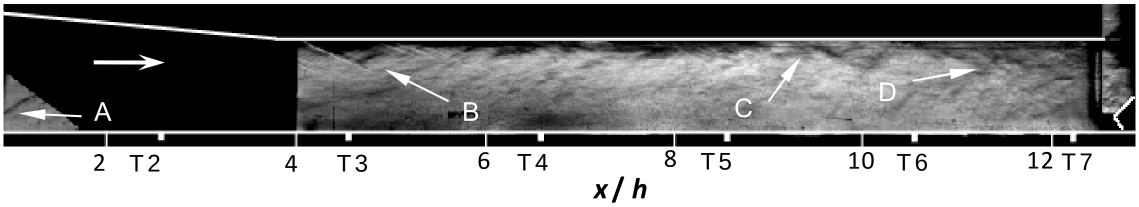

Figure 5.18 Schlieren image (acquired with a horizontal knife-edge) showing the lower-amplitude oscillatory unstarted flow in the 6-degree inlet / short-isolator model.

oscillating oblique shock impinges on the inlet ceiling and appears to result in a separated ceiling flow near the isolator entrance (arrow B). What appear to be eddy shocklets are present near the ceiling near the streamwise center of the isolator (arrow C) as well as at the isolator exit (arrow D). The presence of these shocklets indicates that high speed fluid travel near the isolator ceiling all the way until the exit. On the contrary the flow along in the lower wall-normal half of the isolator is seen to be shock free and quiescent. This suggests the flow in the lower wall-normal portion of the isolator is predominantly subsonic. The subsonic flow is most likely a result of the strong oblique shock at the inlet entrance and subsequent separation. With this subsonic flow, acoustic waves would be able to freely propagate in the subsonic portions of the isolator flow. Note that in this unstarted flow, the strong oblique shock is observed to always reside upstream of the inlet or within the inlet section. In other words, unlike the high-amplitude oscillatory unstarted flow discussed in section 3.6, the isolator entrance flow did not appear to go supersonic during parts of the cycle. Perhaps this explains why the current unstarted flow of discussion oscillates near the purely acoustic quarter-wave resonator frequency and the high-amplitude oscillatory unstarted flow of the 6-degree inlet / long-isolator flow oscillated at lower than acoustic frequencies. Still, some questions remain. The first has to do with the non-oscillatory unstarted flow described in section 3.7. In the non-oscillatory unstarted flow of the 6-degree inlet / long-isolator model, an oblique was also always observed upstream of the inlet (e.g, See Fig. 3.28). This shock was also seen to impinge on the inlet ceiling. So why was this flow non-oscillatory? The answer may have to do with the fact that as seen in Fig. 3.28, in the non-oscillatory case, the oblique shock was seen to be farther upstream than the unstarted flow of current discussion. Note that Fig. 3.30 shows that the non-oscillatory unstarted flow has a much more separated ceiling boundary layer compared to the current unstarted flow. This high amount of ceiling boundary layer separation appears to result in the deflection of high-speed fluid into the lower wall-normal portion of the isolator entrance (e.g., see Fig. 3.30c). Perhaps this high-speed, supersonic flow is what prevents the longitudinal propagation of acoustic waves between the inlet entrance and the flap. In addition, another pertinent question remains. Why should the inlet / isolator model act as quarter-wave resonator and not a half-wave resonator? Recall that in the high-amplitude case, the schlieren images clearly showed downstream propagating weak normal compression waves to reflect as shocks (e.g., See Fig. 3.21c and Fig. 3.21d). This reflection of waves is consistent with the isolator exit acting as a solid wall. In comparison, in the current unstarted flow similar compression waves are not observed. However, since the schlieren images for the current unstarted flow were acquired with a horizontal knife edge (sensitive to vertical density gradients), the compression waves would not be expected to be apparent. Still, the flow field in the isolator for the current unstarted flow never becomes completely quiescent which was seen to be the condition in which the compression waves became visible in the high-amplitude oscillatory unstarted flow. In addition, the PIV data for the high-amplitude oscillatory unstarted flow showed that at times the model flow became nearly completely stagnant (e.g, See Fig. 3.24). However, in the case of the current unstarted flow, the oscillating oblique shock (arrow A in Fig. 5.18) tends to reside near the inlet entrance and most of the shock enters the inlet. This means that there is not an opportunity for a high amount of mass spillage. In comparison, it is likely that mass spillage due to a strong bow shock was responsible for the stagnant flows seen during the low pressure portions of the high-amplitude oscillatory unstarted flow cycles. Since there does not appear to be a high amount of mass spillage in the current unstarted flow, a significant amount of mass flow must pass through the isolator exit, which is not consistent with the closed exit required for a quarter-wave resonator. A possible explanation of the oscillations of this case is as follows. Inspection of the current unstarted flow schlieren images show what appear to be shocklets near the isolator ceiling to exist all the way until the isolator exit (e.g., arrows B, C and D in Fig. 5.18). These shocklets are consistent with high speed fluid that may contain supersonic regions. Therefore, the majority of mass flow likely leaves the isolator in a high speed streamtube that exits the isolator near the ceiling. Therefore the subsonic flow in the lower portion of the isolator can be thought of as confined by high speed (possibly supersonic) fluid above it and the flap at the isolator exit. Thus, it is possible that the subsonic floor region allows for the propagation of acoustic waves that reflect off of the flap near the isolator exit. In a sense, the subsonic region that extends from the inlet entrance to the flap can be thought of as a forward facing cavity, which would therefore predict the measured oscillation frequencies that are near that of a quarter-wave resonator. Of course with the available data this discussion is speculative, but this explanation as to how the model acts as a quarter-wave resonator seems to be plausible.

5.2.4 Non-Oscillatory High-Compression Shock System

As discussed above, it was not possible to form a non-oscillatory high-compression shock system by raising the flap in the 6-degree inlet / short-isolator model.

However, such a compression system could be formed by a subsequent lowering of the flap. In another run, an oscillatory high-compression system similar to that discussed above was formed in the isolator by raising the flap to the same angle of 41.3 degrees. The flap was then lowered to the angle of 40.4 degrees, which resulted in the formation of high-compression shock system that was non-oscillatory. Although not shown here, schlieren imaging showed the flow structure of this non-oscillatory high-compression shock system to be very similar to that seen in 5.11e. However, the large streamwise oscillations seen in Fig. 5.13 were not present for the non-oscillatory system. Figure 5.19 gives the mean and *RMS* pressure corresponding to the non-oscillatory compression system. Figure 5.19a shows that the mean pressure distribution is lower than that of the oscillatory compression system seen if Fig. 5.14a. Note that the pressure near the isolator exit at T7 is 15.6 P_∞ in the oscillatory case, whereas in the non-oscillatory case it is about 14 P_∞. However, the non-oscillatory system exhibits substantially lower pressure fluctuations in the isolator. For example, Fig. 5.19b shows that from T4 (x/h = 6.56) to T7 the pressure fluctuations are about 50 % lower than those measured during the oscillatory high-compression shock system (e.g, compare to Fig. 5.14b).

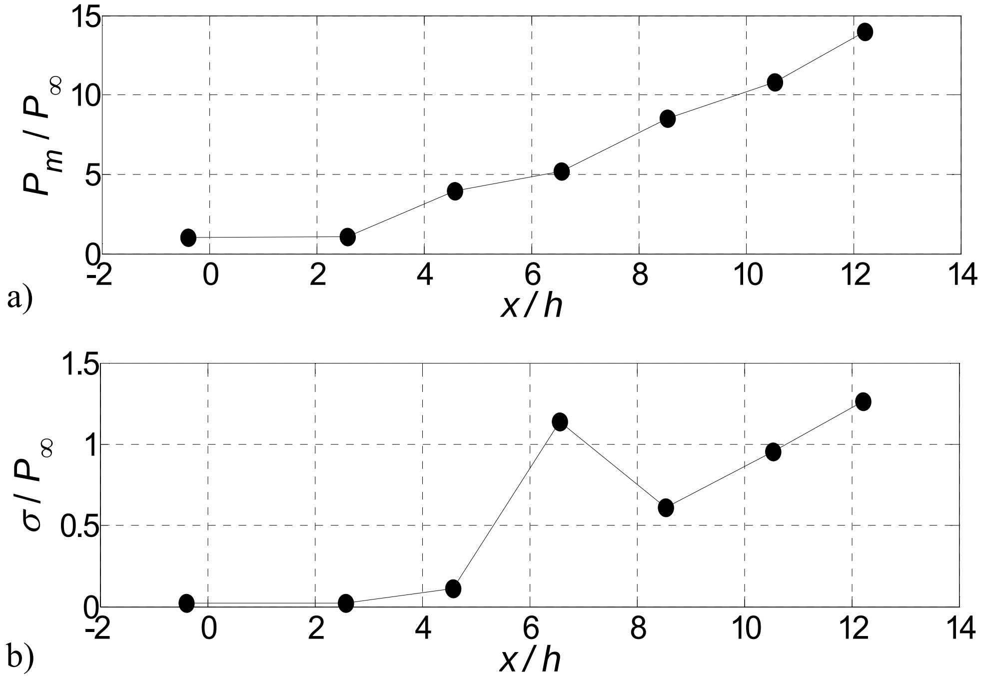

Figure 5.19 6-degree inlet / short-isolator non-oscillatory high-compression shock system: a) mean pressure distribution and b) pressure standard deviation distribution (θ_F = 40.3 degrees).

Pressure power spectra for T7, T6 and T5 are presented for the non-oscillatory high-compression shock system in Fig. 5.20. For the spectra, the acquisition rate was 25 kHz and the number of samples taken was 6,250, which gives a maximum frequency of 12.5 kHz and a resolution of 4 Hz. The broadband sound pressure levels suggest this flow is indeed not oscillatory.

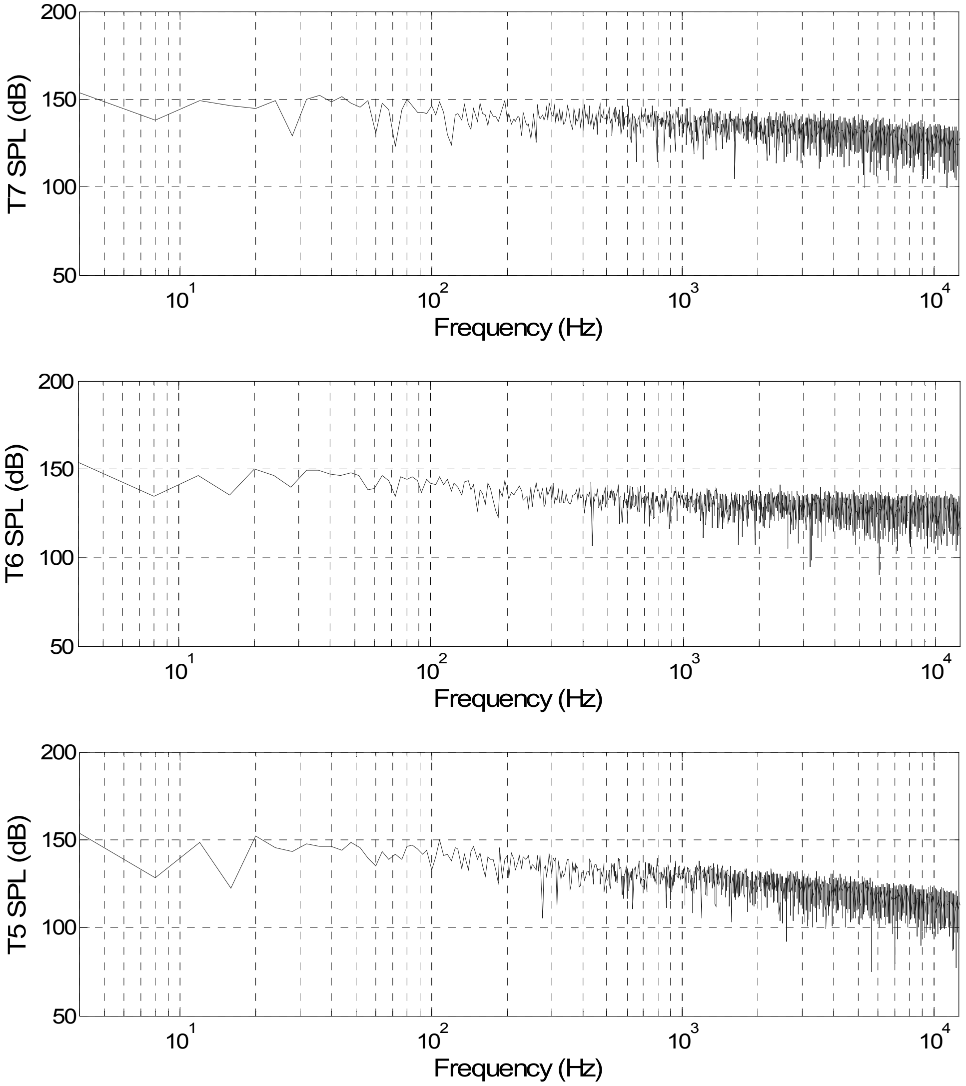

Figure 5.20 Power spectra of the pressure at T7, T6 and T5 for the 6-degree inlet / short-isolator non-oscillatory high-compression shock system flow.

5.3 8-DEGREE INLET / SHORT-ISOLATOR RESULTS

5.3.1 Fully Supersonic Started Flow (flap-fully down)

The mean and *RMS* pressure distributions for the 8-degree / short-isolator fully supersonic started flow are shown in Fig. 5.21. In addition, a schlieren image corresponding to this flap-fully down flow can be seen in 5.22a. All three compression ramp shock reflections can be seen in this image as labeled with arrows A, B and C. With the exception of an anomaly to be discussed below, both the schlieren image and the pressure distributions are very similar to those of the 8-degree / long-isolator case (e.g., See Figs. 4.9 and 4.11). Therefore, in the interest of brevity, a lengthy discussion of this flow will not be given here. More details on this started flow are given in section 4.2.1, where the same reasoning should apply to the current section. The mentioned anomaly has to do the *RMS* pressures at T5 (*x/h* = 8.54). Note that the *RMS* pressure at T5 in Fig. 5.21b is about half of that given in Fig. 4.9b, which suggests the presence of a bias error. It is likely that this error arose from noise in the T5 signal for the run corresponding to the 8-degree inlet / long-isolator results.

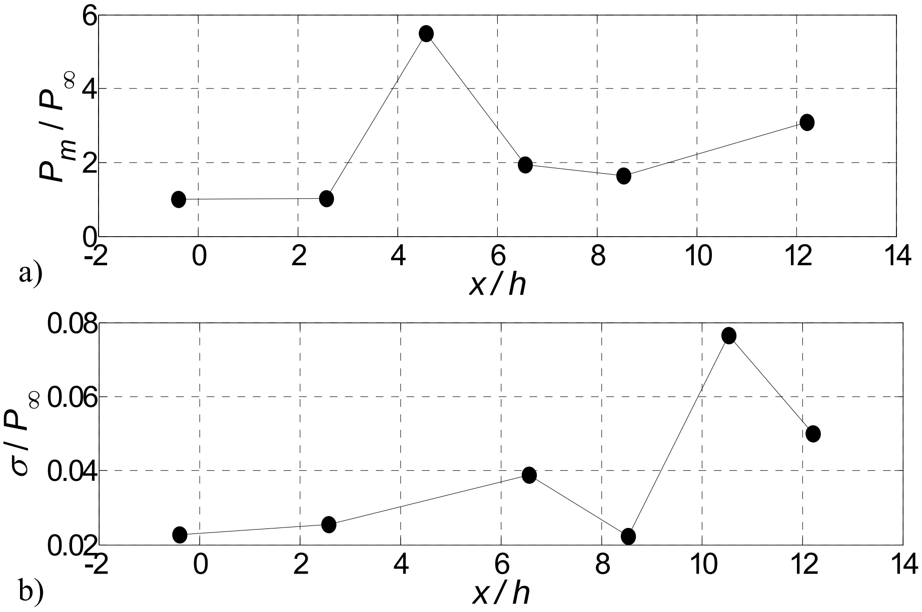

Figure 5.21 8-degree inlet / short-isolator fully supersonic started flow: a) mean pressure distribution and b) pressure standard deviation distribution.

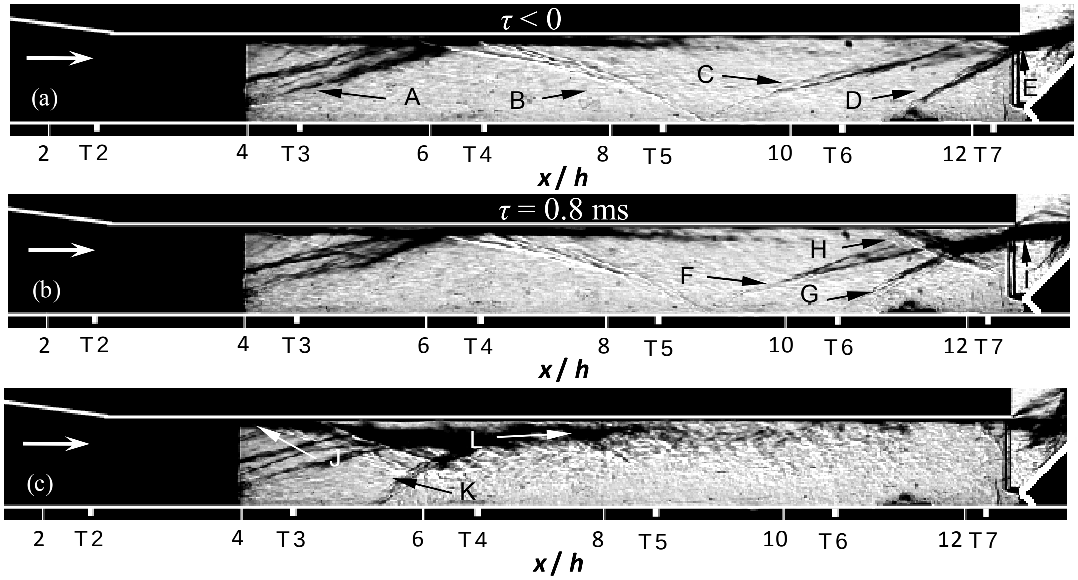

Figure 5.22 Schlieren images showing the formation of a non-oscillatory high-compression shock system in the 8-degree inlet / short-isolator model: a) $\tau < 0$, prior to the set up process, b) $\tau = 0.8$ ms into the set up of the compression system, and c) after the compression system set up ($\theta_F = 45.0$ degrees).

5.3.2 T7 Time History During High-Compression Shock Systems, Unstart and Unstarted Flows

Figure 5.23 shows the T7 pressure time history corresponding to the formation of a high-compression shock systems, unstarted flow and restart. From 0 to about 0.4 seconds the flap is fully-down and the flow is fully supersonic throughout the model. At about 0.4 seconds the flap is raised to the angle of 43.1 degrees. At about 0.7 seconds the flap reaches 43.1 degrees and is held stationary until the time of about 0.87 seconds. During this time span, the T7 pressure is elevated due to the presence of a detached flap shock similar to that seen in Fig. 5.22a (arrow D). Next at about 0.87 seconds, the flap angle is increased to 45.0 degrees. When the flap reaches this angle and is near stationary a sudden pressure increase is observed at about 0.97 seconds which corresponds to the formation of a non-oscillatory high-compression shock system. The flap is then held at the 45.0 degrees, which maintains the non-oscillatory system. At about 1.2 seconds the flap is raised further to 45.9 degrees, which results in an oscillatory high-compression shock system being formed. Next at 1.45 seconds, the flap begins to rise again to the angle of 46.8 degrees which increases the magnitude of T7 pressure fluctuations. However, the T1 time history shows that the shock system remains within the model. Similarly, the flap begins to rise once more at 1.7 seconds to the angle of 47.8 degrees, which once again, increases the magnitude of the oscillations but does not result in unstart. Finally, at 1.95 seconds the flap angle is increased to 48.7 degrees. The result is another increase in T7 fluctuations and a lower-amplitude oscillatory unstarted flow.

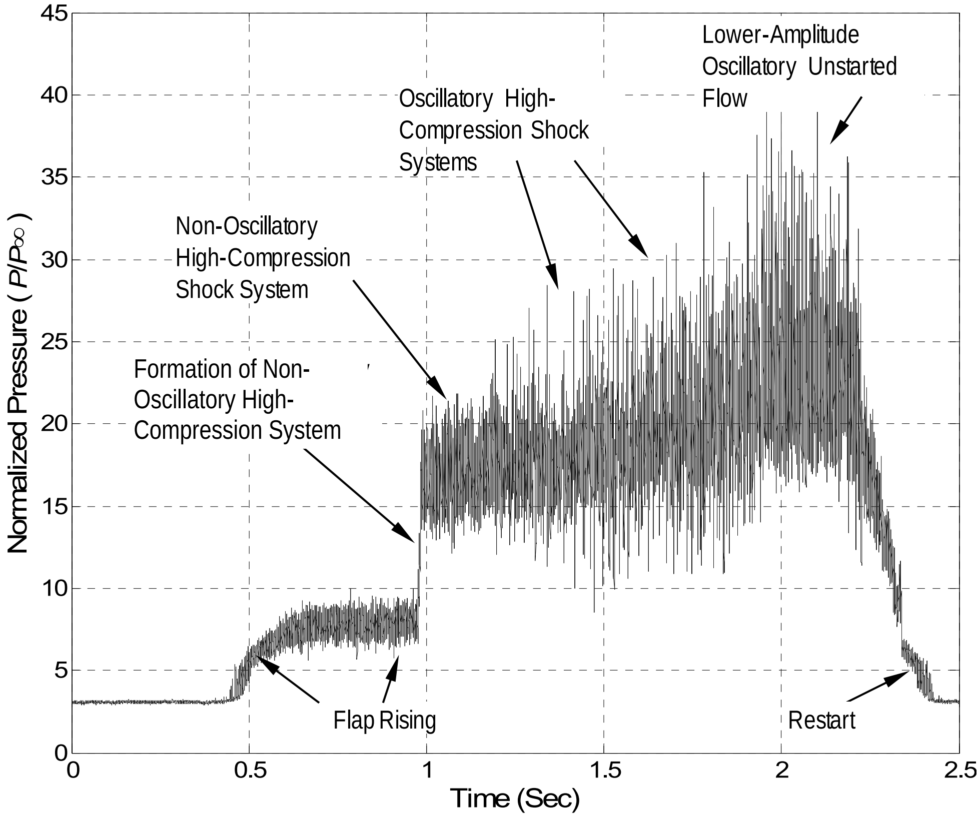

Figure 5.23 8-degree inlet / short-isolator T7 pressure time history corresponding to the formation of high-compression shock systems, unstarted flow and restart.

5.3.3 Schlieren Imaging and Pressure Measurements of High-Compression Shock Systems and Lower-Amplitude Oscillatory Unstarted Flow

Figure 5.22 presents schlieren images (taken with a horizontal knife-edge) showing the formation of the non-oscillatory high-compression shock system in the 8-degree inlet / short-isolator model. In Fig. 5.22a the flap is raised but not to an angle great enough to form a high-compression shock system. The detached flap shock (arrow D) is seen to leave the isolator exit where it appears to interact with the fourth reflection of the inlet-ramp shock (arrow E). This image serves to demonstrate the complexity of the flow field that is involved even before the formation of the high-compression shock system is initiated. When the flap reached the angle of 45.0 degrees, the flap shock was observed to propagate far enough upstream to result in its impingement on the ceiling. As with each of the other five models tested, the ceiling impingement resulted in boundary layer separation, which apparently induced the formation of the high-compression shock system. Figure 5.22b, acquired at τ = 0.8 ms into the formation process, shows the high-compression shock system to be a combination of complex shock wave / boundary layer and shock-shock interactions. For example, the third reflection of the compression ramp shock (arrow F) intersects and interacts with the detached flap shock (arrow G) and ceiling separation shock (arrow H). As a result, a strong shear layer (arrow I) is seen to exit the isolator above the flap. In subsequent images not shown here, the high-compression shock system was seen to propagate upstream with a flow structure very similar to that seen during the unstart process of the 8-degree inlet / long-isolator model (e.g., See Figs. 4.11a to 4.11e). However, obviously unlike the unstart event in the long-isolator case, the high-compression shock system stops in the isolator taking the form seen in Fig. 5.22c. Following the logic of the above 0- and 6-degree discussions, the fact that the flap is not enclosed by the isolator side walls is a possible explanation as to why a high-compression system could be formed by raising the flap in this model. The schlieren image of Fig. 5.22c shows that the non-oscillatory compression system consists of both a ceiling separation shock (arrow J) and a floor separation shock (arrow K). As a result of these shocks, a prominent shear layer (arrow L) is seen to exist within the isolator. Note that in the current case, it was possible to form a non-oscillatory compression system by raising the flap, but in the 6-degree case this was not possible with raising the flap alone.

The mean and *RMS* pressures corresponding to the non-oscillatory high-compression shock system described above are given in Fig. 5.24. The mean pressure plot of Fig.5.24a and *RMS* pressure plot of Fig. 5.24b demonstrate that the compression system remains downstream of T3 ($x/h = 4.57$). The mean pressure in the isolator is seen to increase in a nearly linear fashion. At T7 near the isolator exit, the pressure has increased to nearly 17 P_∞. The *RMS* plot shows a similar trend to that seen in both of the other short-isolator non-oscillatory high-compression shock systems. Namely, the pressure fluctuations measured at T4 ($x/h = 6.56$) are greater than those measured at T5 ($x/h = 8.54$). As discussed above, the reason for this is likely that the fact that T4 was the closest transducer downstream of the leading shock of the high-compression system. From T5 to T7 the pressure fluctuations increase with increasing streamwise distance. Finally, at T7 near the exit, the *RMS* pressure is about 1.5 P_∞.

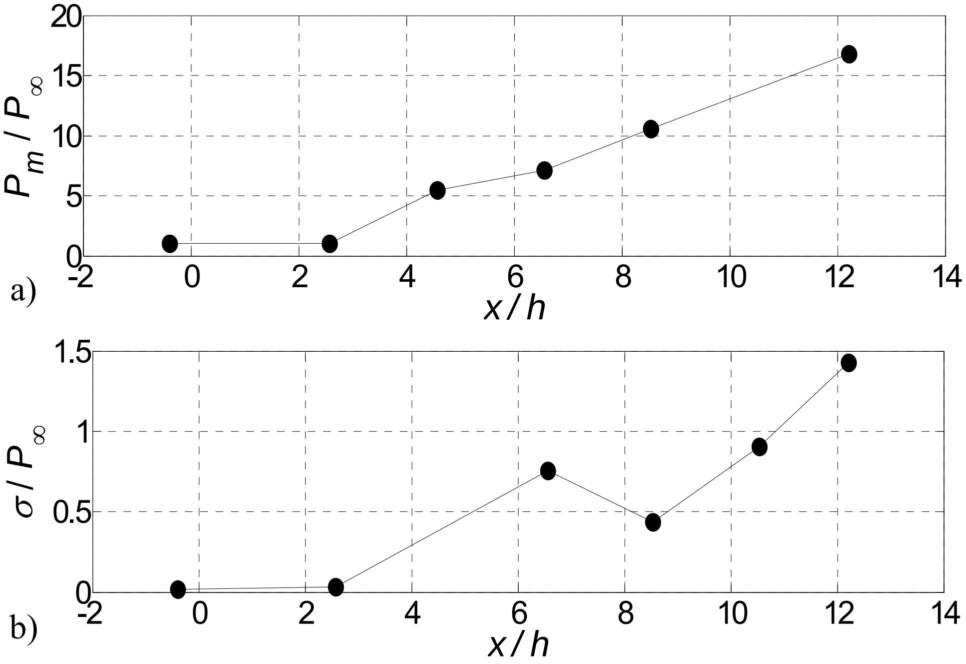

Figure 5.24 8-degree inlet / short-isolator non-oscillatory high-compression shock system: a) mean pressure distribution and b) pressure standard deviation distribution (θ_F = 45.0 degrees).

Figure 5.25 shows the pressure power spectra at T7, T6 and T5 for the non-oscillatory compression system. For the spectra, the acquisition rate was 25 kHz and the number of samples taken was 4,750, which gives a maximum frequency of 12.5 kHz and a resolution of 5.3 Hz. The spectra were generated using the same runs as that corresponding to Fig. 5.23 over the time span of 0.99 to 1.18 seconds. Inspection of the spectra does not show a dominant frequency peak and the distributions are fairly broadband. Therefore, this high-compression system is non-oscillatory.

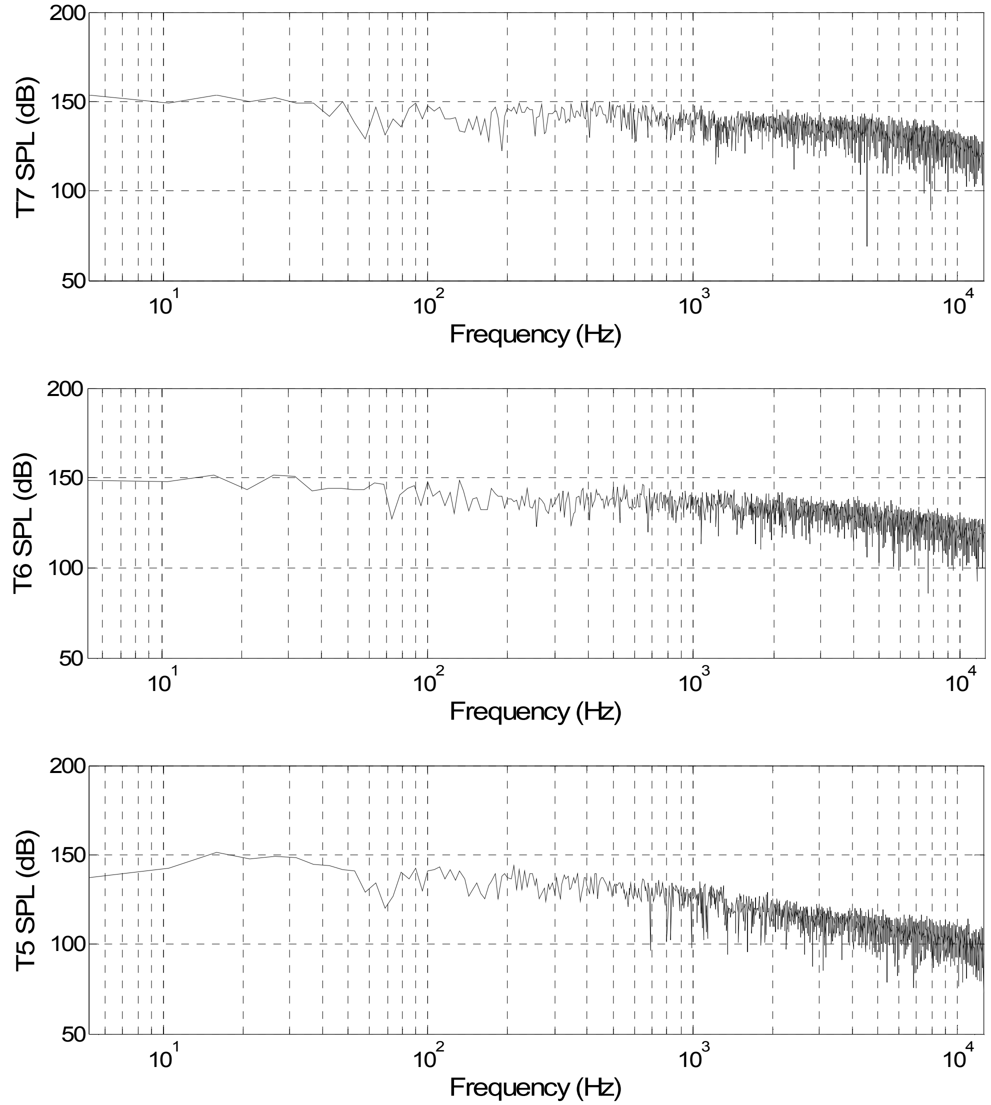

Figure 5.25 Power spectra of the pressure at T7, T6 and T5 for the 8-degree inlet / short-isolator non-oscillatory high-compression shock system flow.

As seen in Fig. 5.23, following the formation of the non-oscillatory system, oscillatory systems with greater T7 fluctuations were generated by increasing the flap angle. When the flap angle was increased to 48.7 degrees, the model was seen to unstart which was determined with inspection of the T1 (*x/h* = -0.4) pressure time history.

Figure 5.26 shows the mean and *RMS* pressures corresponding to this lower amplitude oscillatory unstarted flow. The trends seen in both the mean (Fig. 5.26a) and the *RMS* (5.26b) are very similar to the lower-amplitude oscillatory unstarted flow seen in 6-degree case of Fig. 5.16.

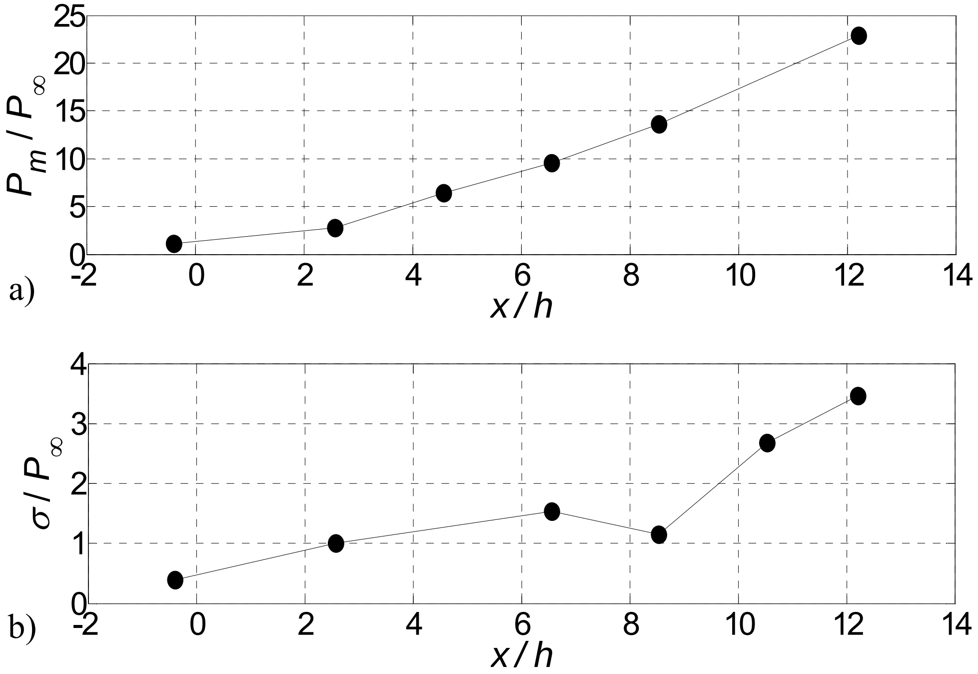

Figure 5.26 8-degree inlet / short-isolator lower-amplitude oscillatory unstarted flow: a) mean pressure distribution and b) pressure standard deviation distribution.

What is more, Fig. 5.27 shows that the pressure power spectra at T7, T6 and T5 have peak *SPL* values at frequencies similar to those seen in the 6-degree lower-amplitude unstarted flow (e.g., compare to Fig. 5.17). The peak sound pressure levels at T7, T6 and T5 were measured to be 162.4, 160.5, and 153.2 dB, respectively. The frequency corresponding to the T7 and T5 peaks was measured to be 244 Hz (f *=0.21) and the frequency of the T6 peak was measured to be 304 Hz (f * =0.26). Note that for the spectra, the acquisition rate was 25 kHz and the number of samples taken was 6,250, which gives a maximum frequency of 12.5 kHz and a resolution of 4 Hz. The spectra were generated using the same runs as that corresponding to Fig. 5.23 over the time span of 1.95 to 2.2 seconds. Similar to the 6-degree case described above, this unstarted flow also has dominant frequencies near that of the ideal quarter-wave resonator. The similar trends in pressure distributions for the two oscillatory unstarted flows suggest that similar driving physical mechanisms are responsible for these near acoustic resonant frequencies. In addition, although not shown here, the schlieren imaging for the 8-degree case exhibited a similar structure to that shown above for the 6-degree case. Therefore, it is plausible, by the same reasoning given in section 5.2.3, that the 8-degree lower-amplitude oscillatory unstarted flow pressure fluctuations are a result of quarter-wave resonator phenomenon. However, it should be noted that the near quarter-wave frequencies may be nothing more than a coincidence.

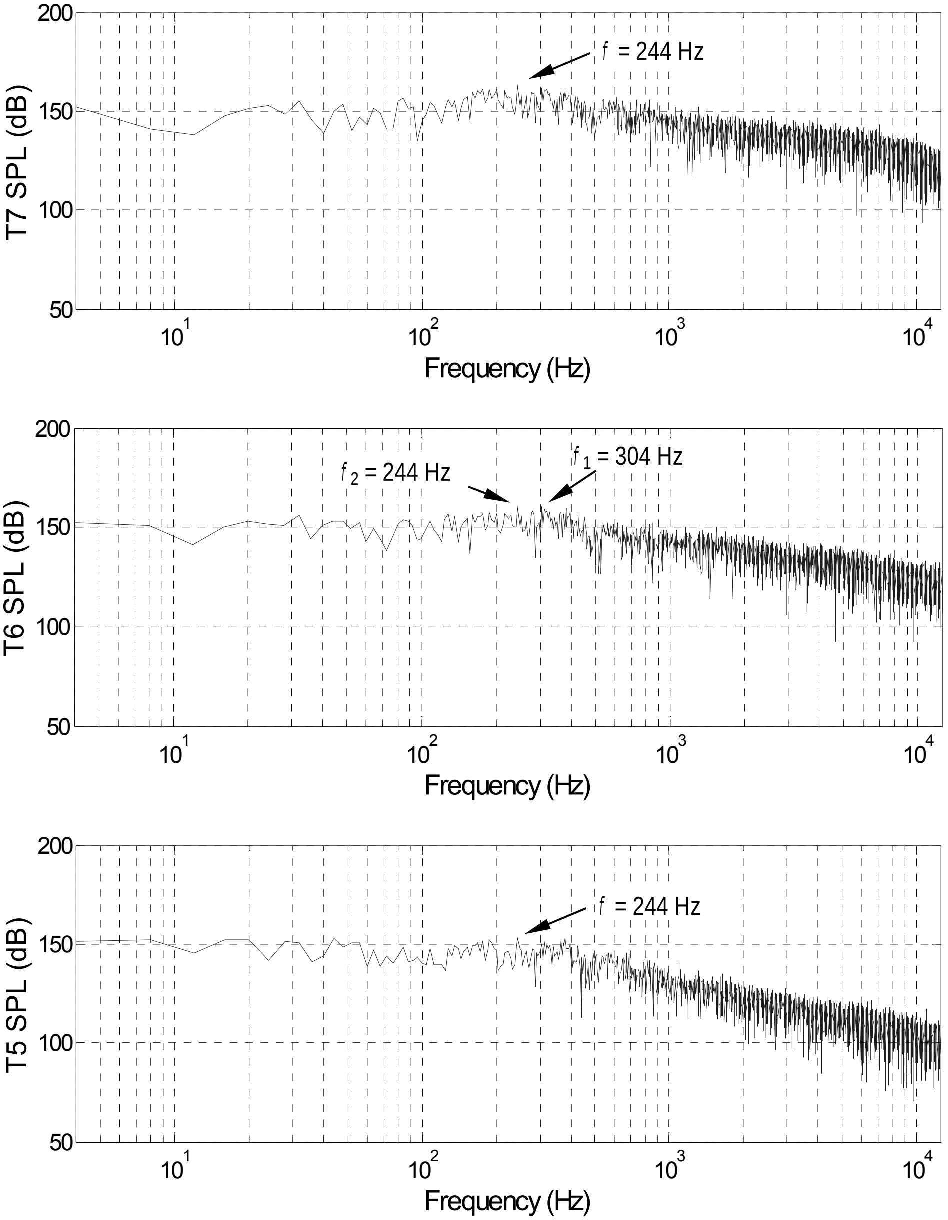

Figure 5.27 Power spectra of the pressure at T7, T6 and T5 for the 8-degree inlet / short-isolator lower-amplitude oscillatory unstarted flow.

5.4 SUMMARY OF HIGH-COMPRESSION SHOCK SYSTEMS IN ALL 6 INLET / ISOLATOR MODELS

This section presents a brief summary of the high-compression shock system results of all six models tested. In each of the three inlet / long-isolator models, it was not possible to form a high-compression shock system by raising the flap alone. This was attributed to the total blockage at the isolator exit being too great to maintain a non-transient shock system. This total blockage consisted of the physical blockage of the flap that was partially enclosed by the isolator sidewalls, as well as the viscous blockage (boundary layer separation) that was seen to develop rapidly at the onset of unstart. This rapid separation can be thought of as a rapid increase in blockage that may be analogous to an additional rapid flap angle increase. On the other hand, it was possible in all three inlet / short-isolator models to set up a high-compression shock system within the isolator by raising the flap alone. In this case of the formation of these high-compression shock systems, the flow structure and propagation velocities were seen to be very similar to those in the downstream portions of the model during the unstart of the long-isolator models. It was suggested that a possible reason as to why high-compression shock systems could be formed by raising the flap in the short-models might be related to the fact that the flap was downstream of the isolator exit. Thus, the flap shock / sidewall boundary layer interactions (glancing interactions) occurred over a smaller surface area than in the long model. In the 0- and 8- degree cases, it was possible to form non-oscillatory high-compression systems by raising the flap alone. On the contrary, the 6-degree inlet / short-isolator model required an oscillatory internal shock system to be formed first. Following the set up of this oscillatory high-compression shock system, the flap could then be lowered to form a non-oscillatory high-compression shock system. Finally, after unstarting the 6- and 8-degree inlet / long-isolator models, high-compression shock systems could be stabilized in the isolators with a subsequent lowering of the flap. In the 0-degree case this was not seen to be possible. Although very slight decreases in flap angle (0.2 degrees) were attempted, the flow either remained unstarted or restarted to the fully supersonic flow mode with a detached flap shock (e.g., see Fig. 4.3a).

Table 5.2 below summarizes the maximum isolator exit pressure (at T7) that was sustainable for the non-oscillatory shock systems in each of the 6 models tested. Recall that as discussed in section 1.2.3, the exit pressure is a pertinent performance parameter for inlet / isolators. Again, the amount of pressure increase that the inlet / isolator can tolerate without unstarting is a direct measure of the amount of fuel that can be burned in combustion and therefore a direct measure of the thrust that an engine can create (Rodi et al., 1996). In addition, the maximum sustainable pressures are compared to the corresponding normal shock pressure gains for the freestream conditions. Recall that in a constant area duct, the maximum pressure gain can be near, but is always less than that of a single normal shock at the duct entrance Mach number (Matsuo et al. 1999). Moreover, table 5.2 gives the run number corresponding to the pressures shown, which allows for the corresponding run flow conditions to be looked up in Appendix A.

Table 5.2 Comparisons of the T7 (exit) pressures of the maximum strength non-oscillatory high-compression shock systems in all six inlet / isolator models

Inlet / Isolator	T7 P, P_∞	T7 P, kPa	T7 Normal Shock %	Appendix A Run Number
0-degree / Long	N/A	N/A	N/A	N/A
6-degree / Long	12.7	68.3	46 %	244
8-degree / Long	11.9	58.5	39 %	479
0-degree / Short	11.6	55.5	38 %	493
6-degree / Short	14.0	72.2	44 %	100
8-degree / Short	16.8	80.5	56 %	495

As a final note, the high-compression shock systems in the 6- and 8-degree inlet / long-isolators did not appear to be pseudo-shocks containing shock-trains. For instance, neither their flow structures (Matsuo et al., 1999) nor pressure distributions (Waltrup and Billig 1973, and Billig, 1993) were consistent with those of pseudo-shocks. There was however some evidence to suggest that the strong compression shock system of the the 6-degree inlet / long-isolator model might be the separation-shock mode described by Penzin (1998). Encouraging to this argument was the fact that the pressure distribution was significantly lower than that expected for a pseudo-shock. In further support, it was noted that when displacement thickness effects were considered, Equation 1.14 of Penzin (1998), predicted the high-compression shock system should take the separation shock form. In comparison, Equation 1.14 predicted that the 0-degree inlet / short-isolator high-compression shock systems should be of the pseudo-shock form and the pressure distribution for this flow showed this could be the case. However, the uncertainty in the pressure measurements for this flow precluded a meaningful conclusion from being reached.

CHAPTER 6

6. Summary and Conclusions

Unstart dynamics were investigated experimentally in inlet / isolator models mounted on the floor of a Mach 5 wind tunnel using high-speed schlieren imaging, fast-response pressure measurements and PIV. The most extensively studied (baseline) model consisted of an inlet with a 6-degree compression ramp followed by a rectangular isolator that was 25.4 mm high by 50.8 mm wide by 242.3 mm long. The incoming boundary layer thickness was about 19 mm, which was a large fraction of the inlet height of 34.9 mm. Unstart was initiated by raising a flap at the exit plane of the isolator. Varying the flap rise time did not show any discernible effects with regard to unstart time-scales or unstart flow structure. Near the unstart condition, a rapid increase in boundary layer separation was observed near the isolator exit owing to the interaction of a reflected inlet shock and the flap shock on the ceiling of the isolator. The average velocity of unstart propagation as determined with the pressure measurements in the isolator section was about 0.035 U_∞ (26 m/s), whereas the average velocity of unstart for the inlet was about 0.10 U_∞ (74 m/s). The average propagation velocity of the unstart shock system through the entire inlet / isolator was about 0.05 U_∞ (37 m/s).

Both the PIV and the schlieren imaging showed the upstream propagation of the unstart shock system to be associated with shock-induced separation that resulted in the formation of prominent shear layers. As unstart progressed upstream, the strength of separation increased and reverse flow velocities up to about 300 m/s were induced both near the ceiling and the floor. During the unstart process, velocity differences as high as 1000 m/s were measured over wall-normal distances less than 12 mm. The side-view, wide-field PIV pseudo-sequence indicated that the unstart shock system propagated through the inlet / isolator as strong shock-induced separation occurred first near the floor and then near the ceiling. This shift from the floor to the ceiling of the shock-induced separation appeared to occur at the location corresponding to the ceiling impingement point of the second ramp shock reflection. As the unstart shock system propagated upstream, it appeared to take the "path of least resistance," as the flow separated in regions of pre-existing adverse pressure gradients corresponding to the impingement locations of the initial compression ramp reflected shock system. These observations suggested that the flow structure of the unstart process was therefore dependent on inlet geometry. Furthermore, measurements made in the plan-view plane at the wall-normal centerline, showed the unstart process in the baseline model to be highly three-dimensional. Unstart progressed through the isolator first with separation of the sidewall boundary layers. In other words, in the wall-normal centerline plane, unstart moved upstream first along the sidewalls. As the unstart shock system reached the streamwise center of the isolator, sidewall separation was no longer seen to lead the rest of the unstart shock system. Rather, with further upstream propagation, the unstart shock system was seen to take the form of an undulated shock. Comparison to the side-view data suggested the undulated shock was the floor separation shock seen to form during unstart.

Once the six-degree inlet / isolator unstarted, a highly oscillatory unstarted flow was seen to form with a frequency of about 124 Hz or 0.11 a_0 / L. Simultaneous schlieren imaging and pressure measurements showed the mechanism for these oscillations to be related to downstream propagating compression waves that reflect off the flap at the isolator exit. The pressure increase during the high-amplitude oscillatory unstarted flow mode occurred in less time than the initial pressure rise that characterizes the initial unstart event. This observation is likely related to the fact that pressurization during unstart appeared to be highly dependent on flow separation, whereas pressurization during the oscillatory unstarted flow was seen to be partly dependent on downstream propagating compression waves at near acoustic velocities. Side-view PIV data were also used to provide insight into the high-amplitude oscillatory unstarted flow. The PIV data show that when isolator pressures were near a minimum, the flow is nearly completely stagnant. The dominant frequency of the oscillations was seen to be less than half that expected for a quarter-wave resonator. PIV data showed that during cycle times when the pressures were increasing, the isolator entrance flow was supersonic. Also, consistent with the schlieren imaging, the PIV data showed that the pressure increases during the cycles were dependent on upstream traveling shock systems not acoustic mechanisms. These upstream traveling shock systems traveled at velocities far smaller than acoustic velocities ($\approx 0.3a_0$). Thus, lower than acoustic frequencies are to be expected for the high-amplitude oscillatory unstarted flow.

The characteristics of the unstarted flow could be dramatically altered with flap position changes. For example, lowering the flap was seen to result in the flow going from a high-amplitude oscillatory mode to a non-oscillatory mode with substantially lower pressure fluctuations. This non-oscillatory unstarted flow was seen with the schlieren imaging to always contain an oblique shock upstream of the inlet entrance that appeared to result in the separation of the model's ceiling boundary layer. The mean flowfield as given with PIV data showed a ceiling separation bubble near the isolator entrance having mean reversed velocities. The separation shock associated with the bubble resulted in the downward turning and subsequent impingement of high-speed supersonic fluid on the isolator floor. It was suggested that the floor impingement of this supersonic fluid might be responsible for the lack of oscillations seen during this unstarted flow.

High-compression shock systems could not be formed in the baseline model by raising the flap alone apparently due to high levels of shock-induced separation at the isolator exit. However, following unstart, the model could be restarted to a high-compression shock system mode by lowering the flap. Schlieren imaging and the PIV data showed the flow structure of the high-compression shock systems to be very similar to that seen in the unstart process when the unstart shock system was near a location similar to that of the high-compression shock systems. Furthermore, the flow structure and wall pressure distribution of the high-compression shock systems were not consistent with those reported in the literature for shock-trains (pseudo-shocks). Although not entirely conclusive, there was evidence to suggest that the high-compression shock system might be of the separation-shock form, which is reported far less often in the literature. The fact that the inlet ingested a thick boundary layer was given as a possible reason for the apparent separation-shock mode that was observed.

Since the 6-degree baseline model suggested that the unstart process was dependent on inlet geometry, experiments were conducted using a flat plate inlet and an eight-degree compression ramp inlet in conjunction with the long-isolator. In both inlet / isolator models, unstart was seen to begin in a similar fashion to that in the 6-degree model. Namely, high levels of shock-induced separation were seen to lead to unstart. In the 8-degree model, the flow structure as seen with schlieren imaging was similar to that of unstart in the 6-degree model. Specifically, the flow structure was clearly dependent on the location of the initial reflected oblique shock system that was generated at the ramp leading edge. On the contrary, in the 0-degree (no inlet) case, the flow structure remained fairly constant. In addition, compared to the propagation velocities during unstart of the 6- and 8-degree models, the 0-degree propagation velocity was seen to be much more constant. Moreover, the propagation velocities of unstart in the isolators were seen to increase with increasing compression ramp angle. For example, in the 8-degree configuration, the average unstart propagation velocity was 150% that in the 0-degree configuration. This might be explained by the fact that with increased compression ramp angle, the unstart shock system propagates against a lower momentum flow. Inlet geometry was also seen to influence the peak pressures reached during unstart. Typical peak pressures in the 6- and 8-degree unstart events were seen to be near those which would be given by a stationary normal shock in the freestream. However, for the 0-degree model, the peak pressures were seen to be less than 70% the freestream normal shock value. In addition, the flow that followed unstart was also different for each model. Following unstart in the 8-degree model, an oscillatory flow with a frequency of about 100 Hz (f^*=0.090) was observed. However, this flow was seen to have significantly lower pressure fluctuations at the isolator exit compared to the flow that followed unstart in the 6-degree model. In even starker contrast, the flow that followed unstart in the 0-degree model was seen to be non-oscillatory. Finally, the ability for a given inlet / long-isolator model to contain a stable high-compression shock system was also seen to be dependent on inlet geometry. For both compression ramp inlet models, it was possible to form high-compression shock systems in the isolator by lowering the flap following unstart. This was not seen to be the case for the 0-degree model.

Since in all three inlet / long-isolator models it was not possible to form high-compression shock systems by raising the flap alone, tests were conducted using a shortened isolator. The short-isolator was tested in combination with each of the three inlets. In each inlet / short-isolator model, it was possible to set up a high-compression shock system by raising the flap. It was suggested that the ability of the short-isolator models to contain stable high-compression systems was related to the fact that the flap in the short-isolator models was not enclosed by the sidewalls. The flow structure during the formation of the high-compression shock systems was seen to be very similar to that observed during unstart, of the long-isolator model counterparts. Interestingly, so were the propagation velocities. The inlet geometry was also seen to affect the type of compression shock system that could be set up by raising the flap. For example, in the 0- and 8-degree / short-isolator models, non-oscillatory systems were formed by raising the flap. However, in the 6-degree case only an oscillatory high-compression system could be formed by raising the flap alone. Moreover, the type of flow that followed unstart in the short-isolator models was also seen to be dependent on inlet geometry. In the 0-degree inlet / short-isolator model, the unstarted flow was seen to be non-oscillatory. However in the 6- and 8-degree inlet / short-isolator models oscillatory unstarted flows were observed. The dominant frequencies of these unstarted flows were seen near those of an ideal quarter-wave resonator. This was attributed to the fact that a strong oblique shock always resided near the inlet entrance allowing for the model entrance flow to be subsonic. With subsonic entrance flow, the entrance could act as an open end of an acoustic resonator. It was suggested that the lower portion of the isolator contained subsonic fluid from the inlet entrance up until the flap. Above the subsonic fluid, there appeared to be high-speed and possibly supersonic fluid. It was proposed that the high-speed streamtube enclosed the top of the subsonic region. If this were the case, then the internal model would be analogous to a cavity, which should act as a quarter-wave resonator.

Tests were also conducted with the baseline 6-degree inlet / long-isolator model to assess the effects of tripping the three otherwise naturally developing boundary layers. The boundary layer trips were clearly seen to result in a decreased unstart propagation velocity in the inlet and upstream portion of the isolator. The reasons behind the decreased propagation velocity in the case of the boundary layer tripped inlet are possibly related to those given above for a decrease in compression ramp angle. Specifically, a tripped, turbulent boundary layer will result in a fuller velocity profile compared to a laminar boundary layer. Thus, for the tripped case, the unstart shock system propagates against a higher momentum fluid.

APPENDIX A

A. Run Conditions

This appendix gives selected run conditions corresponding to each figure in chapters one through five. Table A.1 provides the run number for a given figure and Table A.2 shows the run conditions corresponding to the run number. The run conditions given in Table A.2 include the plenum pressure (P_0), the mean pressure measured at T1, (taken to be the freestream pressure, P_∞), the number of heater banks used (1 or 2), the plenum temperature (T_0), and the freestream Mach number (M_∞).

Table A.1 Figures and their corresponding run numbers to allow the run conditions to be looked up in A.2.

Figure Number(s)	Run #(s)	Figure Number(s)	Run #(s)
3.1a	21	3.21 to 3.23	21
3.1b	25	3.24 to 3.25	248
3.2	469	3.26a, 3.26b	21
3.3	245	3.26c, 3.26d	248
3.4 to 3.6	21	3.27	21
3.7	21*	3.28	26
3.8	21	3.29, 3.30a	21
3.9, 3.10	25	3.30b	248
3.11a	218	3.31, 3.32	21
3.11b	220	3.33	46
3.11c	219	3.34	41
3.11d, 3.11e	225	3.35	46
3.11f, 3.11g	218	3.36, 3.37	41
3.12a, 3.12b	21	3.38, 3.39	247, 248
3.12c to 3.12e	218	3.40	41, 247, 248
3.13a, 3.13b	21	3.41	41
3.13c to 3.13e	219	3.42	21, 502**
3.14a, 3.14b	21	4.1 to 4.4	491
3.14c to 3.14e	225	4.5	491*
3.15a, 3.15b	21	4.6 to 4.7	491
3.15c to 3.15e	218	4.8 to 4.12	492
3.16a to 3.16b	218	4.13	492*
3.17a, 3.17b	21	4.14 to 4.16	492
3.17c to3.17e	218	4.17	479
3.18a	459	4.18	21, 491, 492
3.18b, 3.18c	460	5.1 to 5.10	493
3.18d	459	5.11 to 5.18	92
3.18e	458	5.19, 5.20	100
3.18f	460	5.21 to 5.27	495
3.19	460		
3.20	458		

* Denotes figures where averages were calculated using nominally similar conditions.

** Run 502 was the tripped inlet run.

Table A.2 Wind tunnel flow conditions by run number.

Run #	P_0, kPa	T1 P, kPa	# of Heaters	T_0, K	M_∞
21	2433	5.38	1	333	4.9
25	2448	5.38	1	339	4.9
41	2482	5.31	1	338	4.9
46	2434	5.17	1	336	4.9
92	2489	5.38	1	333	4.9
100	2434	5.17	1	340	4.9
218	2517	5.17	1	339	4.9
219	2517	5.38	1	337	4.9
220	2517	5.38	1	336	4.9
225	2517	5.38	1	331	4.9
245	2517	5.38	1	330	4.9
247	2517	5.38	1	330	4.9
248	2517	5.38	1	333	4.9
458	2517	5.38	1	333	4.9
459	2517	5.38	1	333	4.9
460	2517	5.38	1	333	4.9
469	2517	5.58	1	316	4.9
479	2517	4.92	2	339	5.1
482	2517	4.73	2	339	5.1
491	2517	4.90	2	343	5.1
492	2517	4.83	2	343	5.1
493	2517	4.79	2	342	5.1
495	2517	4.67	2	340	5.1
502	2517	5.07	2	344	5.1

APPENDIX B

B. Additional Flap Information

B.1 FLAP GEOMETRY AND MOUNTING LOCATION DETAILS

Figure B.1 shows a schematic of the flap when it is in the fully down position. Although not shown, the spanwise width of the flap is 1.95 *h*. Note the hinge (pivot) location is at the wall-normal location of y/h = -0.2. Therefore, when the flap is raised the leading edge moves upstream as is demonstrated with Fig. B.2.

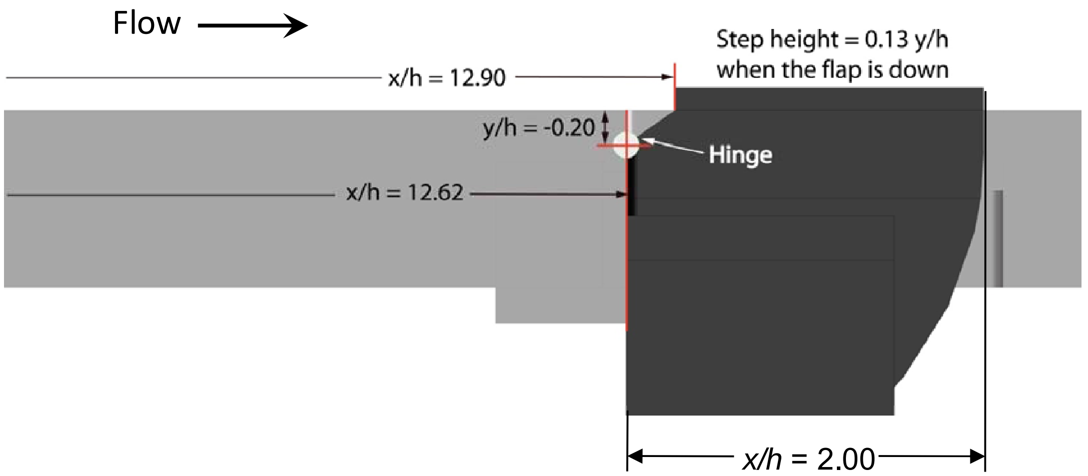

Step height = 0.13 y/h when the flap is down

Figure B.1. Flap geometry schematic with the flap in the fully down position.

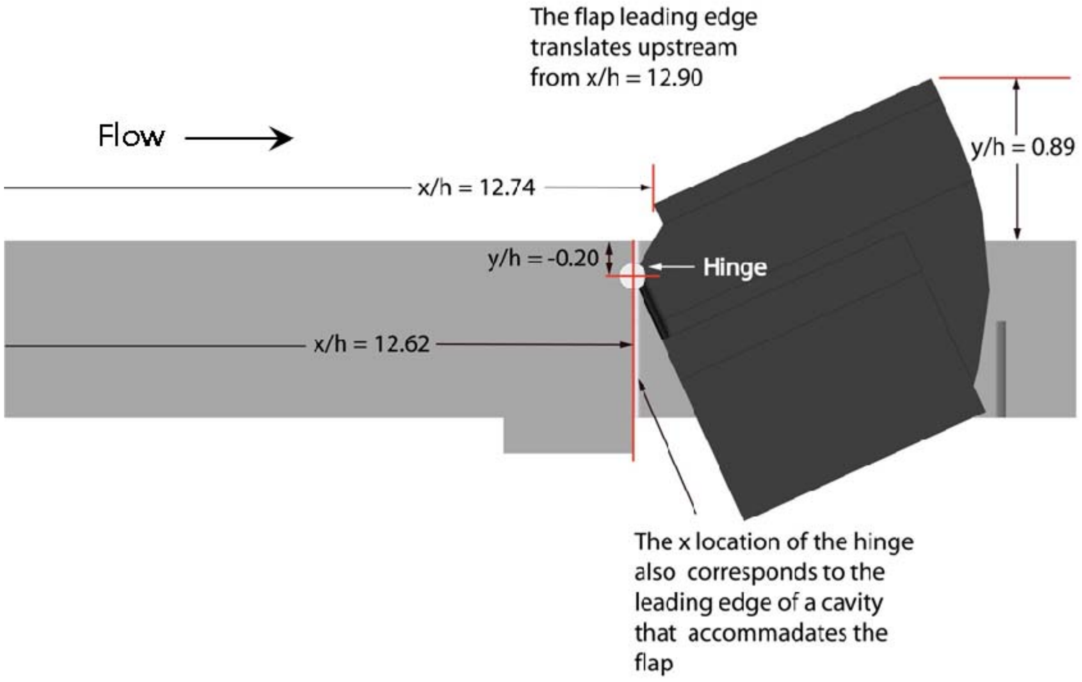

The flap leading edge translates upstream from x/h = 12.90

The x location of the hinge also corresponds to the leading edge of a cavity that accommadates the flap

Figure B.2. Flap geometry schematic with the flap raised to an angle of 24.4 degrees.

B.2 FLAP ANGLE UNCERTAINTY ANALYSIS

Before each run (if necessary), the flap was angle was zeroed to the position as shown in Fig. B.1. During a run, the flap angle could be set precisely using the flap control drive system described in section 2.3. The flap angle varied linearly with the turn angle of the pinion gear which could be set using the motor control system. Flap angles reported herein are based on a calibration that consisted of measuring the flap angle over the range of pinion turn angles used in the experiments. Thirty points in total were used to generate an initial calibration line, which gave flap angle as a function of pinion turn angle. In an iterative process, all measurements outside of ± 0.5 degrees were discarded and the line was re-calculated such that each point fell within ± 0.5 degrees. Therefore, the uncertainty in flap angle due to the calibration process is estimated to be ± 0.5 degrees. Another source of uncertainty in the flap angle was that due to mechanical play in the system. In order to gage the play, a high-speed imaging experiment was conducted where the flap occupied the majority of the field of view. This allowed for its angle to be accurately determined. In order to see how much the flap angle varied with flow and without flow, a high-speed pre-run video was acquired for the same program of flap angles as the actual run. The flap was raised in the 8-degree inlet / short-isolator model to eight different angles. Comparing the pre-run to run images showed that on average, the flap angle was 1.1 ± 0.4 degrees lower during the run (based on 95 % confidence intervals). This result was expected as the flow should remove the play during a run by pushing the flap down. It should be noted that although there was play, typically the flap angle was not seen to fluctuate during a run. On the contrary, the flow was seen to push the flap down slightly, thus removing the play but keeping the flap angle stationary. Therefore, all flap angles reported herein were computed by subtracting 1.1 degrees from the angle the flap would otherwise reach when there was no flow. The estimated uncertainty in these angles is the root-sum-square value of the calibration uncertainty (± 0.5 degrees) and the uncertainty from the flap play test (± 0.4 degrees). This computes to ± 0.6 degrees. Although there is an absolute uncertainty of ± 0.6 degrees, this does not imply that smaller changes in flap angle could not be achieved. For example, in many instances herein, results are presented where the flap angle was varied by small increments such as 0.2 degrees and it is believed that the flap angle could be adjusted with such precision. Therefore the uncertainties given above are with respect to the absolute flap angle and not the change in angle.

B.3 FLAP HEIGHT AT THE EXIT OF THE LONG ISOLATOR MODELS

Figure B.3 gives the flap height versus flap angle at the isolator exit. The curve fit shown in the figure was computed using only the calibration points that were used generate the final flap angle calibration line. This plot is provided to show the exit blockage as a function of flap angle.

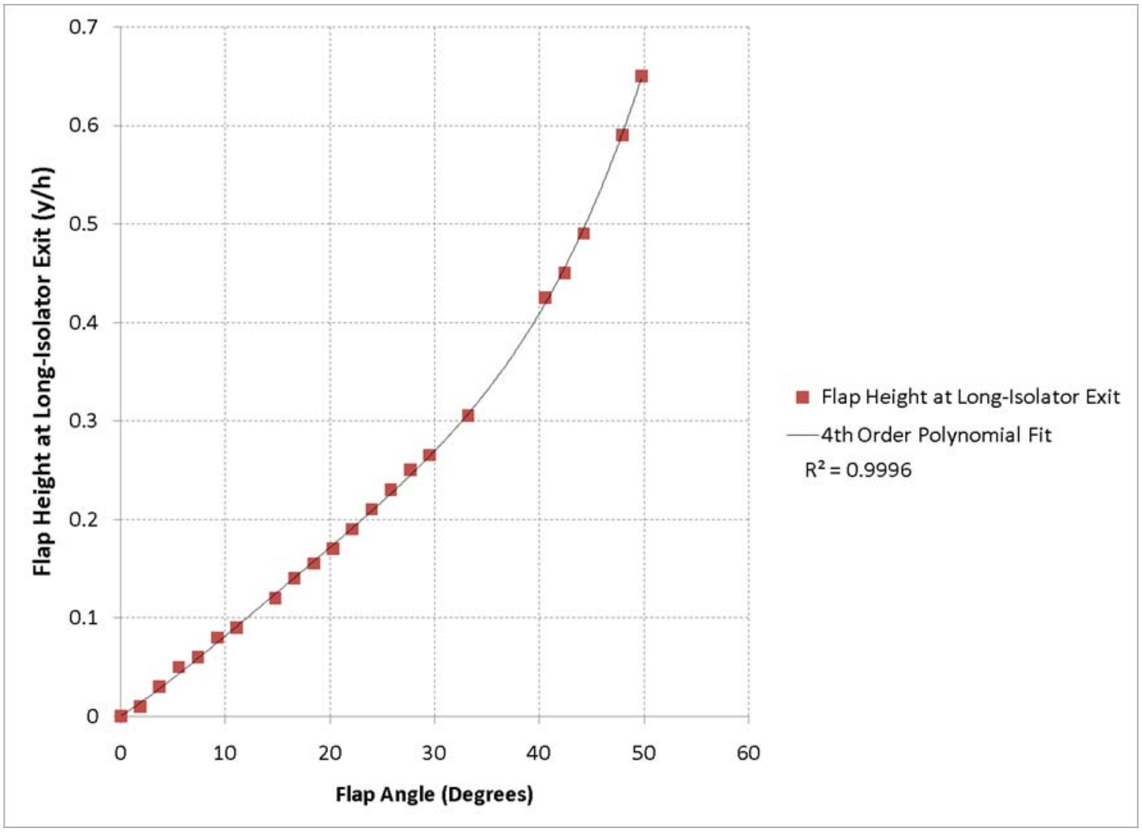

Figure B.3. Flap height (area blockage) at the exit of the long-isolator models as a function of flap angle.

APPENDIX C

C. PIV Uncertainty Analysis

C.1 SIDE-VIEW UNCERTAINTIES

This section addresses uncertainties in the PIV data that arise from a variety of sources. These sources include laser pulse separation time variations ($\delta_{\Delta t}$), calibration (image registration) uncertainty (δ_{Cal}), uncertainties incurred during the PIV data reduction process (δ_{Proc}) and precision uncertainty (δ_{Prec}).

C.1.1 Laser Pulse Variations and Image Registration Uncertainties

The typical laser pulse separation time was 2 μs. Using the variations in laser pulse separation times reported by Beresh (1999) yields an estimated uncertainty $\delta_{\Delta t}$ of 0.1% of a given velocity measurement.

The side-view measurements required that the calibration grid be placed and imaged at the laser sheet location which was near the spanwise center of the wind tunnel. Once the grid was imaged, conversion to physical space was achieved using the built in calibration function of Davis 7.2. In order to place the grid, both the upstream and downstream edges of the grid were placed at the same spanwise distance away from the sidewall using a ruler. Although care was taken during this process, inspection of calibrations where the grid was at the same nominal location showed that the image magnification could vary by up to about 0.5 %. Therefore, the estimated uncertainty due to image registration uncertainty (δ_{Cal}) is 0.5 % of a given velocity value.

C.1.2 Processing Uncertainty

C.1.2.1 During Unstart

Several factors can lead to increased uncertainties in the PIV data reduction process. Important parameters which affect an algorithm's ability to accurately detect velocity vectors include the out of plane motion of seed particles, the magnitude of velocity gradients over an interrogation window and the seeding density (Keane and Adrian, 1992 and Westerweel, 1997). Typically, the out of plane particle motion is limited by decreasing the laser pulse separation time or by increasing the laser sheet thickness. Obviously, this is a compromise as shorter pulse separation times alone will lead to greater uncertainties and a thicker sheet will lead to decreased resolution.

This section will compare the abilities of what are referred to as “classical” and “advanced” (nomenclature after Beresh 2008b) PIV processing algorithms to detect vectors in the presence of high velocity gradients. A more detailed discussion on this subject can be found in Beresh (2008a and 2008b). Herein, classical algorithms are those that use digital cross-correlation analysis and discrete window offsets (e.g., Keane and Adrian, 1992). Advanced algorithms are those which use fractional window offsets as well as what is called window deformation. The fractional window offsets help to mitigate errors associated with peak-locking (i.e., the tendency of an algorithm to return displacements at integer pixel values) and the window deformation increases the algorithm’s robustness in the presence of velocity gradients (Scarano and Riethmuller, 2000). High velocity gradients can have detrimental effects on a processing algorithm’s ability to detect valid velocity correlations (vectors) as they tend to broaden and even split correlation peaks (Keane and Adrian, 1992 and Westerweel, 1997). Still, if valid correlations are detected, then significant bias error (typically toward low velocities) as well as an increased random error can decrease the accuracy of the detected vector (Keane and Adrian, 1992). To circumvent these ill effects, in earlier or classical algorithms two prevalent guidelines exist in the literature, which suggest limits for a velocity gradient over an interrogation window. In order to maintain correlation detection probabilities greater than 95%, Keane and Adrian (1992) recommended limiting pixel displacement variations over an interrogation window to less than 3% the diameter of the interrogation window (d_I). More specifically, Westerweel (1997) recommended limiting the pixel displacement variation percentage over an interrogation window to be less than the recorded particle image diameter (d_τ) to interrogation window diameter ratio (i.e, d_τ/d_I). He noted that typically d_τ/d_I is about 3-5%, which is therefore consistent with the recommended limit of Keane and Adrian. Neglecting lens aberrations, the recorded particle image diameter, d_τ can be calculated using Equations C.1 to C.3 (Adrian, 1997)

$$d_\tau^2 = d_e^2 + d_r^2 \qquad \text{(C.1)}$$

$$d_e^2 = d_s^2 + M_0^2 d_p^2 \qquad \text{(C.2)}$$

$$d_s^2 = 2.44(1 + M_0) f^{\#} \lambda \qquad \text{(C.3)}$$

where d_s is the diffraction limited spot size of the particle image, d_e is the actual particle image size, d_p is the particle diameter, d_r is the CCD pixel diameter, λ is the light source wavelength, $f^{\#}$ is the lens f-number, and M_0 is the image magnification. For the experiments herein M_0 was about -0.08, the *f*-number was 8 (for the side-view) and the pixel diameter was 9 µm, which yields a recorded image diameter of about 1.6 pixels. Note that 1.6 pixels is exactly 5% the interrogation window width. So according to Westerweel (1997), the variation in displacement over a given window should not vary by more than about 2 pixels. In the case of the fully supersonic data started flow, pixel displacements typically were seen to vary by less than 2 pixels over a given interrogation window. However, for vector fields that contained a stable high-compression shock system or transient shock systems, this classical limit was often exceeded. For example, inspection of the PIV results corresponding to the strong-compression shock system showed instances where over the height of an interrogation window, the displacement given by valid vectors could vary by over 16 pixels. Fortunately, advanced processing algorithms such as those used by DaVis 7.2 are more able to cope with high gradients. These algorithms utilize a technique known as window deformation (Scarano and Riethmuller, 2000). In this technique, after a first pass, the shape of a given interrogation window is deformed in accordance with the velocity vectors given on the first pass. Scarano and Riethmuller showed in a backwards facing step experiment (U_∞ = 3.8 m/s) that velocity gradients that yielded changes in pixel displacements of 50% of d_I could be successfully measured. In addition, they showed with synthetic (simulated) PIV data, that pixel displacements up to 20% d_I over a 32 × 32 pixels interrogation window resulted in *RMS* displacement errors of only 0.1 pixels (compared to 1 pixel without window deformation). The above discussion shows that advanced algorithms that utilize window deformation are more able to handle velocity gradients. Specifically, the use of window deformation increases the vector detection probability as well as decreases the errors of the detected vectors (Scarano and Riethmuller, 2000). However, there does not appear to be a way in the literature to estimate the errors associated with the use of such algorithms. This seems especially true in regard to actual experimental data. As was shown in chapter 3 and as will be discussed further in this section, the flowfields of interest in the current study were not ideal for PIV measurements. It seems it would be an extreme underestimate to assume that the *RMS* errors of 0.1 pixels seen in the synthetic PIV results of Scarano and Riethmuller (2000) should apply to the real data of the current study. Moreover, in addition to the problem of high gradients, the current PIV data was seen to contain regions of low seeding density and regions of increased out of plane particle motion. Note that the following observations may be hard to see with a printed copy of this figure. They are more readily seen if this document is viewed electronically.

In Fig. C.1, sample particle images corresponding to the fully supersonic flow (Fig. C.1a) and at a time *t* = 4 ms into the unstart process (Fig. C.1b) are shown. In Fig. C.1a, the seeding density is seen to be lower near the floor due to the presence of the thick turbulent floor boundary layer. However, other than this, the seeding density is fairly uniform. In comparison, the image acquired at *t* = 4ms into unstart shows the seeding to be highly non-uniform. As labeled, the unstart shock system is seen to result in two large regions of reversed and separated flow. The region near the floor extends all the way until the field of view exit. Compared to the fully supersonic flow, out of plane particle motion was seen to be more of a problem in the separated regions. In the ceiling separation region, the seeding density is seen to be particularly low. This is the result of the ceiling boundary layer separating and occupying more of the image field of view. In the center of the image of Fig. C.1b, an area of high seeding density is seen that is the result of the flow being diverted around the ceiling and floor separation regions. This region does not contain distinct particle images but instead large areas of saturated pixels. Therefore, a combination of high velocity gradients, out of plane particle motion and seeding non-uniformities are expected to significantly increase the uncertainty of the PIV measurements during unstart. Since there does not appear to be another reliable, straightforward way to estimate the uncertainties due to these ill effects, the following method was utilized.

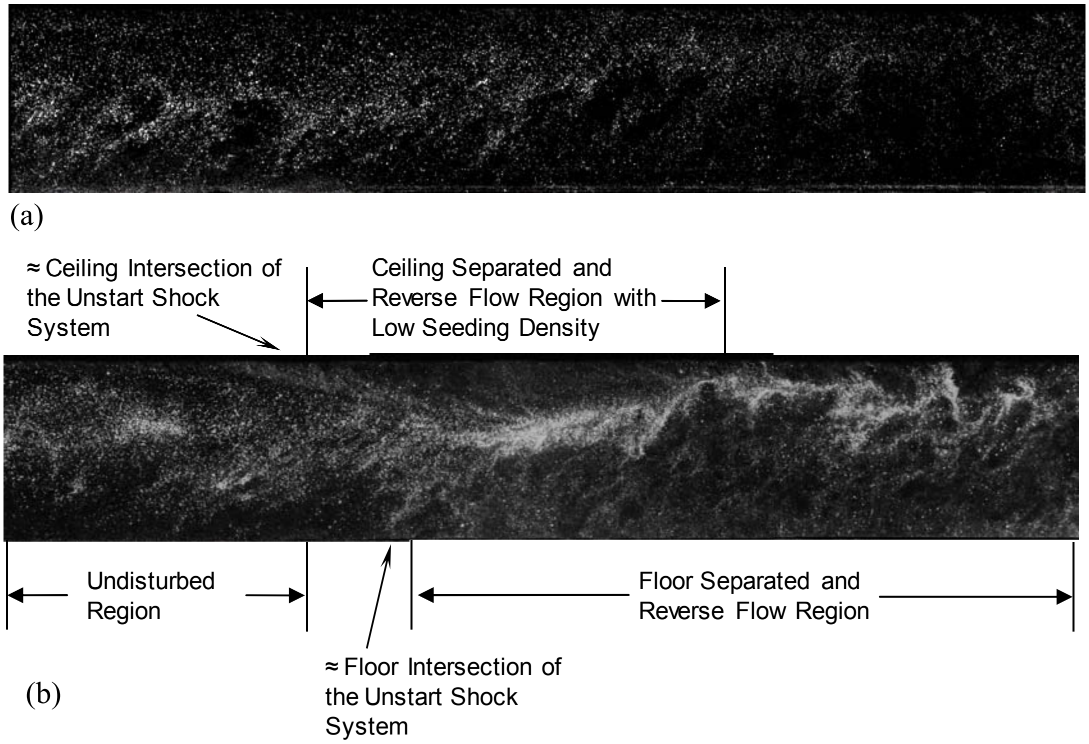

Figure C.1 Sample particle images showing the side-view wide field of view: a) fully supersonic flow, and b) t = 4ms into the unstart process.

Since it was necessary to have overlap, there were identical regions of the flow that were imaged by different cameras. In the side-view PIV, there was a region between the upstream and middle cameras as well as a region between the middle and downstream cameras. Therefore, for each spatial location (i.e., interrogation window) where the fields of view overlapped, there existed two independent PIV measurements at each spatial location. In order to estimate the uncertainty associated with the PIV processing algorithm (δ_{Proc}), the velocities given by the two independent measurements were compared. This comparison was made for an entire column of vectors common to the upstream and middle fields of view and similarly for an entire column between the middle and downstream fields of view. Figure C.2 shows the location of these two columns at *x/h* = 6.5 and *x/h* = 8.46. Note that the columns compared were not along the field of view edges. Rather, the columns compared were 2-4 columns away from the edges to try and avoid the influence of edge effects. Also, note that the overlapping measurements were at very similar spatial locations, but not at exactly the same location. Therefore, in order to have measurements data at the exact same spatial location, linear interpolation was used to map data in question from the two fields of view onto the same coordinate space. In addition, since this comparison uses data from different cameras, the uncertainties associated with the cameras are also included in the PIV processing uncertainty, δ_{Proc}.

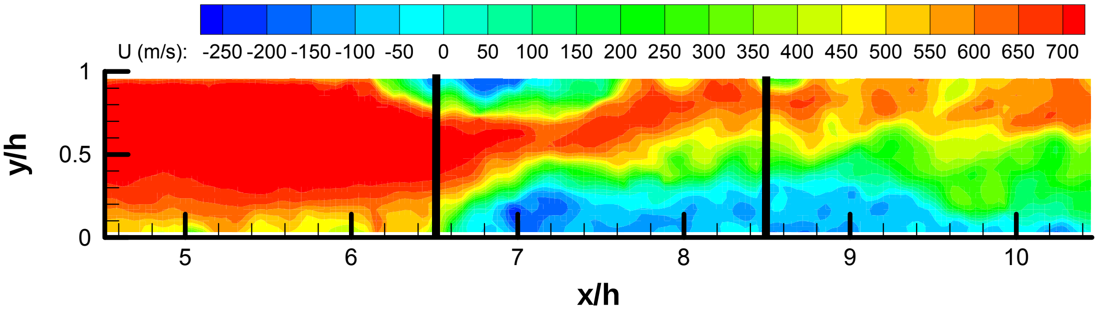

Figure C.2 Streamwise velocities t = 5 ms into the unstart process with lines showing the spatial locations used for comparisons to estimate the PIV processing uncertainty.

Figure C.3 shows the histogram of velocity differences measured at the same times and spatial locations during the unstart process. As seen in the distribution, the highest numbers of velocity differences reside near 0. With increasing difference magnitude, the histogram shows the number of samples to fall somewhat dramatically. This difference distribution was not seen to follow a random (Gaussian) distribution. For example, instead of 68%, 80% of the samples lie between $\pm\sigma$ (± 51 m/s or ± 0.069 U_∞)

and instead of 95%, 92% of the samples lie between ± 2σ (± 102 m/s or ± 0.138 U_∞). Assuming the velocity differences to be the uncertainties, these values give the side-view

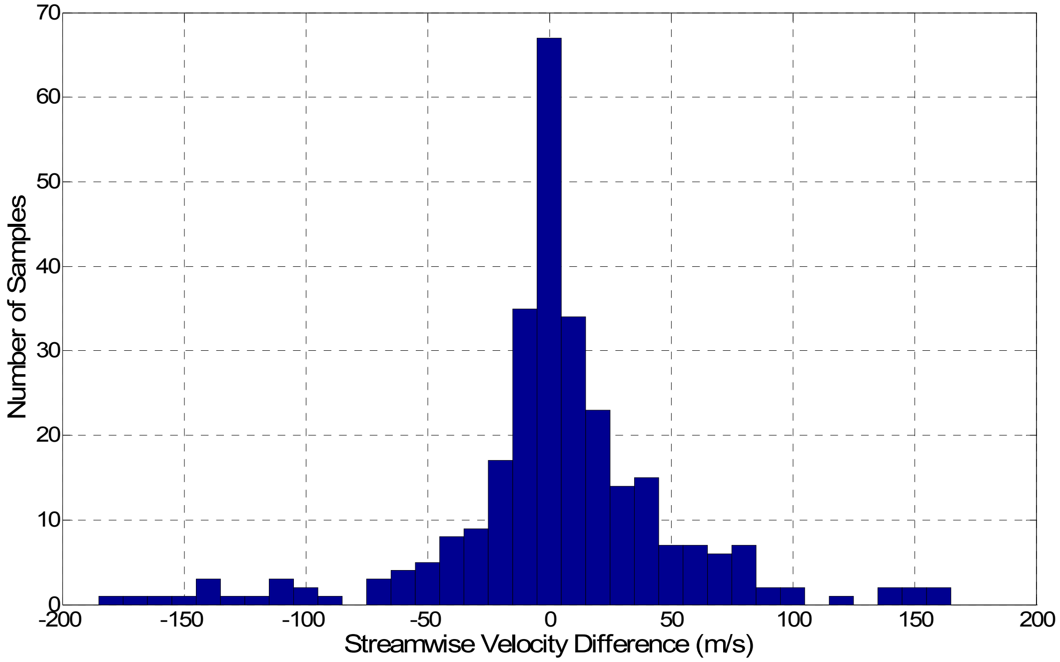

Figure C.3 Histogram of streamwise velocity differences measured at identical spatial locations during the unstart process for side-view PIV data.

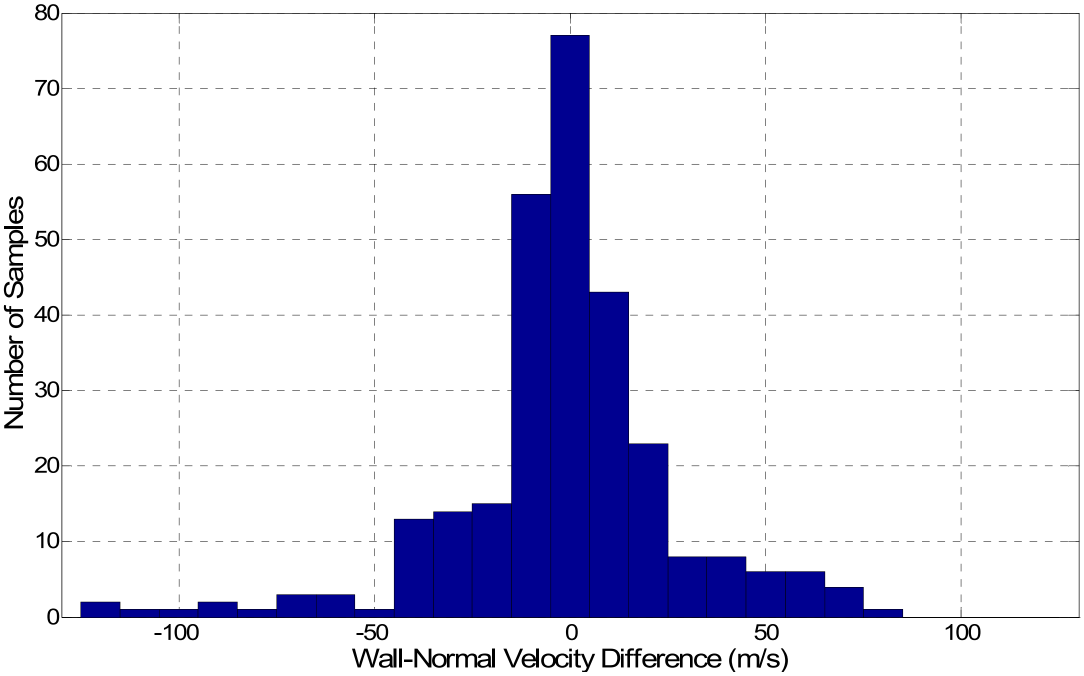

Figure C.4 Histogram of wall-normal velocity differences measured at identical spatial locations during the unstart process for side-view PIV data.

unstart process uncertainties. (The previously mentioned laser pulse separation time and calibration uncertainties are negligible in comparison.) Figure C.4 shows the histogram of wall-normal velocity measurement differences. Similarly, this distribution is not Gaussian. Rather, 77% of the samples fall between ±σ (± 23 m/s or ± 0.031 U_∞) and 92% of the samples fall between ± 2σ (± 45 m/s or ± 0.061 U_∞). Both the histograms of Fig. C.3 and Fig. C.4 show distributions where the velocity differences are preferentially near zero. Near the center, the distributions decay much faster than Gaussian. However, compared to a Gaussian distribution the tails are seen to have more outliers. Inspection of the PIV data showed that these higher differences at the tails were measured at spatial locations within the unstart shock system. Specifically, the greatest difference magnitudes were seen to occur when the separation shocks of the unstart shock system were just at the measurement comparison location. For example, note in Fig. C.2 that the common spatial location column at *x/h* = 6.5 is near the impingement location of the floor separation shock. Inspection of the vectors corresponding to the upstream and middle fields of view showed that the location of this shock was at slightly different locations in the data corresponding to the two fields of views. Specifically, the in the upstream field of view, the shock appeared to be about 1 mm upstream compared to the middle camera field of view. Inspection of the particle images with the spatial coordinates applied did not suggest this 1 mm difference was due to a grid imaging error. Therefore, the difference in the two fields of view is either due to the data reduction process, camera noise, or a combination of the two. Whatever the case, a 1 mm streamwise distance difference in the location of the floor separation shock was seen to lead to large differences in velocities measured. Figure C.2 also shows the ceiling separation shock to reside near the common measurement column. For similar reasons, large velocity differences were measured in this region as well.

C.1.2.2 During the Fully Supersonic Flow

The same technique of comparing vectors at the same spatial locations was undertaken for the mean fully supersonic started flow. As expected, the differences were much smaller. The uncertainties were taken as the $\pm 2\sigma$ values of the differences in velocities measured. For the streamwise velocities this was ± 4 m/s, or $\pm 0.005\ U_\infty$. For the wall-normal velocities this was ± 2 m/s, or $\pm 0.003\ U_\infty$.

C.1.2.3 During the High-Compression Shock System Flow

For this flow data at the same spatial location was compared along a column at *x/h* = 8.5. The upstream and middle overlapping column was not included in the uncertainty estimate for this flow. This was due to the fact that the upstream camera had shifted sometime between the acquisition of calibration grid image and the acquisition of data. Since the both the floor and ceiling separation shocks were near the overlapping area of the upstream and middle cameras (e.g., See Fig. 3.38), this camera shift lead to unnaturally high *RMS* velocity differences. Therefore, only the overlapping region between the middle and downstream cameras was used to estimate the uncertainty. The uncertainties were taken as the ± 2σ values of the differences in velocities measured and for the streamwise velocities this was ± 30 m/s, or ± 0.041 U_∞.

C.1.3 Precision Uncertainty in Mean Velocities

Since a limited number of vector fields were acquired for the mean flowfields reported herein, precision uncertainty was a non-negligible uncertainty source. The precision uncertainty, δ_{Prec} is equal to $2\sigma_U/\sqrt{n}$, where n is the number of vector samples used in the mean calculation and σ_U is the standard deviation of U at a given spatial location. Although about 90 vector fields were used in the computation of both the fully supersonic and high-compression shock system mean velocities, only valid vectors were used to calculate the mean. In the upcoming section, mean velocity profiles are presented for the fully supersonic and high-compression shock system flows. For these profiles, the minimum number of vectors (and therefore n) used to calculate the mean at a given point was about 50 for the fully supersonic flow and 40 for the high-compression shock system.

C.1.4. Total Uncertainty in the Mean Velocities

Assuming that the uncertainty sources are independent, the total estimated uncertainty in mean velocities reported herein is therefore to equal to the root-sum-square of the four sources described above, i.e.,

$$\delta_{Mean} = \sqrt{\delta_{\Delta t}^2 + \delta_{Cal}^2 + \delta_{\mathrm{Pr}\,oc}^2 + \delta_{\mathrm{Pr}\,ec}^2} \qquad \text{(C.4)}$$

Figure C.5 shows the mean streamwise velocity profile at the streamwise location of *x/h* = 6.5. The presence of the thick floor and thin ceiling boundary layers are seen in profile. Figure C.6 shows the mean streamwise velocity profile at *x/h* = 8.5 for the high-compression shock system. Near the floor the velocity is seen to be reversed on average. However, the uncertainty bands show that all that can be said definitively is that the velocities are near zero. Note in comparison to Fig. C.5, the uncertainty ranges in C.6 are substantially broader. This is due to higher PIV processing errors as well as higher precision uncertainties.

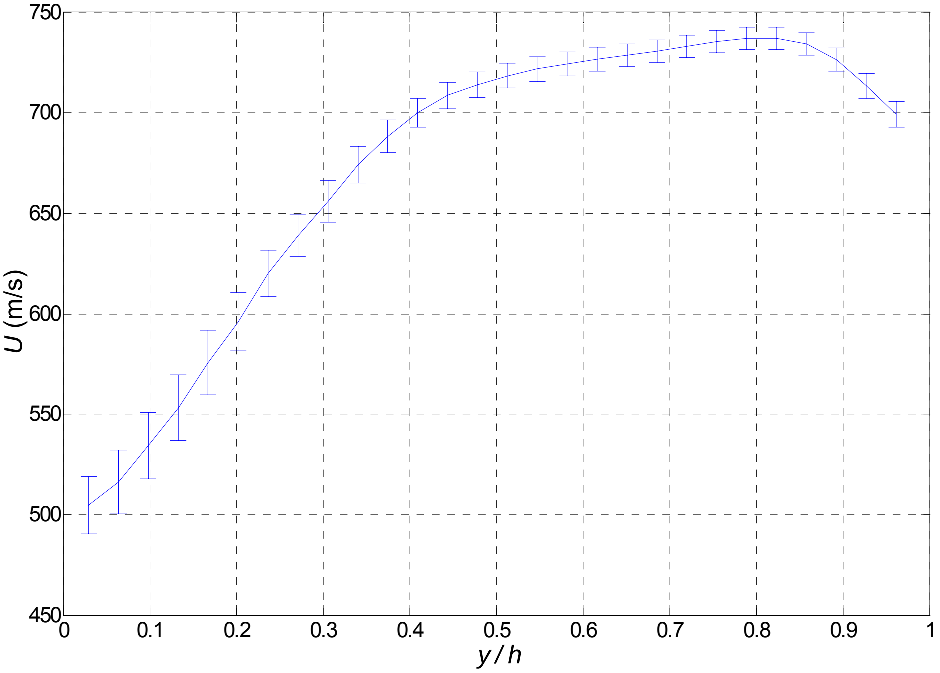

Figure C.5 Mean streamwise velocity profile and uncertainties for the fully supersonic started flow at *x/h* = 6.5.

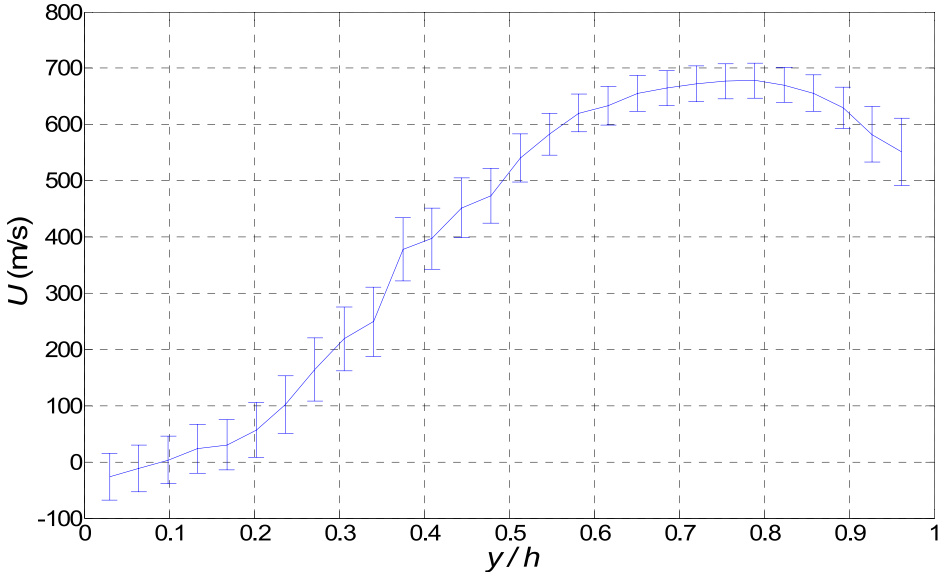

Figure C.6 Mean streamwise velocity profile and uncertainties for the strong-compression shock system flow at x/h = 8.5.

C.2 PLAN-VIEW UNCERTAINTIES

C.2.1 Image Registration Uncertainties

The uncertainty associated with the grid calibration was estimated for the plan-view data in the same way as described for the side-view. However, for the plan-view grid imaging, it was much easier to place the grid at a more consistent location. This was because the grid was placed on top of a base of known height (y/h = 0.5) as opposed to placing it using rulers as in the side-view grid. Therefore, the estimated uncertainty in the image registration process (δ_{Cal}) was seen to be only about 0.1% for the plan-view data.

C.2.2 Processing Uncertainties

C.2.2.1 During Unstart

The only plan-view data presented was acquired during the unstart process. The method of approximating the processing uncertainty as well as that due to camera noise was the same as that described in section C.1.2. However, since four cameras were used, there were three overlapping regions from which three columns of vectors were compared. The resulting differences in streamwise velocities are shown in Fig. C.7. Similar to the side-view velocity difference distributions and for similar reasons, the plan-view differences are not Gaussian. For example, 82% of the samples fall between $\pm\sigma$ ($\pm$ 31 m/s or $\pm$ 0.042 U_∞) and 93% of the samples fall between $\pm$ 2σ ($\pm$ 63 m/s or $\pm$ 0.085 U_∞). Assuming the velocity differences to be the uncertainties, these values give the plan-view unstart process uncertainties. (The previously mentioned laser pulse separation time and calibration uncertainties are negligible in comparison). The estimated plan-view PIV processing uncertainty is seen to be significantly less than that corresponding to the side-view. One reason for this is the fact that the plan-view measurements were acquired in the wall-normal center plane where the seeding densities were seen to be higher. Another possible reason might be the higher *f*-number of 16 used in the plan-view experiments. Using equations C.1 to C.3 and with all other parameters the same as those given for the side-view (which is nearly the case), the recorded pixel diameter (d_τ) computes to be 3.2 pixels. This doubling of d_τ therefore doubles the suggested pixel displacement variation ratio limit of (d_τ/d_I) given by Westerweel (1997).

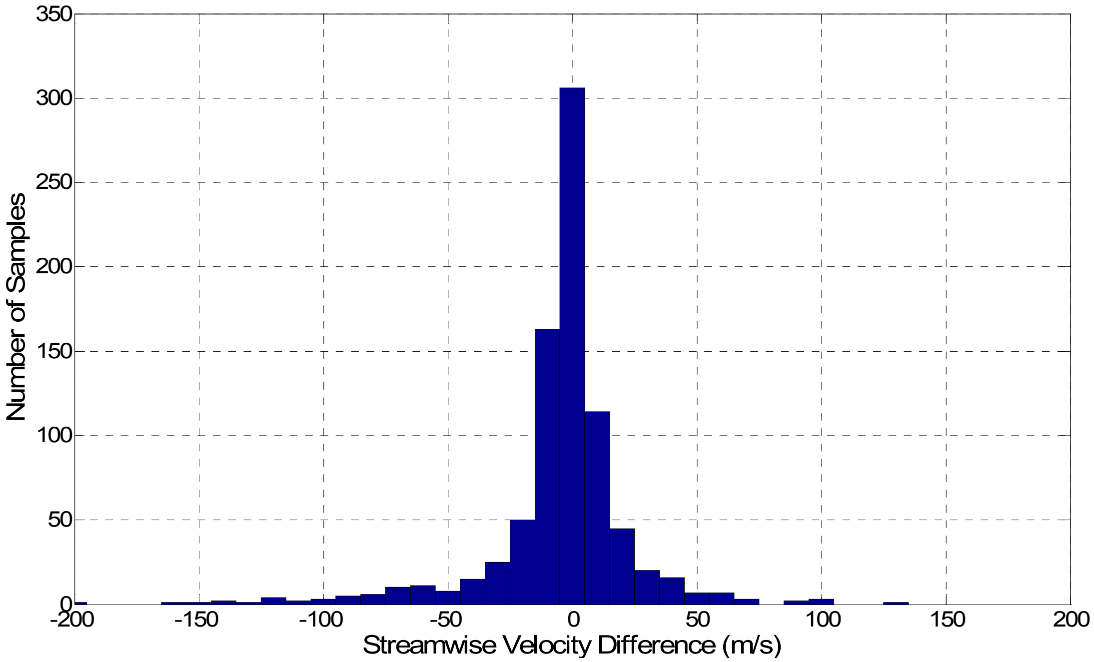

Figure C.7 Histogram of streamwise velocity differences measured at identical spatial locations during the unstart process for plan-view PIV data.

APPENDIX D

D. Discussion Regarding the Freestream Conditions

D.1 EXPERIMENTS WITH TWO HEATER BANKS

Plan-view PIV measurements were made at a height of 38.1 mm to measure the freestream velocity. These tests were conducted at plenum temperature of 344 K. At this plenum temperature, U_∞ was measured to be 753 m/s. Note that assuming isentropic flow through the nozzle and using the energy equation along with the measured freestream velocity and plenum temperature gives a freestream temperature of 61.9 K and a freestream Mach number of 4.77. Beresh (1999) reported a similar value of 750 m/s at a plenum temperature of 355 K. (Note that seeding particles were injected into the plenum for his freestream measurements.) Again assuming isentropic flow, these two measurements yield a freestream temperature of 75.1 K and a much lower freestream Mach number of 4.32. On the other hand, Beresh reported that test section Pitot pressure measurements along with the measured plenum pressure and temperature predicted that the freestream velocity should have measured 769 m/s which gives a freestream Mach number of 4.9. Considering the uncertainties in his measurements he concluded that a likely culprit for the freestream velocity discrepancy was not measurement uncertainty, but rather losses between through the nozzle between the plenum and test section. He noted specifically that a drop in stagnation temperature of 17 K would be enough to explain the freestream velocity and Mach number discrepancies. Since the current freestream measurements also showed lower than expected freestream velocities, tests were conducted using a test section stagnation temperature probe. During these tests, the test section stagnation temperature and the plenum temperature were simultaneously recorded. The result seen on two separate runs, was that the test section stagnation temperature was measured to be 8 K lower than that measured in the plenum. If this 8 K decrease is subtracted from the T_0 value of 344 K recorded for the freestream velocity of 753 m/s, the freestream temperature then equals 54 k and the freestream Mach number then computes to be 5.1.

In addition, test section Pitot pressure measurements were made to compute the freestream Mach number. Based on the plenum pressure and test section Pitot pressure, the freestream Mach number was found to be 4.99 ± 0.03. However, note this calculation depends on the plenum pressure. Since the stagnation temperature was seen to decrease in between the plenum and test section, it is possible that the stagnation pressure increased (i.e., cooling effects). In comparison, the previous M_∞ computation of 5.1 above is based only on the test section conditions. This measurement is considered better than the Pitot probe Mach number which was based on the plenum pressure. Therefore as given in Table 2.1, for the experiments that used two heater banks, the freestream Mach number and velocity were about 5.1 and 750 m/s (2460 ft/s). However, it is noted that an easier alternative would be to measure M_∞ at a single point in the test section using a Pitot-static probe.

D.2 EXPERIMENTS WITH ONE HEATER BANK

Plan-view PIV measurements were made at a height of 38.1 mm to measure the freestream velocity. These tests were conducted at plenum temperature of 328 K. At this plenum temperature, U_∞ was measured to be 734 m/s. In the PIV images from experiments conducted with one heater, there was consistently seen to be a significant increase in condensate as compared to experiments conducted with both heater banks. This condensate is believed to be water, oxygen or a combination of both that condensed during the nozzle expansion process. Condensation of water or oxygen would lead to flow heat addition, which would lead to an increase in static pressure.

In order to see if the condensation did in fact increase the freestream pressure, wall pressure measurements near the test section entrance were made using the same factory-calibrated precision dial gage (Heise Model CMM) that was used to calibrate the Kultite transducers. In addition, static pressure measurements were made with a freestream probe directly connected to the precision dial gage. However, in total, these static pressure measurements provided only five data points for both the one and two heater bank tests. Therefore, to reduce precision uncertainty, three additional wall pressures as measured at T1 were included for each case. Note that the same calibration line was used in comparing the T1 pressure data for the one and two heater tests. The final sample size was a total of eight measurements of static pressure for both the one and two heater cases. For the one heater tests, the mean static pressure was 0.78 ± 0.03 psia (5.38 ± 0.21 kPa). For the two heater tests, the mean static pressure was 0.72 ± 0.02 psia (4.96 ± 0.14 kPa). Therefore, it does appear that heat addition due to condensation did result in a small but non-negligible freestream pressure increase. To make for an easy calculation, the resulting freestream Mach number due to this heat addition can be estimated if the flow in the nozzle is first assumed to expand to the two heater bank Mach number of 5.1 and is then subjected to one-dimensional heat addition (i.e., Rayleigh flow) due to condensation. In other words the way that the test section flow reaches its final M_∞ is approximated as a two step process. Using the one to two heater bank pressure ratio of 1.08 and assuming Rayleigh flow, the freestream Mach number for the one heater tests then computes to 4.9. As a check, if the heat addition is in fact real, then this should result in an increase in stagnation temperature. In the one heater run where U_∞ was measured, the plenum temperature was measured to be 328 K. However, similar to the two heater case, a decrease in stagnation temperature of 8 K was measured between the plenum and test section entrance. Therefore it is approximated that the test section stagnation temperature for the run where U_∞ was measured was equal to 320 K. However, if there was in fact condensation, stagnation of the flow would result in heat absorption (gas cooling). Therefore, the heat addition due to condensation would not be measurable using a stagnation probe. For heat addition that results in the decrease in Mach number given above, Rayleigh flow predicts a stagnation temperature increase from 320 to 323 K. Using the computed one heater M_∞ of 4.9 and the predicted stagnation temperature of 323 K gives a freestream temperature of 56 K. The freestream velocity then computes to be 735 m/s which is in excellent agreement with that given by the PIV data of 734 m/s. Therefore, as given in Table 2.1, for the experiments that used one heater bank, the freestream Mach number was taken to be 4.9. In addition, it is noted that a Pitot-static probe would not be able to correctly measure M_∞ in the presence of condensation since the stagnated gas would cool due to evaporation.

APPENDIX E

E. Repeatability of the Unstart Flow Structure as seen with Schlieren Imaging

This Appendix shows the repeatability of the unstart flow structure using high-speed schlieren imaging. To demonstrate this point, three different unstart events with nominally the same flow conditions are compared for unstart events in the 6-degree inlet / long-isolator model. The flow structure and dynamics of unstart in this model are discussed in detail in chapter 3.

For each of the three unstart events, three schlieren images were chosen that corresponded to the unstart shock system being located at three different streamwise locations. The unstart shock system locations for each event were near the isolator exit, near the streamwise center of the isolator and near the isolator entrance. Figure E.1 shows three different unstart events where the unstart shock system is located near the isolator exit. The figure shows the flow structure to be very similar for all three of the unstart events. The unstart times are also given in each image to demonstrate further that the timescales of unstart are not entirely repeatable. The repeatability of unstart timescales and velocities were discussed quantitatively in sections 3.4 and 3.5. Figure E.2 gives the instantaneous isolator pressure distributions corresponding to the images in Fig. E.1. The instantaneous pressure distributions all show a similar trend. In Fig. E.3, the unstart shock system in each event has propagated to near the streamwise center of the isolator. Again, the flow structure of each unstart event is very similar. The instantaneous pressure distributions corresponding to Fig. E.3 are given in Fig. E.4. The greatest difference between distributions is about 4.4 P_∞, which occurs at T6 (x/h = 10.53). Finally, Fig. E.5 shows images where the unstart shock system has propagated to near the isolator entrance. Again, the flow structure corresponding to each image is seen to be similar. In addition, the instantaneous isolator pressure distributions are given in Fig. E.6. Each pressure distribution follows a similar trend.

Collectively, the schlieren images of Fig. E.1, Fig. E.3 and Fig. E.5 show the flow structure of the unstart process in the 6-degree inlet / long-isolator model to be highly repeatable.

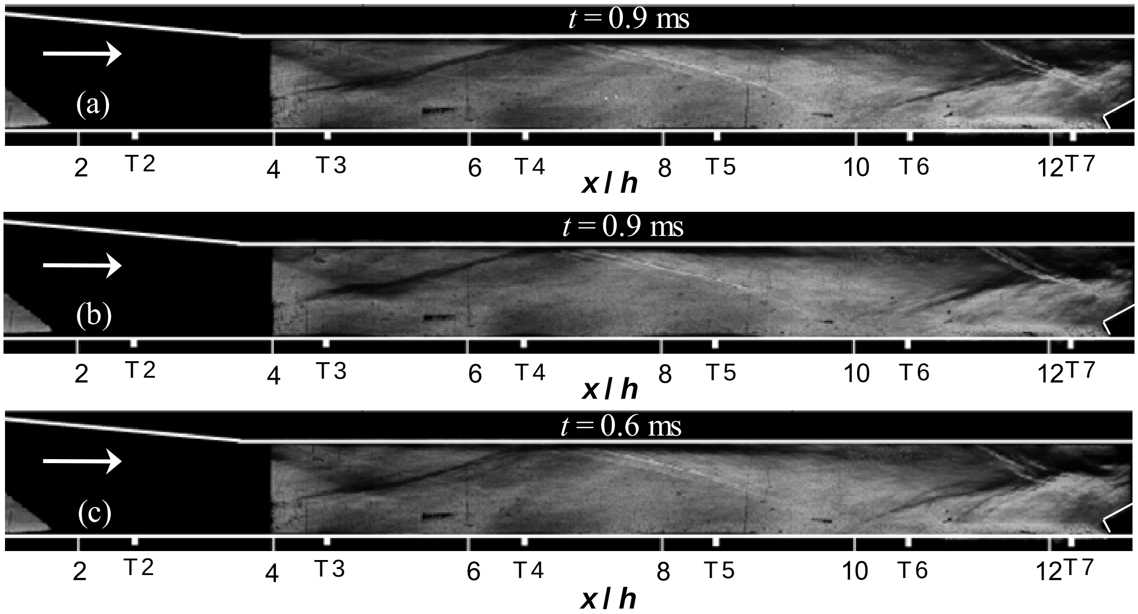

Figure E.1. Schlieren images (acquired with a horizontal knife-edge) from different unstart events showing similar flow structure at times: a) $t = 0.9$ ms (corresponds to test A in Fig. E.2), b) $t = 0.9$ ms (corresponds to test B in Fig. E.2), and c) $t = 0.6$ ms (corresponds to test C in Fig. E.2).

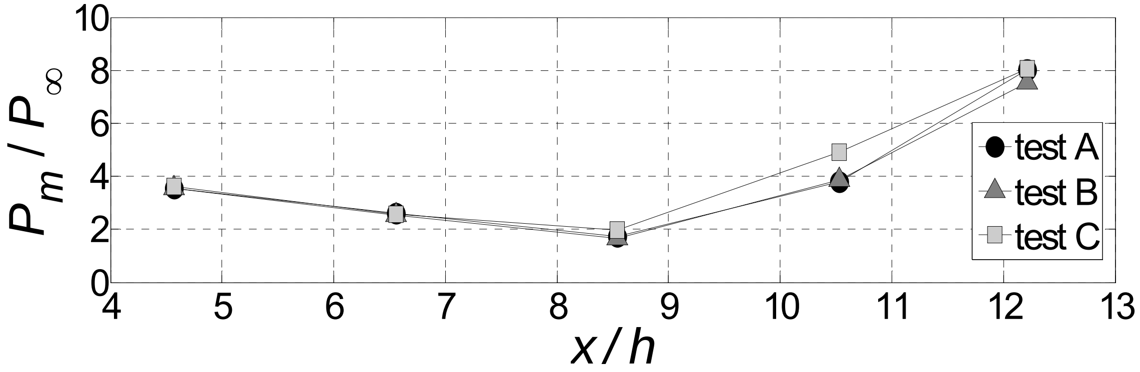

Figure E.2 Instantaneous pressure distributions corresponding to the schlieren images in Fig. E.1, where tests A, B and C correspond to Figs. E.1a, E.1b and E.1c, respectively.

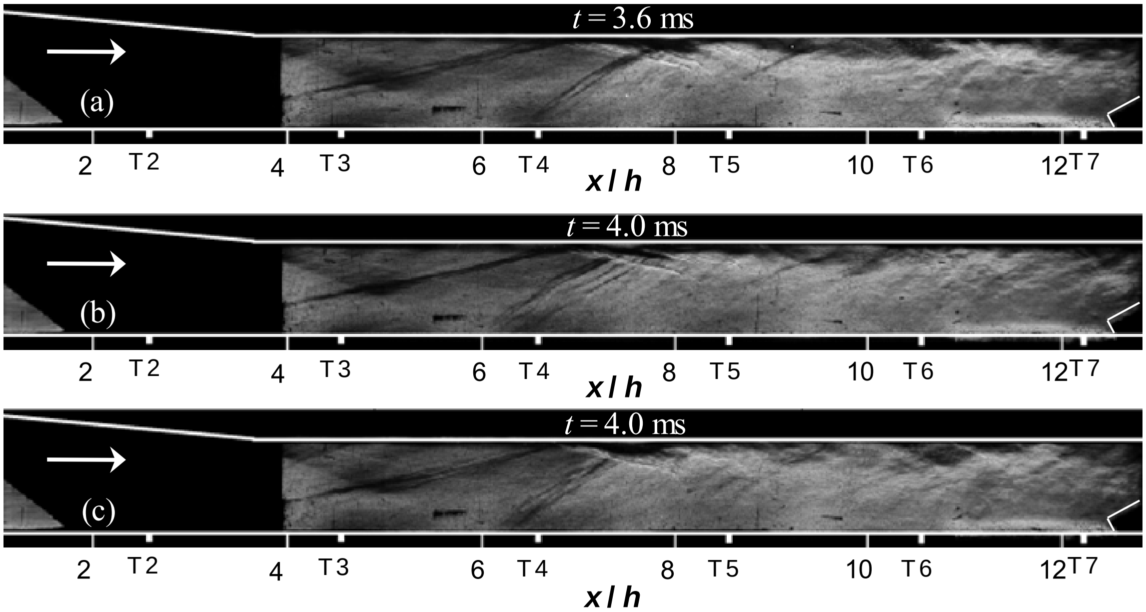

Figure E.3. Schlieren images (acquired with a horizontal knife-edge) from different unstart events showing similar flow structure at times: a) *t* = 3.6 ms (corresponds to test A in Fig. E.4), b) *t* = 4.0 ms (corresponds to test B in Fig. E.4), and c) *t* = 4.0 ms (corresponds to test C in Fig. E.4).

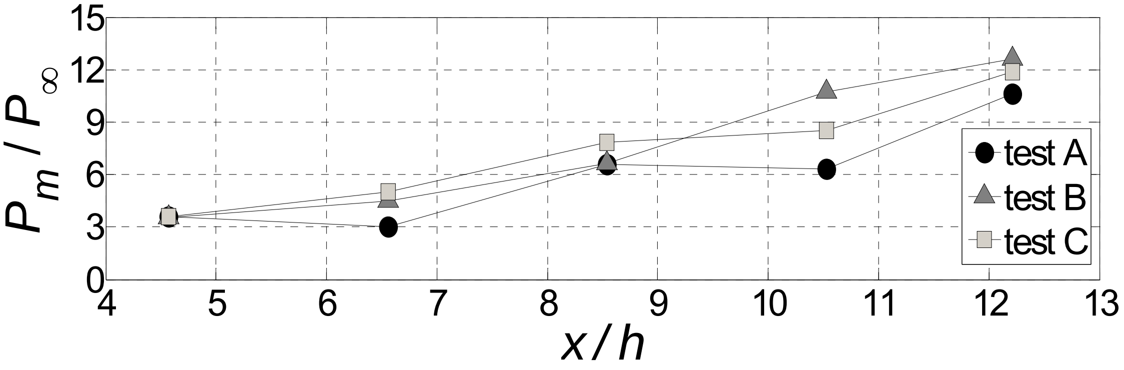

Figure E.4 Instantaneous pressure distributions corresponding to the schlieren images in Fig. E.3, where tests A, B and C correspond to Figs. E.3a, E.3b and E.3c, respectively.

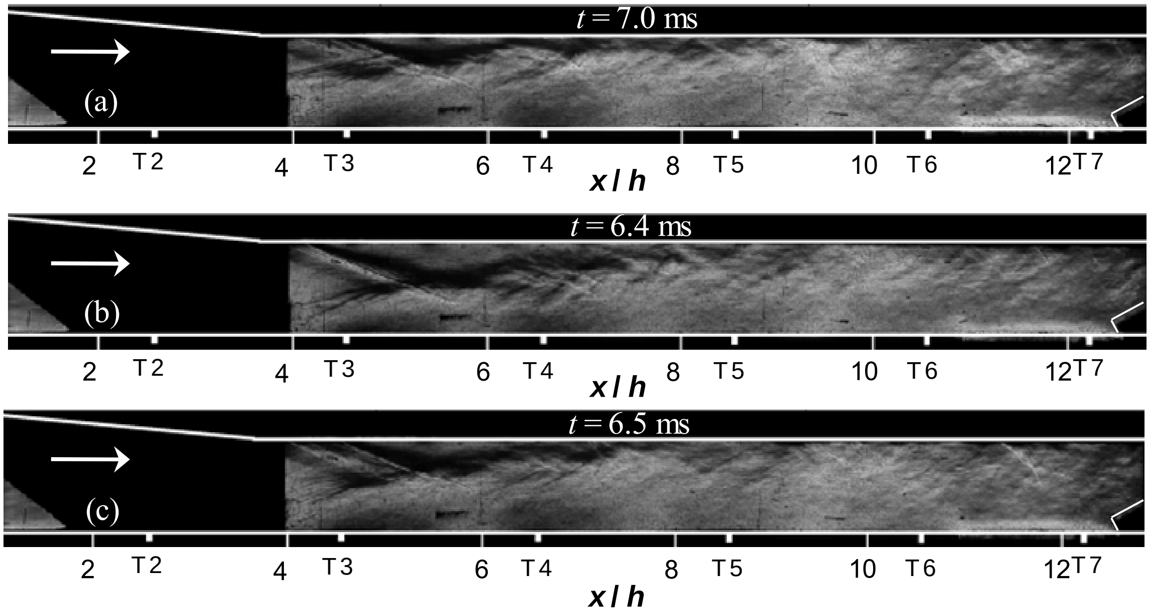

Figure E.5. Schlieren images (acquired with a horizontal knife-edge) from different unstart events showing similar flow structure at times: a) *t* = 7.0 ms (corresponds to test A in Fig. E.6), b) *t* = 6.4 ms (corresponds to test B in Fig. E.6), and c) *t* = 6.5 ms (corresponds to test C in Fig. E.6).

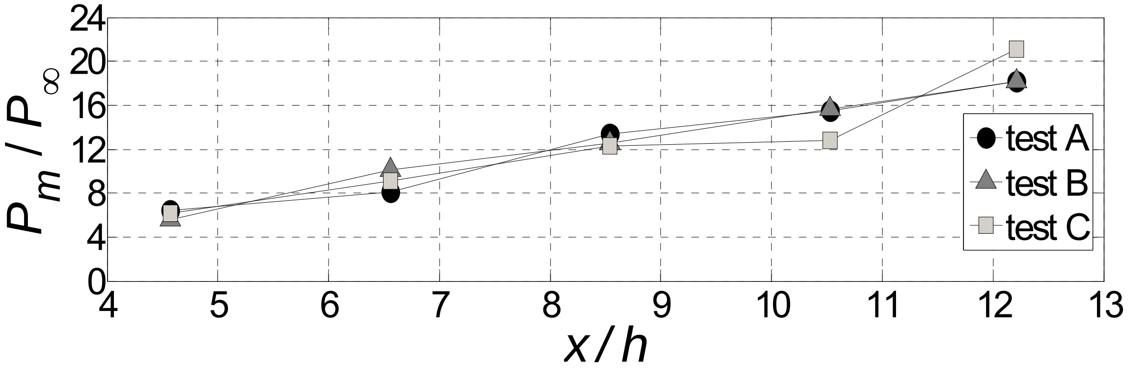

Figure E.6 Instantaneous pressure distributions corresponding to the schlieren images in Fig. E.5, where tests A, B and C correspond to Figs. E.5a, E.5b and E.5c, respectively.

References

Adrian, R. J. (1997), "Dynamic ranges of velocity and spatial resolution of particle image velocimetry," *Measurement Science and Technology*, Vol. 8, No. 12, 1997, pp. 1393-1398.

Anderson, G. Y., McClinton, C. R. and Weidner, J.P. (2000), "Scramjet Performance," *Scramjet Propulsion*, edited by E. T. Curran and S. N. B. Murthy, Vol. 189, Progress in Astronautics and Aeronautics, AIAA, Reston, VA, 2000.

Andreadis, D., (2004), "Scramjet Engines Enabling the Seamless Integration of Air & Space Operations," *The Industrial Physicist*, August/September 2004.

Bachchan, N. and Hillier, R. (2004), "Effects of Hypersonic Inlet Flow Non-Uniformities on Stabilising Isolator Shock Systems," AIAA Paper 2004-4716, August 2004.

Barter, J. W. (1995), "Prediction and Passive Control of Fluctuating Pressure Loads Produced by Shock-Induced Turbulent Boundary Layer Separation," Ph.D. dissertation, Dept. of Aerospace Engineering and Engineering Mechanics, The University of Texas at Austin.

Beresh, S. J. (1999), "The Effect of the Incoming Turbulent Boundary Layer on a Shock-Induced Separation Flow Using Particle Image Velocimetry," Ph.D. dissertation, Department of Aerospace Engineering and Engineering Mechanics, The University of Texas at Austin.

Beresh, S. J., (2008a), "Evaluation of PIV Uncertainties using Multiple Configurations and Processing Techniques," AIAA Paper 2008-239, January 2008.

Beresh, S. J., (2008b), "The Influence of Velocity Gradients on PIV Measurements of Turbulence Statistics: A Preliminary Study," AIAA Paper 2008-3710, June 2008.

Billig., F. S. (1993), "Research on Supersonic Combustion," *Journal of Propulsion and Power*, Vol. 19, No. 4, 1993, pp. 499-514.

Bueno, P., Wagner, J. L., Searcy, J., Ganapathisubramani, B., Clemens, N. T., Dolling, D. S. (2006), "Experiments in Pulsed Forcing of Mach 2 Shock Wave/Boundary Layer Interactions", AIAA Paper 2006-878, January 2006.

Carroll, B. F. and Dutton, J. C. (1990), "Characteristics of multiple shock wave/turbulent boundary-layer interactions in rectangular ducts," *Journal of Propulsion and Power*, Vol. 6, No. 2, 1990, pp. 186-193.

Cockrell, C.E., Auslender, A. H., White, J.A. and Dilly, A.D. (2002), "Aeroheating Predictions for the X-43 Cowl-Closed Configuration at Mach 7 and 10," AIAA Paper 2002-0218, January 2002.

Crocco L. (1958), "One-dimensional treatment of steady gas dynamics," *Fundamentals of Gas Dynamics*, Princeton University Press, Princeton, 1958, pp. 110-130.

Curran, E. T. and Stull, F. E. (1964), "The Utilization of Supersonic Combustion Ramjet Systems at Low Mach Numbers," Aero Propulsion Lab., RTD-TDR-63-4097, Wright-Patterson AFB, OH, Jan. 1964.

Curran, E. T., Heiser, W. H. and Pratt, D. T. (1996), "Fluid Phenomena in Scramjet Combustion Systems," *Annual Review of Fluid Mechanics*, Vol. 28, 1996, pp. 323-360.

Emami, S., Trexler, C. A., Auslender, A. H. and Weidner, J. P. (1995), "Experimental Investigation of Inlet-Combustor Isolators for a Dual Mode Scramjet at a Mach Number of 4," NASA TP-3502, May 1995.

Engblom, W. A. (1996), "Numerical Investigation of Hypersonic Flow over a Forward-Facing Cavity," Ph.D. dissertation, Dept. of Aerospace Engineering and Engineering Mechanics, The University of Texas at Austin.

Erbland, P. J. (2000), "Development and application of carbon dioxide enhanced Rayleigh scattering for high speed low density flows", Ph.D. thesis, Princeton University, Princeton, New Jersey, 2000.

Silton, S. I., and Goldstein, D. B. (2005), "Use of an axial nose-tip cavity for delaying ablation onset in a hypersonic flow," *Journal of Fluid Mechanics* Vol. 528, 2005, pp. 297-321.

Hawkins, W. R. and Marquart, E. J. (1995), "Two-Dimensional Generic Inlet Unstart Detection at Mach 2.5 – 5.0", AIAA Paper 95-6016, April 1995.

Heiser, W. H., and Pratt, D. T. (1994), *Hypersonic Air Breathing Propulsion*, AIAA Education Series, New York, 1994.

Hill, P. G. and Peterson, C. R. (1992), *Mechanics and Thermodynamics of Propulsion*, Addison-Wesley Publishing Company, 1992.

Hou, Y. X. (2003), Particle Image Velocimetry Study of Shock Induced Turbulent Boundary Layer Separation, Ph.D. dissertation, Department of Aerospace Engineering and Engineering Mechanics, The University of Texas at Austin.

Kantrowitz, A., and Donaldson, C. (1945), "Preliminary Investigation of Supersonic Diffusers," NACA WR L-713, 1945.

Keane, R. D., and Adrian, R. J. (1992), "Theory of Cross-Correlation Analysis of PIV Images," *Applied Scientific Research*, Vol.49, No. 3, 1992, pp. 191-215.

Korkegi, R. H. (1975), "Comparison of Shock-Induced Two- and Three-Dimensional Incipient Turbulent Separation," *AIAA Journal*, Vol. 13, No. 4, 1975, pp. 534, 535.

Le, D. B., Goyne, C. P., Krauss, R. H., and McDaniel, J. C. (2006), "Shock Train Leading Edge Detection in a Dual-Mode Scramjet", AIAA Paper 2006-0815, January 2006.

Le, D. B., Goyne, C. P., Krauss, R. H., and McDaniel, J. C. (2008), "Experimental Study of a Dual-Mode Scramjet Isolator," *Journal of Propulsion and Power*, Vol. 24, No. 5, 2008, pp. 1050-1057.

Love, E. S. (1955), "Pressure-Rise Associated with Shock-Induced Boundary-Layer Separation," NACA TN 3601, December 1955.

MacCormack, R. W., and Baldwin, B. S. (1975), "A numerical method for solving the Navier-Stokes equations with application to shock-boundary layer interactions," AIAA Paper 1975-1, Jan 1975.

Mahoney, J. J. (1990), *Inlets for Supersonic Missiles*, AIAA Education Series, Washington D.C., 1990.

Masuya, G., Komuro, T., Murakami, A., Shinozaki, N., Nakamura, A. and Murayama, O. (1995), "Ignition and Combustion Performance of Scramjet Combustors with Fuel Injection Struts," *Journal of Propulsion and Power*, Vol. 11, No. 2, 1995, pp. 301-307.

Matsuo, K., Miyazato, Y., and Kim, H.-D. (1999), "Shock train and pseudo-shock phenomena in internal gas flows," *Progress in Aerospace Sciences*, Vol. 35, 1999, pp. 33-100.

McDaniel, K. S. and Edwards, J. R. (2001), "Three-Dimensional Simulation of Thermal Choking in a Model Scramjet Combustor," AIAA Paper 2001-0382, January 2001.

McLafferty, G. H., Krasnoff, I. L., Ranard, E. D., Rose, W.G. and Vergaro, R. D. (1955), "The Investigation of Turbojet Inlet Design Parameters," R-0790-13, United Aircraft Corp., East Harford, Connecticut, December 1955.

Melling, A. (1997), "Tracer Particles and Seeding for Particle Image Velocimetry," *Measurement Science and Technology*, Vol. 8, No. 12, 1997, pp. 1406-1416.

Neaves, M. D., McRae, S., and Edwards, J. R. (2001), "High-Speed Inlet Unstart Calculations Using An Implicit Solution Adaptive Mesh Algorithm", AIAA Paper 2001-0825, January 2001.

Nedungadi, A., and Van Wie, D. M., (2004), "Understanding Isolator Performance Operating in the Separation Shock Mode," AIAA Paper 2004-3832, July 2004.

O'Byrne, S., Doolan, M., Olsen, S. R. and Houwing, A. F. P. (2000), "Analysis of Transient Thermal Choking Processes in a Model Scramjet Engine," *Journal of Propulsion and Power*, Vol. 16, No. 5, 2000, pp. 808-814.

Penzin, V. L. (1998), “Experimental Investigations of Supersonic Flows with Separated Regions In Ducts,” AFRL-PR-WP-TR-1998-2140, August 1998.

Reinartz, B. U, Herrmann, C. D. and Ballmann, J. B. (2003), “Aerodynamic Performance Analysis of a Hypersonic Inlet Isolator Using Computation and Experiment,” *Journal of Propulsion and Power*, Vol. 19, No. 5, 2003, pp. 868-875.

Rice, T. (2003), “High Aspect Ratio Isolator Performance for Access-to-Space Vehicles,” AIAA-2003-7041, Dec. 2003.

Rodi, P. E. , Emami, S., and Trexler, C. A. (1996), “Unsteady Pressure Behavior in a Ramjet/Scramjet Inlet,” *Journal of Propulsion and Power*, Vol. 12, No. 3, 1996, pp. 486-493.

Sabel’nikov, V. A. and Penzin, V. I. (2000), “Scramjet Research and Development in Russia,” *Scramjet Propulsion*, edited by E. T. Curran and S. N. B. Murthy, Vol. 189, Progress in Astronautics and Aeronautics, AIAA, Reston, VA, 2000.

Samimy, M. and Lele, S. K. (1991), “Motion of Particles with Inertia in a Compressible Free Shear Layer," *Phy. Fluids A*, Vol. 3-8, 1991, pp. 1915-1923.

Sato, T. and Kaji, S. (1992), “Study on Steady and Unsteady Unstart Phenomena Due to Compound Choking and/or Fluctuations in Combustor of Scramjet Engines,” AIAA Paper 92-5102, December 1992.

Scarano, F., Riethmuller, M. L. (2000), “Advances in iterative multigrid PIV image processing,” *Experiments in Fluids*, Vol. 29, No. 7, 2000, pp. 51-60.

Sedon, J. and Goldsmith, E. L., (1999), *Intake Aerodynamics*, AIAA Education Series, Reston, VA, 1999.

Shapiro, A. H., (1953), *The Dynamics and Thermodynamics of Compressible Fluid Flow Volume I*, John Wiley and Sons, New York, 1953.

Shimura, T., Mitani, T., Sakuranaka, N. and Izumikawa, M. (1998), “Load Oscillations Caused by Unstart of Hypersonic Wind Tunnels and Engines,” *Journal of Propulsion and Power*, Vol. 14, No. 3, 1998, pp. 348-353.

Sullins, G. and McLafferty, G. (1992), “Experimental Results of Shock Trains in Rectangular Ducts,” AIAA Paper 92-5104, December 1992.

Van Wie, D. M. (2000), “Scramjet Inlets,” *Scramjet Propulsion*, edited by E. T. Curran and S. N. B. Murthy, Vol. 189, Progress in Astronautics and Aeronautics, AIAA, Reston, VA, 2000, pp. 447–511.

Van Wie, D. M., Kwok, F. T. and Walsh R. F. (1996), “Starting Characteristics of Supersonic Inlets,” AIAA Paper 96-2914, July 1996.

Waltrup, P. J. and Billig, F. S. (1973), “Prediction of Precombustion Wall Pressure Distributions in Scramjet Engines,” *Journal of Spacecraft and Rockets*, Vol. 10, No. 9, 1973, pp. 620-622.

Wang, C.-P., Zhang, K.-Y. and Cheng, K.-M. (2006), "Pressure Distribution Measurements in Scramjet Isolators under Asymmetric Supersonic Flow," AIAA Paper 2006-818, Jan. 2006.

Westerweel, J. (1997), "Fundamentals of Digital Particle Image Velocimetry," *Measurement Science and Technology*, Vol. 8, No. 12, 1997, pp. 1379-1392.

White, F. M. (1991), *Viscous Fluid Flow*, McGraw-Hill, Boston, 1991, pp. 500-502.

Wieting, A. R. (1973), "Exploratory Study of Transient Unstart Phenomena in a Three-Dimensional Fixed-Geometry Scramjet Engine," NASA TN D-8156, March 1976.

Yuceil, W. A. (1995), "An Experimental Investigation of a Forward-Facing Nose Cavity on a Blunt Body at Mach 5," Ph.D. dissertation, Dept. of Aerospace Engineering and Engineering Mechanics, The University of Texas at Austin.

Vita

Justin Lawrence Wagner was born in Houston, Texas on July 16, 1981, the son of Margaret Beth and Gerald Lawrence Wagner. He graduated from Newburgh Free Academy in Newburgh, New York in June of 1999. Following high school, he enrolled at the State University of New York at Buffalo where he received his Bachelor of Science degree in Aerospace engineering in 2003. Shortly thereafter, in August 2003, he started graduate school in the department of Aerospace Engineering and Engineering Mechanics at The University of Texas at Austin.

Permanent Address: 1658 Route 300, Newburgh, NY 12550

This dissertation was typed by the author.